PHOTOCONDUCTIVE MICROSCOPY OF STRAINED DONOR BOUND EXCITONS IN SILICON

PIERANDREA CONTI

A thesis submitted for the degree of
DOCTOR OF PHYLOSOPHY

UNIVERSITY COLLEGE LONDON

LONDON CENTRE FOR NANOTECHNOLOGY

PHYSICS & ASTRONOMY

August 26, 2024

All'Anna

I, Pierandrea Conti confirm that the work presented in this thesis is my own. Where information has been derived from other sources, I confirm that this has been indicated in the thesis.

August 26, 2024 *Pierandrea Conti*

ABSTRACT

PHOTOCONDUCTIVE MICROSCOPY OF STRAINED DONOR BOUND EXCITONS IN SILICON

PIERANDREA CONTI

The silicon donor spin has one of the longest coherence times among quantum systems and has shown great potential for quantum information and magnetic sensing applications. Among the research focus on the challenge of donor spin readout, the donor bound exciton (D^0X) optical transition offers a promising hybrid optical-electrical spin readout method, spin-selectively ionising the donor via Auger decay.

This work explores the miniaturisation of D^0X photoconductive readout to the microscale in silicon devices. The electrical detection of $\sim$2000 shallow implanted phosphorus donors is achieved with a 2 µm focused laser beam within a pair of microfabricated metal-oxide planar contacts. High frequency D^0X detection is further demonstrated by LC-resonant RF reflectometry, and it is employed to achieve microsecond pulsed D^0X detection.

Donor bound excitons are sensitive to lattice strain due to the strong silicon valence band spin-orbit coupling, yielding broadened, split peaks, a key factor in thermally strained microfabricated devices. The effect of strain on the D^0X transition is first explored in an isotopically purified ^{28}Si:P sample subject to calibrated uniaxial strain, detecting D^0X induced spin polarisation by electron paramagnetic resonance. Strained bound excitons in micro-devices are then studied by means of laser scanning microscopy, showing good agreement with theoretical predictions by FEM solid mechanics simulations and highlighting the potential of donor bound excitons for micro-strain sensing.

Finally, D^0X induced donor spin polarisation is explored in microfabricated devices, with neodymium magnets and PCB antennas for magnetic field and microwaves generation. Electron spin polarisation is achieved under a continuous laser pump, and its sensitivity to experimental conditions is studied. Transient pump-probe and optical-microwave spin driving is explored, displaying a total absence of lasting donor spin polarisation and suggesting likely fast spin relaxation.

IMPACT STATEMENT

Donor spins in silicon have demonstrated some of the longest coherence times among quantum systems. Leveraging the advanced development of the semiconductor industry, they show promise in key applications such as quantum memory and magnetic sensing.

This thesis develops and downscales the sensitive, hybrid donor spin readout technique of photoconductive donor bound exciton readout. Having previously been limited to the millimetre scale, this work advances the miniaturisation of donor bound exciton readout to the microscale, approaching the diffraction and the few donors detection limit.

Novel electrical techniques are developed for the sensitive electrical detection of donor bound excitons in silicon, validating experimental parameters for future fabrication. MOS contacts are demonstrated to be sensitive to local donor ionisation and suitable for near interface detection. Donor bound exciton detection is further demonstrated for the first time at high frequencies via LC-resonant RF reflectometry, opening the way to fast transient electrical detection. These new electrical techniques open the way to sensitive, near interface photoconductive detection in silicon, with potential for fast detection approaching the sub-microsecond Auger limit.

The subject of strain in microfabricated devices is explored, and a novel technique is developed to locally detect the strain of near-surface donors, producing accurate, near diffraction scanning microscopy maps of local donor strain. This result advances donor bound exciton readout as a promising and accurate surface strain mapping technique. Photoconductive readout is demonstrated near oxide interfaces, pushing the microscale limit of D^0X devices.

Finally, through pump-probe experiments in magnetic fields, this work highlights the potential spin depolarising effect induced by the electrical measurement fields, introducing a delicate and crucial topic that should be explored in future research.

This work explores all key aspects of microscale photoconductive donor bound exciton detection: optical electrical, mechanical and magnetic. Novel techniques were developed or adapted from other fields, and multiple issues were identified, in the hope that they may be considered and addressed in future work on the subject, with the goal of fully developing this technique for microscopic photoconductive magnetic resonance of donors in Silicon. Furthermore, beyond the specific case of donor bound excitons, some of these techniques could also find use in other areas of semiconductor photoconductive detection, as well as for sensitive strain sensing applications.

ACKNOWLEDGEMENTS

This work was only possible thanks to the help and support of many great people, colleagues and friends. Here I would particularly like to thank:

John Morton, for offering me this opportunity and going above and beyond in supporting me throughout this PhD. Thank you for all the advice and patience, for leaving me the freedom to explore, yet guiding me when I got lost. Thank you in particular for the much-needed help and encouragement at a time when I most needed it.

Siddharth Dhomkar, for teaching me everything I know about optics and helping me in the design and construction of this works' optical and cryogenic setups. Thank you for guiding and encouraging me, but most of all thank you for your contagious enthusiasm and unwavering optimism.

Philipp Ross, for introducing me to the world of donor bound excitons, and fabricating the amazing, resilient silicon devices this work is based on.

John Mansir, for introducing me to the world of silicon, strain and ESR, and for guiding me through the first steps, and long experimental nights, of my PhD.

Christoph Zollitsch, for helping and advising on this works' electrical and cryogenic setups. Thank you for teaching me so much, particularly early on when even coaxial cables and soldering seemed exotic, and for your coffee expertise, as well as your wonderful sense of humour.

Simon Schaal, for advising on the design of this works' reflectometry setup, for all the good chats and for somehow having no flaws beyond your passion for pineapple on pizza.

Oscar Kennedy, for helping me with cleanroom fabrication, x-ray diffraction and for always enthusiastically offering insightful advice and encouragement.

The LCN cleanroom staff, for the invaluable training, support and advice throughout the years: Rohit Khanna, for the invaluable electronic prototyping and support. Steve Etienne, Lorella Rossi and VJ Krishnan for the cleanroom and wire-bonding training and support.

David Wise, for struggling with me through two optics labs and a surprising amount of plumbing. Thank you for your incredible insight on every topic imaginable, the unmatched graph styling advice, and for sharing my same passion for taking totally unnecessary coding tangents, as well as your ability to always get everyone to the pub on a Friday.

James O'Sullivan, the most adventurous physicist I know inside and outside the lab. Thank you for all the wild ideas, the shared lunches, the Simpsons

quotes that are now permanently stuck in my head, and for always contributing to a light-hearted atmosphere during our PhDs.

Felix Donaldson, for sharing with me the ups and downs of optical and cryogenic design and debugging, for your enthusiasm and all the good chats.

Gavin Dold, for all the advice, the always unique and inventive insights and the beer expertise.

All the past and present members of the QSD group I had the privilege to meet, work, drink and play football with: Virginia Ciriano, Jingyu Duan, Joe Alexander, James Williams, Ed Thomas, Sofia Patomäki, Gareth Jones, Michael Fogarty, Salahuddin Nur, Naitik Panjwani, Anasua Chatterjee, HeeJin Lim, Leonid Abdurakhimov and Mantas Šimėnas.

Christopher Simpson, for being a great friend, for all the climbing, tennis, brunches and drinks, and for reminding me to sometimes get out of the lab.

Martina De Pascalis, for being a wonderful flatmate and friend, always motivating me to try new things and meet new people.

Edoardo Crimini, for all the sailing adventures that kept me clear-headed throughout this PhD and for being an unwavering friend I can always rely on.

Antonio Vagnerini, for always cheering me up with your contagious enthusiasm and for all the memorable ski trips.

My sister Margherita and my brother Lorenzo, for always being there to cheer me up.

My late aunt Annamaria, for having always been a key soothing presence in my life who inspired me to be better.

My Mum and Dad, for always supporting and encouraging me no matter what, and somehow putting up with me throughout the ups and downs of a long education.

CONTENTS

1. INTRODUCTION

1.1. SILICON DONOR SPINS

Silicon and the invention of the MOS transistor have defined the modern information age. Seventy years of research and industrial development have made silicon the purest and most cost-effective semiconductor with applications in the computing, photonics and energy sectors. In the past 25 years, since the proposal of the donor spin-based Kane quantum computer [1], silicon has further been the subject of renewed attention as a host material for a spin quantum memory and magnetic sensing. The high purity and established fabrication techniques make silicon an ideal, well understood platform for solid state research. With the use of isotopic purification to isolate the spin-0 ^{28}Si isotope, long spin coherence times have been demonstrated in the order of seconds for the electron [2, 3] and almost an hour for the donor [4], rivalled only by trapped ion qubits [5, 6].

Due to its small magnetic dipole and periodic wavefunction, there has been a considerable focus on the difficult tasks of coherent coupling and readout of the donor spin. Traditional electron paramagnetic resonance (EPR) is fundamentally limited to trillions of spins using 3D macroscopic resonators and thousands of spins using thin film superconducting resonators [7]. To overcome this sensitivity limit, hybrid detection techniques have been explored, generally involving the coupling and conversion of a spin state to a more readily detectable quantum system.

Beyond the sensitivity of traditional, macroscopic ESR resonators, millimeter superconducting resonators have been studied with the goal to couple donor spin ensembles to superconducting qubits, providing a long coherence quantum memory to an advanced platform which has already demonstrated systems consisting of hundreds of qubits [8] and practical quantum computing results [9]. Effectively, superconducting resonators also have a use as sensitive ESR resonators, having achieved the detection of an ensemble of 2000 donor spins [7], while schemes for the nanoscale detection of a single donor have been proposed [10]. The limitations again pertain to the required millikelvin temperatures and the quantum sensitivity limit from the small magnitude of the spin magnetic moment.

Quantum dots are promising qubits of their own accord, with gate and spin coherence times in the region of nanoseconds and milliseconds respectively [11].

Recently, research has strived to couple the dot electron to the donor spin to access their longer coherence lifetimes. This field has advanced remarkably in the past few years, successfully coupling to individual donor spins via the spin blockade [12] and electron exchange [13, 14]. Quantum dots are unparalleled in single donor detection sensitivity, while practical limitations mostly involve the need for millikelvin dilution refrigeration temperatures to reach acceptable charge lifetimes, as well as the need for state-of-the art CMOS nanoscale fabrication.

This work falls within the framework of hybrid spin detection for quantum information and magnetic sensing, exploring, developing and downscaling the optical-electrical readout of the donor spin through the optical D^0X bound exciton transition and its electrical Auger decay.

1.2. Donor Bound Exciton Readout

The donor bound exciton state (D^0X) consists of an electron-hole exciton bound to a neutral D^0 donor, practically a 3-particle electron-electron-hole bound state. Although it can naturally form through the pinning of free excitons, the resonant optical excitation has drawn considerable attention due to the possibility of coherently pumping the state via a sharp, resonant near infrared $\sim 1\,\mu\mathrm{m}$ optical transition. This narrow resonance has been measured down to $10\,\mathrm{neV}$ [15] in $^{28}\mathrm{Si}$ and is theoretically lifetime limited to only $2.5\,\mathrm{neV}(600\,\mathrm{kHz})$. This allows for the resolution of donor electron and nuclear spin states, allowing for spin-selective optical pumping.

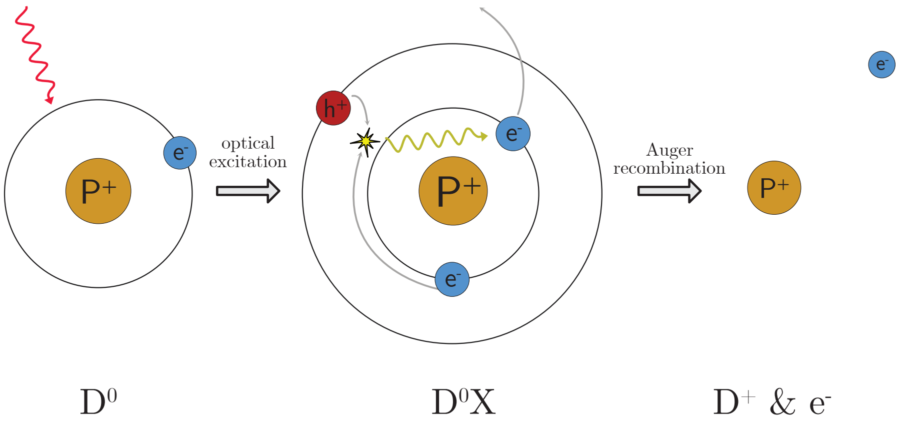

Figure 1.1: D^0, D^0X and D^+ donor states with their transitions.

More notable, however, is the decay path of the D^0X state: its radiative lifetime is comparatively long at a few milliseconds, and the dominant decay mechanism is through Auger recombination, where the hole and an electron recombine, transferring the resulting energy to the second electron, which is ionised into the conduction band as a hot electron. The Auger lifetime is relatively short, 270 ns for a phosphorus donor [16], thus effectively generating a spin-selective, transition $D^0 \rightarrow D^+$, effectively a technique for spin to charge conversion. Electrical readout has attracted significant interest as it is potentially simpler than photoluminescent detection, it may be able to overcome the 1 µm diffraction limit and reach a higher detection efficiency.

The donor bound exciton transition has been studied extensively, with most research initially focused on purely optical pumping and detection of the donor bound exciton no-phonon line and phonon replicas [17–21]. The Auger decay pathway was first proposed by Nelson [22], and new interest was sparked by the Kane proposal [1] of a silicon spin quantum computer.

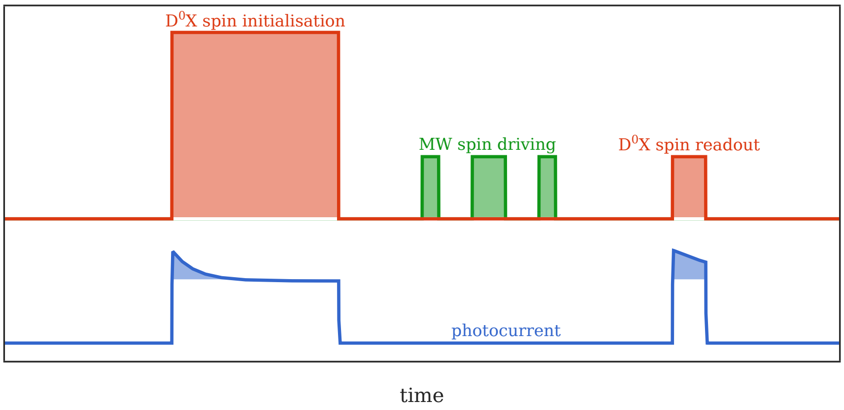

Figure 1.2: D^0X photoconductive spin initialisation, manipulation and readout sequence.

Only as recently as 2015, Lo [23] demonstrated the full optical-electrical initialisation and readout of the phosphorus electron spin state in an epitaxial ^{28}Si sample, together with microwave spin manipulation. Franke [24] used D^0X electrical readout to achieve donor electron nuclear double resonance (ENDOR). Ross further demonstrated bulk level capacitive D^0X detection and spin readout [25, 26], again in a ^{28}Si phosphorus doped sample.

Previous D^0X work has so far focused on bulk level donor detection and near millimetre detection. The smallest detection geometries employed before this work were a pair of 700 µm long contacts with 100 µm separation under millimetre sized beam illumination [23]. Loippo performed electrical detection on a 50 µm laser spot on a bulk doped sample [27], however without donor spin polarisation detection. Attempts to scale down and electrically detect D^0X Auger electrons in nanoscale devices such as finfets were so far not fruitful [28], likely due to the large shifts of the optical line under strain, a major topic of this work, as well as possibly the high electric field conditions near metal interfaces.

D^0X photoconductive readout stands out compared to other spin detection techniques in allowing for comparatively high temperature operation, only requiring liquid helium temperatures. The electrical detection further promises efficiencies outclassing photoluminescence and magnetic sensing.

Finally, optical scanning microscopy offers flexibility of operation and local spin selectivity down to the diffraction limit, with proposed schemes to scale below it using strain and electrical selectivity.

1.3. This Work

This work expands on previous research of electrically detected donor bound excitons by exploring the downscaling of electrical detection to the near diffraction limit through the use of scanning close-working distance optical setup and microfabricated optical devices.

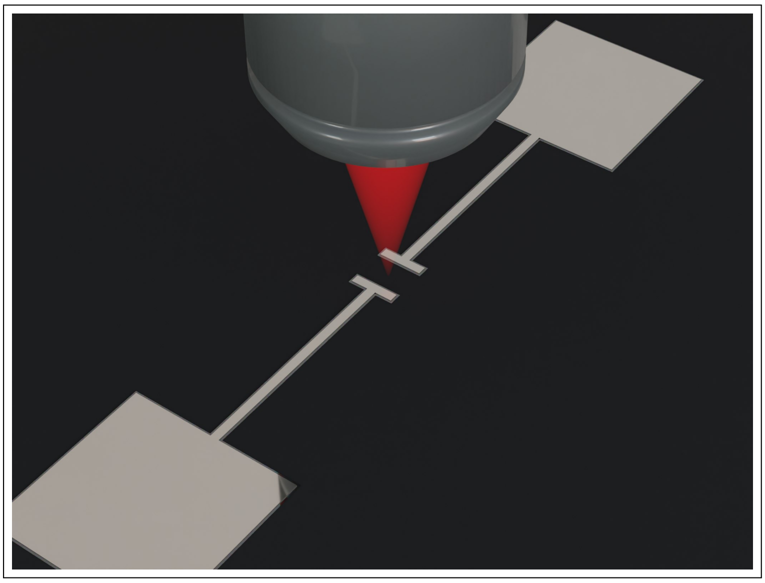

Figure 1.3: Render of this works' D^0X laser microscopy technique.

Chapter 2 discusses the physics and literature relevant to this work. The topic of semiconductor silicon transport at low temperatures is discussed, crucial to develop an understanding of electrical devices at liquid helium temperatures. Shallow donors are then discussed, in particular regarding their role as a model Bohr atom and spin platform in a solid state system. Finally, the physics of the donor bound exciton state is explored, with particular emphasis on magnetic and strain theoretical models.

Chapter 3 describes the experimental methods employed in this work: the experimental devices, optical and electrical setups as well as the hardware and software used and developed.

Chapter 4 explores electrical detection technique of the D^0X transition in microscale devices under focused laser illumination of a few thousand localised donors, analysing the impact of contact chemistry and detection techniques. Regarding the choice of contacts, it is shown that Schottky contacts lead to a strong sensitivity to the low-density residual bulk donors of nominally intrinsic silicon, but fail in detecting local implanted donors. It is then shown that metal-oxide-semiconductor (MOS) contacts are able to effectively detect the D^0X ionisation of local donors, with only a marginal signal from the bulk residual donors. Then, two techniques are explored and optimised for sensitive detection of the D^0X signal: low frequency capacitive detection and radio frequency LC resonant reflectometry.

Chapter 5 explores the crucial theme of strain in microfabricated devices. The issue of strain splitting and broadening of the D^0X spectrum has been explored extensively before, and strain appears to have so far hindered attempts of D^0X device downscaling significantly. D^0X detection in silicon-on-insulator (SOI) substrates, which would eliminate the issue of substrate background signal, has so far proved elusive due to the large built-in strain from the oxide interface stress [29], and for the same reason attempts at detecting donor bound excitons in nanodevices have not been fruitful [28]. This chapter explores strain in microfabricated device employing a focused laser scanning microscopy setup, demonstrating position dependent strain splitting. The strain profile of multiple microscale devices is analysed, with contact separations down to 5 µm and directly underneath thin oxide layers.

Finally, Chapter 6 explores the use of D^0X photoconductive readout for donor electron spin polarisation and readout. Donor bound exciton photoconductive spectra are explored and modelled in magnetic fields parallel and perpendicular to the dominant strain axis, and donor spin polarisation is demonstrated under D^0X continuous optical pumping, but is observed to be short-lived, undetectable in transient experiments. The cause of spin relaxation is investigated, with the measurement AC electric field identified as the likely cause of the short lived spin polarisation. Finally, experimental methods and attempts at transient donor spin polarisation experiments and hybrid microwave pEDMR experiments are discussed.

2. Theory and Background

2.1. Semiconductor Silicon

Monocrystalline silicon, shown in Figure 2.1a(a), is a diamond cubic lattice, with each atom sharing a valence electron with one of 4 nearest neighbours in a covalent bond, and a lattice constant of 5.42 Å [30]. A hard, brittle crystal, silicon is usually grown from a molten precursor and a crystal seed. The most popular growth technique is the Czochralski method, where a seed attached to a rod is dipped in molten silicon and slowly pulled out, crystallising as it cools [31]. Silicon owes its industrial popularity to the efficiency and scalability of its fabrication as much as its electrical properties, and Czochralski silicon (CZ-Si) amounts to 90% of worldwide production and can reach resistivities up to 2 kΩ [32].

Sensitive optical and electrical applications, of which this work is a prime example, require an even higher crystal purity with lower concentrations of impurities, as these can lead to a multitude of issues such as carrier emission, trapping and scattering, localised strain, magnetic noise and optical broadening. Higher purity is primarily achieved with the float-zone silicon growth technique, starting with a polycrystalline rod and a seed crystal at one end. A thin heating coil wraps around the rod, and sweeps through the rod, melting the polycrystal, which then crystallises as the coil sweeps away [33]. Most impurities originally present in the rod are segregated in the molten zone, and thus float to one end of the rod where they can be discarded. The higher purity of float-zone silicon (FZ-Si) leads to resistivities upwards of 10 kΩ cm and impurity concentrations down to 10^{11} cm^{-3}. Other techniques can be employed for specialised applications, most notably epitaxial growth for depositing thin silicon layers on a multitude of base substrates.

2.1.1. Electronic Properties

The electronic structure of a crystal describes the energy and momentum states electrons may occupy and arises from the overlapping atomic potentials of the individual atoms in the lattice. Thanks to the periodicity of the crystal, the wavefunction of an electron can be described as the product of a set of products

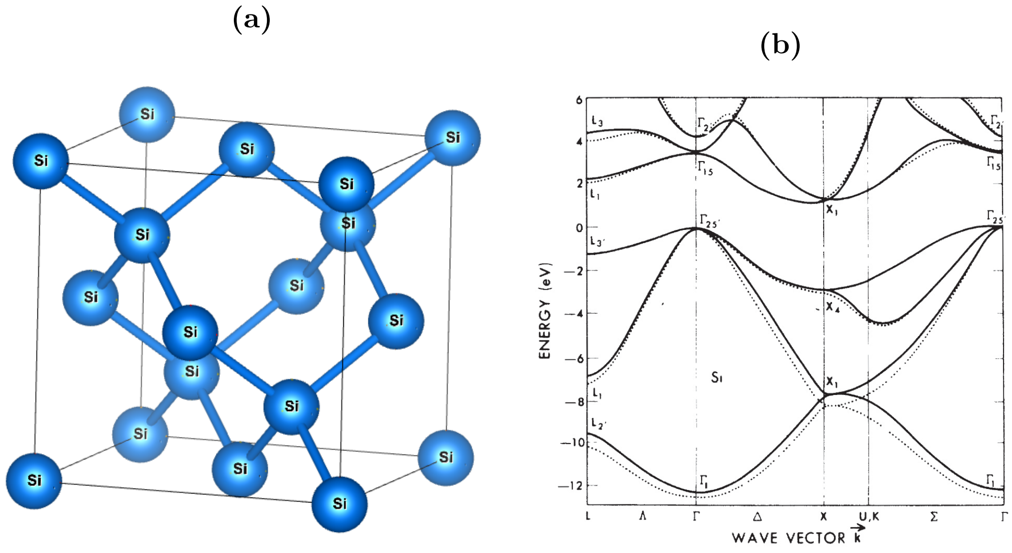

Figure 2.1: (a) Silicon crystal structure, modelled in VESTA 3 [34]. (b) Silicon electronic band structure, reproduced from Chelikowsky [35]

of local functions, bound within a unit cell, and periodic terms [36, p. 21].

$$\Psi(x) = \sum_k A_k u_k(x) e^{ikx} \tag{2.1}$$

This basis set is employed to solve the energy equation of the potential energy equation of the overlapping atomic potential, leading the band structure, which describes the energy-wavevector relation which derives from solving such wavefunction equation in the crystal potential. It can be limited to a small range of wavevectors $\left(-\frac{\pi}{a_{\text{Si}}}, \frac{\pi}{a_{\text{Si}}}\right)$ due to the periodicity of the lattice.

As shown in Figure 2.1b, silicon is a semiconductor due to the indirect bandgap at the Fermi level, 1.12 eV [37] at room temperature. The valence band lies at the $k = 0$ center of the Brillouin zone and consists of 3 bands due to the spin-orbit coupling. At the top there are 2 degenerate $|S = \frac{3}{2}, m_s = \pm\frac{1}{2}\rangle$,$|S = \frac{3}{2}, m_s = \pm\frac{3}{2}\rangle$ light and heavy hole bands and one $|S = \frac{1}{2}, m_s = \pm\frac{1}{2}\rangle$ split-off band. The conduction band does not present significant spin-orbit coupling, but instead consists of 6 symmetric minima at the k_0 points perpendicular to the cubic cell faces [001].

The electronic structure of a solid determines its electrical properties. The forbidden band gap determines the semiconductor behaviour of silicon, and the quadratic band bending determines the electrical transport properties. This arises from the Bloch formulation of the electron wavefunction of Equation 2.1 and the effective mass approximation. As the energy bands have a dominant parabolic term at their minima, they follow the quadratic relation [36, p. 69]

$$E_k = E_0 + \frac{\hbar^2 k^2}{2m^*} \tag{2.2}$$

where m^* determines the band parabolic shape but can classically be interpreted as an effective mass of the carrier in the band from the energy momentum equation. Thus, effective mass theory simplifies the lattice field as generating a band dependent mass tensor. In silicon, the electron has an effective mass of $0.92m_\mathrm{e}$ along its bands and $0.19m_\mathrm{e}$ perpendicular to them [38]. The valence band requires a spin orbit correction, and results in two different relative effective masses depending on the spin quantum number of $0.17m_\mathrm{e}$ for the light hole and $0.46m_\mathrm{e}$ for the heavy hole in the [001] axis [39], as well as a separate split-off band.

In its pure, undoped and unbiased form, the Fermi level lies exactly between the valence and conduction band, and silicon is effectively an insulator. The Fermi level can be shifted with charged impurities or the application of a bias voltage, thus tuning the conductivity between an insulator and a conductor. Donors substitute a silicon atom in the crystal matrix but have one or more valence band electrons. The silicon valence band is full, so the extra electron is promoted to the conduction band. The extra charge of the dopant atom would bind the electron in a local conduction band state, so doping is usually achieved with shallow dopants with low binding energies that can be overcome thermally, leading to a free conduction band electron and conductive silicon. This is usually achieved with group V dopants such as phosphorus (P), arsenic (As), antimony (Sb) and bismuth (Bi), while group VI elements form deeper impurities with 2 extra valence electrons. Inversely, group III acceptors such as boron (B), aluminium (Al) and gallium (Ga) have one less valence electron, thus generating a hole in the valence band.

2.1.2. OPTICAL PROPERTIES

Silicon is a high dielectric ($\epsilon_{Si} = 11.7$ [40]) material employed in a wide variety of optical applications, such as photovoltaics, sensitive light detectors and photonics.

The optical properties of silicon can be divided in two broad categories: bulk and impurity based. Bulk optical absorption is largely due to band to the band electron transitions, leading to significant absorption cross sections only above the bandgap level. The bandgap sits in the near infrared region and has a mostly quadratic temperature dependence, which is well described by Varshni's empirical model [41], unifying the asymptotic linear dependence where $T \gg \theta_\mathrm{D}$ and quadratic dependence where $T \ll \theta_\mathrm{D}$, with $\theta_\mathrm{D} = 645\mathrm{K}$ the Debye temperature for silicon.

$$E_\mathrm{g}(T) = E_\mathrm{g0} - \frac{\alpha T^2}{T + \beta} \tag{2.3}$$

This model is used in this work for all temperature dependent transport calculations presented in Section 2.2, and still gives a reasonable match down to zero temperature, however it loses some accuracy at the very low liquid helium temperatures employed in this work, which is crucial for the accurate modelling of the temperature dependent $\mathrm{D^0X}$ energy shifts. In this $<5\,\mathrm{K}$ low temperature regime, the bandgap is well described by the model of Cardona [42].

$$E_g(T) = E_{g0} - AT^4 \tag{2.4}$$

The temperature dependence of the bandgap leads to a strong temperature dependence of the absorption spectrum as shown in figure 2.2. The experimentally measured bandgap at low temperature is 1.17 eV at 10 K [37]. silicon is an indirect semiconductor: its valence band maximum and conduction band minima are at different k-points, shown in Figure 2.1b, which means that optical band to band transitions must be phonon assisted, apart from transitions to higher, $k = 0$ bands. This means that bulk optical absorption can still occur below the bandgap where phonons exist with sufficient energy, leading to a broad absorption slope at high temperatures, and a sharp transition at low temperatures as the phonon population energy cools down.

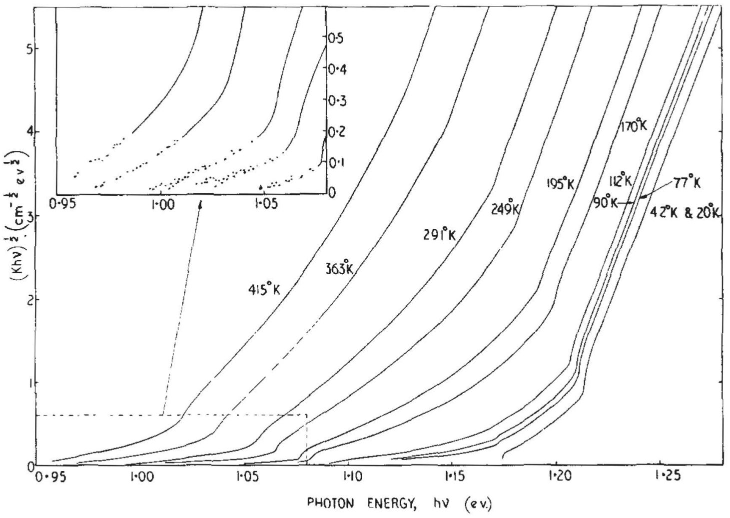

Figure 2.2: Experimental temperature dependent optical absorption of silicon, adapted from Macfarlane [43].

In the near infrared region below the bandgap, roughly between 1–7 µm [44] and especially at low temperatures, the bulk is largely transparent to illumination with low losses and a large dielectric constant. Also thanks to the low cost and quality of silicon fabrication, resulting from the maturity of the industry, silicon photonics has flourished [45], opening the possibility for the donor bound excitons to be combined with photonic structures, as it has already been demonstrated by Nur [46].

While the bulk of silicon is highly transmissive in the below bandgap NIR and FIR regions, impurity states and lattice defects can be optically active. Regarding donor states, which are the subject of this work, various schemes for optical donor and spin manipulation have been explored. Orbital transitions of the shallow donor are the equivalent of the Bohr atom orbital transitions and lie in the far infrared terahertz region of 30–40 µm [47–49], while increasing up to 3 µm for deeper donors such as selenium [50]. In this regard, silicon has not been nearly as popular as other optically active impurity platforms such as diamond vacancy centres [51] or more recently silicon carbide [52]. Recently, colour centres such as T and G centre defects have attracted attention due to their optical activity in the popular NIR region [53, 54], which is also the reason why the here discussed donor bound excitons are of particular interest.

2.2. TRANSPORT IN CRYOGENIC SILICON

Using the approximations of effective mass theory, the transport of electrons and hole carriers in silicon can be derived from the semiclassical transport equation [36, p. 205].

$$m^* \left(\frac{d^2 x_i}{dt^2} + \frac{1}{\tau} \frac{dx_i}{dt} \right) = -E_i \tag{2.5}$$

Where the first order term represents scattering of the carrier with an average time constant τ. Solving for the velocity and using the definition of current $J_i = nq\frac{dx_i}{dt}$, with n the density of carriers and q the carrier charge, gives the general transport equation [55, p. 74]

$$\begin{aligned} J_{i,drift} =& nq\frac{dx_i}{dt} \\ =& n\frac{q\tau}{m^*}E_i \\ =& n\mu E_i \end{aligned} \tag{2.6}$$

where $\mu = \frac{q\tau}{m^*}$ is the carrier mobility. This yields the conductivity $\sigma = \frac{1}{\rho}$ from the Ohmic current relation, which including transport from both electron and hole carriers is $\sigma = q\left(\mu_e n_e + \mu_h n_h\right)$ [36, p. 205]. Simplistically, the conductivity of a semiconductor is equal to the number of carriers multiplied by their ability to move unscattered.

The above is relatively straightforward for non-interacting carrier transport, however the charged carriers generate a potential of their own, with non-isotropic carrier densities leading to a potential gradient and consequently a diffusion current

$$J_{D,i} = -qD\frac{\partial n}{\partial x_i} \tag{2.7}$$

where the diffusion constant $D = \frac{\mu k_B T}{q}$ comes from the Einstein relation [55, p. 179][56, p. 119]. The two currents are generally referred to as drift current from an applied electric field, and diffusion currents from a carrier density gradient, yielding the total current

$$J_i = e\left(n\mu_e + p\mu_h\right)E_i + eD_e\frac{dn}{dx_i} - eD_h\frac{dp}{dx_i} \tag{2.8}$$

At room temperature transport is dominated by the carrier density, which mostly depends on the intrinsic and doping carrier density $n = n_i + n_n$. Mobility is limited by electron-phonon scattering, and thus more or less independent of doping density. At low temperatures, however, several notable changes must be accounted for, invalidating several semiconductor assumptions and requiring a careful analysis which is given below.

2.2.1. INTRINSIC CARRIER DENSITY

The electron and hole carrier density of a semiconductor in the absence of a potential gradient depends on the intrinsic thermal carrier density and the ionised dopant densities, N_D^+, N_A^+. Electrons and holes are fermions and thus follow Fermi-Dirac statistics. For non-degenerate, low carrier densities this can however be safely approximated to a Boltzmann distribution, leading to the conduction and valence band populations from Equation 2.9.

$$n_e = N_c e^{\frac{E_f - E_c}{k_B T}}, \qquad n_h = N_v e^{\frac{E_v - E_f}{k_B T}} \tag{2.9}$$

N_c here is the effective density of states of the conduction band, E_F is the Fermi energy and E_c if the conduction band energy. The intrinsic carrier density is the carrier density of the silicon crystal without any doping, and is given by [55, p. 110]

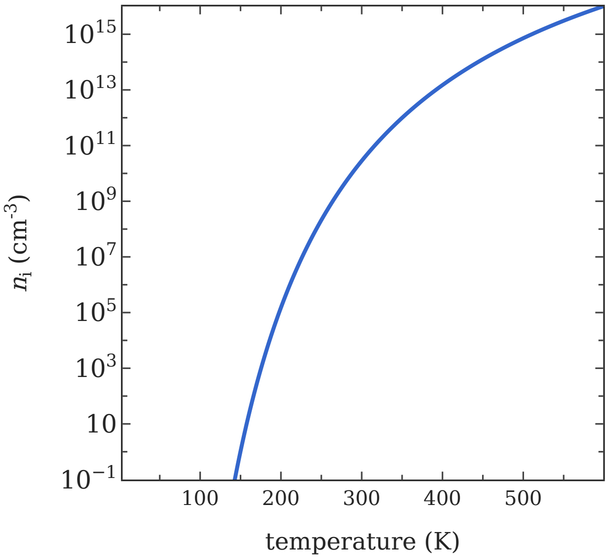

Figure 2.3: Temperature dependent intrinsic carrier density n_i of silicon calculated from Equation 2.10.

$$n_i = \sqrt{n_\mathrm{e} n_\mathrm{h}} = \sqrt{N_c N_v}\, e^{-\frac{E_g}{2k_B T}} \tag{2.10}$$

At room temperature the intrinsic carrier density is a non-negligible $\sim 10^{10}\,\mathrm{cm}^{-3}$, but quickly vanishes at lower temperatures, as shown in Figure 2.3, and can be safely ignored at the typical liquid helium temperature of 4 K employed in this work($\ll$1 cm^{-3}). This means that, without some form of carrier generation mechanism, such as optical excitation, impurity ionisation or junction injection, at cryogenic temperatures silicon is a perfect intrinsic insulator, resembling the behaviour of high bandgap semiconductors at room temperature.

2.2.2. IMPURITY CARRIER FREEZEOUT

Charged dopant impurities are the main source of free carriers in the regular room temperature operation of semiconductor. The typical substitutional dopant impurity is typically assumed ionised in light of its low, 10s of meV binding energy. Phosphorus, which is employed in this work, has a ground state binding energy $E_0 = 45.59$meV [57]. The ionised impurity assumption however no longer holds at low temperatures where $k_\mathrm{B}T \ll e_0$, and the relative populations of the neutral D^0 and ionised D$^+$ must be expressively calculate. The bound D^0 and A^0 state against the free conduction and valence band states respectively follow the Fermi-Dirac distribution of a two-level system, similarly to the calculation for the intrinsic carrier density.

$$\frac{N_{\mathrm{D}^+}}{N_{tot}} = \frac{1}{1 + 2e^{\frac{E0-E_f}{k_B T}}} \tag{2.11}$$

Gutierrez solves this for the Fermi energy [58, p. 24]

$$E_f = \frac{1}{2}\left(E_c + E_d\right) + \frac{1}{2}k_B T \ln\left(\frac{N_d}{2N_c}\right) - k_B T \sinh^{-1}\left(\sqrt{\frac{N_c}{8N_d}}\, e^{\frac{E_d - E_c}{2k_B T}}\right) \tag{2.12}$$

which can then be substituted in eq.2.11 and 2.9 to get the ionisation ratio. As shown in Figure 2.4, at room temperature shallow impurities are almost completely thermally ionised, thus shifting the fermi level and contributing to the conduction band density. This decreases with temperature, sharply below 30 K to the point where all carriers are effectively frozen in the impurity neutral D^0 state. At ~4 K, the conduction band carrier density is at a negligible 10^{-13} cm^{-3}. The calculation is potentially more complex when accounting for the fermi level shift from both donor and acceptor impurities, however, under the low carrier density conditions typical of this work, the fermi level of electrons and holes can be treated independently under the quasi fermi level approximation [55, p. 220].

Finally, these approximations do not take into account the donor interactions, which is safe for the low to medium doping densities considered in this work but breaks down at high doping densities above ~10^{19} cm^{-3}, where donor-donor exchange interactions and appreciable donor ionisation are observed even at low temperatures [59, 60].

Overall, at the low temperature and dopant concentrations employed in this work, the thermal equilibrium has all shallow impurities frozen in the D^0 state, requiring non-thermal mechanisms such as optical, impact and field ionisation for the generation of ionised impurities and free carriers.

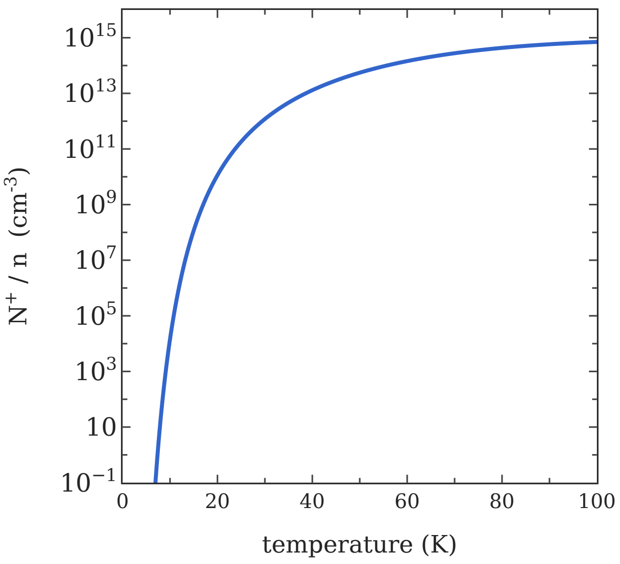

Figure 2.4: Theoretical temperature dependent conduction band carrier density for silicon doped with $10^{15}\,\mathrm{cm}^{-3}$ phosphorus donors.

2.2.3. CARRIER MOBILITY

Mobility determines the ability of a charge carrier to move unscattered, as described in Equation 2.6, and it is related to the carrier effective mass and scattering time constant τ [55, p. 160]

$$\mu = \frac{q\tau}{m^*} \tag{2.13}$$

Carrier scattering is temperature dependent and includes a series of diverse processes. At room temperature this is largely dominated by phonon scattering, but as the phonon energy decreases other scattering processes begin to dominate. At deep cryogenic temperatures, the main scattering processes to consider are phonon scattering, neutral and ionised impurity scattering, and velocity saturation. Carrier-carrier scattering and surface scattering are still potentially relevant at low temperatures, however in the low carrier density, bulk conditions employed in this work they can be safely ignored.

$$\frac{1}{\tau} = \frac{1}{\tau_{\mathrm{ph}}} + \frac{1}{\tau_{\mathrm{i}^0}} + \frac{1}{\tau_{\mathrm{i}^+}} + \frac{1}{\tau_{\mathrm{vs}}}, \qquad \mu = \left(\mu_{\mathrm{ph}}^{-1} + \mu_{\mathrm{i}^0}^{-1} + \mu_{\mathrm{i}^+}^{-1} + \mu_{\mathrm{vs}}^{-1}\right)^{-1} \tag{2.14}$$

Several mobility models have been proposed, in particular for the usually dominant, and related, phonon and charged impurity scattering. Notably, the Conwell-Weisskopf model [61] treats the low concentration unscreened regime and the Brooks-Herring model [62] the screened impurity one. Ridley reconciles the two models with a thorough theoretical treatment [63]. A popular model is the Caughey-Thomas model which treats phonon and ionised impurity scattering together [64]. Here, a variation of this model developed by

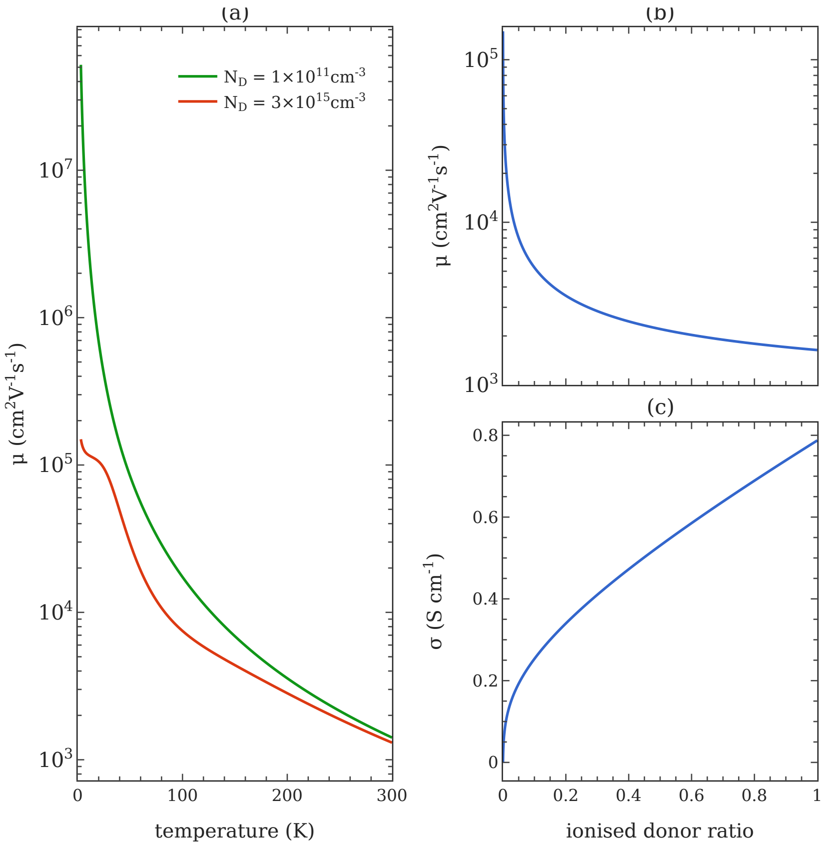

Figure 2.5: Mobility and conductivity of silicon at cryogenic temperatures. (a) Temperature dependence of electron mobility for float-zone residual and medium donor densities. (b) electron mobility and (c) electron conductivity against ionisation ratio at 3 K and $3 \times 10^{15}\,\mathrm{cm}^{-3}$ phosphorus doping.

Klaassen [65, 66] is employed, due to its independent temperature treatment of the phonon and impurity scattering components. Other popular models are the [67] and Dorkel-Leturg [68] models. Phonon scattering, also known as lattice scattering, is theoretically complex, depending on the frequencies of the acoustic and optical phonons. For this reason, a phenomenological temperature model is used instead, following a power law with experimental parameter $\theta = 2.285$ for silicon electrons [66].

$$\mu_{\mathrm{ph}} = \mu_{\mathrm{max}} \left(\frac{300}{T}\right)^{\theta} \tag{2.15}$$

Impurity scattering is caused by the Coulomb potential of donor and acceptor centres, and occurs for both ionised and neutral impurities, although clearly the former is stronger. Klaassen derives a phenomenological model [65] from the Caughley-Thomas model and then applies a temperature dependence to the individual terms [66]

$$\mu_{\mathrm{i+}} = \frac{\mu_{\mathrm{max}}^2}{\mu_{\mathrm{max}} - \mu_{\mathrm{min}}} \left(\frac{T}{300}\right)^{3\alpha_1 - 1.5} \left(\frac{N_{\mathrm{ref}}}{N_{\mathrm{D+}}}\right)^{\alpha_1} + \frac{\mu_{\mathrm{min}}\mu_{\mathrm{max}}}{\mu_{\mathrm{max}} - \mu_{\mathrm{min}}} \left(\frac{300}{T}\right)^{\frac{1}{2}} \frac{n}{N_{\mathrm{D+}}} \tag{2.16}$$

where both $\mu_{\mathrm{min}}, \mu_{\mathrm{max}}$,$N_{\mathrm{ref}}$,$\alpha_1 = 0.711$ and $\theta = 2.285$ are material specific parameters determined experimentally.

Neutral impurity scattering is an important low temperature scattering mechanism which is usually overlooked, as above ~50 K most impurities are ionised and charged impurity scattering dominates. The model from Sclar [69] and Li [70] has shown good agreement with experimental data and it is used in this work, in the form presented by by Li

$$\mu_{\mathrm{i}^0} = \frac{1}{3}\mu_{\mathrm{N}}\left(2\sqrt{\frac{k_B T}{E_N}} + \sqrt{\frac{E_N}{k_B T}}\right) \tag{2.17}$$

$$\mu_{\mathrm{N}} = \frac{2\pi q^3 m^*}{5\epsilon_{\mathrm{Si}} h^3 N_{\mathrm{D}^0}} \times 10^{-2} \tag{2.18}$$

Figure 2.5a shows the temperature dependent mobility under thermal equilibrium freeze-out for both doped and undoped silicon, with significant differences due to neutral impurity scattering at low temperatures. Figures 2.5a,b further show that there is a large change in mobility under donor ionisation, due to the higher scattering from ionised impurity than neutral ones, yielding a non-linear conductivity-ionised donor ratio relationship.

Finally, as mobilities tend to increase significantly at very low temperatures, velocity saturation must be accounted for, leading to a field dependent mobility [55, p. 170], although this effect is only usually relevant at high electric fields. and high mobilities.

2.2.4. Donor Impact Ionisation

It was established that at low temperatures shallow impurities such as donors are thermally frozen in the neutral D^0 state. There are however other non-thermal pathways for donor ionisation, including the subject of this work, optical ionisation. On top of that, donors can be ionised even at the low fields $F < 10^5 \mathrm{Vcm}^{-3}$, from the often-overlooked process of shallow level impact ionisation. In the case of a donor, this involves an electron gathering sufficient kinetic energy, usually from an electric field, to ionise a D^0 neutral donor and generating a D^+ charged donor and a conduction band electron. This is similar in principle to the process of band-to-band impact ionisation but requires far less energy due to the small binding energy of the shallow donor, and is thus favourable at low temperatures and low fields. The subject has been explored extensively [71–73], but has proven quite difficult to treat, as it is not simply a matter of considering the average carrier energy, but the full distribution as to be modelled, as the high energy tails can have a significant effect. Dierickx and Simoen explore the subject in depth from a theoretical standpoint [74–80], in particular at the relevant 4 K liquid helium regime, and produce a useful semi-empirical expression for the rate of shallow donor impact ionisation rate coefficient A_{I} [78]

$$A_{\mathrm{I}}(F) = \sqrt{\frac{2}{\pi}}\sqrt{\frac{2E_{\mathrm{d}}}{m^*}}\frac{\sigma_0}{x^{\frac{3}{2}}} I(x) \tag{2.19}$$

where

$$\begin{aligned} I\left(x\right) =& \left(x^2+2x^3\right)e^{-\frac{1}{x}} - \left(3x^2+2x^3\right)e^{-\frac{2}{x}} \\ x =& \frac{(\frac{1}{2}+\alpha)F^2m^*\mu^2+k_\mathrm{B}T}{E_d} \end{aligned} \tag{2.20}$$

This is useful to get a broad approximation for the magnitude of the effect and the regime where it is relevant. Notably, impurity impact ionisation depends strongly on the carrier mobility, as naturally high mobility carriers are less frequently scattered and thus able to gather the threshold kinetic energy at lower fields, indicating that the use of high-quality FZ-silicon and low doping densities enhances this effect. Figure 2.6 shows how for a high mobility $\mu = 10^5\,\mathrm{cm^2V^{-1}s^{-1}}$ impact ionisation starts to become significant at electric fields as low as $10^3\,\mathrm{V\,m^{-1}}$, and is maximised at around $10^4\,\mathrm{V\,m^{-1}}$, low fields employed throughout this work. At higher fields, other ionisation mechanisms become relevant, namely Poole-Frenkel and tunnelling ionisation [81], which are however not explored in this work. There are also some limitations to this model, such as the difficult definition of the field dependent α parameter determining the kinetic energy of a drift carrier $kT + (\frac{1}{2}+\alpha)m^*v_d^2$.

2.2.5. Donor Electron Capture

As electrons are ionised from donors, they can also be recaptured to the energetically favourable D^0 state, and although the complete freeze-out of carriers may suggest otherwise, this is often a slow process. The subject is strictly related to shallow impurity impact ionisation, and it usually is the competing mechanism at low temperatures. In general, the capture cross section of a charged impurity is given by

$$\sigma = \frac{4\pi r_c^3}{3\lambda} \tag{2.21}$$

The thermal capture rate is extended and calculated by Dierrickx under an electric field [78]

$$\begin{aligned} B_T\left(F\right) =& \sqrt{\frac{2}{\pi}}\frac{2\pi r_c^3}{\lambda}\sqrt{\frac{2k_\mathrm{B}T}{m^*}}\frac{1-\left(y+1\right)e^{-y}}{\sqrt{y}} \\ y =& \frac{k_\mathrm{B}T}{k_\mathrm{B}T+\left(\frac{1}{2}+\alpha\right)m^*\mu^2F^2} \end{aligned} \tag{2.22}$$

The capture rate is thus partially related to the impurity impact ionisation rate, and as shown in figure 2.6, they follow an opposite relation where A_I increases and B_T decreases with electric field. At the high mobilities typical of high resistivity float-zone silicon, this crossover occurs near the $3\times10^3\,\mathrm{V\,m^{-1}}$, which is very relevant to this work as it is equivalent to only 60 mV across 2 contacts 20 µm apart, although a significant voltage drop at the interfaces must be accounted for.

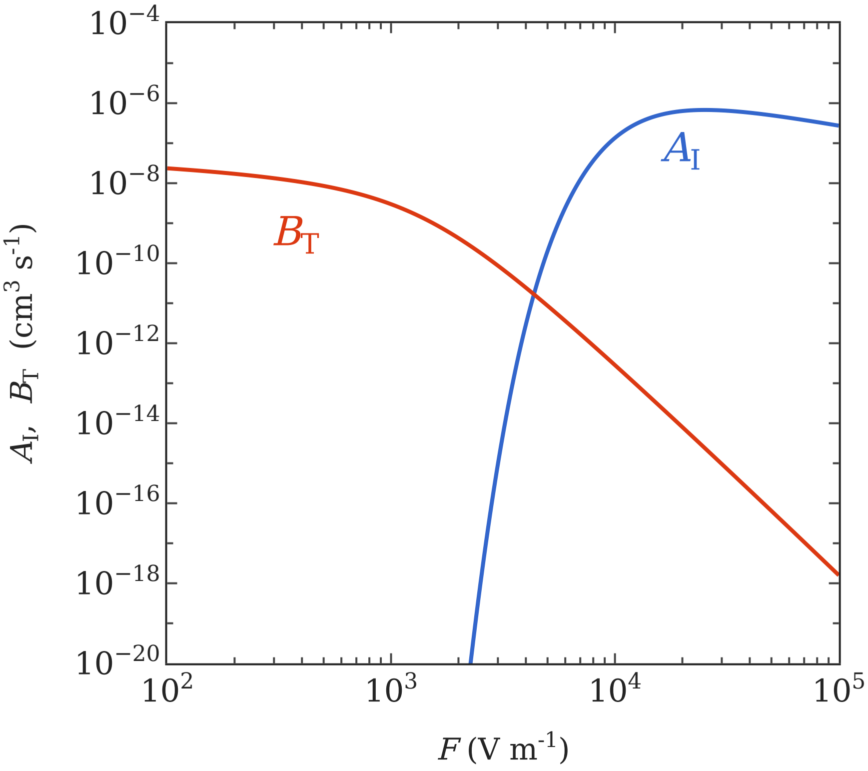

Figure 2.6: Impact ionisation(A_I) and thermal capture(B_T) rate coefficients against electric field in silicon at 4 K, mobility $\mu = 10^5\,\mathrm{cm^2V^{-1}s^{-1}}$. Higher drift energies of conduction band electrons increase the cross-section of impact ionisation and reduce that of thermal capture.

In the absence of additional ionisation and capture processes, the first order differential of the capture-ionisation process is given by

$$\frac{dN_{\mathrm{D}^+}}{dt} = n\left(A_\mathrm{I}N_{\mathrm{D}^0} - B_\mathrm{T}N_{\mathrm{D}^+}\right) \tag{2.23}$$

Equilibrium is reached where $\frac{dN_{\mathrm{D}^+}}{dt} = 0$, yielding an equilibrium ionisation ratio of

$$N_{\mathrm{D}^+} = N_\mathrm{D}\frac{A_\mathrm{I}}{A_\mathrm{I} + B_\mathrm{T}} \tag{2.24}$$

thus independent of carrier density. Further solving the full differential yields an exponential where changes in ionisation occur with a time constant

$$\tau = \frac{1}{n\left(A_\mathrm{I} + B_\mathrm{T}\right)} \tag{2.25}$$

2.2.6. Carrier Diffusion

As described in Equation 2.7, a carrier density imbalance generates a potential gradient and resulting diffusion current. Although this is largely avoided with modern trenched finfets or similar nanoscale devices, diffusion currents and their timescales are extremely important for microscale bulk devices such as those presented in this work. The diffusion current is related to drift current by the Einstein relation, $D = \mu k_\mathrm{B} T$, meaning that the diffusion-to-drift current ratio is lower at cryogenic temperatures, but the diffusion constant itself may increase due to the large nobilities observed at low temperatures, in particular for nominally intrinsic high resistivity silicon.

Full diffusion dynamics requires complex finite-element-methods simulations which are particularly difficult to converge at low temperatures [82], but a simple back-of-the-envelope calculation can already yield important information on the relevant timescale for the process with an order of magnitude estimate [83].

$$\tau_\mathrm{D}(r) \sim \frac{r^2}{2D_n} \tag{2.26}$$

2.3. Stress-Strain Formalism

Stress and strain describe the mechanical deformation of a solid under compressive, tensile and shear forces. As strain is a major topic of this thesis, this section presents a brief introduction to the relevant formalism employed in this thesis, which is employed in the next sections of this chapter as well as in Chapter 5.

Strain describes local, infinitesimal distortion of a lattice $\epsilon_{ij} = \frac{\partial u}{\partial x_i}$, which can be viewed as the deformation of the lattice's frame as [84, p. 9]

$$\hat{\boldsymbol{x}'} = (1 + \epsilon_{xx})\,\hat{\boldsymbol{x}} + \epsilon_{xy}\hat{\boldsymbol{y}} + \epsilon_{xz}\hat{\boldsymbol{z}} \tag{2.27}$$

and similarly for the other $\hat{\boldsymbol{y}'}$ and $\hat{\boldsymbol{z}'}$ axes. Strain is a 2-rank symmetric tensor.

$$\epsilon_{ij} = \begin{pmatrix} \epsilon_{xx} & \epsilon_{xy} & \epsilon_{xz} \\ \epsilon_{xy} & \epsilon_{yy} & \epsilon_{yz} \\ \epsilon_{xz} & \epsilon_{yz} & \epsilon_{zz} \end{pmatrix} \tag{2.28}$$

Strain is induced by forces acting on a solid, which is usually described in a form normalised by surface area as stress, which when normal to a surface can be simplified to the simple definition of force divided by area. Like strain, stress is also a 2-rank tensor.

$$\sigma_{ij} = \begin{pmatrix} \sigma_{xx} & \sigma_{xy} & \sigma_{xz} \\ \sigma_{xy} & \sigma_{yy} & \sigma_{yz} \\ \sigma_{xz} & \sigma_{yz} & \sigma_{zz} \end{pmatrix} \tag{2.29}$$

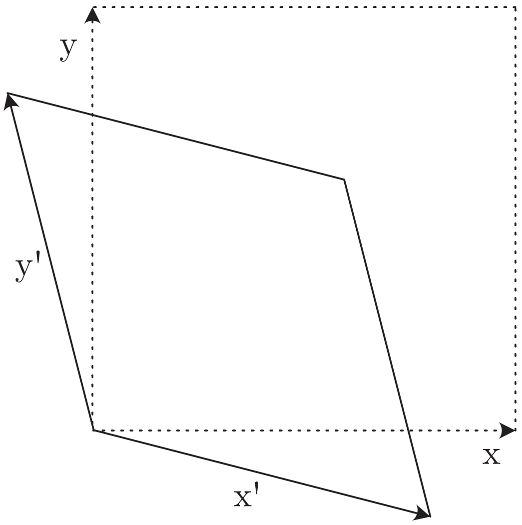

Figure 2.7: Deformation of a 2D square under [110] strain displays both axial and shear strain components.

For small, elastic deformations, stress and strain are related by the 3-dimensional generalised Hooke's law and is governed by a fourth rank tensor pair, the elasticity tensor C_{ijkl} and compliance tensor K_{ijkl}, with $C_{ijkl}S_{ijkl} = 1$ [85].

$$\begin{aligned}\epsilon_{ij} &= S_{ijkl}\sigma_{kl} \\ \sigma_{ij} &= C_{ijkl}\epsilon_{kl}\end{aligned} \tag{2.30}$$

The elasticity and compliance tensors simplify significantly under the cubic symmetry of crystalline silicon to having only 3 independent components: $c_{11} = 165\text{GPa}$, $c_{12} = -65\text{GPa}$ and $c_{44} = 80\text{Gpa}$ at $0\,\text{K}$ [86]. c_{11} represents the deformation response in the axis where stress is applied, c_{12} the Poisson like deformation of the perpendicular axes, and finally c_{44} the shear deformation.

Practically, it is often easier to work with the matrix-vector pair described in Equation 2.31, where thanks to the tensor symmetry the stress and strain tensors are flattened to 6×1 vectors, and the stress and compliance tensors can be expressed as matrices

$$\begin{pmatrix}\epsilon_{11}\\ \epsilon_{22}\\ \epsilon_{33}\\ 2\epsilon_{23}\\ 2\epsilon_{13}\\ 2\epsilon_{12}\end{pmatrix} = \begin{pmatrix} s_{11} & s_{12} & s_{12} & 0 & 0 & 0\\ s_{12} & s_{11} & s_{12} & 0 & 0 & 0\\ s_{12} & s_{12} & s_{11} & 0 & 0 & 0\\ 0 & 0 & 0 & s_{44} & 0 & 0\\ 0 & 0 & 0 & 0 & s_{44} & 0\\ 0 & 0 & 0 & 0 & 0 & s_{44}\end{pmatrix} \begin{pmatrix}\sigma_{11}\\ \sigma_{22}\\ \sigma_{33}\\ \sigma_{23}\\ \sigma_{13}\\ \sigma_{12}\end{pmatrix} \tag{2.31}$$

As an example, a stress T applied along the $\hat{\boldsymbol{x}}$ axis gives

$$\boldsymbol{\epsilon} = \begin{pmatrix} s_{11} & s_{12} & s_{12} & 0 & 0 & 0 \\ s_{12} & s_{11} & s_{12} & 0 & 0 & 0 \\ s_{12} & s_{12} & s_{11} & 0 & 0 & 0 \\ 0 & 0 & 0 & s_{44} & 0 & 0 \\ 0 & 0 & 0 & 0 & s_{44} & 0 \\ 0 & 0 & 0 & 0 & 0 & s_{44} \end{pmatrix} \begin{pmatrix} T \\ 0 \\ 0 \\ 0 \\ 0 \\ 0 \end{pmatrix} = \begin{pmatrix} s_{11}T \\ s_{12}T \\ s_{12}T \\ 0 \\ 0 \\ 0 \end{pmatrix} \tag{2.32}$$

which in matrix form is

$$\boldsymbol{\epsilon}_{[100]} = \begin{pmatrix} s_{11}T & 0 & 0 \\ 0 & s_{12}T & 0 \\ 0 & & s_{12}T \end{pmatrix} \tag{2.33}$$

Notably however, as silicon is anisotropic, the above holds where the principal axes are perpendicular to the [100] planes. New compliance matrices must be computed where that is not the case, which is done numerically. However, in this work it is preferred to work in the [100] coordinate frame and rotate the stress tensor where needed, as most parameters and conventions are in the [100] frame.

For example, expressing uniaxial strain is straightforward in the case of uniaxial stress applied along one of the principal axes, where all elements of the stress tensor are 0 except for one σ_{ii} component. However, where stress is applied at an angle, the stress tensor is non-trivial and requires a rotation of the stress matrix. This is best achieved applying a rotation matrix to the stress tensor.

A generalised 3-dimensional rotation matrix is given by the Rodrigues formula in Equation 2.34 [87], which rotates a vector $u' = Ru$, and a matrix as $M' = RMR^T$. The rotation matrix can be constructed in a few different ways, here the generalised Rodrigues formula is employed, where a rotation θ around an arbitrary unit vector $\hat{\boldsymbol{\omega}} = (\omega_x, \omega_y, \omega_z)$ is given by

$$\boldsymbol{R} = \begin{pmatrix} \cos\theta + \omega_x^2\left(1-\cos\theta\right) & \omega_x\omega_y\left(1-\cos\theta\right) - \omega_z\sin\theta & \omega_x\omega_z\left(1-\cos\theta\right) - \omega_y\sin\theta \\ \omega_x\omega_y\left(1-\cos\theta\right) - \omega_z\sin\theta & \cos\theta + \omega_y^2\left(1-\cos\theta\right) & \omega_y\omega_z\left(1-\cos\theta\right) - \omega_x\sin\theta \\ \omega_x\omega_z\left(1-\cos\theta\right) - \omega_y\sin\theta & \omega_y\omega_z\left(1-\cos\theta\right) - \omega_x\sin\theta & \cos\theta + \omega_z^2\left(1-\cos\theta\right) \end{pmatrix} \tag{2.34}$$

Hence to find the stress tensor along a generalised direction, one starts with a principal tensor and applies the required rotation. For example, to express uniaxial stress applied in the [110] direction, one can start with a uniaxial strain tensor in the $\hat{\boldsymbol{x}}$ axis and rotate it by 45° on the $\hat{\boldsymbol{z}}$ axis, yielding

$$\sigma_{[110]} = \boldsymbol{R}_z(45^\circ)\boldsymbol{\sigma}_{[100]}\boldsymbol{R}_z^T(45^\circ) \tag{2.35}$$

It should be noted that the rotation formalism can be applied to the stress tensor, which is isotropic by definition. However, it cannot be applied to the strain tensor due to the anisotropy of the compliance matrix.

2.4. SHALLOW DONORS IN SILICON

Shallow dopants are key to the tunability of a semiconductor's electrical properties, shifting the fermi energy level and increasing the bulk carrier density. Donors are atoms that have more valence electrons than silicon, thus providing an extra electron to the conduction band, as described in Section 2.1. A main assumption of doping theory is that, at room temperature, thermal energy is sufficient to overcome the binding energy of the donor nucleus, leaving the extra donor electron free and unbound in the conduction band and an ionised, positively charged nucleus, a state referred to as D^+. However, as discussed extensively in Section 2.2, when the thermal energy is sufficiently low the donor binds the electron in the stable neutral state D^0, often described as a solid-state hydrogen atom due to its singly charged nucleus and single electron. The shallow donor state has some notable physical properties as a model hydrogen atom. Due to the high dielectric constant in silicon of 11.7 [40], the Bohr radius of the phosphorus donor is extremely large at 1.8 nm [88], against the vacuum hydrogen atom Bohr radius of 52.9 pm [89], while deeper impurities have smaller radiuses due to the stronger localised potential.

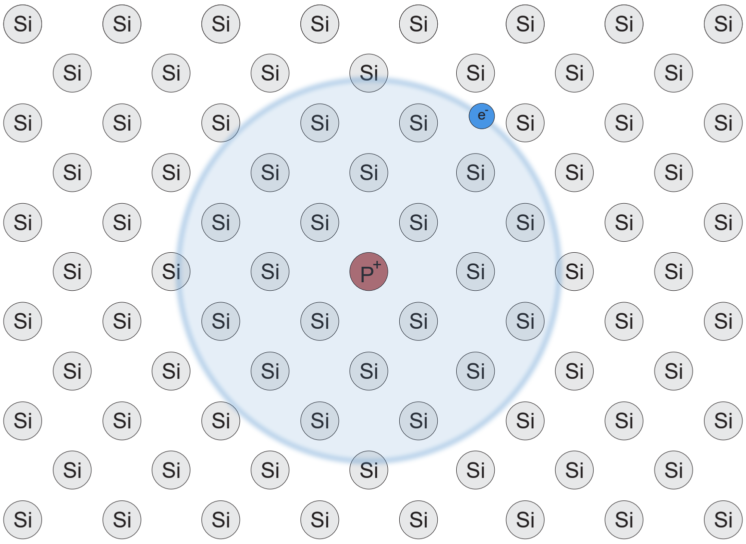

Figure 2.8: Representation of a substitutional phosphorous donor in Silicon(Si : P) and its bound electron. Drawing not to scale: the Bohr radius of the phosphorus donor is 1.8nm [88], the silicon covalent bond length is approximately 0.236nm [30].

The silicon D^0 state is well modelled under the Kohn-Luttinger effective mass theory of an electron in a perturbed periodic potential [90], with multivalley and central cell corrections. The bound electron wavefunction must solve the Hamiltonian [91, 92]:

$$\left(-\frac{\hbar^2}{2m}\partial_i^2 + V\left(\boldsymbol{r}\right) + U\left(\boldsymbol{r}\right)\right)\Psi\left(\boldsymbol{r}\right) = E\Psi\left(\boldsymbol{r}\right) \tag{2.36}$$

where V is the periodic potential of the semiconductor, and U is the Coulomb potential of the donor's nuclear charge, which includes a screened Coulomb term U_c and a central cell correction U_cc [93].

$$U_c\left(\boldsymbol{r}\right) = -\frac{e^2}{\epsilon_{Si}|\boldsymbol{r}|}, \quad U_\mathrm{cc} = \frac{e^2}{\epsilon_{Si}|\boldsymbol{r}|}\left(1 - B|\boldsymbol{r}|\right)\mathrm{e}^{-b|\boldsymbol{r}|} \tag{2.37}$$

The central cell correction, with parameters specific for each impurity, is necessary due to the asymptotic behaviour of the dopant's potential, which is screened in the far limit $r >> r_{Si}$ but unscreened near the impurity centre. Various approaches have been explored, including phenomenological corrections [94]. Here the potential form by Hui [93, 95] is presented. B and b are experimental parameters determined from the A_1 energy level.

The donor Hamiltonian can be solved under the effective mass approximation by the product of a series of envelope and Bloch functions.

$$\Psi = \sum_i F_i\left(\boldsymbol{r}\right)\Phi\left(\boldsymbol{k}_i\boldsymbol{r}\right) \tag{2.38}$$

where $\Phi\left(\boldsymbol{k}_i\boldsymbol{r}\right) = u_i(\boldsymbol{k},\boldsymbol{r})e^{i\boldsymbol{k}\cdot\boldsymbol{r}}$ are the Bloch functions centred around the conduction bad minima k_i. $F_i(\boldsymbol{r})$ is the envelope function, which must solve the hydrogen equation now devoid of the periodic term, but with the effective mass tensor m_i^*.

$$\left(-\frac{\hbar^2}{2m_i^*}\partial_i^2 + U\left(\boldsymbol{r}\right)\right)F_i\left(\boldsymbol{r}\right) = EF_i\left(\boldsymbol{r}\right) \tag{2.39}$$

Effectively, the donor electron wavefunction is the product of the conduction band Bloch functions and a hydrogen-like envelope function in a screened medium. Notably, this means that the wavefunction is oscillating, with periodicity determined by the conduction band minima wavevector k_0.

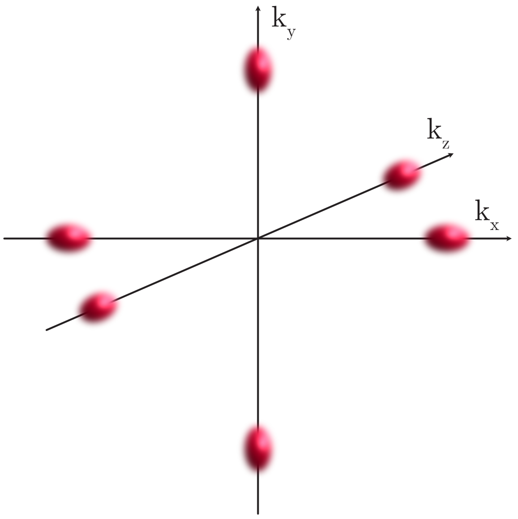

Figure 2.9: Conduction band valleys of silicon in k-space

Finally, a valley orbit correction must be included, to account for the interactions between the conduction band minima due to the localised potential [96–98]. Silicon has six conduction minima, symmetrically at the k_0 points on the [001] planes.

$$H_{\text{VO}} = \begin{pmatrix} E_0 & (1+\delta)\Delta & \Delta & \Delta & \Delta & \Delta \\ (1+\delta)\Delta & E_0 & \Delta & \Delta & \Delta & \Delta \\ \Delta & \Delta & E_0 & (1+\delta)\Delta & \Delta & \Delta \\ \Delta & \Delta & (1+\delta)\Delta & E_0 & \Delta & \Delta \\ \Delta & \Delta & \Delta & \Delta & E_0 & (1+\delta)\Delta \\ \Delta & \Delta & \Delta & \Delta & (1+\delta)\Delta & E_0 \end{pmatrix} \tag{2.40}$$

Where Δ is the interaction of perpendicular bands, and $(1+\delta)\Delta$ is the interaction between opposite bands. This leads to a splitting in the ground state energy level in valley states with separation of the order of a few meVs.

Modern computational resources allow one to go beyond the effective mass approximation and fully solve the Hamiltonian numerically in k-space around the conduction band minima [99], or with tight binding models [100], leading to the calculation of accurate parameters. However, multivalley effective mass theory remains an accurate and insightful approximation to understand the energy level and its shifts under for example electric or strain fields.

2.4.1. THE DONOR SPIN STATE

As a solid-state hydrogen atom equivalent, the Bohr-like D^0 neutral donor offers a spin system in a favourable amagnetic material. Beyond its electronic and optical properties, silicon also has important magnetic properties. Of the 3 stable, naturally occurring silicon isotopes, ^{28}Si (92.2%) and ^{30}Si(3.1%) have zero spin angular momentum [89]. Only ^{29}Si, with a natural occurrence of 4.7 % has a spin of $1/2$ [101]. Silicon is thus an excellent magnetic insulator, and it can be further improved through the isotopic isolation of the ^{28}Si isotope [102].

A neutral shallow donor(D^0) in silicon can be modelled as a Bohr atom according to effective mass theory, as described above. The spin system of such atom comprises the spin-$1/2$ negatively charged electron orbiting a single, positively charged atom with a spin dependent on the nuclear species, $m_{\text{I}} = 1/2$ in the case of the ubiquitous phosphorus employed in this work. The spin system is modelled, just like the Bohr atom, as a 2-particle system, with two Zeeman terms and a hyperfine interaction term [103].

$$\hat{H}_{\text{r}} = \sum_{x,y,z} \left(\frac{g_{\text{e}}\mu_B}{\hbar} B_i \hat{S}_i + \frac{g_{\text{n}}\mu_n}{\hbar} B_i \hat{I}_i + A_{\text{hf}} \hat{S}_i \hat{I}_i \right) \tag{2.41}$$

Here $\hat{S}_i$ represents the electron spin operators $\hat{S}_x, \hat{S}_y, \hat{S}_z$ of the electron, and $\hat{I}_i$ the nuclear spin operators. In the case of the phosphorus donor those are both spin-$\frac{1}{2}$ Pauli operators. g_e is the electron g-factor, which is a 2 rank tensor:

the whole term is given by $B_i g_{ij} J_j$. The g-factor of the electron can be derived from effective mass theory, and for a single valley it is anisotropic with principal components $g_{||} = 0.87$ and $g_{\perp} = 1.92$ respectively parallel and perpendicular to the valley axis [104, 105], which are dependent on the directional effective mass and donor potential. Under symmetric contributions by all the 6 valleys this still results in an isotropic, scalar g-factor, with some anisotropy resulting from the symmetry breaking due to large strains or electric fields [106]. The nuclear Zeeman term is much smaller than the electron's due to the higher mass of the nucleus, to which the magneton constant is related by $\mu = \frac{C\hbar}{2m}$. This leads to a nuclear Zeeman term about 3 orders of magnitude smaller than the electron's. The main contribution of the nucleus results from the hyperfine term, which is due to the contact interaction of the electron and nucleus, effectively the overlap of the electron and nuclear wavefunctions [107–109]. The hyperfine constant A_{hf} represents the strength of the electron-nuclear spin interaction and is proportional to the electron wavefunction amplitude at the nucleus.

$$A_{\mathrm{hf}} \propto |\Psi_e^2(0)| \tag{2.42}$$

In the case of the phosphorus donor, the hyperfine constant is 117.53 MHz [21], with deeper donors such as bismuth presenting higher hyperfine couplings in the gigahertz region.

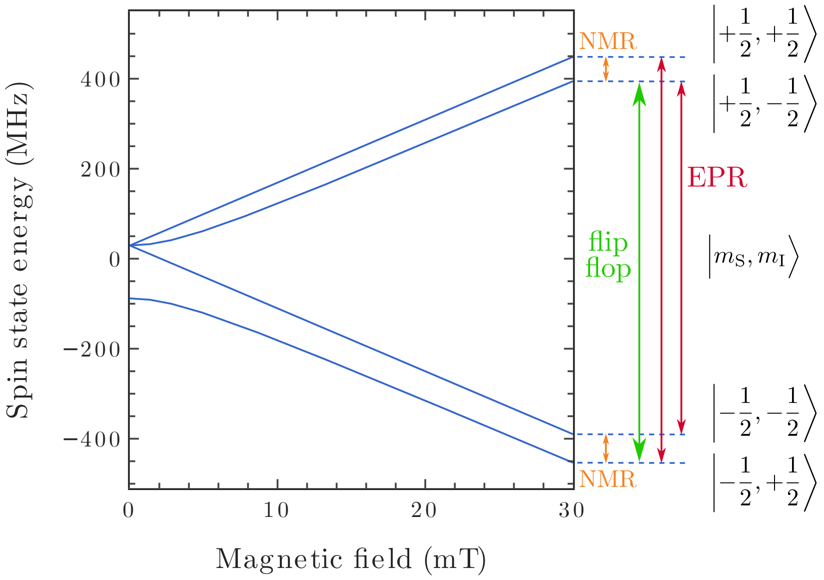

Figure 2.10: Simulation of the phosphorus donor spin energy levels in a magnetic field for the states $|\mathrm{m_s}, \mathrm{m_I}\rangle$ in the limit $g_e B >> A_{hf}$, and allowed flip-flop, electron paramagnetic resonance(ESR) and nuclear magnetic resonance(NMR) transitions. The sixth transition is forbidden having $\Delta m_S = 2$.

The manipulation of the donor spin is usually achieved with the use of a small oscillating magnetic field $B_1(t) = cos(2\pi f t + \phi)$ perpendicular to the static magnetic field B_0. This can be understood in terms of the Larmor precession of a magnetic dipole or alternatively the time evolution of 2-state system. The full Hamiltonian is given by $H = H_0 + H_1(t)$, each resulting from the static and oscillating magnetic field components.

Figure 2.10 shows the resulting 4 energy levels of the phosphorus donor spin system, with zero field splitting given by the hyperfine constant, and 2 pairs of states at higher magnetic field states.

This electron state has shown extremely long relaxation times exceeding seconds [105, 110, 111]. Coherence times at low temperatures are mainly limited by the coupling to the magnetic ^{29}Si isotopes but can reach lifetimes in the order of seconds [2] in isotopically purified ^{28}Si. The nuclear state is significantly more difficult to drive due to the small hyperfine and nuclear magnetic moment but has shown extremely long coherence times of almost one hour [4]. The ^{29}Si spin is indeed a source of decoherence and local strain, however it can also be harnessed as a nuclear spin quantum memory [112].

2.4.2. STRAINED DONORS

The silicon donor spin is relatively impervious to strain, due to the vanishing spin-orbit coupling of the conduction band. The main strain effects are a quadratic shift due to the relative valley energy shifts inducing repopulation and consequent g-factor anisotropy, as well as a linear hyperfine modulation due to the hydrostatic strain component.

The conduction valley strain can be expressed in the valley reference [113, 114]

$$\Delta_{\mathrm{cb}} = \Xi_d \mathrm{Tr}\left\{\epsilon_{ij}\right\} + \sum_{i=\pm x,y,z} \Xi_u \hat{\boldsymbol{x}}_i \epsilon_{ii} \tag{2.43}$$

One must thus solve the valley orbit Hamiltonian with the added valley strain energy shifts and add the hydrostatic component

$$H_{\mathrm{VO}}\left(\epsilon_{ij}\right) = \Xi_d \mathrm{Tr}\left\{\epsilon_{ij}\right\} + \begin{pmatrix} E_0 + \Xi_u \epsilon_{xx} & (1+\delta)\Delta & \Delta & \Delta & \Delta & \Delta \\ (1+\delta)\Delta & E_0 + \Xi_u \epsilon_{xx} & \Delta & \Delta & \Delta & \Delta \\ \Delta & \Delta & E_0 + \Xi_u \epsilon_{yy} & (1+\delta)\Delta & \Delta & \Delta \\ \Delta & \Delta & (1+\delta)\Delta & E_0 + \Xi_u \epsilon_{yy} & \Delta & \Delta \\ \Delta & \Delta & \Delta & \Delta & E_0 + \Xi_u \epsilon_{zz} & (1+\delta)\Delta \\ \Delta & \Delta & \Delta & \Delta & (1+\delta)\Delta & E_0 + \Xi_u \epsilon_{zz} \end{pmatrix} \tag{2.44}$$

leading to a repopulation of the electron population to the energetically favourable valley. As the g-tensor is anisotropic for each valley, and only becomes isotropic from the symmetrical valley contributions, this leads to a quadratic change in the g-factor and anisotropy.

Although the conduction band shifts are non-negligible, the g-factor effect is small and only become significant at large strains $\gg 10^{-5}$. At small strains, the dominating effect is a linear hydrostatic tuning of the hyperfine constant [115, 116]. Nevertheless, these effects are small compared to the sensitivities of the D^0X optical transitions of this work. The conduction band shifts are indeed relevant and are incorporated, but the spin shifts are ignored as below the resolution limit.

2.5. Donor Bound Excitons in Silicon

The Silicon donor bound exciton is a remarkable, short lived state with properties and applications concerning all of semiconductor silicon's key themes: optical, magnetic and electrical. This section explores the literature of donor bound excitons, as well as theoretical models that are employed in the following experimental chapters.

2.5.1. Wannier Excitons

Electrons and holes in a semiconductor interact through the Coulomb force and can go as far as forming a two particle bound state: the exciton. The exciton state is generally divided in two species depending on the strength of the Coulomb attraction: ionic crystals have electrons and holes tightly bound around the nuclei thus forming tight, unscreened excitons known as Frenkel or molecular excitons [117, 118]. In the opposite regime, semiconductors with high dielectrics and screened carriers, such as silicon, typically form loosely bound excitons known as Wannier-Mott excitons [119, 120]. These large excitons can be well modelled by effective mass theory. The dynamic can be separate between a hydrogen like interaction dynamic with a coordinate $\boldsymbol{r} = \boldsymbol{r_e} - \boldsymbol{r_h}$ and a centre of mass coordinate $\boldsymbol{R}$ dynamic [36, pp. 279–280]

$$-\frac{\hbar}{2M} \bigtriangledown^2 \psi(\boldsymbol{R}) = E_R \psi(\boldsymbol{R}) \tag{2.45}$$

$$\left(-\frac{\hbar}{2\mu} \bigtriangledown^2 - \frac{e^2}{4\pi\epsilon|r|}\right) \phi(\boldsymbol{r}) = E_r \phi(\boldsymbol{r}) \tag{2.46}$$

Hence the exciton behaves as a donor state moving within the semiconductor as a free particle with reduced mass $\frac{1}{\mu} = \frac{1}{m_{\mathrm{e}}^*} + \frac{1}{m_{\mathrm{h}}^*}$.

The semiconductor exciton is a neutral quasi-particle composed of an electron and a hole, electrostatically bound to each other. Similar to the two-particle hydrogen atom, it is usually excited optically by the promotion of valence band electron to the conduction band, leaving a hole in the valence band. In silicon, free excitons cannot be excited by a direct photon transition due to the indirect bandgap, but must be excited via a phonon assisted transition, with the phonon compensating for the electron momentum.

Excitons can exist as free, drifting particles, but they are often and easily pinned around impurities, leading to an energetically favourable bound state, the bound exciton.

2.5.2. DONOR BOUND EXCITONS

Excitons can be bound to impurities forming localised states known as bound excitons. Generally binding can occur to both charged and neutral impurity centres, however in Silicon only neutral impurity centres give rise to a stable bound state, as ionised impurities cannot bind excitons since $m_e^* \gg m_h^*$ [121]. This weak binding occurs through a London like dispersion force, as both the donor and the exciton have a symmetrical charge distribution. Optically, donor bound excitons are of particular interest as, lacking the kinetic energy broadening of free excitons, they often display very narrow linewidths. This work focuses specifically on the donor bound exciton state $\mathrm{D^0X}$, which has attracted significant research due to its narrow, spin resolved phononless optical transitions, as well as its electrical Auger decay.

The donor bound exciton is overall a complex, three particle state with individual and interaction terms [26, p. 83].

$$H_{\mathrm{D^0X}} = H_{e1} + H_{e2} + H_h + H_{e1,e2} + H_{e1,h} + H_{e2,h} \tag{2.47}$$

which can indeed be treated employing tight binding numerical methods. On a practical level, significant insight can be gained by considering the individual terms of the bound exciton transition, which takes the single particle e to the three particle eeh state.

$$E_{\mathrm{D^0X}} = E_g - E_{\mathrm{X}} - E_{\mathrm{bX}} + E_{\mathrm{es}} + E_{\mathrm{hs}} \tag{2.48}$$

Here, E_g is the bandgap, E_{X} is the free exciton binding energy, E_{Xb} is the exciton binding energy, and finally $E_{\mathrm{es}} + E_{\mathrm{hs}}$ are the excited electron and hole spin energies. Notably, the excited electron spin state must be opposite to that of the $\mathrm{D^0}$ electron. Throughout this section the analysis of the bound exciton energy states is done in terms of the terms above, where E_{X} and E_{bX} are generally assumed fixed, with most shifts and splittings arising from the bandgap and spin terms.

2.5.3. OPTICAL EXCITATION OF THE $\mathrm{D^0X}$ STATE

The silicon donor bound exciton state can be excited via a phononless optical transition. Free excitons require the electron to be excited to a specific valley state k_i and hence assume a finite momentum. Due to the donor potential, the 6 conduction valleys interact, as described in 2.4, leading to a ground state symmetric superposition with net wavevector $k = 0$, hence allowing a phononless transition under conservation of momentum.

The $\mathrm{D^0X}$ single photon transition is amplified by a giant oscillator effect [122], which yields an oscillator strength amplified by

$$f_{\mathrm{D^0X}} = \left(\frac{E_0}{E_b}\right)^{3/2} f_{int} \tag{2.49}$$

where E_b is the exciton binding to the donor and E_0 is the exciton bandwidth $\hbar\Delta k$. Due to the low, meV binding energy and large, eV bandwidth, this results in an amplification of ~10^4 for silicon shallow donors, and a large oscillator strength of 7.1×10^{-6} for Si:P [123]. A simplistic interpretation suggests that the primitive unit cell oscillator strength is multiplied by the number of unit cells within the large radius of the bound exciton, as this is the collective excitation valence band electrons, not the single D^0 conduction band one.

2.5.4. DECAY THE D^0X STATE

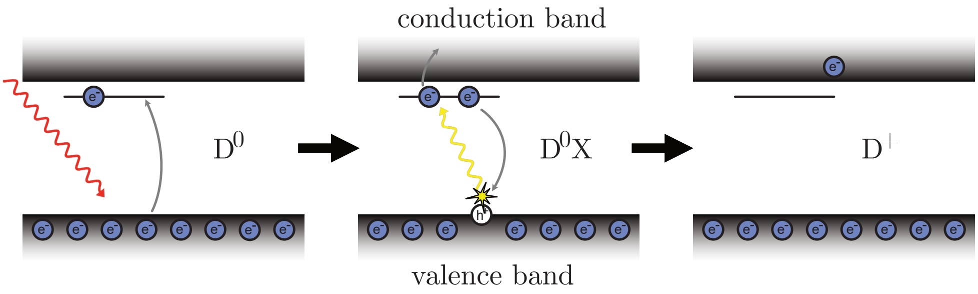

Figure 2.11: D^0X optical excitation and Auger decay process.

The D^0X state can decay via two pathways: phononless radiative emission and Auger decay, and is largely dominated by the latter, which is the focus of this work. Radiative emission can be derived from the oscillator strength and yields a lifetime of ~2 ms [16].

The Auger decay mechanism, first suggested by Nelson [22], involves an electron and a hole pair annihilation, with the resulting energy absorbed by the remaining electron, which is thus excited into the conduction band. The Auger decay rate is related to the radiative emission rate.

$$\begin{aligned} \Gamma_{auger} &= \alpha \Gamma_{rad} \\ \alpha &= \frac{a4k_{Aug}}{(a_0 k_{rad})^3} \end{aligned} \tag{2.50}$$

Which results in an Auger lifetime almost 4 orders of magnitude shorter than the radiative lifetime at 272 ns [16, 124], severely limiting the radiative quantum efficiency. Nevertheless, Purcell enhancement has been explored for increasing the radiative efficiency through the use of photonic cavities, such as in the work of Nur [46].

The dominant Auger decay mechanism effectively renders the donor bound exciton transition a spin selective $D^0 \rightarrow D^+$ spin-to-charge converting transition, which has been demonstrated in electrical spin resonance [23, 25, 26, 125] and nuclear spin resonance [24] experiments.

2.5.5. DONOR BOUND EXCITONS IN A MAGNETIC FIELD

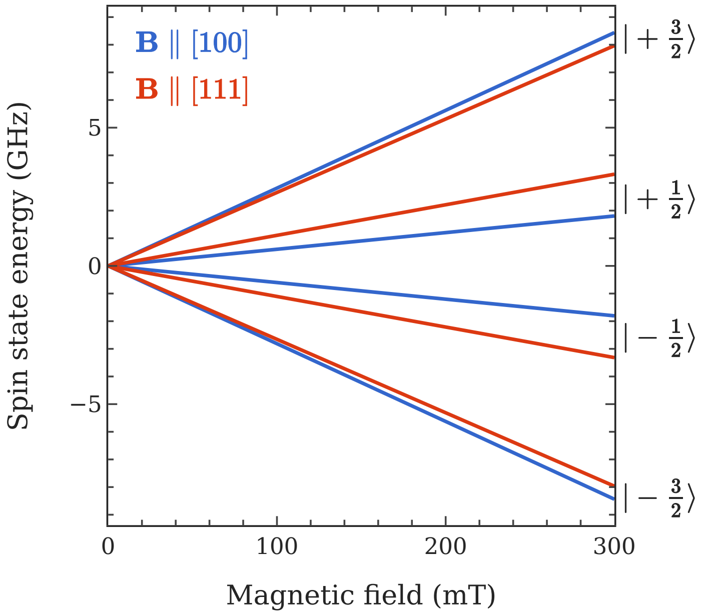

Figure 2.12: Simulation of the D^{0}X hole spin energy levels in a magnetic field along the — [100] and — [111] crystallographic axes.

The D^{0}X Hamiltonian in a magnetic field depends on the hole Zeeman Hamiltonian [126]. The system is similar to that of a hole spin qubit [127], with the difference that there is no hyperfine interaction with the nucleus, as the nucleus and hole have the same charge, and due to Coulomb repulsion $|\Psi_h^2(0)| = 0$.

$$H_h(\boldsymbol{B}) = \mu_B \sum_{i=x,y,z} \left(g_1 J_i B_i + g_2 J_i^3 B_i \right) \tag{2.51}$$

Unlike the electron, the hole Zeeman Hamiltonian is strongly anisotropic, and due to the cubic J_i^3 term it has a different g-factor for the light $m_j = \pm\frac{1}{2}$ and heavy $m_j = \pm\frac{3}{2}$ hole. Figure 2.12 shows the hole Hamiltonian for $B \parallel [001]$ and $B \parallel [111]$ orientations. This model breaks down at higher fields $B \gg 1\,\mathrm{T}$, where the hole state displays diamagnetic properties [128], but this is not a concern in the low field regime explored in this work.

In the D^{0}X state two electrons are present with opposite spin state and the Zeeman terms cancel out. Magnetically, the D^{0}X transition magnetic component is the difference between the hole Zeeman and the electron spin from the D^0 state.

$$\Delta E_{\mathrm{D^0X}}(B) = E_h(B) - E_e(B) \tag{2.52}$$

with the electron energy levels discussed in Section 2.4. This potentially leads to 8 distinct transitions, 16 including the D^0 hyperfine splitting. However,

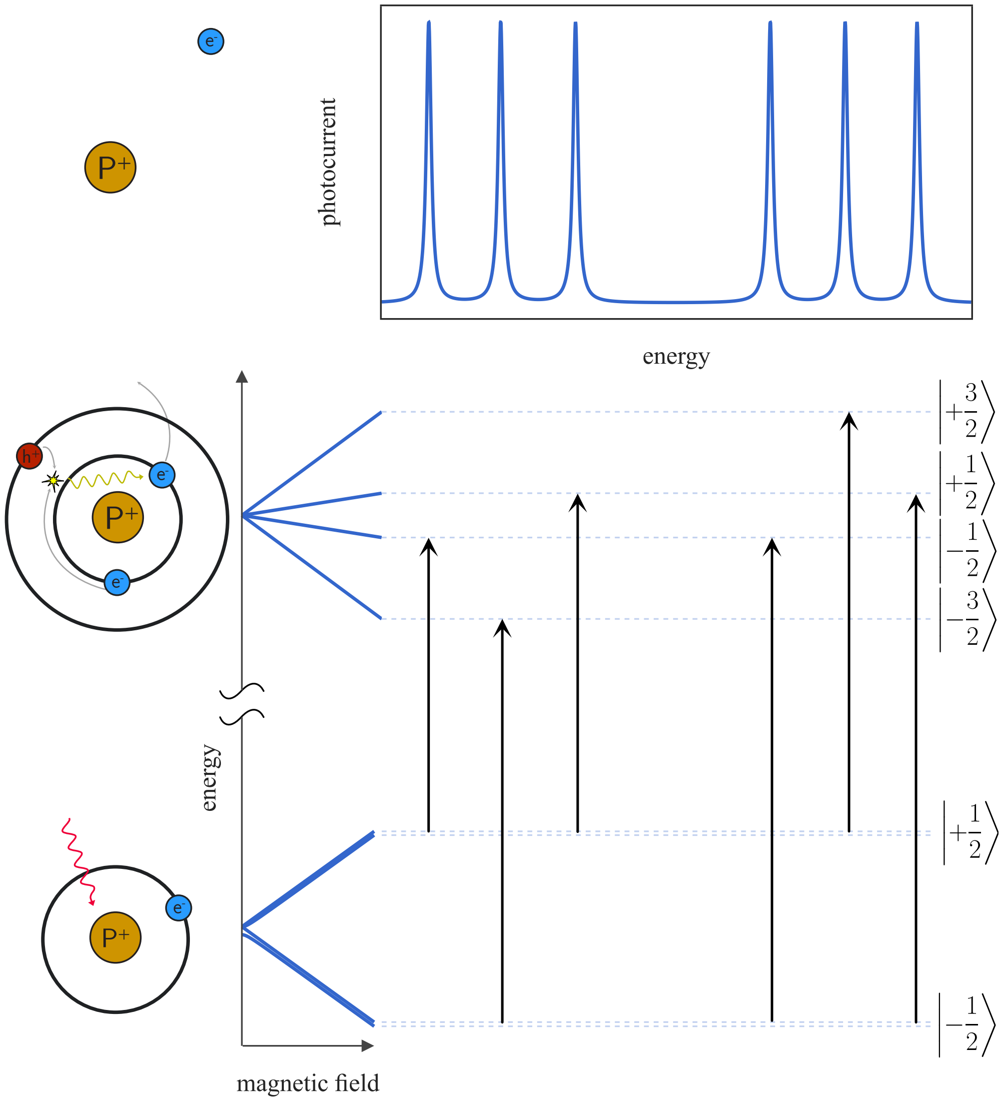

Figure 2.13: Energy levels and transitions of the $D^0 \rightarrow D^0X$ transition under a magnetic field $\boldsymbol{B} \parallel [001]$.

conservation of spin number forbids two of these, as optical dipole transitions must have $\Delta m_j = 0, \pm 1$. Hence the $-\frac{1}{2} \rightarrow \frac{3}{2}$ and $\frac{1}{2} \rightarrow -\frac{3}{2}$ are forbidden, leaving a total of 6 transitions, 12 with the hyperfine splitting. This work is largely based on samples and conditions where the hyperfine is not resolved, therefore it will be ignored. However, it is important to note that the hyperfine lines can and have been resolved in ^{28}Si samples at low, $\sim$1 K temperatures [18, 21].

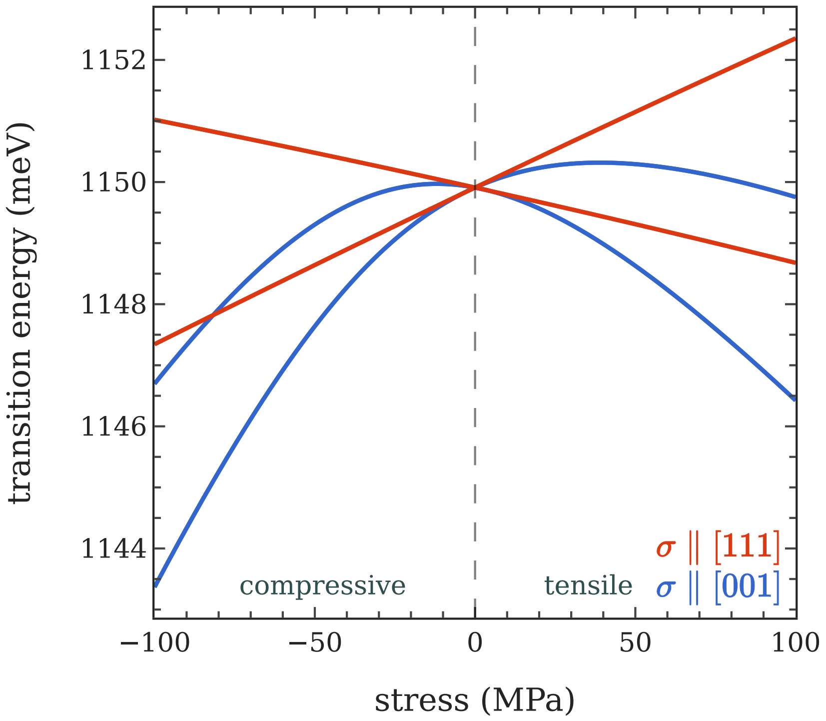

Figure 2.14: Simulation of the D^0X light and heavy hole transition energies under uniaxial stress along the — [100] — [111] crystal axes.

2.5.6. Strained Donor Bound Excitons

The silicon donor bound exciton state is strongly affected by lattice strain due to the spin orbit coupling (SOC) of the valence band. This is one of the main themes of this thesis, as well as much past research on the subject, as small amounts of strain can lead to large shifts and splittings in the D^0X transition energy lines. Unlike the conduction band, the valence band of silicon displays strong spin orbit coupling, this is well described with the Kohn-Luttinger $k \cdot p$ model.

The D^0X hole spin splitting under strain has been observed to follow closely the Pikus-Bir Hamiltonian [129].

$$\hat{H}_{\mathrm{pb}} = a\mathrm{Tr}\{\epsilon\} + b\sum_i (\hat{J}_i^{\,2} - \frac{5}{4}\hat{I})\epsilon_{ii} + \frac{2d}{\sqrt{3}} \sum_{j>i} \left\{\hat{J}_i \hat{J}_j\right\} \epsilon_{ij} \tag{2.53}$$

with a similar effect resulting from the application of electric fields [130].

The D^0Xstate generates 2 electrons and a hole, thus the strain shift will be the sum of the hole strain shift and the electron strain shift, which is described in Equation 2.43 from Section 2.4.2

$$\Delta_{D^0X}\left(\boldsymbol{\epsilon}\right) = \Delta E_e + \Delta E_h \tag{2.54}$$

The resulting strain shift, shown in Figure 2.14, is anisotropic, with a linear shift only under uniaxial stress along the [111] axis, and quadratic terms for all other orientations. Notably, however the strain shift is equal and linear for small, $\lesssim 5\,\mathrm{MPa}$ stresses.

Strain is a key theme of donor bound excitons, with discernible splitting arising even from small mounting strains. It has even been proposed that strain may be responsible for the natural silicon line broadening due to the random distribution of ^{29}Si and ^{30}Si isotopes.

Attempts to work with donor bound excitons in silicon-on-insulator (SOI) substrates have particularly been hampered by the high interface strain [29], which leads to high deformations of the silicon device layer.

3. Setup and Experimental Methods

3.1. Silicon Devices

The silicon samples employed in this work are lithographically defined, microfabricated devices consisting of aluminium metal contacts, dry silicon thermal oxide and phosphorus ion implants. The substrate is a commercial high resistivity (10 000 Ω), 250 µm float-zone grown silicon wafer. The devices were designed and fabricated by Dr Marc Philipp Ross in the London Centre for Nanotechnology cleanroom, except for the dry oxide growth at the Southampton Nanofabrication Centre and the donor implantation at the Surrey Ion Beam Centre. The fabrication is fully described in Dr Ross' PhD Thesis [26, p. 70], where characterisation and some photoconductive experiments are also presented.

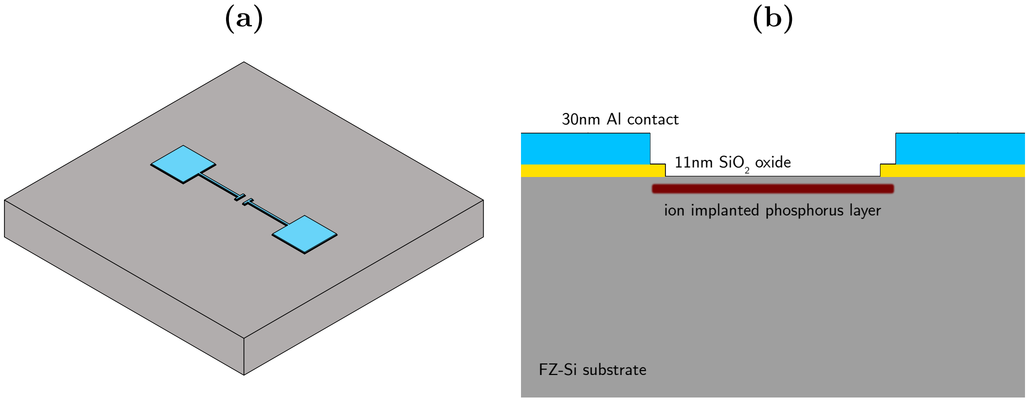

Figure 3.1: Electrical D^0X device model. (a) device model including feed line and bond pad. (b) device model MOS contacts and phosphorous implant side view.

All fabricated structures are defined with a photolithography mask. The devices, with an example shown in Figure 3.1, consist of 10 µm wide metal capacitors of various length and separations within the photolithography process limit, connected to a pair of 200 × 200 µm bonding pads by a 10 µm wide feed line. The metal contacts are composed of 30 nm thermally evaporated aluminium. The oxide consists of an 11 nm thick SiO_2 layer grown in an oxygen atmosphere (5 min, 950 °C). The oxide is etched everywhere except for under the metal to limit the substrate strain, extending ~2.5 µm off the metal to prevent a direct contact. The phosphorus donor patches consist of 100 nm thick ion beam implants at the shallow depth of 150 nm. The implantation dose is $7 \times 10^{10}\,\text{cm}^{-2}$, resulting in a peak density of $5 \times 10^{15}\,\text{cm}^{-3}$. Although higher donor densities would yield a stronger photoconductivity response, the D^0X transition is sensitive to large donor densities due to long range exciton interactions, leading to significant linewidth broadening [123, 125]. A low donor concentration also enables the investigation of the few-donor photoconductive D^0X detection limit, but this needs to be balanced against the residual substrate donors for local selectivity.

3.2. CRYOGENIC SAMPLE MOUNTING

3.2.1. CRYOGENIC SAMPLE REFRIGERATION

The coherent manipulation of donor and bound exciton spin states requires cryogenic temperatures to maximise spin and exciton states lifetimes and minimise the transitions narrow linewidths, allowing the resolution of the spin fine structures. Cryogenic cooling to liquid helium temperatures is achieved with a Montana Instruments S100 Cryostation[1]. This is a 2-stage closed-cycle cold finger cryostat designed for low working distance optical access with a room temperature objective.

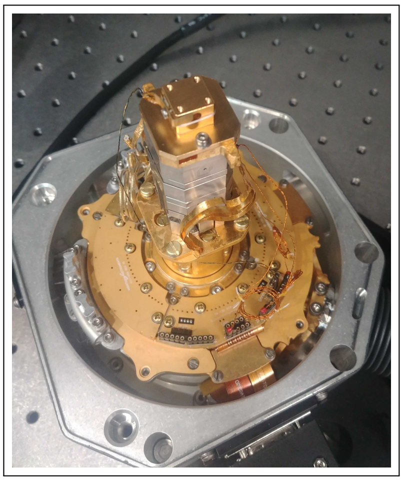

Figure 3.2: Sample space of the Montana Instruments S100 cryostat, with 3-axis Attocube piezo-stack for top sample mounting and positioning.

The sample chamber, shown in Figure 3.2, consists of a sample platform enclosed by an aluminium radiation shield, itself enclosed by a vacuum housing.

---

[1] `https://www.montanainstruments.com/products/s100`

The vacuum housing creates a sealed enclosure for establishing a vacuum. This is essential as any gas would thermally couple the sample to the enclosure and thus room temperature. The radiation shield is thermally coupled to the 1st stage of the cryocooler, reaching down to approximately 30K, and is designed to shield the sample from the radiation of the warm room temperature environment. The sample platform is thermally coupled to the 2nd, coldest stage of the cryocooler by a thermally conductive metal connection, referred to as cold finger, and can reach down to a temperature of 2.8K under optimal operating conditions.

The cryostat has electrical access through 4 high frequency SMP coaxial cables and 10s of single wire dip connectors. The sample chamber and cryocooler are mounted on an optical table, taking advantage of the vibration dampening from its pneumatic stabilisation. The air-cooled helium compressor is located in a service vault outside the optical laboratory, and connects to the cryocooler via two supply and return helium high pressure lines of approximately 15m length. The compressor is the largest source of noise and vibration of the entire system, and its delocalisation further reduces vibrations to the sample. The vacuum pump and control unit are placed on the floor under the optical table.

This configuration of the S100 cryostat is set up for vertical optical access: the sample is mounted at the very top of the sample chamber, as close as possible to the radiation shield window to allow the use of a low working distance, high magnification objective. The distance between the bottom of the radiation shield window and top of the vacuum housing windows is only0 mm. This allows the achievement of a near diffraction limited spot diameter of ~2 µm, crucial to this work investigating the dimensional limits of D^0X devices. Previous D^0X research was limited to larger laser spot diameters upwards of 30 µm [26, 27], due to the use of longer optical working distance setups.

3.2.2. PCB Sample Mounting

The sample is mounted on the piezo stage via a printed circuit board (PCB) with soldered SMP electrical connectors. After the PCB is assembled, the sample is glued to the PCB with the use of silver paste or cryogenic GE varnish, for a secure positioning and thermal connection. Extreme care is placed on limiting mounting strain by using minimal adhesive located far from the active device. The active devices, at most two per run, are connected to the PCB by ultrasonic aluminium wire bonding. Two wire bonders were used over the course of this work: a Kulicke & Soffa 4123 wedge manual wire bonder with a 75 µm wire, and a Bondtec 56i series automatic bonder with a 25 µm wire. Special care is placed on achieving low profile bonds to limit capacitive coupling to the cryostat radiation shield and outright contact shorts. To achieve this, the bonds are run PCB-to-silicon so that the tall, loopy side of the bond sits lower on the PCB. Unusually low loop heights are employed, and the second bond is performed with a closed clamp to further bring down the bond height. Overall, the bond height over the silicon does not normally exceed 100 µm, enduring sufficient clearance to the cryostat's radiation shield. This low profile bonding tends to create a degree of stress on the bonds, and the narrower bond-wire is highly preferred to minimise any tension on the sample mounting adhesive. Finally, the bottom PCB is mounted on to the piezo stage via 2 non-magnetic titanium screws, with a thin layer of cryogenic thermal grease (Apiezon N grease) for improved thermal transfer.

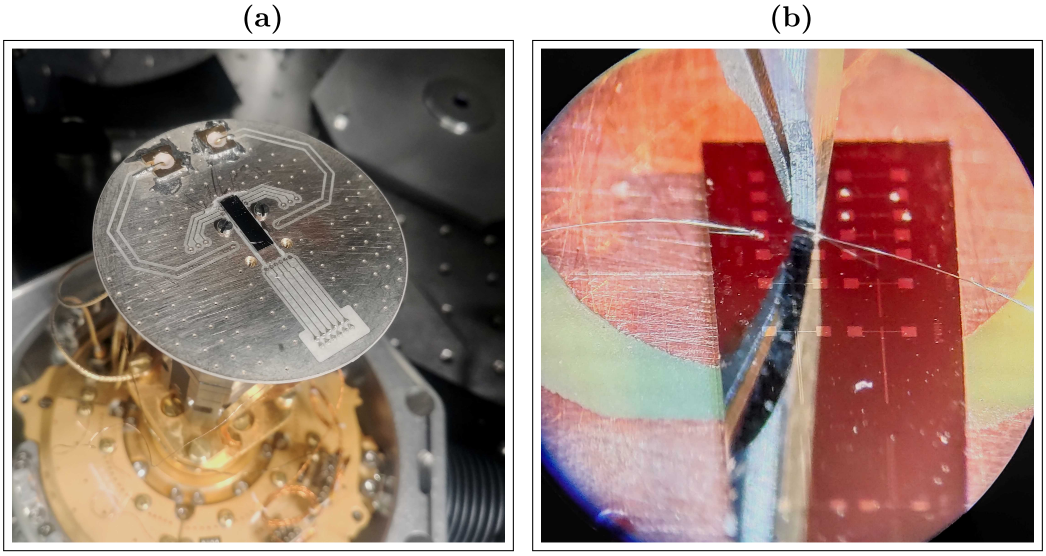

Figure 3.3: (a) D^0X device sample mounted on a custom PCB on the S100 cryostat piezo-stack (b) Low profile device wire bonding process.

The first iteration displayed in Figure 3.3 is designed for both 50 Ω impedance matched AC lines, as well as simple dip DC lines. Subsequent PCBs only included impedance matched lines, as the DC lines proved unsuitable for the low noise electrical measurements involved in D0X detection. They presented high levels of noise and electromagnetic interference despite the cryostat's metal shielding and the use of twisted pairs. The 50ohm impedance matched lines are connected to flexible coaxial cables via SMP connectors and then routed outside the cryostat through rigid coaxial cables. The AC traces are therefore ground shielded in their entirety, except for the short, 5 to 10mm wire bond, and result in a noise level at least an order of magnitude lower than the DC lines.

In subsequent PCB versions the Montana mounting stage is removed, and a double stacked PCB setup is employed to allow for the mounting of neodymium permanent magnets under the silicon samples. As displayed in Figure 3.4, a first PCB is screwed onto the piezo stage. A second PCB is then attached to the second PCB via brass standoffs and custom modified low-profile screws. Regular screws have a thickness of 1mm or more that clashes with the cryostat's radiation shield. The screws are filed by attaching them head down to a pillar drill, as if they were drill bits, and then pushing them against files or filing

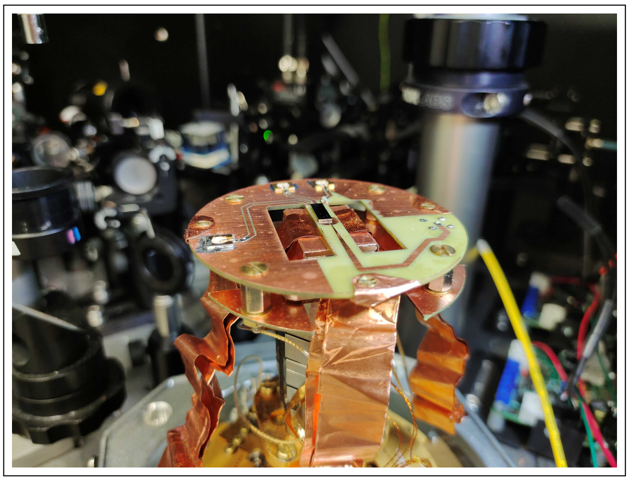

Figure 3.4: Double stacked PCB sample mount, with underside niobium magnets, OFHC copper thermal coupling ribbons and flexible SMP coaxial cables.

paper. Where necessary, the screw slot is deepened with a thin hacksaw. The drill rotation allows for rotationally symmetric filing. The screw head can be filed down to approximately 200um, below the silicon sample thickness while still maintaining sufficient functional integrity.

Regarding thermal connections, PCBs have thin ∼30 µm copper layers and thus limited thermal conductivity. To avoid the thermal coupling having to traverse two PCBs, the top PCB is directly connected to the base temperature stage via 3 oxygen-free high thermal conductivity (OFHC) copper strips. These are screwed to the PCB on one side and clamped to the cryostat on the other side. All thermal joints are again improved with a thin layer of cryogenic thermal grease.

All PCBs were designed using software suites DipTrace and KiCad and manufactured by Martin Scott in the UCL department of electronic and electrical engineering on a FR-4 or RO4003C laminate.

3.3. OPTICS

The optical setup for all microscale D^0X experiments is built around the Montana S100 cryostat vertical optical access window. Two distinct optical setups were built in succession throughout this work: a simple, tube mounted and single laser access setup with a 0.35NA objective followed by a more complex, optical table based, multi-laser setup with a 0.65NA objective. These setups were designed and built together with Dr Siddharth Dhomkar, with parts of the setup later modified for photoluminescent detection by Felix Donaldson.

In both setups, the key elements are two tunable 1078 nm lasers:

Toptica DL-Pro diode single frequency laser with DLC Pro controller. The laser has a linewidth of 20 kHz and a coarse tuning range between 1070–

1160 nm. The continuous, mode-hop tuning range is however limited to 100 pm mainly via piezo tuning of the laser cavity but also of the diode current and temperature. The laser has a free space output in a form of an elliptical, linearly polarised laser beam, which is fed through a 90-10 beam-splitter and collimated in a polarisation maintaining (PM) and a single mode fibre respectively, as shown in Figure 3.5b The PM fibre is fed to the main experimental optical path via a collimator, while the single mode fibre is plugged in a wavemeter.

NKT-photonics koheras adjustik Y10 single frequency diode laser with a 20 kHz linewidth, a wavelength range of 1077.5–1078.5 nm tunable via the diode temperature and 20 pm piezoelectric cavity fine tuning window. The output power is practically limited to ∼50 mW due to internal reflections. The laser is internally fed through a non-polarisation maintaining single mode fibre, giving an output with slow, large fluctuations in linear polarisation angle and likely circular polarisation components.

Two wavemeters are employed for determination of the laser frequency mode, a HighFinesse WS6 and WS7. The WS7 alone is used throughout most of the work, except for the dual laser pump-probe experiments in Chapter 6 where both wavemeters are employed simultaneously.

3.3.1. Single Laser Optical Setup

The first optical setup, whose diagram and photo are displayed in Figure 3.5, consists of a manual 3-axis linear stage holding an array of tube mounted optics. One of the two 1078nm lasers is fed via a fibre collimator, taken through a 10 nm bandpass filter and a ND2 filter, deflected through a 50/50 beamsplitter and focused on the sample by a Nikon CF Plan 20x 0.35NA objective through the cryostat window. The laser reflection from the device surface goes through the beamsplitter and is imaged on a tube mounted Thorlabs DCC1545M 1280 × 1024 CMOS camera with a plano-convex lens focused at infinity.

A 1050 nm LED is placed right above the optical window to apply broad illumination to the sample for navigation and above bandgap carrier generation, yielding an image of the sample surface on the camera. A 1078nm band-stop filter is placed before the camera to limit the incident focused laser power and bring the intensity of the imaged laser spot close to the LED illuminated surface image. The result is a crisp image of the device surface and the laser spot at the same time, as shown in Figure 3.6, making the steering and targeting of the laser spot straightforward. For alignment and focusing, the 3-axis linear stage enables rough alignment of the objective above the cryostat window and is only used once after a cooldown.

The 3-axis ANPx101-ANPz101 Attocube piezo-actuator tower inside the cryostat finely positions the device under the objective and brings the sample surface into focus, allowing for remote controlled sample navigation using the

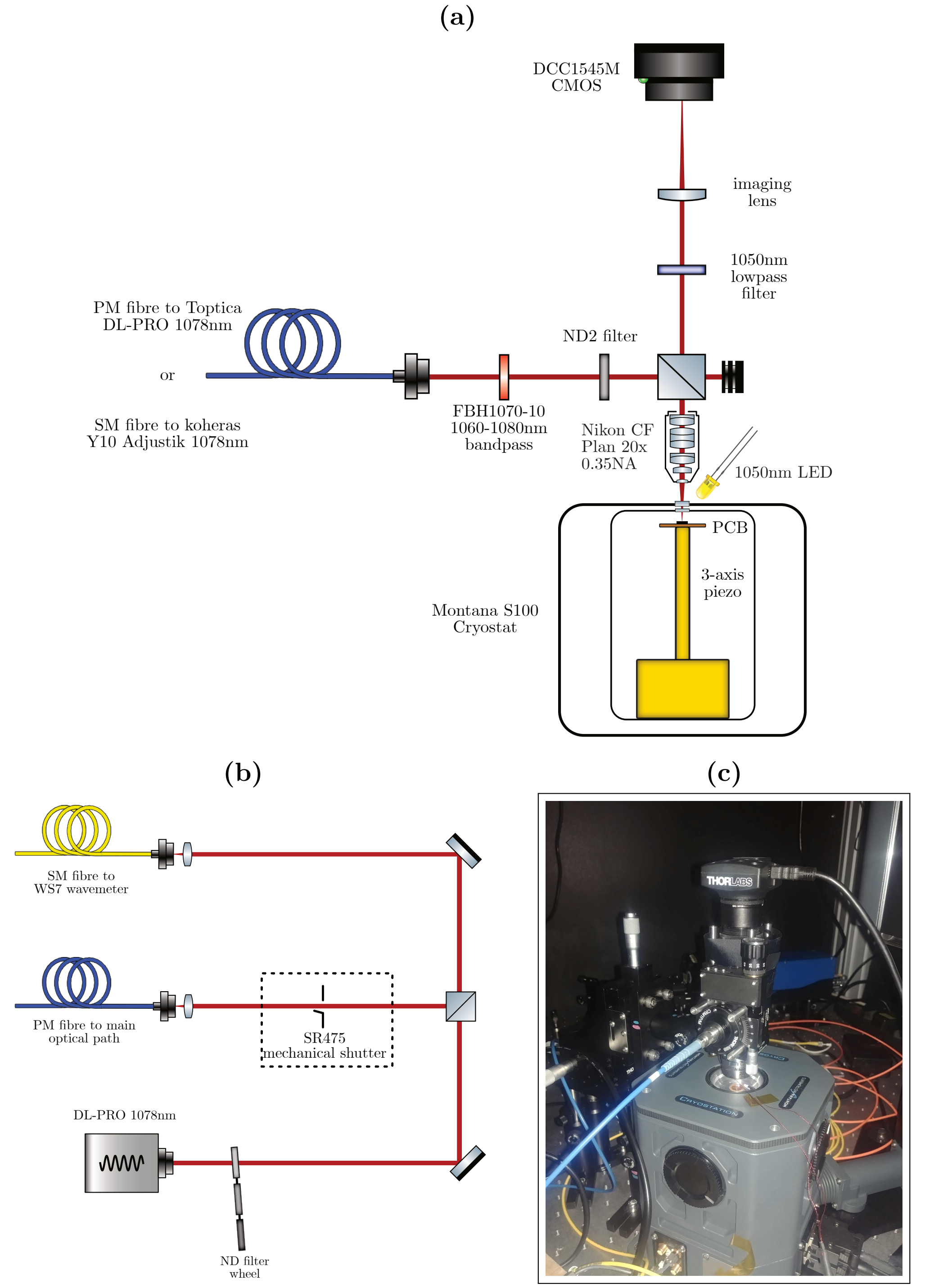

Figure 3.5: Single laser optical setup (a) Optical setup diagram. (b) Toptica DL-pro dual fibre coupling (c) Photograph of the optical setup. [2]

experiments.

---

[2] Optical vector components adapted from the "gwoptics ComponentLibrary" by Alexander Franzen, `http://www.gwoptics.org/ComponentLibrary` 🅭.

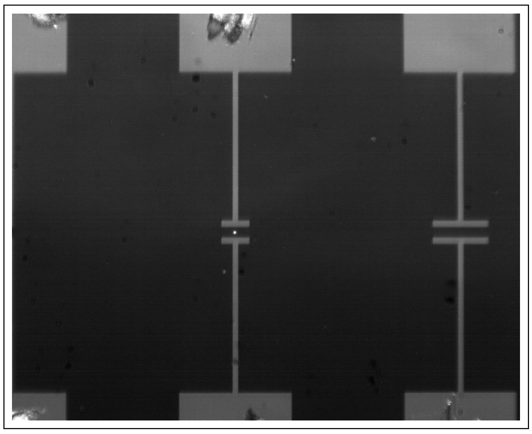

Figure 3.6: CMOS image of D^0X devices and 1078 nm laser spot, captured with single laser optical setup and illuminated with an out-of-cryostat LED.

3.3.2. IMAGE CONVOLUTION FOR AUTOMATIC POSITIONING

The live feedback of the CMOS camera and the fine, nanometre steps of the cold piezo-actuator allow for very accurate manual positioning, at least better than the laser spot resolution of 3 µm. The piezo-actuator alone is not however suitable for positioning and scanning, due to this model's lack of position feedback. A small uncertainty on the step size builds up over large scans, and displays significant hysteresis when inverting motion, essential for any 2D scan. On top of this, occasional missteps lead to very inaccurate scanning maps. All the data needed for precise positioning is however already recorded in the form of the CMOS camera images, and indeed it is already used for manual positioning: all that is really needed is a software routine to translate this information into a precise position.

To perform accurate 2D scanning maps, a software routine is developed in Python to determine the device relative position from the CMOS image, generating a software level positioning feedback loop with the piezo-actuators to accurately position the laser spot and perform consistent, precise 2-dimensional scanning maps.

This use case only requires translation detection, where more general scenarios can also include transformations such as rotation, scaling and shear. Many options exist, including edge and shape detection techniques. Here, a 2-dimensional convolution is employed, as it was found to be suitably robust and precise. This is achieved using the OpenCV library function $matchTemplate()$ with the TM_CCORR_NORMED method [131]. This is a 2-dimensional convolution, where the position image is multiplied by the reference image over a range of offsets in the x and y axes, yielding a global maximum where the images overlap, as shown in Figure 3.7.

The procedure works as follows: At the start of an experiment, the user records and stores a reference image for position $(0, 0)$. Then, he moves to two

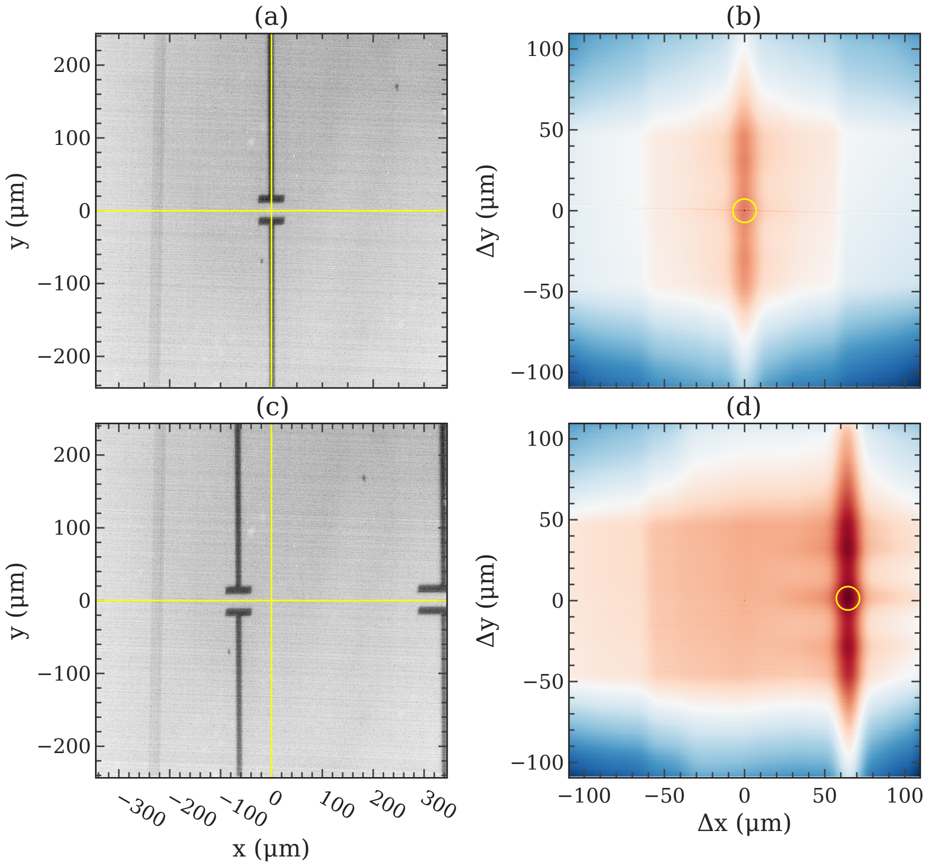

Figure 3.7: Device photos and their 2D convolutions for software device positioning. (a),(b) are microscopic device photos before and after a ∼65 µm device translation by the piezo-actuator. (b),(d) are plots of a of each photo's 2D convolution with a reference photo(a crop of (a)). The circled global maxima of the convolution plots precisely measure the vector displacement of the device.

more known positions $(x1, 0)$, $(y1, 0)$ to calibrate the absolute units of position and the approximate piezo-actuator step-size. To move to an arbitrary position (x, y), an image is recorded for the current position. A 2D convolution with the reference image determines the current position (xc, yc). If the difference $dx = x - x$c or $dy = y - yc$ exceeds the accepted tolerance, the piezo-actuator is instructed to move by the estimated distance dx and dy, and the procedure is repeated until dx and dy are below the accepted tolerance.

The position precision is limited by the CMOS camera resolution in relation to the objective and camera lens magnification, which works out to approximately 700 nm per pixel, well below the objective resolution. A brief thought was also given to z-axis autofocus, which can be achieved via contrast detection of the substrate surface features, similar to how certain modern mirrorless cameras achieve autofocus. However, this was not implemented as the z-axis proved sufficiently stable even over long, multi-day scans, as well as over fears a software error could crash a device into the radiation shield under focus wandering. In the x and y axes the PCB is in fact designed not to be able to crash into the radiation shield even under full actuator extension, which was not possible in the z-axis.

3.3.3. MULTI-LASER BENCHTOP OPTICAL SETUP

The optical setup built around the S100 optical cryostat was expanded to allow for greater component flexibility, stability and the incorporation of multiple lasers in the optical path, as well allowing for unrelated photoluminescence experiments.

The crucial vertical periscope, shown in Figure 3.8 is composed of three 1″ pillar posts. Two of these are placed at opposite ends of the cryostat, with a sliding breadboard mount holding the objective a downward periscope mirror and the Olympus 50X, 0.65NA objective with correction collar (LCPLN50XIR). The breadboard also holds a removable mount for the camera system consisting of a cage mounted beamsplitter, lens and CMOS camera. The third post, directly opposite the objective periscope, holds two periscope mirrors for elevating the table level optical path. A Thorlabs GVS012 2-axis galvo-scanner is placed before the periscope, followed by two lenses to steer and expand the beam by approximately a factor of 2. Before the galvo-scanner, the optical path is split by a 50-50 beamsplitter on a flip-mount. When the beamsplitter is removed, the system becomes a full photoluminescence setup, with a 980 nm laser fed through a 960 nm dichroic mirror. When the beamsplitter is active, it connects to the optical path of the two 1078 nm lasers for D^0X readout and pumping. The first laser's optical path, starting from a fibre collimator, is focused on an acousto-optic modulator in single pass mode, and then collimated again after beam clipping with an iris. The acousto-optic modulator is an Isomet M1404-T150L-0.25 employed in a single pass configuration. The second laser, again starting from a fibre collimator, is pulsed using a Thorlabs mechanical shutter. The two lasers optical paths are combined using a 50-50 beamsplitter. Common optical elements are added after the beamsplitter, including a 10 nm bandpass filter, a linear optical polariser or alternatively an optical depolariser, and a neutral density filter wheel.

The PL excitation path is still used for the above bandgap laser input, a 980 nm fibre laser and the device area illumination. The simple LED area illumination technique is not possible here, as the objective is now directly against the cryostat window, with a clearance of only about 100um. Instead, an incandescent light source is used, inserted in the optical path via a flip-mounted beam-splitter and focused on the objective by a plano-convex lens, such as to illuminate a large surface area, as shown in Figure 3.8c.

Finally, a silicon amplified photodetector is added to capture all 3 lasers off of the combining beam-splitter. With its output connected to the oscilloscope or the digitizer card, this allows for the live detection of all the laser powers, and it is further calibrated by recording the laser power at the objective input

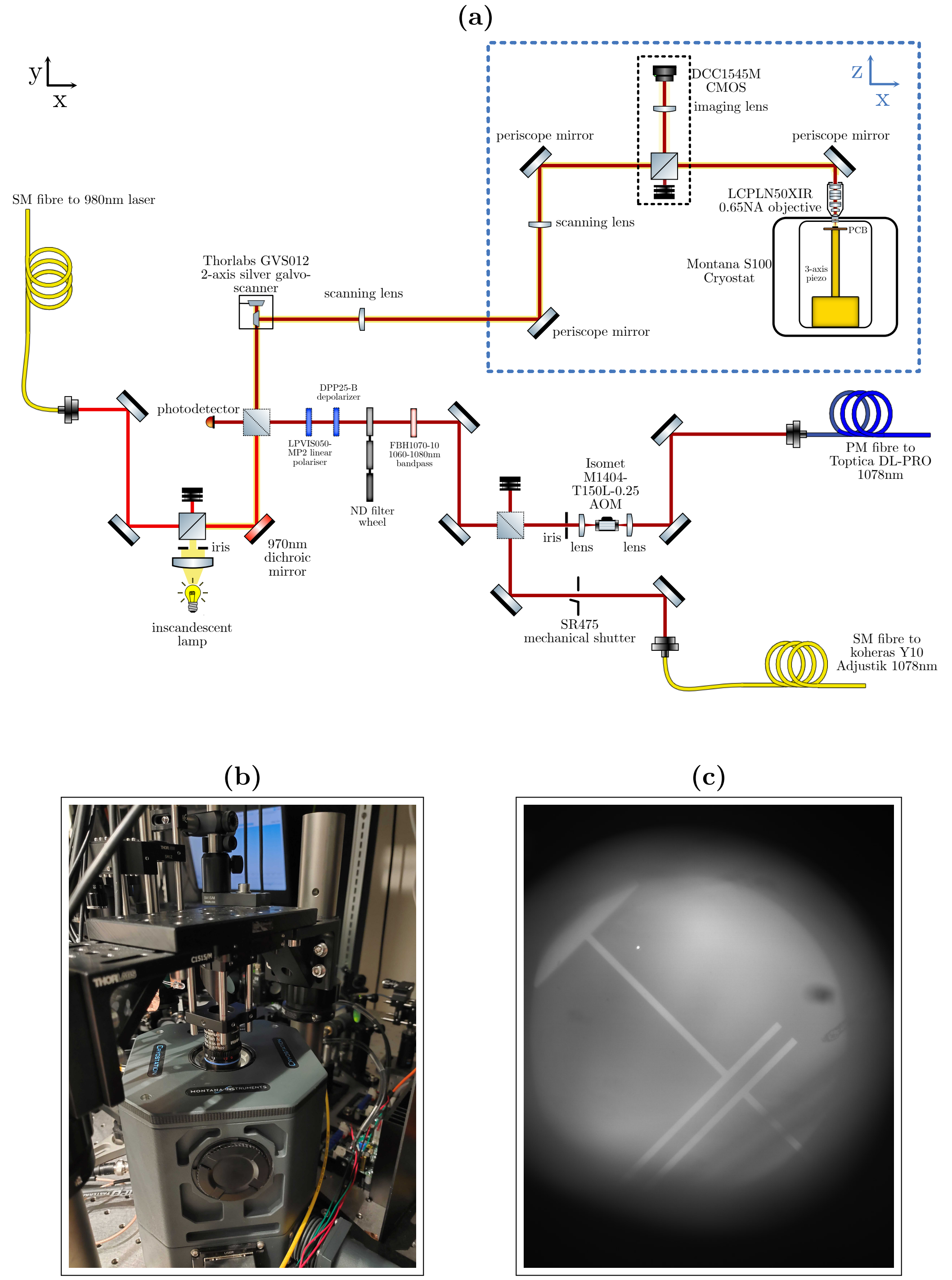

Figure 3.8: Multi-laser optical setup with for fast amplitude modulation and 2D galvo-scanning. (a) Optical diagram, dashed optical elements are either on flip-mounts or on removable magnetic posts [3](b) removable periscope photo (c) Epitaxial illumination CMOS image with visible ghosting.

---

[3] Optical vector components adapted from the "gwoptics ComponentLibrary" by Alexander Franzen, `http://www.gwoptics.org/ComponentLibrary` ©.

at the beginning of a cooldown. The laser power is further used to perform a slow, software level power stabilisation routine.

3.4. Electrical Setup

3.4.1. Lock-in Capacitive detection

The low-frequency photocurrent measurements presented in Section 4.2 were performed using the 2-port current amplification lock-in setup as shown in Figure 3.9. Every connection but the aluminium wire-bonds are 50 Ω lines: CPW transmission lines on PCB and SMA or BNC coaxial cables elsewhere. Impedance matching is not particularly important at low frequencies, and this is done for shielding for shielding purposes as the single wire lines of the cryostat were found to introduce large amounts of electromagnetic noise.

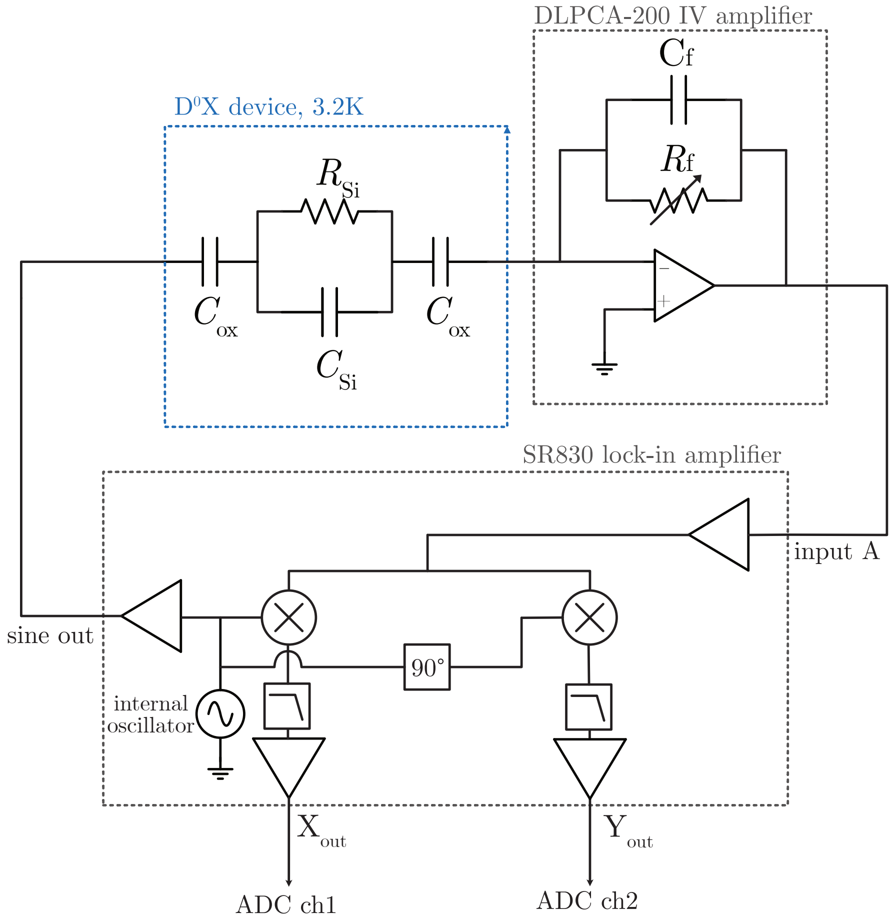

Figure 3.9: Low frequency lock-in detection setup. All external connections use coaxial SMA and BNC cables for shielding purposes.

The device input port is driven by the SR830 internal oscillator amplified output, with a V_{rms} range 0.004–5 V. The device output is connected to a low noise transimpedance amplifier, specifically the femto DLPCA-200. This is preferred to the SR830 on-board IV amplifier for the lower noise figure and the low footprint, which allows the placement on the optical table right outside the cryostat, minimising cable length, parasitic capacitance and triboelectric noise. An amplification of 10^6–10^7 V A^{-1} is used depending on the signal strength and driving frequency. The voltage output of the IV amplifier is then fed to the lock-in input, where it is further amplified, demodulated against the internal oscillator and filtered. The quadrature X and Y outputs are then connected to two channels of either a DSO2014A oscilloscope or a National Instruments USB-6341-BNC IO card for transient photocurrent detection in response to the 1078 nm laser pulses. The SR830 is thus allowed to run continuously, while the digitizer detection is triggered by the laser shutter pulse itself or a sync pulse. The pulse/sync pulses are generated with a variety on instruments, depending on availability, including the internal waveform generators of the DSO2014A and NI card or an external Keysight Agilent 33522A 30 MHz 2-channel AWG or a 33220A 20 MHz 2-channel AWG.

3.4.2. RF Reflectometry

RF reflectometry is a single port measurement technique to detect small changes in a complex impedance by embedding it in a high-Q, line-impedance matched LC resonator. Changes in the resonator impedance affect the reflection according to

$$\Gamma = \frac{Z - Z_0}{Z + Z_0} \tag{3.1}$$

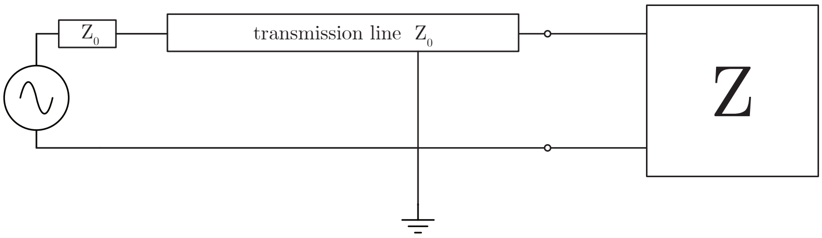

Figure 3.10: General RF reflectometry diagram.

The reflectometry measurement consists of a time-resolved reflection measurements, akin to an S11 reflection measurement performed with a vector network analyser (VNA). The reflectometry measurements are performed with a Rohde & Schwarz SMC100A 1.1 GHz source and a custom built reflectometry bridge. As described in the diagram of Figure 3.11 and shown in Figure 3.12(a), the source first connects to the first Mini-Circuits ZX30-15-5-S+ directional coupler, providing a ∼ 0dBm input to the IQ mixer LO. The coupling signal (−17dB) is instead routed to a second directional coupler, such that the input has a high loss (−17dB) while the output is unattenuated. High transmission return could alternatively be achieved with a circulator. The input signal is then routed into the cryostat and to the PCB via a series of 50 Ω coaxial cables. The return signal is routed to a series pair of ZX60-112LN+ low noise RF amplifiers, and then to a Polyphase Microwave AD0540B quadrature demodulator. The I and Q quadrature outputs are finally low pass filtered and fed to two channels of a DSO2014A oscilloscope or a National Instruments USB-6341-BNC IO card for laser pulse triggered transient detection, exactly like for the low-frequency setup. The reflectometry bridges employed were designed, assembled and tested by Simon Schaal, Virginia Ciriano, Sofia Patomaki, Edward Thomas and Jingyu Duan.

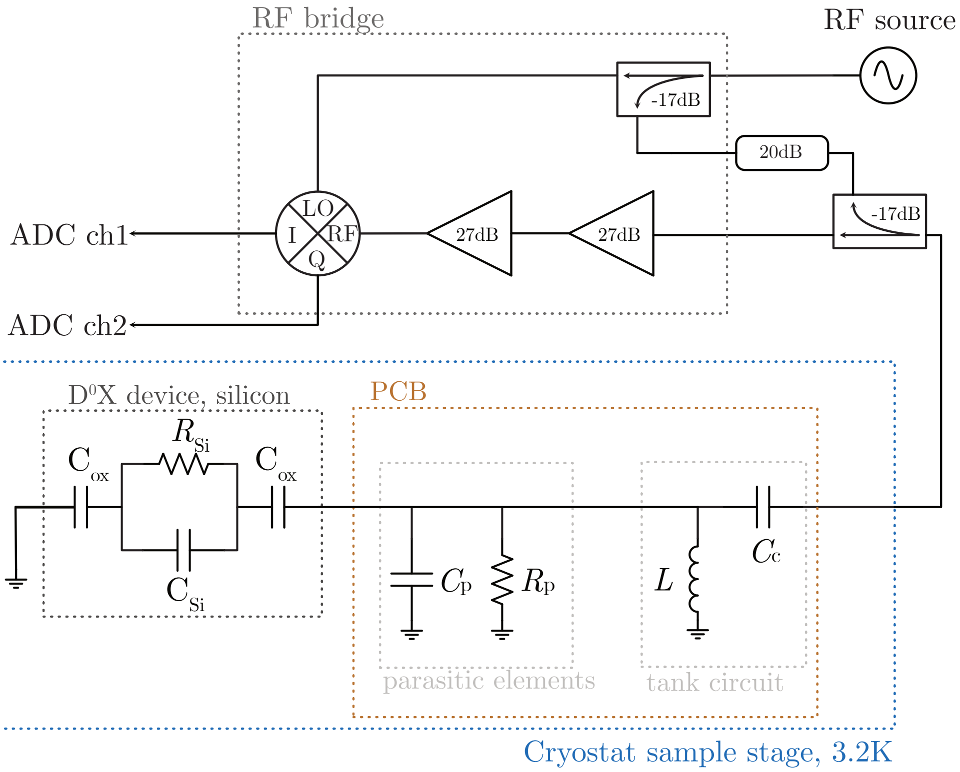

Figure 3.11: RF reflectometry measurement setup. All external lines are 50 Ω SMA/SMP coaxial cables with grounded shields. The PCB lines are GCPW lines.

Normally, the second directional coupler and at least one amplification stage are placed inside the cryostat at low temperatures to take advantage of the lower thermal noise or even quantum noise limited amplification [132]. Here, the amplification stages are all at room temperature due to surmountable yet tricky space and design constraints, as well as to provide a like-for-like comparison with the low frequency lock-in technique.

The on-PCB LC resonator consists of a series coupling capacitor and a parallel inductor. This is described in full details in Section 4.3. The PCB lines are the same 50 Ω CPW transmission lines used for the low frequency experiments, with a small gap cut with a scalpel for the coupling capacitor and a hand wound 0.5 mm wire soldered across ground as a inductor.

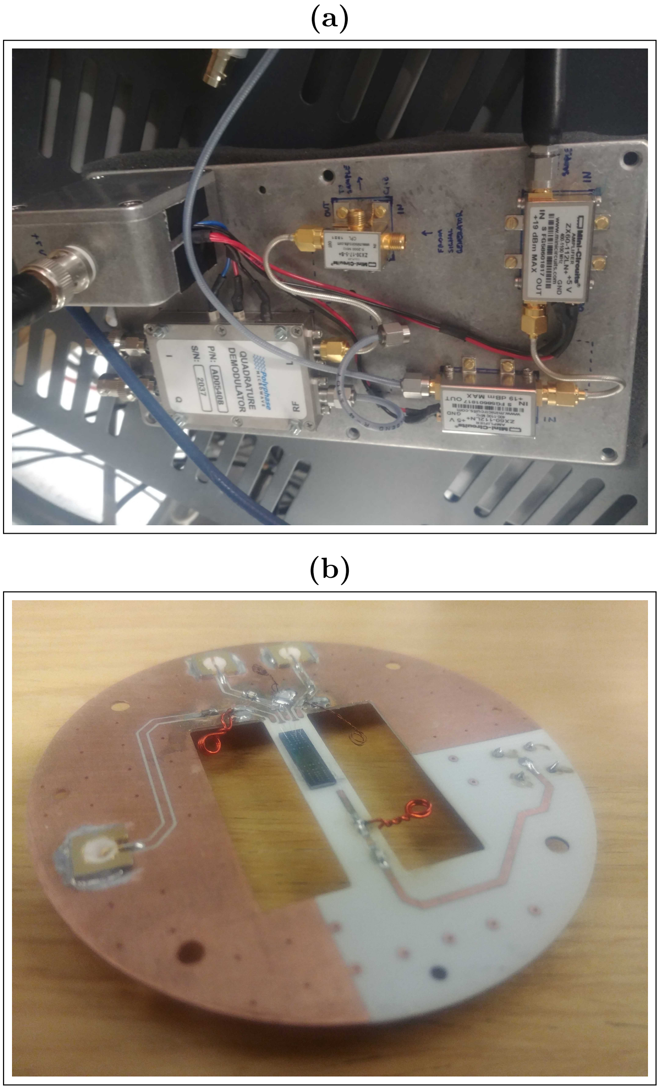

Figure 3.12: Reflectometry Setup (a) Reflectometry bridge (disconnected) (b) Measurement PCB modified with coupling capacitor and parallel inductor for RF reflectometry.

3.4.3. MICROWAVE GENERATION

Vector microwave pulses for the attempted hybrid optical-microwave D^0X experiments of Section 6.3 were generated with a Rohde & Schwarz SGS100A 12GHz Vector Signal Generator, amplified with a solid-state amplifier. Pulse modulation and IQ vector analogue modulation was generated with a Swabian Instruments Pulse Streamer 8/2 AWG with 2 125 $\mathrm{MSa\,s^{-1}}$ analogue channels and 8 1 $\mathrm{GSa\,s^{-1}}$ digital channels. Transmission to the PCB is done with the cryostat built-in hard coaxial lines and flexible coaxial lines with SMP connectors. For the Abe antenna experiments, a circulator with a 50 Ω terminator is added after the amplifier to prevent standing waves and reflections. For the wire transmission setup, a 50 Ω terminator is added on the cryostat's microwave output port. Full details of the microwave antennas and choice of pulse sequence is presented in Section 6.3.

3.5. ELECTRON SPIN RESONANCE SETUP

The hybrid optical-microwave experiment described in Section 5.1 was performed using an X-band cavity inside a liquid helium cryostat and a custom assembled microwave spectrometer. These were the only low temperature experiments presented in this performed on a different cryostat than the Montana S100. Therefore, the whole setup is different, including cryostat, optical path and microwave setup, and are described separately in this section to avoid confusion with the main D^0X photoconductive setup.

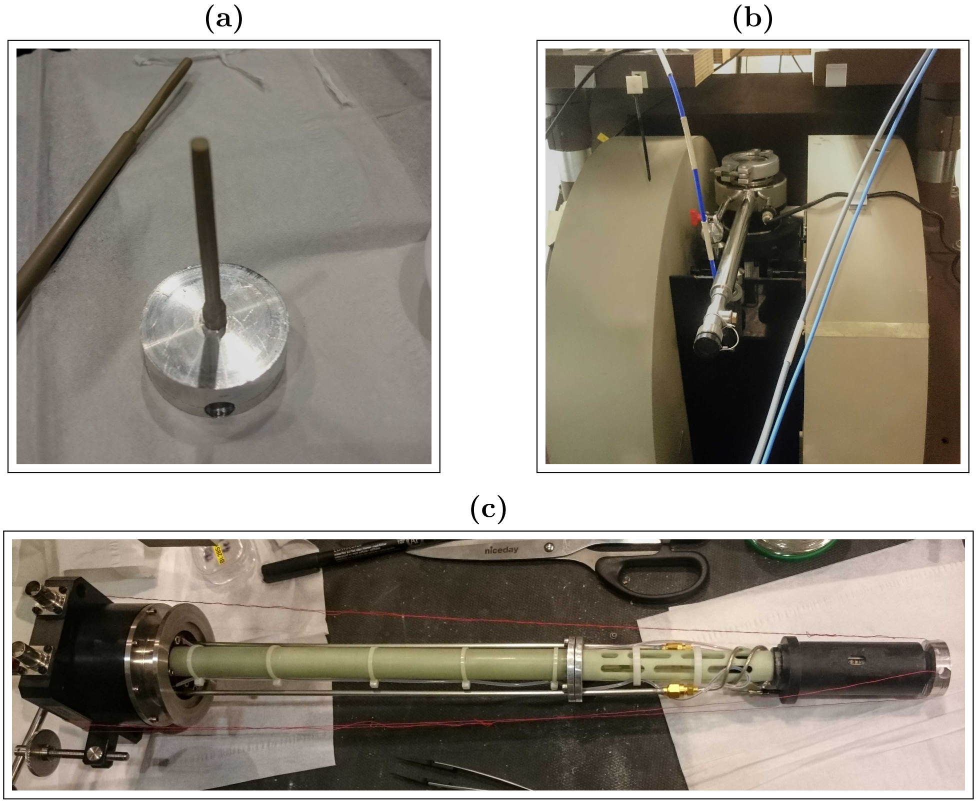

Figure 3.13: Strained D^0X ESR setup. (a) Base and top portion of the peek rods for sample straining. (b) Cryostat and magnet. (c) Bruker X-band resonator.

The cryostat is an Oxford Instruments CF935 liquid helium flow cryostat, shown in Figure 3.13b operated by a coaxial transfer arm connection to a

120 L liquid helium dewar from BOC. The cryostat is operated with helium naturally flowing out of the dewar in overpressure mode, thus achieving a base temperature of 4.2 K.

3.5.1. X-BAND CAVITY RESONATOR

Paramagnetic resonance usually employs a resonator to achieve a strong and uniform microwave B_1 field. Here a cylindrical sapphire cavity resonator is used, with a diameter of ∼6 mm, in the form of a Bruker Flexline EN 4118X-MD4W1 resonator, shown in Figure 3.13c with its whole loading mount and strain rod attached. A warm mounting of the resonator is performed to avoid unnecessary thermal shocks to the strain rod setup. The cavity antenna is tuned to a rough value of 1000 to balance the need for amplified but short microwave pulses.

3.5.2. PULSED ESR SPECTROMETER

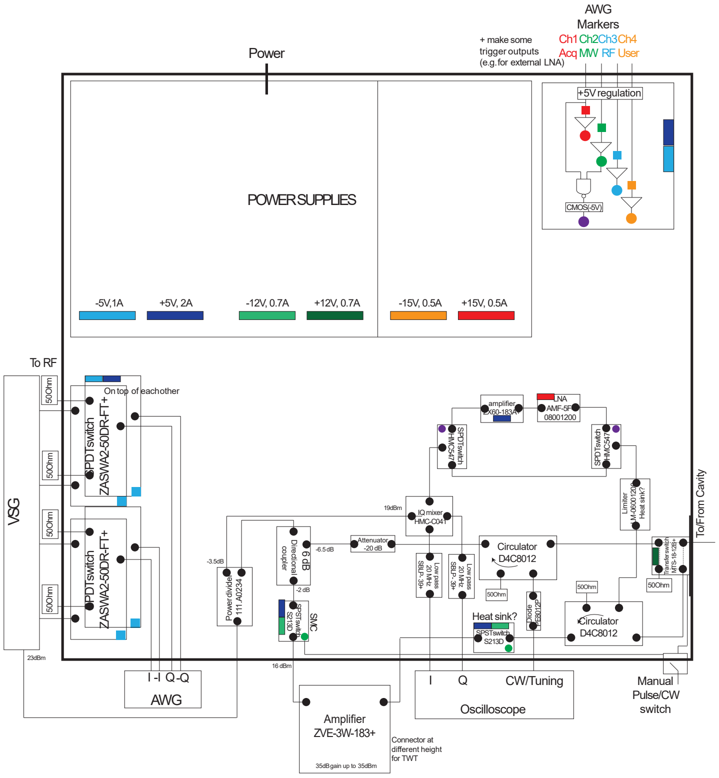

Figure 3.14: Zoidberg X-Band pulse spectrometer, design, and assembly by G. Wolfowicz and M.P. Ross. Diagram reproduced from Ross [26, p. 78].

The pulsed ESR experiments to detect the donor spin polarisation were performed using a custom built X-band pulsed ESR bridge, designed and built by Dr Gary Wolfowicz and Dr Philipp Ross. The microwave signal is generated by a Keysight E8267D vector signal generator (VSG), with IQ envelopes, switch and detection triggers from a Keysight 81180B AWG. The demodulated quadrature IQ signal is detected with a Keysign Agilent MSO3014A oscilloscope. The spectrometer is operated using the GARII custom Matlab programme by G. Wolfowicz and M.P. Ross., which handles instrument communication, pulse sequence design and data saving.

3.5.3. RESONANT BULK SAMPLE ILLUMINATION

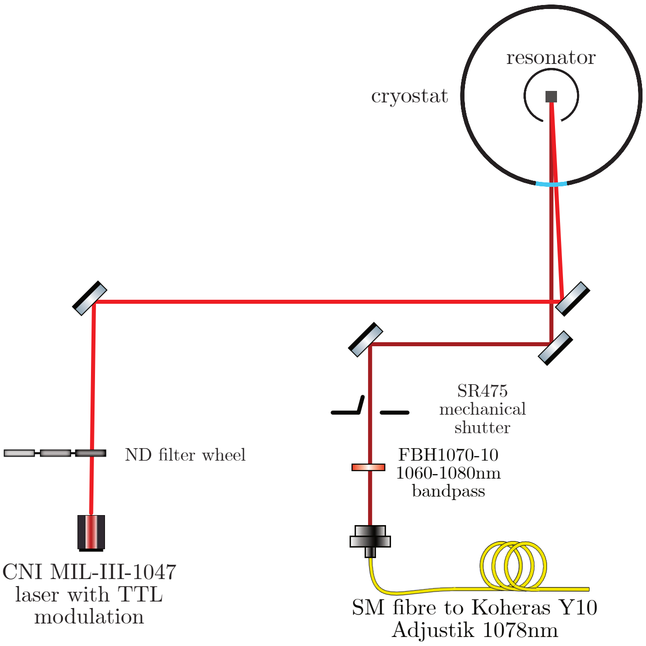

Figure 3.15: Optical setup for the bulk ^{28}Si sample illumination inside the helium flow cryostat and X-band resonator. [4]

The donors of the bulk silicon sample are illuminated with the same NKT-photonics koheras adjustik Y10 1077.5–1078.5 nm used throughout other parts of this work. A simple optical path is setup on the optical table behind the cryostat to steer and route the laser's fibre collimated output beam through a mechanical SR475 mechanical shutter, an ND filter wheel and finally through the cryostat window and to the cold silicon sample. A second, above-bandgap CNI MIL-III-1047 500 mW laser is employed to reset and repopulate the donor spins, with heavy ND filtering and slightly staggered optical paths to combine the beams.

---

[4] Optical vector components adapted from the "gwoptics ComponentLibrary" by Alexander Franzen, `http://www.gwoptics.org/ComponentLibrary` ©.

3.6. Software and Hardware

All experiments presented in this work, apart from the ESR one from Section 5.1, are run in a Jupyter Lab/Notebook interface using the Python programming language and data acquisition framework QCoDeS [133]. QCoDeS handles instrument communication as a wrapper to the pyvisa class, on top of the NI-VISA driver. Many instruments are already wrapped, while custom classes are create for those not present. Data saving is also handled by QCoDeS, which saves the recorded data in a series of SQLite databases.

Analogue and digital pulse generation is performed with a variety of waveform generators, including a Keysight Agilent 33522A 30 MHz 2-channel AWG and a 33220A 20 MHz 2-channel AWG. For the dual laser and microwave experiments of Chapter 6, where more than two channels are needed, as well as fast pulse modulation of a WURST microwave pulse, a Swabian Instruments Pulse Streamer 8/2 AWG with 2 125 $\mathrm{MSa\,s^{-1}}$ analogue outputs and 8 1 $\mathrm{GSa\,s^{-1}}$ digital channels. All analogue transient signals are recorded with a DSO2014A oscilloscope or a National Instruments USB-6341-BNC IO card for transient photocurrent detection in response to the 1078 nm laser pulses. The lock-in experiments are performed with a Stanford Research SR830 lock-in amplifier. A low noise Keysight B2962A power source is used for the DC measurements of Section 4.1, and for powering LEDs.

4. PHOTOCONDUCTIVE D^0X DETECTION IN MICROSCALE DEVICES

This chapter investigates the electrical characteristics of microscale devices for the electrical detection of donor bound excitons. The devices investigated, described in more detail in Section 3.1, consist of a planar capacitor structure with two rectangular, aluminium contacts of width 10 µm and length 10–800 µm separated by 2–50 µm. Each capacitor is connected via a 10 µm thick feed line to a large 200 × 200 µm contact pad for wire bonding the device to a custom PCB. The contact pads and the feed line are always isolated from the silicon via a thin, ∼11 nm oxide layer. Regarding the capacitors, three contact types are investigated: Schottky contacts, where aluminium is deposited directly on the Silicon substrate, n-type pseudo Ohmic contacts where high concentration arsenic dopants are implanted underneath the aluminium contacts, and finally metal-oxide-semiconductor (MOS) type gated contacts where the aluminium contact and silicon substrate are separated by a thin 12 nm layer of thermal oxide. As this chapter discusses, only MOS contacts display electrical sensitivity to local donor illumination. On the other side, Schottky and pseudo-Ohmic contacts display photoconductive responses to bulk donors, with no discernible local selectivity.

Having established a promising contact chemistry, MOS devices are systematically explored, first using low frequency capacitive lock-in detection techniques, and then via LC-resonant RF reflectometry.

4.1. DC DEVICE CONTACT ANALYSIS

4.1.1. DUAL SCHOTTKY METAL CONTACTS

Double Schottky device are often used as photodetectors, known is an MSM type, and are considered sensitive due to the low dark currents and fast [134]. The fundamental idea is that a Schottky contact on silicon tends to be a bad carrier injector but a good collector. This is ideal as under above-bandgap illumination, electron-hole pairs are generated and, without carrier injection, only photocarriers contribute to the current. The matter is naturally more complex when photocarrier generation is asymmetric, such as in this work where D^0X ionisation only generates electrons.

Despite expectations, all attempts on multiple devices displayed a complete lack of sensitivity to the localised near contact implanted donors, and instead showed a response to the low-density donors present in the whole sample, which will be referred to as residual bulk donors.

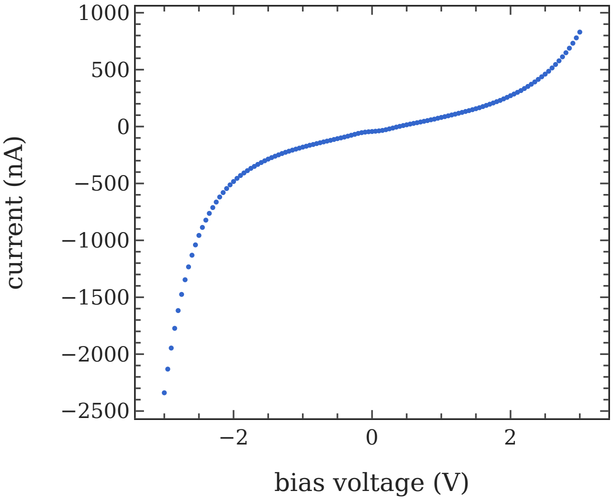

Figure 4.1: IV scan of a 20 × 100 µm dual Schottky contact device.

First, the IV behaviour of Figure 4.1 is characteristic of a double Schottky junction with a relatively high ideality factor. A high ideality factor implies a behaviour dominated by the depletion region of the junction, most likely depletion region recombination [135].

Regarding the photoconductive response, Figure 4.2 shows how IR illumination has relatively little effect on the current, almost undetectable at low voltage levels. The current appears to show a near linear dependence with laser power, with some signs of saturation at the highest power.

A D^0X resonant peak is observed when scanning the resonant 1078 nm laser, consistent with the D^0X transition energy of phosphorus donors, as shown in Figure 4.3. However, the resonant peak appears, mostly identical in shape and magnitude, regardless of whether the laser spot is placed on the implanted device patch or off the device entirely. Furthermore, the peak shows a very low splitting between the mostly overlapping light and heavy hole peaks, incompatible with the strain expected near a silicon-metal interface at cryogenic temperatures. This suggests with certainty that the source of this peak is not, as would be expected, the high density implanted Si:P donors between the metal contacts, but rather the low density Si:P donors of the silicon bulk. Despite the substrate being the highest purity standard float-zone silicon, a residual concentration of phosphorus in the range 10^{11}–$10^{12}\,\mathrm{cm}^{-3}$ is always

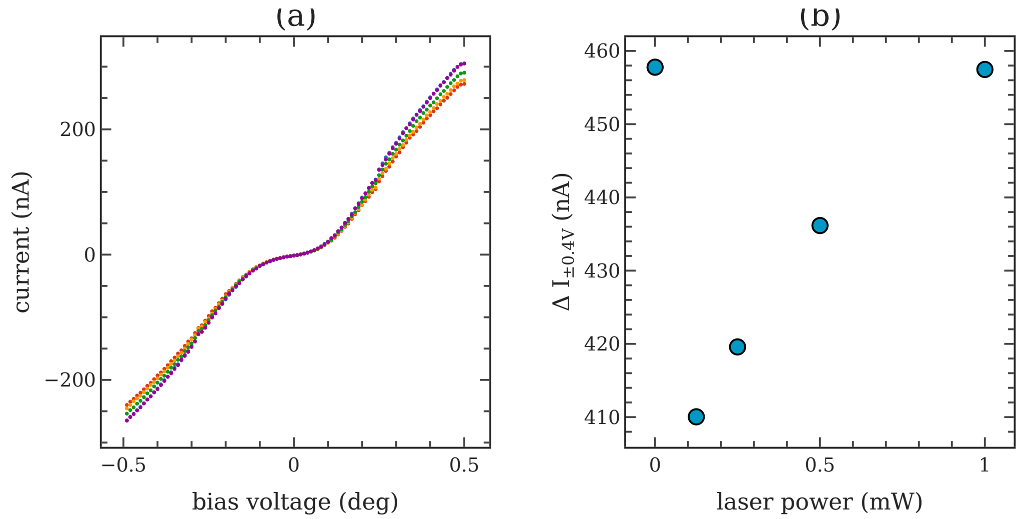

Figure 4.2: 1078 nm illumination dependent IV scan of a 20 × 100 µm dual Schottky contact device. (a)IV curve. (b)Power dependent photocurrent at $V = 0.4\,\mathrm{V}$.

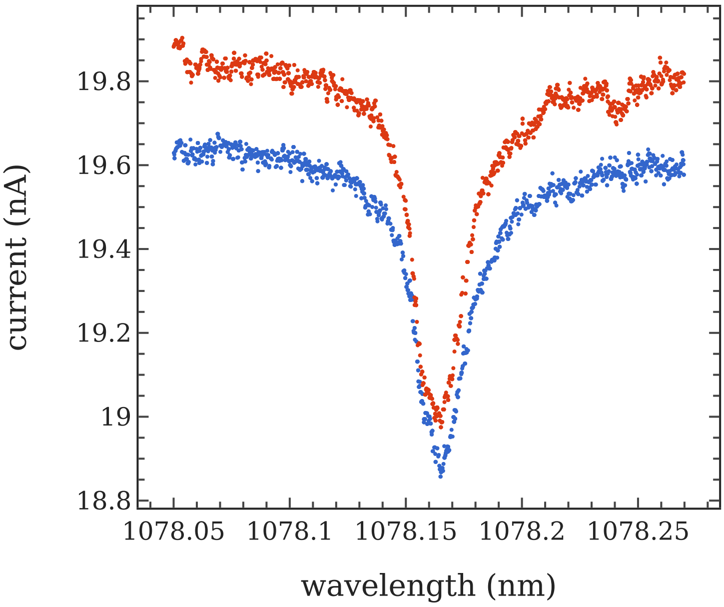

Figure 4.3: D^{0}X photoconductive spectrum in a 20 × 100 µm dual Schottky device, with illumination • ON the device and the implanted donor patch, and • OFF the device entirely.

present. And although the laser beam is focused on the surface, a diverging beam does illuminate the bulk residual donors, albeit at a much lower magnitude. Considering the illumination cone, the volume behind a device can contain a significant number of residual donors. For example, in a substrate of thickness 250 µm, the volume illuminated in the bulk can contain over a million residual donors, against only few thousand that are illuminated in the implanted patch. Even considering the difference in illumination density, the bulk donors can dominate the detection signal if there is no electrical discriminant favouring local photo-carriers.

This result was consistent across multiple devices and extremely similar in pseudo-Ohmic devices, and led to a choice to focus on the much more locally sensitive MOS devices. It should be noted that previous work successfully employed Schottky contacts for the photoconductive detection of donor bound excitons [23, 27], albeit in bulk doped samples. Finally, the potential use of these devices should not be fully ruled out, as the detection of residual donors in a high resistivity sample is itself non-trivial.

4.1.2. DUAL MOS CONTACTS

Conversely to the Schottky contacts, metal-oxide (MOS) contacts displayed a strong sensitivity to the illumination of local implanted Si:P donors, and very little signal from the bulk residual donors.

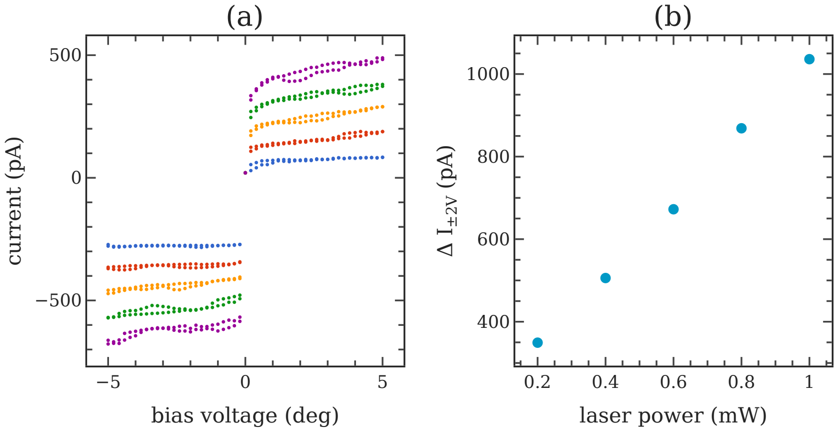

Figure 4.4: 1078 nm illumination dependent IV scan of a $20 \times 50\,\mu\text{m}$ dual MOS contact device. (a)IV curve. (b)Power dependent photocurrent $\Delta I_{\pm 0.2\text{V}}$.

As shown in Figure 4.4, the IV curve of the MOS devices present a constant leakage current, typical of oxide interfaces at low fields, with an almost perfectly linear response to above bandgap illumination, as well as much lower levels of current noise. This is quite surprising behaviour at DC, as a MOS contact should be insulating, especially at the low temperature of 3 K, however both the dark and illuminated current response are compatible with literature observations in thin oxide structures [136]. The behaviour is understood as a tunnelling regime limited not by electric field but by the carrier generation rate in the silicon. A wavelength sweep, displayed in Figure 4.5, unequivocally shows the photoconductive response sensitivity to the resonant D^{0}X illumination of implanted donors between the device contacts. Of the three curves, illumination off the device results in a lower, flat response, while illumination on the implanted donor patch yields a higher current curve with two distinct peaks split by approximately 30 nm, compatible with strain induced light and heavy hole splitting. The absence of the peaks off device indicates that the signal is indeed from the implanted donors, while the difference in off resonance current suggests that even the non-resonant above-bandgap photo-response is due to the implanted donors, specifically their direct ionisation. The third curve is recorded while illuminating the implanted patch on a neighbouring, unconnected device, and again shows no signal, suggesting that the contacts are only sensitive to locally generated electrons.

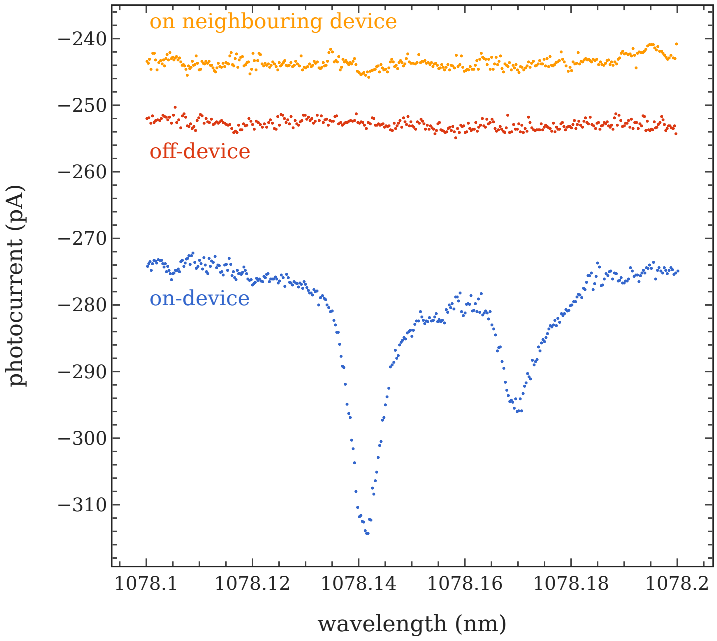

Figure 4.5: D^{0}X photoconductive spectrum in a 20 × 50 µm dual MOS device, with illumination • ON the device and the implanted donor patch, • OFF the device entirely, and • on the implanted donors of a neighbouring, unconnected device.

Having established that MOS contacts present the strongest response to above bandgap illumination, and especially the only response unequivocally attributable to implanted donors, we further explore two electrical detection techniques on MOS devices: low frequency transimpedance detection and RF LC resonant reflectometry.

4.1.3. POWER DEPENDENCE OF THE RESONANT PHOTOCURRENT

The donor bound exciton transition can, in principle, be driven coherently, but is subject to fast electrical Auger decay to the D^+ state with a time constant of 270 ns, hindering any attempt at coherent driving slower or close to this. The first sanity check on the behaviour of the observed photocurrent spectrum is therefore to verify the power behaviour of the D^0X transition. To do this, a photocurrent laser wavelength scan is repeated while varying the laser power. Due to the limited range in laser power, this is then repeated with the addition of a neutral density filter. As shown in Figure 4.6a, at the highest power levels a central peak is also visible, compatible with the residual phosphorus donors of the bulk silicon substrate.

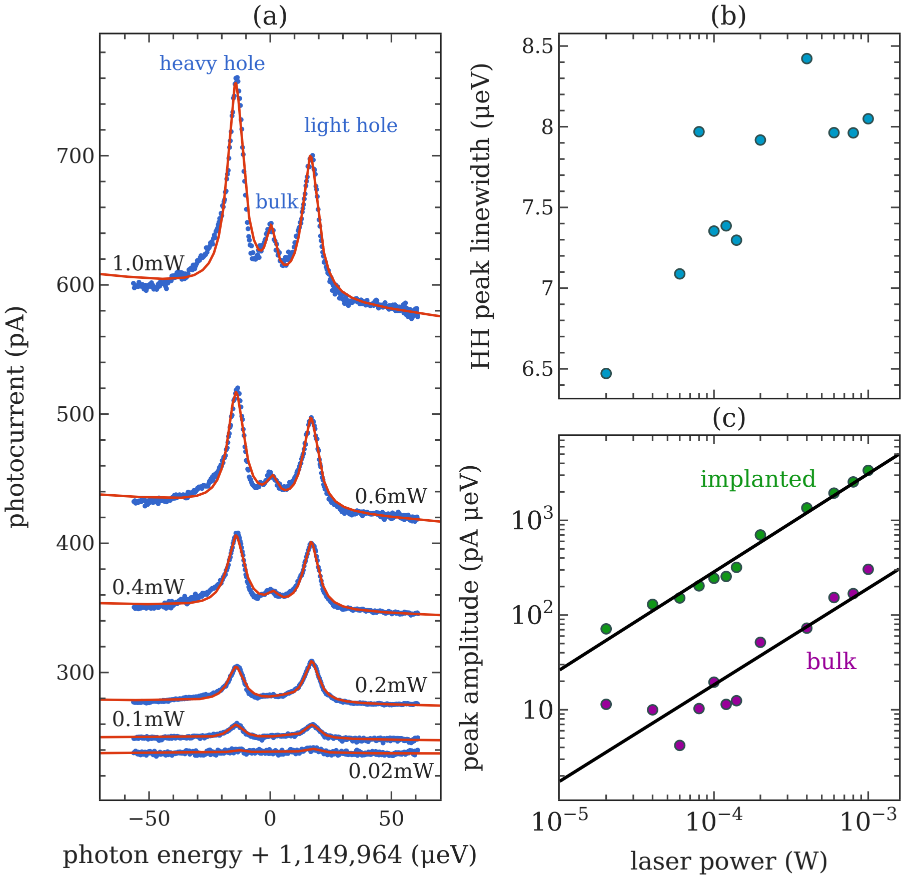

Figure 4.6: Direct current D^0X spectrum under variable laser power. (a) wavelength sweeps (b) heavy hole linewidth against laser power (c) implanted and bulk peak amplitude relationship to laser power.

To extract the peaks amplitude, a three peak Lorentzian model is fitted to the photocurrent curves. Figure 4.6c shows the extracted power dependence. For the implanted donors' peaks, the sum of the amplitudes is plotted. The amplitude power fitting is performed on the respective logarithms $\log_{10}(P) - \log_{10}(A)$ to take advantage of the large power range investigated. Assuming a power law power dependence $A = mP^\alpha$, a log-log fitting gives

$$\log_{10}(A) = \log_{10}(m) + \alpha \log_{10}(P) \tag{4.1}$$

This allows the extraction of the dominant power factor α and the multiplicative factor which is now the intercept. The result is a clear linear fit with $\alpha_{\text{impl}} = 1.03$, $\alpha_{\text{bulk}} = 1.02$ and thus a linear power relation. The amplitude coefficients are more than an order of magnitude apart, with $m_{\text{impl}} = 3.98 \times 10^6$pAµeV and $m_{\text{bulk}} = 0.21 \times 10^6$pAµeV. This sits in stark contrast to what was observed in the double Schottky devices, with a well visible bulk peak and no local strained peaks at all.

The second notable effect of increasing laser power is a visible change in the linewidth of the heavy hole peak with resonant laser power. This may be indicating a degree of power broadening. This is not surprising considering the high power densities resulting from the small laser spot of ∼2.5 µm. The power density range here corresponds to $3.6 \times 10^7\,\text{W}\,\text{cm}^{-2}$ for the lowest 20 µW and $1.8 \times 10^9\,\text{W}\,\text{cm}^{-2}$ for the 1 mW incident power. Power broadening in the D^0X transition has previously been observed by Yang [15] in a pump probe experiment at much lower power densities only up to $10\,\text{W}\,\text{cm}^{-2}$, albeit in an isotopically purified ^{28}Si sample and thus a much smaller intrinsic linewidth. So, it is clear that this is a regime of high power broadening. From a practical standpoint, this is not necessarily an issue for these small levels of broadening, given that the natural FZ-silicon D^0X linewidth is approximately 3 µeV, as confirmed by the bulk peak fit. Various attempts were made at modulating the laser wavelength, showing no impact on amplitude while $\delta\lambda < FWHM_\lambda$, indicating that subset excitation does not affect the amplitude of the peaks. The issue arises if one was to attempt to address a subset of the donor population, resolved by the strain splitting. This is however best addressed in a pump-probe experiment, and the matter is explored further in Chapter 6.

4.1.4. Bias Voltage Shift of the D^0X Energy

The donor bound exciton transition energy has been theoretically predicted to vary with electric field [130, 137, 138], as discussed in detail in Section 2.5.2. Understanding such behaviour is key to the operation of any electrical detection method, as this is likely to involve an electric field and possibly charge noise from free carriers. Ross [26] observed a quadratic electric field shift in a bulk doped device, and Lo [23] observed a linear electric field shift in an epitaxial ^{28}Si device.

Here, this is investigated under direct current conditions on the 20 × 50 µm device discussed in this section, by recording wavelength-photocurrent curves under variable bias a variable voltage bias parameter. The result of this experiment is shown in Figure 4.7(a), where a selection of the recorded curves is displayed. The minimum bias voltage which produced an observable pair of resonant peaks was 15 mV, negative or positive. The curves with observable peaks are fitted to a pair of Lorentzian peaks to extract the parameters of interest: centre, FWHM and amplitude.

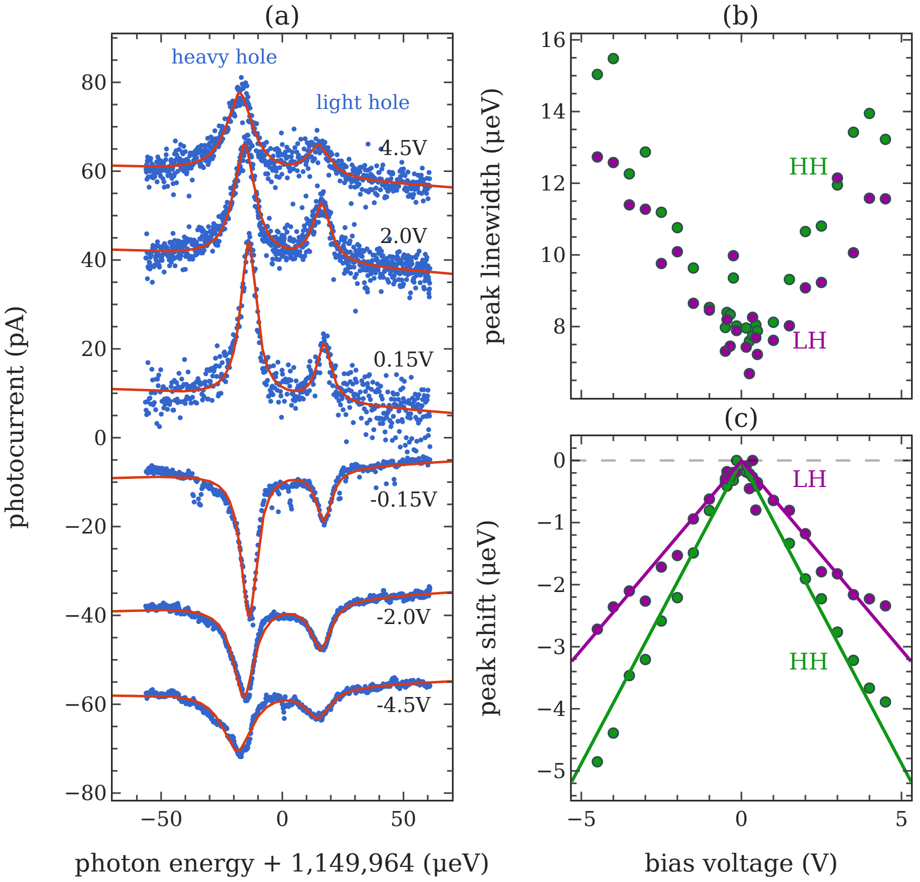

Figure 4.7: Direct current D^0X spectrum under variable voltage bias. (a) wavelength sweeps (b) linewidth against voltage bias (c) Fitted linear light and heavy hole peak ship against voltage bias.

The asymmetry in the noise spectrum should first be addressed, as the positive voltage bias curves are significantly noisier in spite of a similar peak amplitude. The reason for this is not fully understood: the back of the silicon was silver pasted to a metal pad to secure the sample; however this was left floating, unconnected to ground. It is possible that if the bulk was somehow grounded, then the positive bias accumulated carriers generating a higher level of charge noise. In any case, this did not appear to influence the amplitude or bias shifts of the peaks. It could also possibly be a result of a suboptimal, asymmetric response in the current amplifier. Secondly, the amplitude was observed not vary significantly across the bias range, in line with the observation of a flat IV curve for this device. Considering now the peak centres, there is an appreciable, negative linear shift of both peaks following a linear relation

$$\Delta E = -m|V_{\text{bias}}| \tag{4.2}$$

with a slope of $0.98(2)\,\mu\text{eVV}^{-1}(19.6(4)\,\mu\text{eV}\,\mu\text{mV}^{-1})$ for the heavy hole and $0.61(2)\,\mu\text{eVV}^{-1}(12.2(4)\,\mu\text{eV}\,\mu\text{mV}^{-1})$ for the light hole. The issue with quantifying the magnitude of this effect with respect to electric field is that unlike for ohmic contacts, there is likely to be a significant voltage drop across the MOS oxide, making it difficult to estimate the exact electric field in the silicon. However, the values obtained are in reasonable agreement with those of Lo [23], who obtained $33\,\mu\text{eV}\,\mu\text{mV}^{-1}$. This work's lower parameter is most likely explained by the potential drop across the oxide. It is also interesting to compare the light and heavy hole electric field splitting, which Bir predicts following a linear $\Delta E \approx 2p\chi E$ relation at low electric fields [130]. He estimates $2p\chi \approx 10^{-6}\,\mu\text{eVV}^{-1}\text{m}$, which is in reasonable agreement with this works' $6.4(5) \times 10^{-6}\ \mu\text{eVmV}^{-1}$. Finally, there is a very significant, linear broadening of both the light and heavy hole peaks, with the linewidth approximately doubling in the range 0.15–4.5 V. This is possibly related to the shift of the peaks, as it is similar in magnitude. However, it is hard to imagine there is such a large, almost 100% variation of electric field within a small, 4 µm spot at the centre of a 20 µm wide device. The thin, ~100 nm implantation profile further ensures a homogeneous electric field distribution, and the Lorentzian profile suggests a homogeneous broadening mechanism. It is most likely that the high electric field is broadening the peak due to some other mechanism, such as trap capture and emission charge noise. For example, this is a regime where shallow level impact ionisation is expected, and it has already been identified as a source of quenching for the D^0X transition at high fields [139]. It is plausible that an increase in the slow shallow donor or trap ionisation rate, competing with the carrier recapture, could lead to an increase in charge noise.

4.2. AC CAPACITIVE DETECTION

The previous section established that a device consisting of a pair of MOS contacts under a voltage bias can produce a resonant DC current under the D^0X resonant illumination of a small patch of donors. The insulating, high resistance nature of an oxide layer however suggests that this is far from optimal, and an alternating current detection is more suitable, both to lower the impedance of the dielectric oxide layer and to reduce the low frequency 1/f noise, thus improving the sensitivity to the photoconductive response. Capacitive detection of D^0X photoconductivity was demonstrated by Ross [25] in a bulk sample using a pair of metal electrodes, also achieving lasting donor spin polarisation and thus spin to charge conversion. This section advances this concept demonstrating that capacitive detection can be effectively scaled down to the microscale and to the detection of only a few thousand donors.

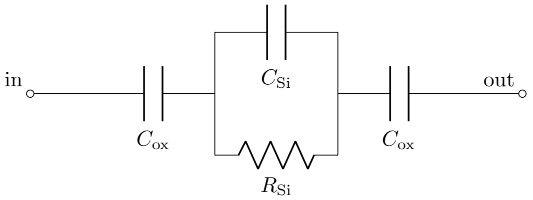

Figure 4.8: D^0X MOS device circuit diagram.

The detection technique presented here involves a simple 2-port low frequency AC detection setup: a small oscillating voltage is applied to one contact, while the second contact is connected to a low noise transimpedance amplifier and onto a lock-in amplifier, where the output is demodulated against the source wave. The demodulated I and Q outputs of the lock-in amplifier are then fed into an oscilloscope for the detection of transient responses. The full list of equipment is described in Section 3.4.1.

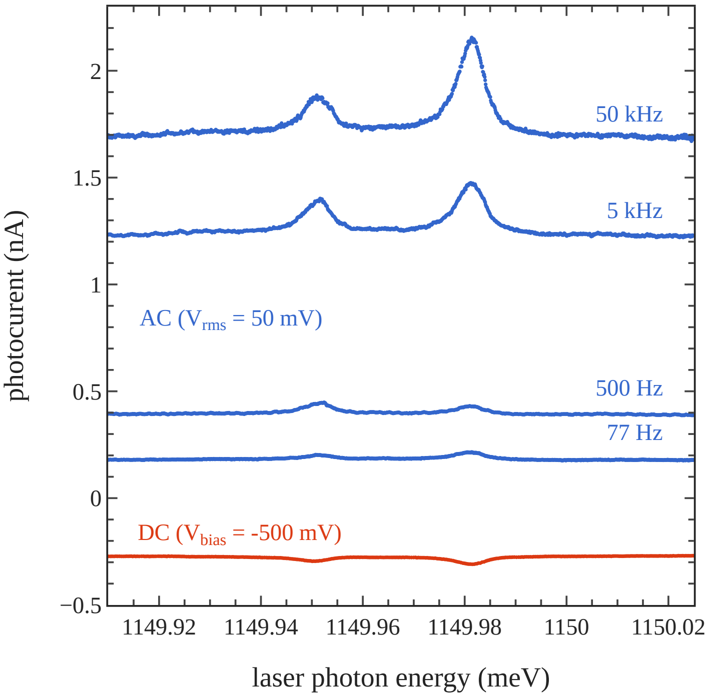

Figure 4.9: Comparison of AC and DC photocurrent D^0X spectra in a $50 \times 20\,\mu\text{m}$ MOS device.

As expected from a capacitive device, a first direct comparison in Figure 4.9 shows that AC voltage driving yields resonant photocurrents over an order of magnitude greater than DC, needing lower voltages. Having established this simple duality, the rest of this chapter focuses on a systematic, multi-parameter study of this detection technique to determine the photo-electrical device behaviour as well as its optimal operating conditions. Regarding the optical setup, the data presented so far in this section was recorded using the 0.35NA single laser setup described in Section 3.3.1. This setup only allows for limited polarisation, power and transient control, as well as limited power calibration and stabilisation. The rest of this chapter is entirely based upon the 0.65NA, multi-laser fast modulation setup described in Section 3.3.3 to present a systematic, well calibrated electrical study.

4.2.1. DEVICE IMPEDANCE

It is first useful to analyse the device frequency dependence impedance. The result of a frequency sweep is shown in Figure 4.10 in fully dark conditions, without illumination. The impedance magnitude here is simplistically obtained from the source voltage and output current as $|Z| = \frac{|V_{\mathrm{rms}}|}{|I_{\mathrm{rms}}|}$, as the absolute phase of the signal is not recorded.

The model is fitted to the simple RC circuit shown in Figure 4.8, consisting of a parallel resistor and capacitor, representing the silicon substrate, sandwiched between two capacitors, representing the oxide layers. This is of course a simplification, as Section 4.1.2 showed that the oxide also has some leakage, but at higher frequencies the dielectric capacitance is expected to dominate. Regarding the silicon, for low carrier densities this can be modelled as a parallel RC circuit, where the capacitance derives from the high dielectric strength of the material, and the non-infinite resistance from the free carriers. The experimental impedance matches this model reasonably well, deviating by only about 10% at the highest frequencies. In the fit, the oxide capacitance C_{ox} is held constant, calculated from the size of the contacts and the oxide dielectric strength and thickness as $C_{\mathrm{ox}} = \frac{A\epsilon_{\mathrm{SiO_2}}\epsilon_0}{t_{\mathrm{ox}}}$, which works out to 1.44 pF. The Silicon parameters are allowed to vary, yielding a resistance of $R_{\mathrm{Si}} = 137\mathrm{M}\Omega$ and a capacitance $C_{\mathrm{Si}} = 255\mathrm{fF}$. Naturally, there are some large approximations involved, as for example the silicon depletion layer capacitance was ignored and incorporated in the oxide capacitance, but the model nonetheless yields some reasonable parameters.

Previous work on donor bound excitons in silicon has shown that a degree of above bandgap illumination is useful for electrical detection of the Auger generated electrons, in order repopulate the donor states. To understand the device behaviour under above bandgap illumination, the frequency sweep of Figure 4.10 is repeated under the continuous illumination of a 980 nm laser with a range of small, picowatt level powers.

The results of this sweep, displayed in Figure 4.11, show a strong dependence of the device impedance on the generated photocarriers, lowering the impedance to less than 1 MΩ with less than 1 nW of power. Furthermore, the simple RC circuit of Figure 4.8 quickly breaks down, indicating a complex behaviour and a frequency dependent capacitance under higher photocarrier

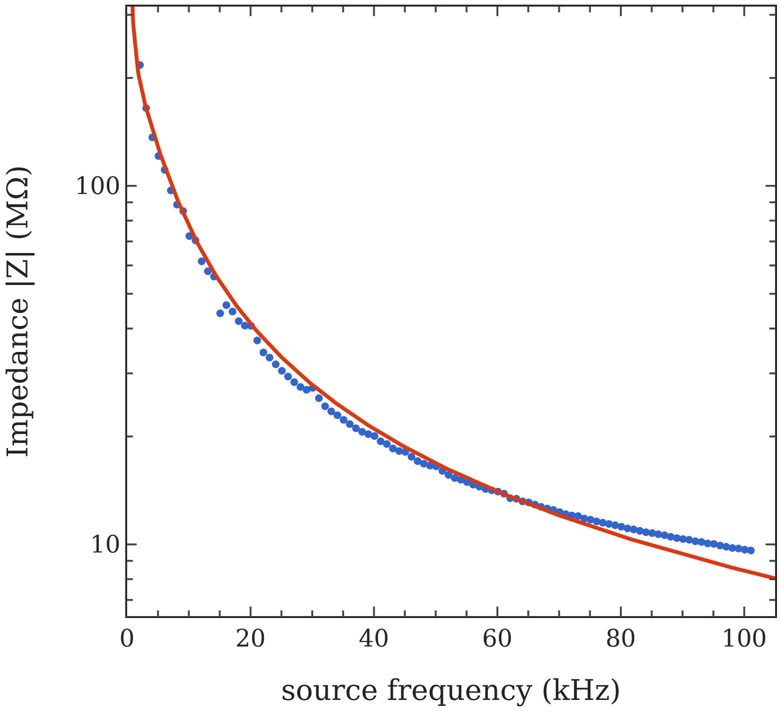

Figure 4.10: Dark impedance magnitude curve of of a $20 \times 50\,\mu$m MOS device, fitted to a simple parallel RC model. The good fit indicates a largely frequency independent MOS interface at low carrier densities.

densities.

4.2.2. D^0X RESONANT PHOTOCURRENT

Figure 4.12 shows the frequency dependent response, recorded by varying the 1078 nm laser on and off the D^0X optical resonance, with a 980 nm laser providing a fixed, minimal 2 pW of above bandgap illumination. The on-resonance response is averaged between the light and heavy hole peaks, while the off-resonance response is recorded ~40 µeV, more than 5σ, from the light hole peak.

Notably, both the on and off resonance photocurrent amplitudes follow a broad, slow rise. The phase and magnitude responses follow similar broad peaks but are slightly offset, with the magnitude leading and the phase following by approximately 15 kHz. Ross suggests that, under capacitive detection, a resonant capacitive response occurs where the silicon resistivity and reactance

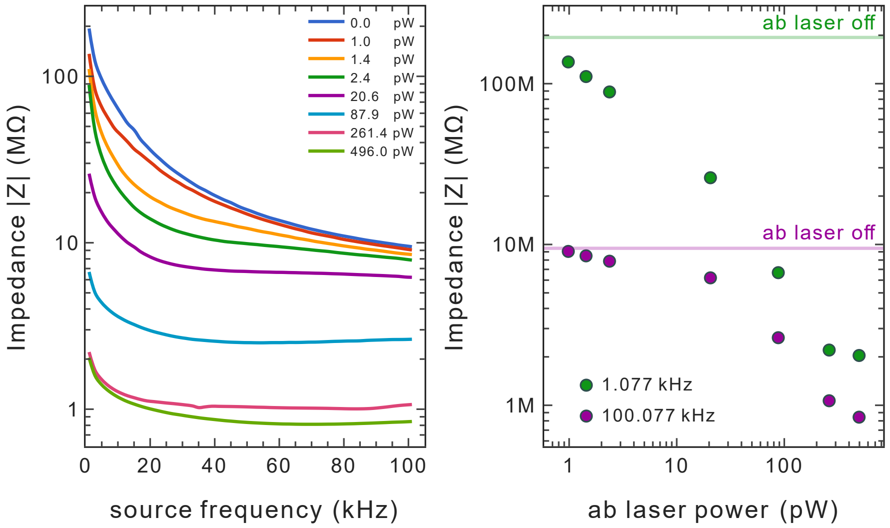

Figure 4.11: Device impedance magnitude ($|Z| = \frac{|V_{\mathrm{rms}}|}{|I_{\mathrm{rms}}|}$) curve of of a $20 \times 50\,\mu\mathrm{m}$ device under variable above bandgap laser illumination. Above bandgap illumination reduces the device impedance due to the carrier generation photoconductivity. The impedance curves at higher illuminations deviate from the simple RC model of Figure, indicating a frequency dependent interface layer at higher conductivities.

match [25], regardless of geometry, demonstrating it on a bulk sample

$$\omega = \frac{\sigma}{\epsilon_{\mathrm{Si}}\epsilon_0} = \frac{en\mu}{\epsilon_{\mathrm{Si}}\epsilon_0} \tag{4.3}$$

This is not strictly a capacitive detection, as no reference capacitor is used, however the same formalism leads to the phase and magnitude response peaks observed. The admittance of the simple model circuit of Figure 4.8 is therefore used to fit the complex response signal. Due to the large changes in magnitude of up to a 50%, the derivative cannot be used, instead, the response is explicitly calculated as $\delta Y = Y(R_{\mathrm{photo}}) - Y(R_{\mathrm{dark}})$. To further prevent overfitting, C_{ox} is kept fixed at theoretical expectation, and C_{Si} and especially R_{dark} are fixed to the value obtained from fitting the dark impedance, shown in Figure 4.10. The fit correctly matches the characteristic phase and magnitude peaks, with a good low frequency match. At higher frequencies, the model appears to break down to an extent, diverging from the experimental data. This is likely due to the approximation of an oxide interface capacitance independent of frequency. Generally, the result of Figure 4.12 appears to confirm the validity of Ross's model in a microscale device and for very small carrier densities, yielding a reasonable fit with a single free parameter.

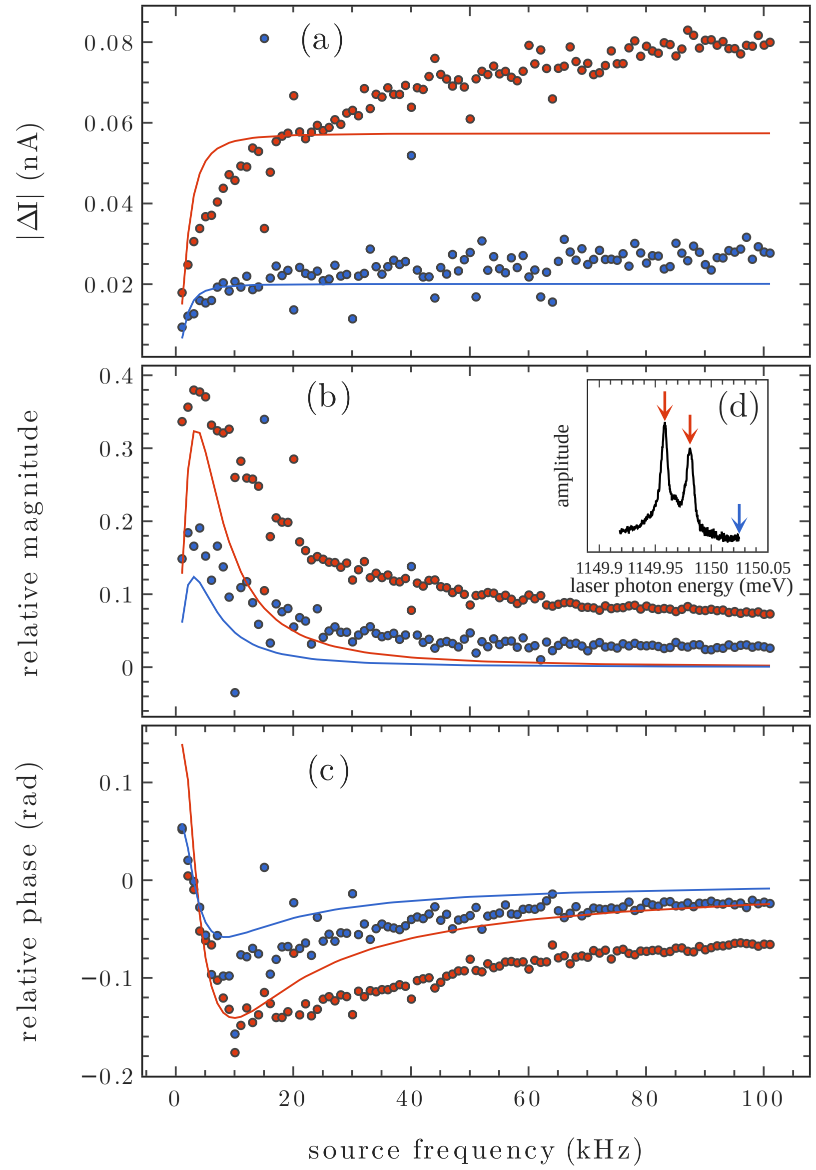

Figure 4.12: (—)off-resonance ($E_{\text{off}} = 1150.025$meV) and (—)on-resonance ($E_1 = 1149.959$meV, $E_2 = 1149.981$meV) AC photoconductive response fitted to the simple RC model from Figure 4.8. (a) photocurrent pulse magnitude (b) relative magnitude response (c) phase response. (d) D^0X spectrum indicating the laser photon energies used for the on and off-resonance response.

4.2.3. Photocurrent Response under AB illumination

Above bandgap illumination is a crucial component to D^0X detection. Several past research works have reported using small amounts of AB illumination

[15, 19, 23, 25, 27] to favour the neutralisation of ionised donors. Poor D^0X photocurrent signals without AB illumination suggest that a quasi-equilibrium state of ionised donors is reached in the absence of an appreciable conduction band density. Furthermore, above bandgap illumination also affects the device's electrical behaviour. Section 4.2.1 discussed how the dual MOS devices effectively behave as a capacitor in parallel with a photoresistor, and Section 4.2.2 showed how there is a peak in the magnitude and phase photocurrent where the silicon resistance matches its reactance. Assuming a constant silicon capacitance, the resonance depends on the silicon conductivity and thus carrier densities. For bulk level illumination and complete freeze-out conditions the carrier density is mostly dependent on the D^0X Auger electrons, but this is no longer the case when illuminating only a few thousand localised donors. Furthermore, the resonant electron generation rate is best left up to one's discretion to control important parameters such as polarisation rate or power broadening. Instead, the carrier density can be modified with the use of very small, picowatt levels of above bandgap illumination, generating free electron-hole pairs and thus tuning the silicon conductivity.

Figure 4.13 shows the validity of this concept, with above bandgap illumination as low as 100 pW shifting the phase and magnitude response peaks from 1 kHz to over 100 kHz. The almost total lack of a resonant signal without AB illumination further highlights an issue that was already observed in bulk level D^0X work, where some above-bandgap illumination was required to observe a D^0X signal [23]. The amplitude of the complex response $|\Delta I|$, displayed in Figure 4.13(c), presents itself with a greater frequency stability above the resistance-admittance resonance, and for this reason it is used for most wavelength-photocurrent curves in this work. However, under stronger illumination it also displays a notable dip at higher frequencies that cannot be explained from the simple RC circuit of Figure 4.8. This is possibly the result of a transition in the MOS interface behaviour under higher carrier densities, or simply a transition to a regime where the impedance is dominated by C_{ox} due to the higher silicon conductance. This results in a frequency dependent capacitance which reduces the photocurrent at higher frequencies. This is also compatible with the flat impedance curves under high illumination shown in Figure 4.11.

Having confirmed the resonant capacitive behaviour under a range of above-bandgap illumination induced carrier densities, the ideal detection conditions are analysed. It is clear from Figure 4.13(a,b,c) that the complex response amplitude $|\Delta I|$ yields a high signal over a broader frequency range. Figure 4.12 analyses the signal strength and signal to noise ratio under variable frequency and illumination conditions, to determine the ideal detection parameters the technique's sensitivity.

Figure 4.14 shows clearly that the ideal signal strength and signal to noise ratio is obtained in a narrow window of low power, ∼2 pW above bandgap excitation. Under these ideal conditions, a photocurrent maximum of 1.2 nA is observed at a frequency of 40 kHz, but the signal to noise ratio is maximised at

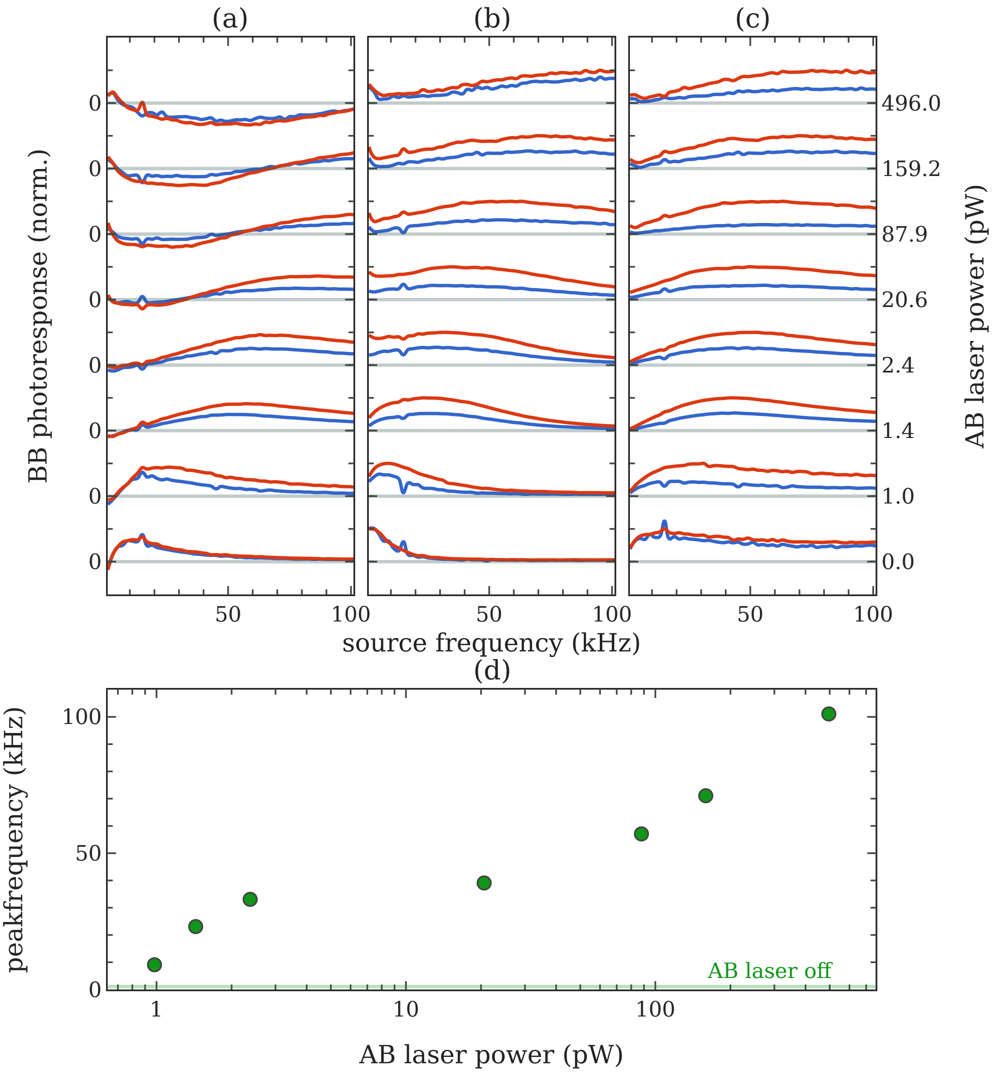

Figure 4.13: —)off-resonance ($E_{\text{off}} = 1150.025\text{meV}$) and (—)on-resonance ($E_1 = 1149.959\text{meV}$, $E_2 = 1149.981\text{meV}$) frequency dependent AC photocurrent response under different levels of above bandgap illumination. (a) phase response (b) amplitude response (c) magnitude of the response (d) AB power dependence of the response magnitude peak$|\Delta I_{\text{photo}}|$.

the highest frequency of 100 kHz nonetheless, most likely due to the dominating 1/f noise. There is also virtually no signal, resonant or not, without above bandgap illumination, a fact already observed in previous D^{0}X work [23, 26]. At higher levels of illumination, the photocurrent response slowly decreases and the noise floor increases, most likely due to the increasing charge noise. The highest signal-to-noise ratio achieved is 25 in a single shot detection window of 20 ms and a resonant laser power of only 20 µW illuminating approximately 2000 phosphorus donors.

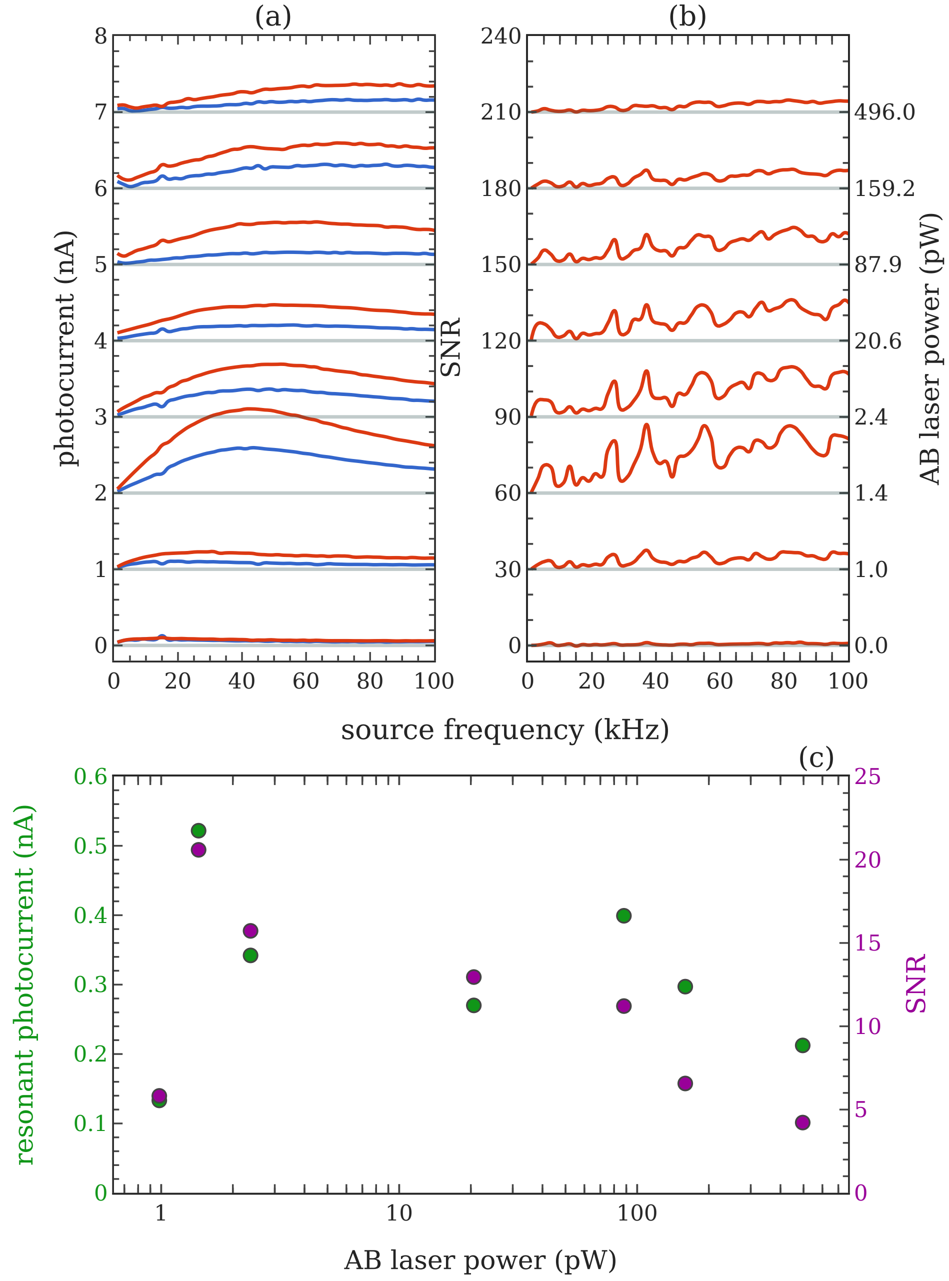

Figure 4.14: —)off-resonance ($E_{\text{off}} = 1150.025$meV) and (—)on-resonance ($E_1 = 1149.959$meV, $E_2 = 1149.981$meV) frequency dependent photocurrent response under different levels of above bandgap illumination, $V_{\text{rms}} = 100$mV (a) photocurrent (b) on-resonance signal to noise ratio(SNR) in a 20 ms detection window (c) AB power dependence of the response photocurrent and SNR. Almost no D^{0}X photocurrent is observed without AB illumination, while the optimal working point is at $\sim$1.5 pW.

4.2.4. Photocurrent Voltage Saturation

Section 4.1.4 discussed extensively the MOS device's behaviour under a DC bias voltage, showing a largely voltage independent photocurrent, as well as a broadening and a shift in the D^0X peak energies. The subject of source amplitude is slightly different under a sinusoidal voltage source, as transport is no longer dominated by the limited oxide leakage, and thus a level of amplitude dependence is expected. Lowering the source amplitude as much as possible however remains of paramount importance, considering the broadening and shifts involved, as well as the impact on donor spin polarisation discussed in Chapter 6. To determine the ideal source voltage, as well as the range of functional amplitudes, the frequency dependent experiment from Section 4.2.3 are repeated while varying the source voltage amplitude.

Figure 4.15 shows a clear saturation in the resonant and non-resonant photocurrent response, with a maximum photocurrent of 1.2 nA and SNR of 25 achieved with a source amplitude of 100 mV. Beyond simple saturation, higher source voltages result in a reduction of the photocurrent, while there is only a slight reduction in signal to noise. Furthermore, the ratio of resonant to non-resonant photocurrent also shows a dependence on the source amplitude, displaying a marked reduction with increasing voltages even before the peak threshold of 100 mV, from a maximum ratio of $\sim$3 to a minimum of $\sim$1.5. Electric field has been previously associated with various phenomena regarding the D^0X state. Weman showed that D^0X photoluminescent is quenched under weak electric fields as low as $5 \times 10^3\,\mathrm{V\,m^{-1}}$, vanishing almost entirely above $1.5 \times 10^4\,\mathrm{V\,m^{-1}}$, following the sample conductivity. This appears to suggest that this is due to the increase of field assisted impact ionisation of the shallow donors, which is explored extensively in Section 2.2. Considering the 20 µm contact separation, this appears to match well the threshold voltage observed at 100 mV, corresponding to an electric field of $5 \times 10^3\,\mathrm{V\,m^{-1}}$. Of course, the field drop across the oxide interface must be accounted for, but for a kilohertz AC voltage and $C_{\mathrm{oc}} > C_{\mathrm{Si}}$ most of the voltage drop should be across the silicon substrate.

4.2.5. Transient Response Analysis

The previous sections explored the amplitude of the photocurrent response under the variable experimental parameters of frequency, voltage and above bandgap illumination. A secondary, yet crucial aspect to consider is the speed and shape of the photocurrent transient. The techniques explored in this chapter are designed to be employed in hybrid pulsed laser-microwave schemes for the detection and manipulation of donor spin states, and the photoconductive transient response limits how fast or slow this sequence could be. Most existing research has been limited to millisecond or higher sequences [23, 24, 26], but raises the question of how fast D^0X Auger detection can be. This section analyses the transient photocurrent response under variable experimental

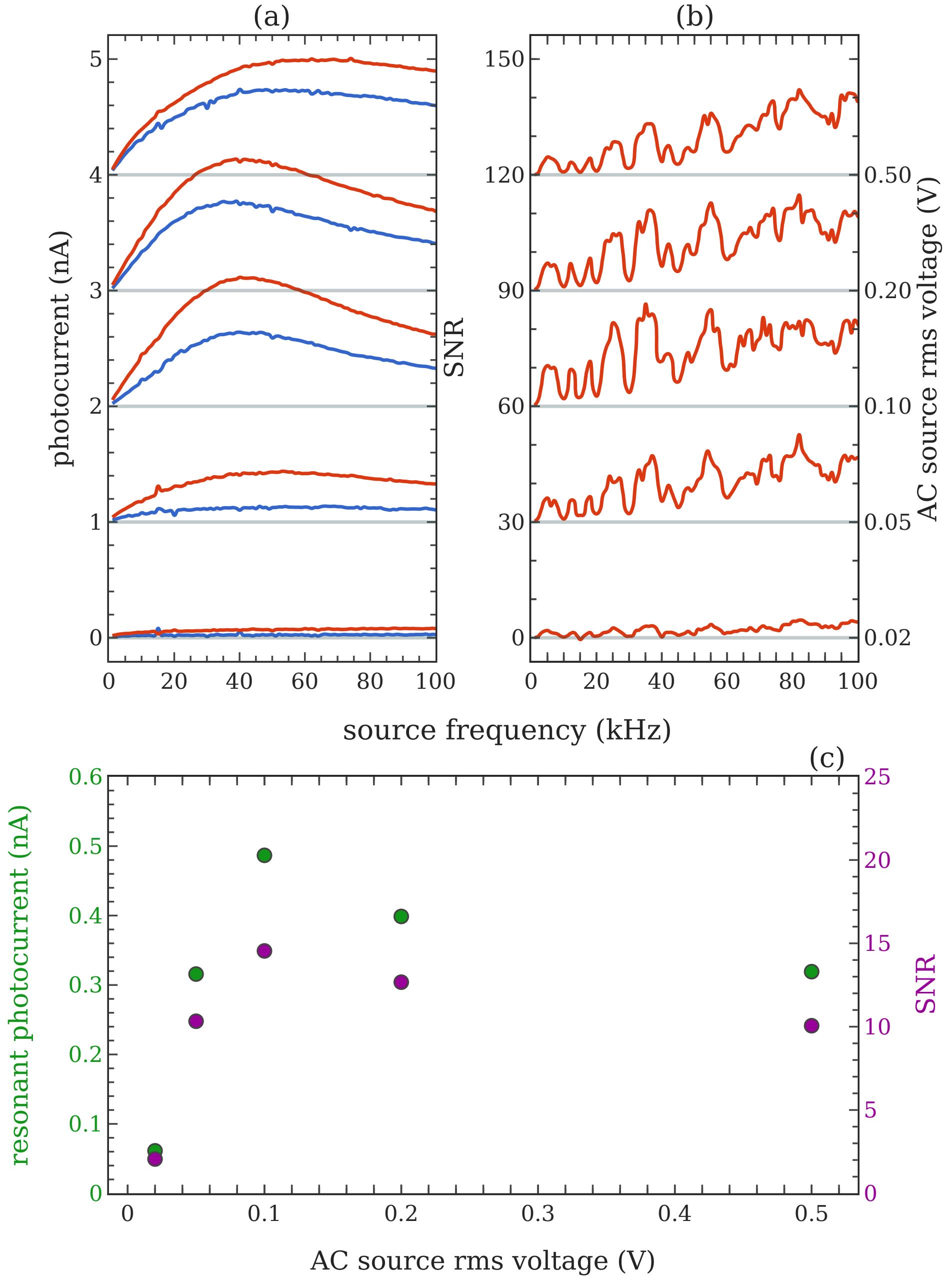

Figure 4.15: —)off-resonance ($E_{\text{off}} = 1150.025\text{meV}$) and (—)on-resonance ($E_1 = 1149.959\text{meV}$, $E_2 = 1149.981\text{meV}$) frequency dependent photocurrent response under different AC source measurement voltages, AB laser power fixed at 2 pW (a) photocurrent (b) on-resonance signal to noise ratio(SNR) in a 20 ms detection window (c) AC voltage dependence of the response photocurrent and SNR.

parameters.

The laser pulses are generated using a fast acousto-optical modulator with a rise-time below 100 ns, described in Section 3.3.3, to ensure that the transients are not limited by the pulse shapes itself. The demodulated signal is fed into the NIDAQ digitizer card, with a sampling rate set at ∼62 kHz. The transimpedance amplifier itself has a bandwidth of 200 kHz for the $10^6\,\mathrm{V\,A^{-1}}$ amplification employed. The risetime is limited by the lock-in filter time constant of 100 µs. Faster transients are discussed in the next section under radiofrequency LC reflectometry.

The clear result is that the photocurrent transients, resonant or not, are slow. Without bandgap illumination the actual value depends largely on the pulsed IR laser power, but it is generally in the range of tens of milliseconds. Illumination with even a small amount of above bandgap light rapidly decreases the transient time constant, also leading to a kink of sort in the risetime.

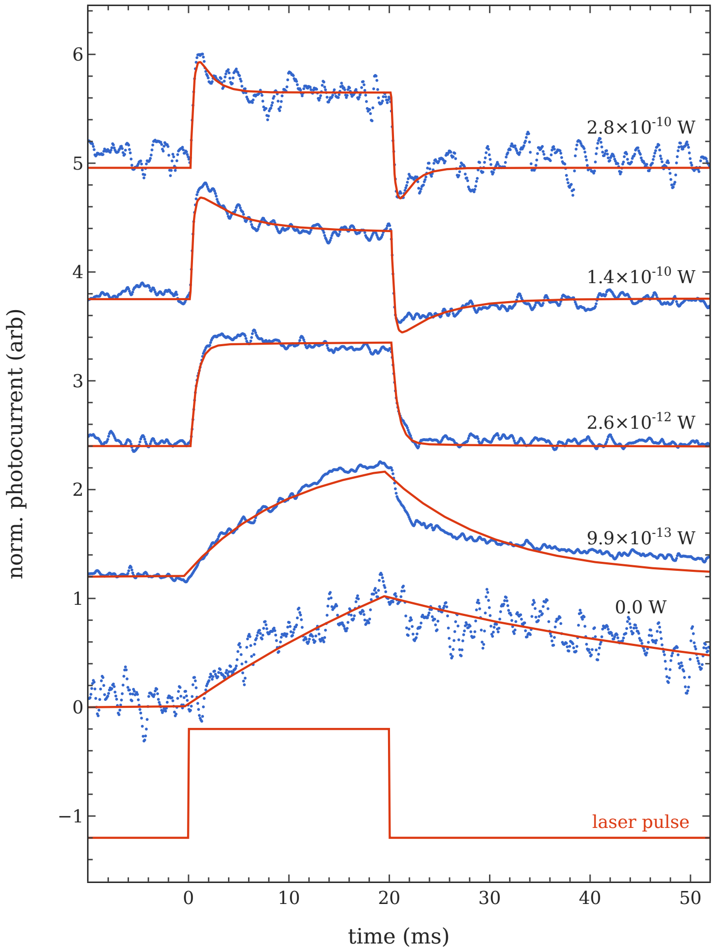

Figure 4.16: Transient photocurrent response to a 20 ms resonant laser pulse under variable continuous above-bandgap illumination, fitted to a pair of exponential pulses.

Figure 4.16 shows the shape of the transient photocurrent resulting from a square, 20 ms laser pulse under a few different AB laser powers. The photocurrent pulses show a marked symmetrical rise and fall, as well as a symmetrical overshoot at higher AB powers where the risetime is short. The overshoot is most definitely a byproduct of the steep (100µs, 12dB/octave) lock-in output low pass filter, as the overshoot occurs where the transient approaches, and likely exceeds the filter time constant, and changes depending on this setting. Furthermore, no overshoot is observed under reflectometry detection in Section 4.3 where a much higher cutoff frequency can be used. The transients can thus be described with two exponentials

$$I\left(t\right) = A_0\left(1 - e^{-\frac{t-t_{\mathrm{on}}}{\tau_0}}\right) - A_1\left(1 - e^{-\frac{t-t_{\mathrm{on}}}{\tau_1}}\right) \tag{4.4}$$

with exactly the same parameters for rise and fall. This appears to describe well most of the curve, apart from a few asymmetries in the fall at low levels of above bandgap illumination. The symmetry of the curve is quite surprising, and it appears to indicate that the limiting factor in the response speed is not the ionisation rate, which would lead to an asymmetric behaviour. Section 2.2 discussed the rate equation, which worked out at

$$\tau = \frac{1}{\Gamma_{\mathrm{D^0X}} + \Gamma_{\mathrm{direct}} + n\left(B_{\mathrm{T}} + A_{\mathrm{I}}\right)} \tag{4.5}$$

Under this assumption, the time constant is largely dominated by the faster rate constant, which would give asymmetric rise and fall times if $\Gamma_{\mathrm{D^0X}}$ was to dominate. Symmetrical transients rather suggest that the dominant rate must be one of the impact ionisation or thermal capture rates

Transient Response under AB illumination

To systematically analyse the transient response, the rise time is fitted to a pair of exponential functions described in 4.5. To accurately capture the time constant, only the pulse rise is fitted, to avoid the small asymmetries in the pulse fall affecting the measurement.

The result, shown in Figure 4.17 shows a time constant rapidly decreasing with above bandgap laser power, from ~15 ms without AB illumination down to 200 µs at 100 pW, most likely limited by the lock-in amplifier time constant. Notably, the optimal working power of 1.3 pW still yields a relatively slow risetime in the region of milliseconds, and only suboptimal, high above-bandgap powers lead to rise times in the region of 100s of microseconds.

It is unclear what may lead to the slow transients observed, although the symmetrical rise and fall transients strongly suggest an electrical process. The potential causes for the slow transients are explored below.

Slow D^0X ionisation The simplest explanation would be for the D^0X ionisation be slow itself, in the order of milliseconds. However, this would result in asymmetrical photocurrent rise and fall transients: the D^0X

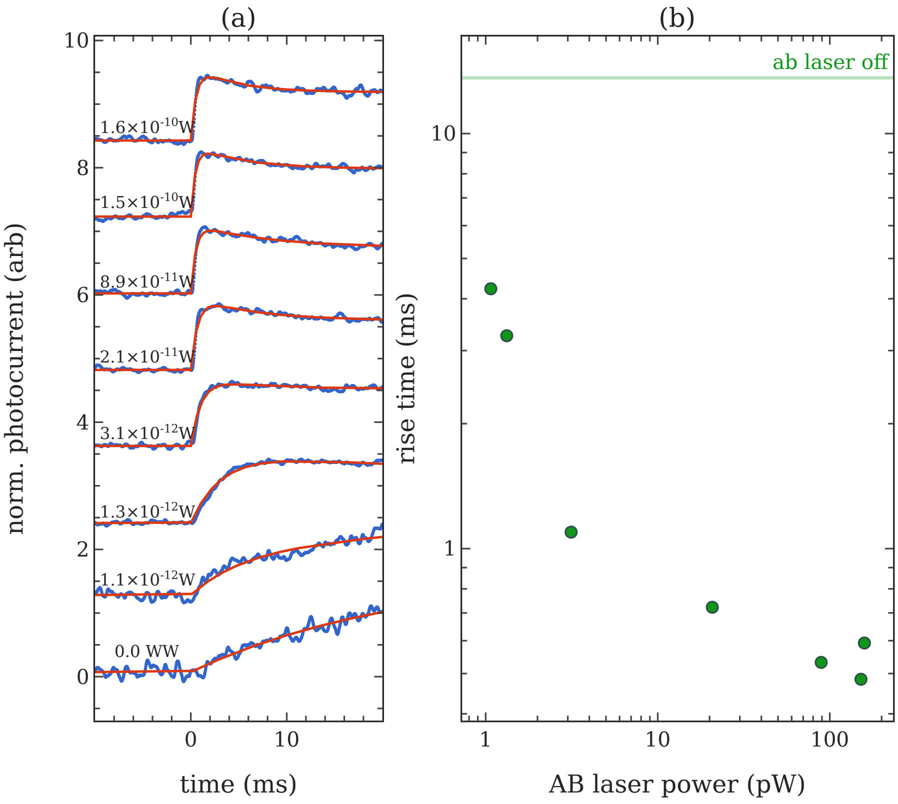

Figure 4.17: Transient photocurrent response to a 20 ms resonant laser pulse under variable continuous above-bandgap illumination. (a) Transient response fitted to a pair of exponential pulses (b) AB laser power dependence of the transient time constant.

ionisation dynamic cannot affect the donor electron capture once the laser is shuttered off. Furthermore, the high power densities employed are expected to cause much faster rates of ionisation, in the order of microseconds and down to the Auger limit. Furthermore, the fast transients observed in Chapter 4.3 would seem to rule out a millisecond rate of D^0X ionisation.

Carrier Diffusion Carrier diffusion is certainly a relevant dynamic in this configuration, as only a small area is illuminated and generates Auger electrons. For device wide conductance, it is reasonable to assume that carriers must diffuse through the whole device, albeit against the ionised donor potential, thus generating a transient. An approximation for the time constant of such an expansion is $\tau_\mathrm{D}(r) = \frac{r^2}{2D_n}$, where $D_n = \frac{\mu_n k_\mathrm{B} T}{e}$ is the electron diffusion constant [83]. Despite the inverse temperature relation, the diffusion process is very fast due to the high mobility $\mu_n \sim 10^5 \mathrm{cm}^2\mathrm{V}^-1\mathrm{s}^-1$, and for a 50 µm it should be in the order of hundreds of nanoseconds. Bulk level diffusion in the order of millimetres can indeed take milliseconds, but it would reasonably be associated decrease in current, as the generated carriers diffuse away.

Oxide charge Conductance of the oxide and the silicon interface depletion layer can display complex dynamics, with charge trapping, neutralisation and asymmetric carrier dynamics with complex transients [79]. The device is illuminated at its centre, thus far from the oxide. However, interface charging and discharging dynamics may still create slow signal transients.

Donor impact ionisation Donor impact ionisation, explored in detail in Section 2.2, could potentially lead to degree of carrier amplification that justifies the observed slow transients. Under this theory, the generated Auger electrons collide with other donors, not necessarily illuminated ones, thus generating more carriers, but at the symmetrical rate determined by the shallow level impact ionisation and thermal impurity capture, $\tau = \frac{1}{n(A_\mathrm{I}+B_\mathrm{T})}$. The time constant would then depend on the electric field and carrier density, which is indeed observed.

Transient Response under variable AC voltage

The AC source voltage was found to cause strong saturation, and even a fall in the photocurrent response in Section 4.2.4. The slow transients observed further suggest that a field dependent mechanism may be at play, possibly donor impact ionisation. Here, the transient rise-time dependence on the source voltage amplitude is analysed by repeating the experiments presented in the previous section under variable AC source voltage.

Figure 4.18 shows a strong, near linear log-log relationship between voltage amplitude and rise time. This is surprising, but it may possibly be explained by the argument made in Section 4.2.4 on the onset of shallow level impact ionisation under high AC voltages. As discussed extensively in Section 2.2, under equilibrium conditions the ionised donor fractions is given by $\frac{N_{\mathrm{D}^+}}{N_{\mathrm{D}^0}} = \frac{A_\mathrm{I}}{A_\mathrm{I}+B_\mathrm{T}}$. At low AB powers the carrier density, and hence conductivity is very small, and thus mostly dependent on the rate of donor ionisation $n \propto N_{\mathrm{D}^+}$. The electric field therefore acts on the time constant in two ways by increasing the rate of impact ionisation and the free carrier density, similarly to above bandgap excitation. As the time constant is given as $\tau = \frac{1}{n(A_\mathrm{I}+B_\mathrm{T})}$, both the increase in n and A_I may affect the response time, although which is dominating is unclear.

Overall, the slow transient behaviour and its dependence on the carrier density and electric field would suggest an electrical, not optically limited mechanism. The dual balance mechanism of shallow level impact ionisation and thermal impurity capture is proposed as a potential explanation, although

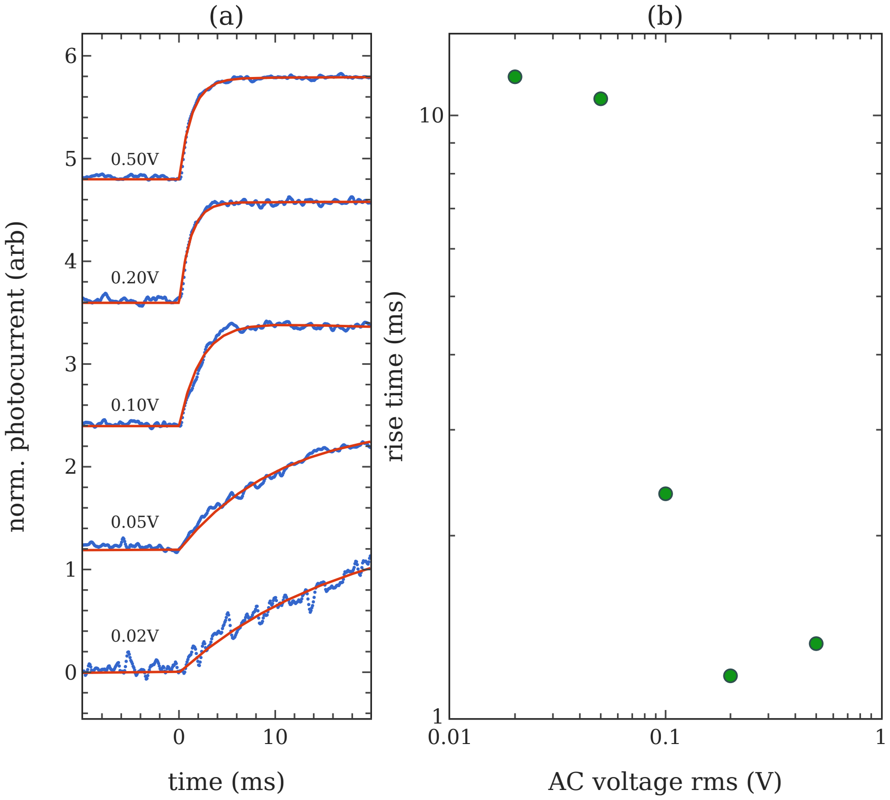

Figure 4.18: Transient photocurrent response to a 20 ms resonant laser pulse and 1.3 pW AB illumination under variable AC source voltage, fitted to a pair of exponential pulses. (a) photocurrent transients (b) plot of transient risetime against voltage.

it cannot be proven with the available experimental data. The matter should certainly be explored further, particularly as the mechanism might also result in a degree of multiplication of the Auger generated electrons, effectively a device level electrical amplification of the small generated D^0X photocarriers.

4.3. LC RESONANT RF REFLECTOMETRY

Section 4.2 explored a low frequency capacitive detection technique aimed at maximising the relative photoconductive response by matching the reactance and conductance of the silicon substrate. It was shown that for useful background carrier densities this optimal window is between the relatively low frequency range of 10–100 kHz. Higher frequencies could not be tested due to equipment's limits, but known parameters such as the circuit's RC time constant and the bandwidth of existing transimpedance amplifiers put a higher bound in the region of ∼1 MHz, confirmed by Ross [25] in a bulk sample. The response time is further increased to as high as milliseconds by an unclear mechanism. Therefore, while such technique has the advantage of being simple yet sensitive, it is fundamentally limited in bandwidth.

To overcome these experimental constraints, this section explores an alternative, high bandwidth detection technique: radio-frequency (RF) LC-resonant reflectometry. In RF reflectometry, a high frequency resonant circuit is designed comprising the device impedance of interest. A high frequency wave is then reflected off this circuit, with the amplitude and phase of the reflected wave depending on the resonant characteristics of the circuit. As the investigated impedance is part of the resonant circuit, any impedance variation will affect the resonance, and thus the reflected wave. Where a narrow resonance is created, a small change in impedance is amplified by the resonator's Q-factor resulting in a large change in the reflected wave.

An LC resonator can generally be simplified to an inductor, capacitor and dissipative resistor in series. Other configurations exist, most notably a parallel configuration, however most circuits can be approximated back to the series case in the limiting high frequency case employed in this work.

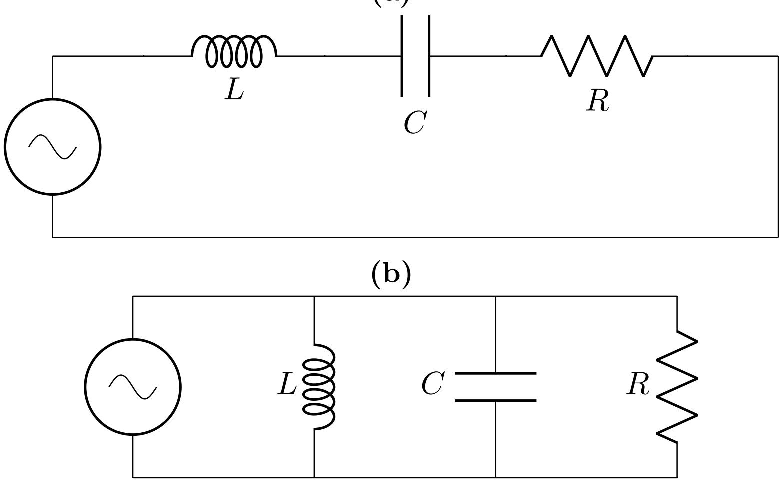

Figure 4.19: LC resonators. (a)Series LC (b)Parallel LC.

The impedance of the series circuit from Figure 4.19 given by

$$Z = R + i\left(\omega L - \frac{1}{\omega C}\right) \tag{4.6}$$

A resonance is present as the impedance is minimised where the imaginary component is zero, at

$$\omega_{\mathrm{r}} = \sqrt{\frac{1}{LC}} \tag{4.7}$$

where the circuit has impedance R. Similarly, the parallel LC resonator has impedance

$$Z = \frac{L^2 R \omega^2}{L^2\omega^2 + R^2\left(CL\omega^2 - 1\right)^2} - i\frac{LR^2\omega\left(CL\omega^2 - 1\right)}{L^2\omega^2 + R^2\left(CL\omega^2 - 1\right)^2} \tag{4.8}$$

The imaginary component is again zero where $\omega_{\mathrm{r}} = \sqrt{\frac{1}{LC}}$, leaving a resonance circuit impedance R.

4.3.1. LC RESONATOR DESIGN

To design and understand an LC resonator including a D^{0}X device, it is first important to develop a circuit model for the latter. The device circuit model described in Figure 4.8 has to be reanalysed in the high frequency limit. In the 100s of megaHertz region $\omega \sim 10^9$, the impedance can be approximated under the limit $\omega C_{\mathrm{ox/Si}} R \gg 1$, yielding

$$Z_{\mathrm{d}} = \lim_{\omega R_{\mathrm{Si}} C_{\mathrm{Si}} \gg 1} \frac{1}{R_{\mathrm{Si}} C_{\mathrm{Si}} \omega^2} - \frac{i}{\omega}\left(\frac{2}{C_{\mathrm{ox}}} + \frac{1}{C_{\mathrm{Si}}}\right) \tag{4.9}$$

This is almost identical to the limiting case of the silicon parallel RC, without an oxide. The only difference is the oxide capacitance term, which is only a small correction as the silicon capacitance is much smaller than the oxide's. It is significantly easier to work with a simple RC pair, which can be achieved with two possible approximations: either assume $C_{\mathrm{ox}} \gg C_{\mathrm{Si}}$ and drop the oxide term entirely, or define a device capacitance $C_{\mathrm{d}} = \frac{1}{C_{\mathrm{Si}}} + \frac{2}{C_{\mathrm{ox}}}$ and a device resistance, $R_{\mathrm{d}} = R_{\mathrm{Si}}\frac{2C_{\mathrm{ox}} + C_{\mathrm{Si}}}{C_{\mathrm{ox}}}$. Although the former would certainly be sufficiently accurate, the latter approach is more generally applicable. Thus, at high frequency an MOS device can fully described as a simple parallel RC pair, mostly dominated by the silicon impedance terms.

As discussed, there are two fundamental types of LC resonators, series and parallel, which although largely equivalent after some rearranging, differ substantially in impedance, which must crucially be matched to the input line 50 Ω impedance for perfect absorbance at resonance. Series LC resonators have been used extensively for relatively small device resistances in the order of 10s of kΩ such as single electron transistors [140, 141], where matching can be achieved with relatively small inductances. Recently, a parallel inductor design has gained popularity, which allows the impedance matching of high device resistances with a small inductor and a small series coupling capacitor. In order to maximise the resonator Q-factor, after discussions with Dr. Simon Schaal the parallel design was chosen in light of the extremely high, > MΩ resistances observed in Section 4.2.

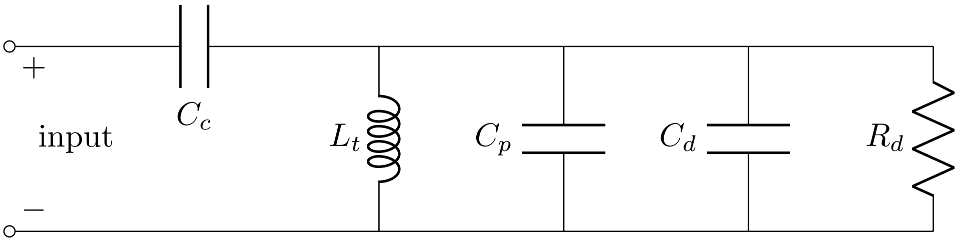

Figure 4.20: Full LC resonant circuit, with the silicon device expressed as capacitor-resistor pair with $C_\mathrm{d} = \frac{1}{C_\mathrm{Si}} + \frac{2}{C_\mathrm{ox}}$ and $R_\mathrm{d} = R_\mathrm{Si}\frac{2C_\mathrm{ox}+C_\mathrm{Si}}{C_\mathrm{ox}}$.

The idea is that the parallel circuit of Figure 4.19b, which would naturally have a very high resonance impedance $Z_{\omega_r} = R_\mathrm{d}$, is modified with the addition of a small, $C_\mathrm{c} \ll C$ series coupling capacitor. This adds a small term to the imaginary component, shifting the resonant frequency

$$Z = \frac{L^2R\omega^2}{L^2\omega^2 + R^2\left(CL\omega^2-1\right)^2} + i\frac{\left(-L^2\omega^2 - R^2\left(CL\omega^2-1\right)\left(L\omega^2\left(C+C_c\right)-1\right)\right)}{C_c\omega\left(L^2\omega^2+R^2\left(CL\omega^2-1\right)^2\right)} \tag{4.10}$$

The resonance frequency has only slightly changed to

$$\omega_\mathrm{r} \approx \sqrt{\frac{1}{L(C+C_\mathrm{c})}} \tag{4.11}$$

The effect on the resonant frequency is small, however substituting this result in the equation above leads to a strong change in the impedance at resonance, which becomes

$$\begin{aligned} Z_{\omega_\mathrm{r}} = & \frac{L^2R\omega^2}{L^2\omega^2 + R^2C_\mathrm{c}^2L^2\omega^4} - i\frac{L^2\omega^2}{C_\mathrm{c}\omega\left(L^2\omega^2 + R^2C_\mathrm{c}^2L^2\omega^4\right)} \\ 2 \approx & \lim_{R^2C_\mathrm{c}^2\omega^2\gg 1}\frac{L\left(C+C_\mathrm{c}\right)}{RC_\mathrm{c}^2} = \frac{1}{RC_\mathrm{c}^2\omega_\mathrm{r}^2} \end{aligned} \tag{4.12}$$

The resonant impedance can thus be reduced at will with relatively small coupling capacitances. Effectively, the coupling capacitor is acting as an LC matching network, where the inductor is incorporated in the resonator inductor.

The impedance can be further expanded near the resonance frequency by applying the substitution $\omega = \omega_\mathrm{r} + \delta\omega$, and expanding to the first order [142, p. 77].

$$Z(\omega_\mathrm{r} + \delta\omega) \approx Z_{\omega_\mathrm{r}} + i\frac{2\left(C+C_c\right)}{C_\mathrm{c}\omega_\mathrm{r}}\frac{\delta\omega}{\omega_\mathrm{r}} \tag{4.13}$$

This can be employed to compute the full complex reflection coefficient $\Gamma = \frac{Z-Z_0}{Z+Z_0}$. However, it if first convenient to extract the energy parameters of the resonator. Generally, the internal(unloaded) Q_{int} of a resonator can be defined as the fraction between averaged stored magnetic energy and resistive power loss [143, p. 278]. An equivalent equation can be derived in terms of stored capacitive energy, but the presence of multiple capacitors complicates that calculation. Ahmed [142, 144] derives a similar expression for the external quality factor.

$$\begin{aligned}
Q_{\mathrm{int}} =& 2\omega_r \frac{E_{\mathrm{L}}}{P_R} = 2\omega_{\mathrm{r}} \frac{\frac{V_{\mathrm{amp}}^2}{4L\omega_{\mathrm{r}}^2}}{\frac{V_{\mathrm{amp}}^2}{2R_{\mathrm{d}}}} = R_d \sqrt{\frac{C + C_{\mathrm{c}}}{L}} = R_{\mathrm{d}} \omega_{\mathrm{r}} \left(C + C_{\mathrm{c}}\right) \\
Q_{\mathrm{ext}} =& \frac{C + C_{\mathrm{c}}}{Z_0 C_{\mathrm{c}}^2 \omega_{\mathrm{r}}} = \frac{\omega_{\mathrm{r}}}{Z_0 C_{\mathrm{c}}^2 L} \\
Q_{\mathrm{L}} =& \left(Q_{\mathrm{int}}^{-1} + Q_{\mathrm{ext}}^{-1}\right)^{-1} \\
\beta =& \frac{Q_{\mathrm{int}}}{Q_{\mathrm{ext}}} = R_{\mathrm{d}} \left(C + C_{\mathrm{c}}\right) Z_0 C_{\mathrm{c}} L = R_{\mathrm{d}} C_{\mathrm{c}}^2 Z_0 \omega_{\mathrm{r}}^2
\end{aligned} \tag{4.14}$$

The

$$\begin{aligned}
\Gamma\left(\omega_{\mathrm{r}} + \delta\omega\right) &= \frac{Z\left(\omega\right) - Z_0}{Z\left(\omega\right) + Z_0} = \frac{\frac{1}{RC_{\mathrm{c}}^2\omega_{\mathrm{r}}^2} - Z_0 + \frac{2(C+C_c)}{C_{\mathrm{c}}\omega_{\mathrm{r}}} \frac{\delta\omega}{\omega_{\mathrm{r}}}}{\frac{1}{RC_{\mathrm{c}}^2\omega_{\mathrm{r}}^2} + Z_0 + \frac{2(C+C_c)}{C_{\mathrm{c}}\omega_{\mathrm{r}}} \frac{\delta\omega}{\omega_{\mathrm{r}}}} \\
&= \frac{1 - \beta + 2Q_{\mathrm{int}} \frac{\delta\omega}{\omega_{\mathrm{r}}}}{1 + \beta + 2Q_{\mathrm{int}} \frac{\delta\omega}{\omega_{\mathrm{r}}}}
\end{aligned} \tag{4.15}$$

Thus, describing the resonator entirely in terms of its dimensionless parameters. Equation 4.15 is used to fit all the complex resonant reflections throughout this section, with the addition of a relative phase correction term $\mathrm{e}^{i\phi}$.

Overall, including the device elements and the inevitable parasitic capacitance, the employed LC resonant circuit is fully described by the diagram of Figure 4.20.

This is entirely identical to the case discussed in Equation 4.10, with the capacitance being given by the sum of the parasitic and device capacitance $C = C_{\mathrm{p}} + C_{\mathrm{d}}$. Notably, no loss terms are added for other resistive losses, such as the series resistivity of the inductor or parasitic conductance. These can generally be incorporated into the device resistance term, although naturally the aim is to keep them small to maximise sensitivity.

The resonator is designed with a target frequency in region of 400–600 MHz, chosen to allow compatibility with the available RF components, as well to avoid potential complications arising from response thresholds at higher, gigahertz frequencies. The design assumes the parameters derived in Section 4.2.1, thus $C_{\mathrm{d}} = 250\,\mathrm{fF}$ and $R_{\mathrm{d}} = 10\,\mathrm{M\Omega}$ as a middle ground for medium levels of illumination. The parasitic capacitance is estimated from the leftover length of stripline at $C_{\mathrm{c}} = 1\,\mathrm{pF}$. This gives an inductance $L_{\mathrm{t}} = 80\,\mathrm{nH}$. The coupling capacitor is calculated from a target impedance of 50 Ω for perfect matching, at $C_\mathrm{c} = 15\,\mathrm{fF}$, rounded to 20 fF as the closest available. The choice of coupling capacitor, as it will be shown, was however most likely incorrect and led to an overcoupling.

The LC tank circuit described in Figure 4.20 is assembled on a standard 50 Ω line, by cutting a small gap with a scalpel where the coupling capacitor C_c is then solder. The coupling capacitor is placed as close as possible to the end of the CPW line to limit the resonator's parasitic capacitance C_p. Practically, the resonator line capacitor is approximately 5 mm, which works out to a parasitic capacitance of approximately 0.7 pF. The inductor is soldered after the coupling capacitor to the ground plane. It consists of a thick, 0.25 mm thick copper wire with two windings, as shown in Figure 3.12. The wire is wound on a small screw bit of the wanted diameter and subsequently twisted to lock the loop in place, yielding an estimated inductance given by:

$$L = \mu_o \left(\frac{d}{2}\right) \left[\ln\left(\frac{8d}{t}\right) - 2\right] \tag{4.16}$$

The inductor series resistance is a sensitive design parameter, so much that previous work used superconducting spiral inductors to maximise the inductor Q-factor [142, 144]. Attempts were originally made to employ a traditional surface mount inductor for a tidier PCB, but these yielded broad resonances with Q-factors as low as 50. This is most likely due to the high frequency skin depth resistance of their thin wired windings. Here the simpler solution of a thick, coiled wire maximises surface area, minimising resistance and thus achieving room temperature Q-factors over 100. Furthermore, these floating inductors allow for a degree of tunability in the circuit resonance, as the winding can be tightened and loosened by hand, modifying the inductance and fine tuning the circuit. A pencil or sloped pen works well for widening and tightening the winding.

An assembled resonator can be observed in Figure 4.21 as measured at room temperature, unconnected. It is slightly over coupled with an internal Q-factor of ∼200, likely limited by the inductor wire resistance or possibly parasitic leakage. Once a dual MOS device is bonded, the resonance vanishes at room temperature due to the comparatively low, kΩ resistance due to the large bonding pads oxide leakage.

4.3.2. DEVICE LC RESONANCE

After cooldown to a 3.2 K base temperature the resonance reappears at a very close central frequency of ∼600 MHz, denoted by the light grey line in Figure 4.22 and a narrower, yet more over coupled and thus less prominent peak. It should be noted that under the used configuration the handcrafted inductor is slightly handled during device and PCB mounting, such that the inductance may have been slightly tweaked since the measurement from Figure 4.19, so the frequency shift should not be trusted further than observing that no large

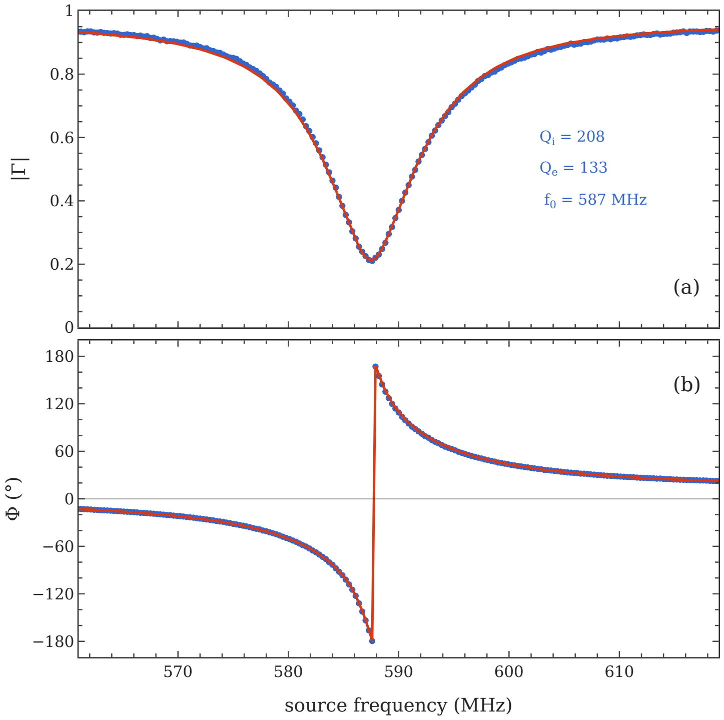

Figure 4.21: (a)magnitude and (b)phase S11 reflection measurements of an LC resonator without device bonds at 300 K.

shift is found. As the PCB is raised with the piezo-stack against the radiation shield, necessary for high-NA optical illumination, the resonance downshifts by ∼10 MHz, most likely do to additional parasitic coupling to the radiation shield and thus ground. It is unclear if this is from the board CPW line or perhaps the wire-bonds.

The blue trace with a red fitting from Figure 4.22 shows the resonance that is employed in these next few subsections for the detection of a D^0X photoconductive readout. It has gained an extremely high Q-factor with $Q_{\mathrm{int}} \sim 700$, but is even more over coupled due to the external Q-factor $Q_{\mathrm{ext}} \sim 250$. The coupling capacitor was chosen under the assumption that some other parasitic resistance would have limited the internal Q-factor beyond the high silicon resistance, but that is clearly not the case. Future designs should consider this and employ smaller coupling capacitors to achieve higher load Q-factors.

To maximise sensitivity to D^0X Auger electrons, it is important that the internal Q-factor be limited by the silicon resistance R_{Si}, and not other dissipative factors such as the inductors series resistance or CPW dielectric leakage. This resonator's Q_{int} is indeed limited by the silicon conductance, and this can be demonstrated by tuning this conductance using above-bandgap illumination. This reduces R_{Si}, which in turn should reduce the internal Q-factor. For this over coupled resonator, this should result in better coupling and a more prominent resonance, while for a perfectly matched resonator it should reduce the resonance dip and broaden the peak. To extract the resonance

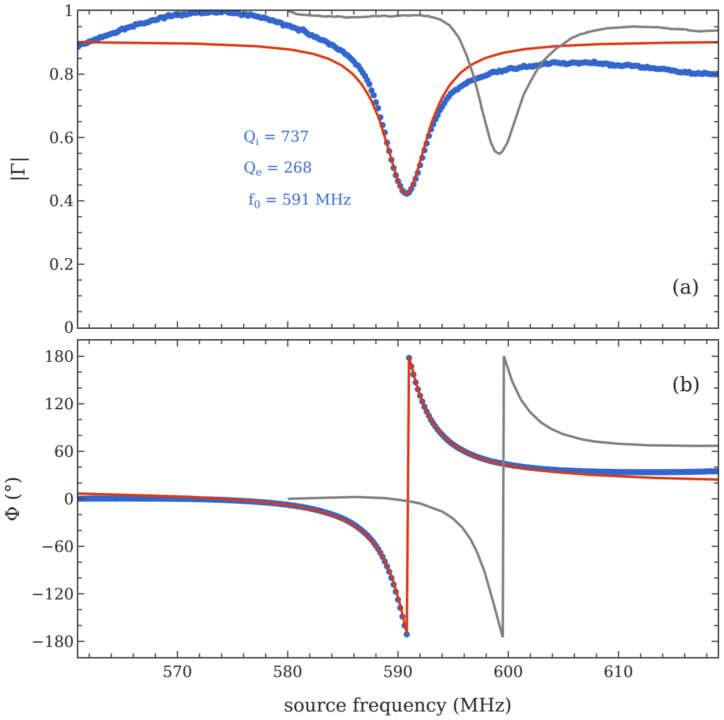

Figure 4.22: (a)magnitude and (b)phase S11 reflection fitted measurements of an LC resonator connected to a dual MOS device at 3.2 K, (—) far from the cryostat radiation shield and (•) close to the radiation field, at operating distance. No resonance is observed at 300 K.

parameters, the complex IQ reflectometry signal is fitted to Equation 4.15. A multiplicative factor to account for line losses is employed, but this is only left as a free parameter for the 0 pW fit, and fixed for the subsequent curves, under the assumption that line losses are independent of the resonator.

Figure 4.23 shows a clear, large inverse dependence for the internal Q-factor, with sub-nanowatt powers reducing the Q-factor from 1300 down to 500, and almost doubling the resonance prominence. A small, linear ∼100 kHz shift is also observed, which may be due to the carrier density effect on the oxide interface capacitance, but this is a marginal effect compared to the order of magnitude tuning of the internal Q-factor.

4.3.3. D^{0}X Reflectometry Response

Having demonstrated a strong resonator response to above-bandgap illumination, the response to below-bandgap illumination is explored both on and off resonance to determine the technique's sensitivity to D^{0}X photocarrier generation. This is investigated using largely the same pulsed technique as presented in Section 4.2, where the 1078nm laser is pulsed and the photo response is obtained by measuring the resulting reflection signal pulse. This performed over a source frequency sweep, and repeated on both light and heavy hole resonant

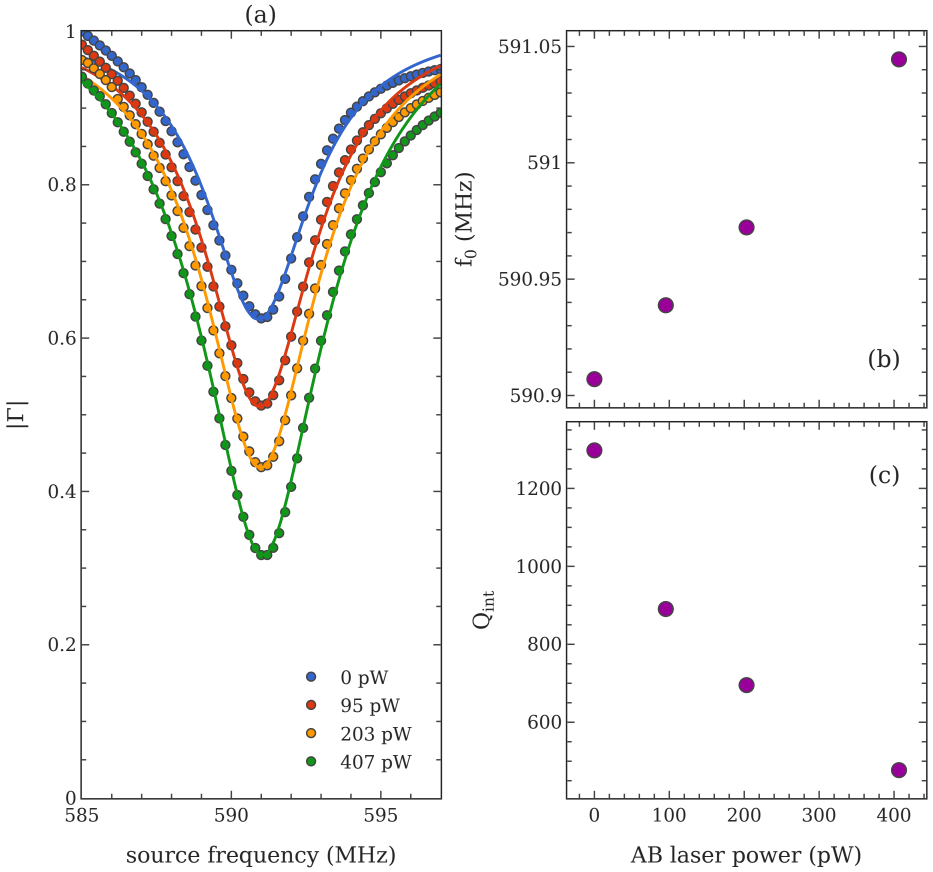

Figure 4.23: AB laser power dependence of the LC resonance. (a) $|Gamma|$ resonances under variable laser power (b) power dependent resonance shift (c) power dependent internal Q-factor of the LC resonator.

energies and at a token, off-resonance wavelength approximately 50 µeV off the light hole line. In order to also compare this detection to the low-frequency technique presented in Section 4.2, all parameters are kept identical, such as 1078 nm power and the range of AB laser powers. A pulse length of 10 ms was used, and 50 shots were recorded at each step. The centre of the resonance f_0 is derived from the pulse measurement itself, fitting the background signal to the resonance Equation 4.15.

The result of the frequency sweep under no above-bandgap illumination is shown in Figure 4.24. There is a clear, albeit small reflectometry response in both magnitude $\Delta|\Gamma|$ and phase $\Delta|\Phi|$, dominated by the former. Both the off-resonance and on-resonance response yielded a well visible signal, the on-resonance response being slightly less than twice the off-resonance signal, similarly to what is observed at low frequencies. The magnitude peak sits approximately 200 kHz below the resonator centre frequency. The phase peak sits roughly 500 kHz above it, while the response amplitude peak sits exactly at f_0.

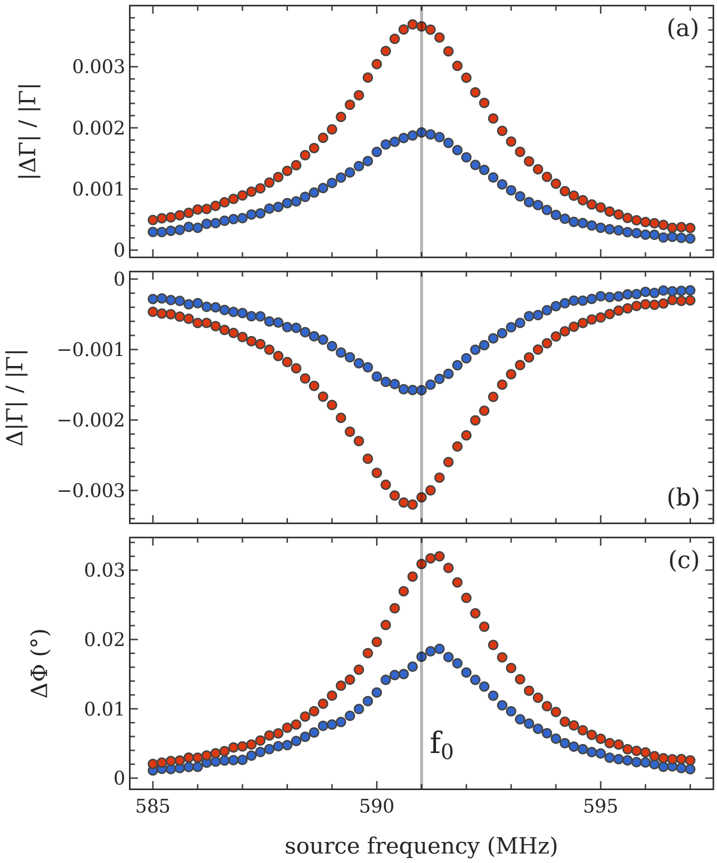

Figure 4.24: (●)off-resonance and (●)on-resonance reflectometry response, withou AB illumination and with a source power of 0 dBm (a) amplitude of the response (b) relative magnitude (c) relative phase.

D^0X **response under above-above bandgap illumination**

The low frequency D^0X response was observed in 4.2.3 to have a strong sensitivity to the substrate carrier density generated by above bandgap illumination, with a sharp increase for low powers, followed by a slow decrease in the signal strength. This is investigated here for RF reflectometry detection, to determine this technique's ideal experimental parameters.

The results are quite different from those of Section 4.2.3, with the non-resonant signal increasing sharply with AB illumination, almost doubling in the range explored. This could however be due to the improved impedance matching under higher illumination. What is, however, notable the resonant response is maximised when no above bandgap illumination is present at all, and gradually decreases with illumination power. This is surprising as almost no signal was observed at low frequencies without illumination, whereas for reflectometry there is little illumination dependence until a sharp drop at high illumination powers.

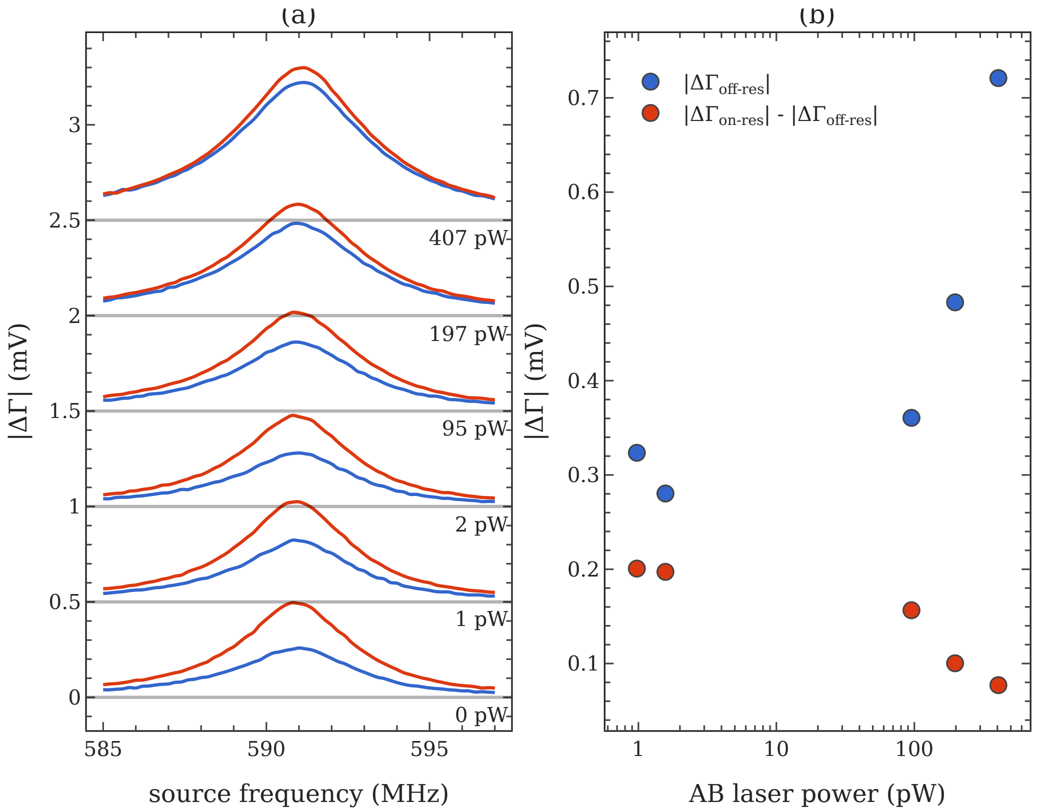

Figure 4.25: —)off-resonance ($E_{\mathrm{off}} = 1150.025\mathrm{meV}$) and (—)on-resonance ($E_1 = 1149.959\mathrm{meV}$, $E_2 = 1149.981\mathrm{meV}$) reflectometry response under variable above-bandgap illumination (a) amplitude of the response (b) AB laser power dependence of the response.

4.3.4. SLOW AND FAST TRANSIENTS

The investigation of LC reflectometry readout was undertaken with the goal of achieving faster detection of the $\mathrm{D}^0\mathrm{X}$ photoconductive response, similarly to how it allowed quantum dot readout to overcome the RC time constant. The matter is a little different here, as the limit of low frequency capacitive detection was not the RC time constant, although it may have become an issue at higher lock-in frequencies. The issue was a fundamental slow response to changes in conductivity. Therefore, the first test transient test of the reflectometry setup is to test whether that is still the case here.

Slow Transient

This experiment was conducted on the same $20 \times 50\,\mu\mathrm{m}$ device the same conditions of above bandgap illumination (0–400 pW) and resonant laser power(20 µW). A slightly faster pulse sequence, with a resonant laser pulse of 10 ms was employed to accommodate the observed faster transients and the need for more averaging due to the lower SNR.

The result is largely similar to what was observed at lower frequencies,

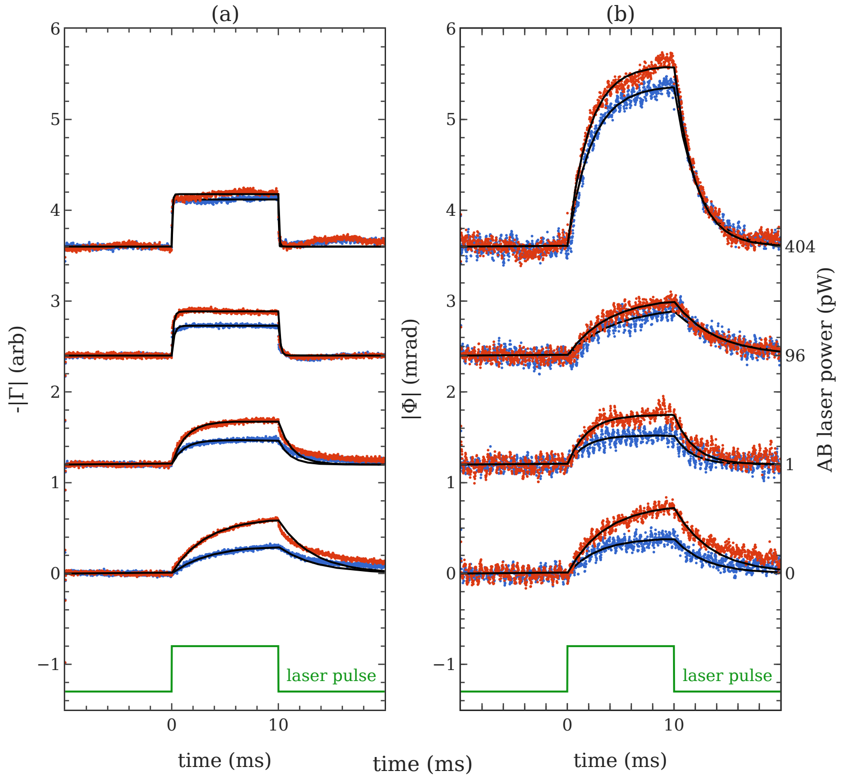

Figure 4.26: —)off-resonance ($E_{\text{off}} = 1150.025$meV) and (—)on-resonance ($E_1 = 1149.959$meV, $E_2 = 1149.981$meV) reflectometry transients from a 10ms rectangular laser pulse with exponential fitting(—) (a) magnitude $-|\Gamma|$, here plotted upside down (b) reflected signal phase Φ.

with some notable differences. Figure 4.26 shows the general shapes of the pulse reflectometry response for a few representative levels of above bandgap illumination. Again, without any illumination, the response is slow at 5 ms. Notably, the transients still have a broadly similar rise and fall, with only some minor asymmetry. Notably, the overshoot that required the use two opposing exponentials is not observed here, with a simple exponential rise fitting well to the experimental data. The other notable difference, which was already discussed in the previous subsection is that the resonant signal is maximised when no above bandgap illumination is employed at all. However, just like for low frequency detection, the general behaviour is that faster transients are observed under stronger AB illumination. Finally, it appears that the phase response follows a completely different transient behaviour than the amplitude response, with slow transients observed all the way to the highest level of illumination, with an increasing amplitude instead. This is most likely because the phase response is due to changes in the oxide interface layer capacitance, which is usually frequency dependent. This is however not particularly worrying as most of the signal is observed in the magnitude response.

Figure 4.27 shows the systematic analysis of the reflectometry rise time constant under variable above bandgap illumination, which is only fitted up

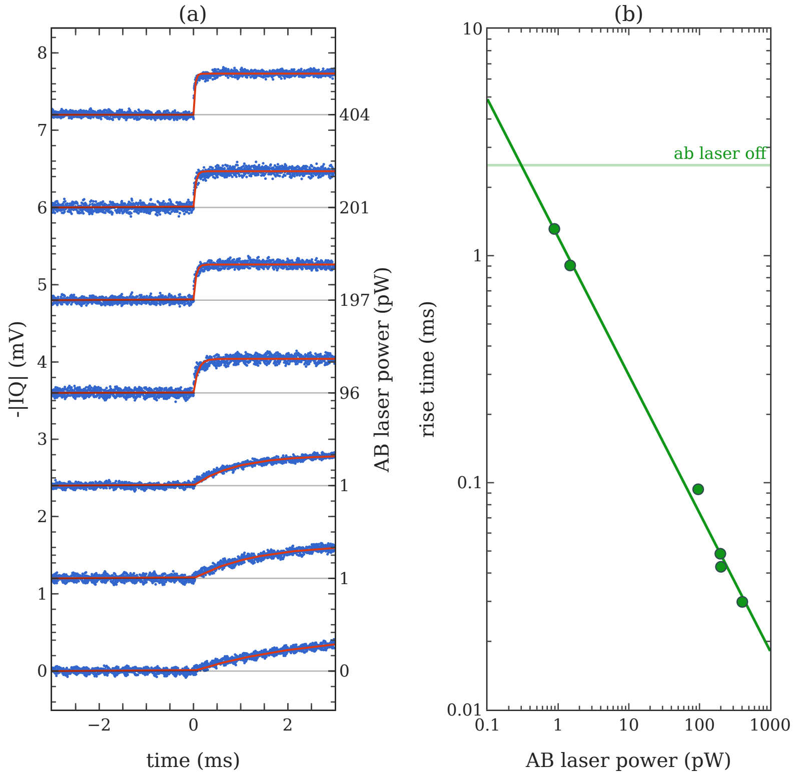

Figure 4.27: (•) $-|\Gamma|$ reflectometry transient from a 10ms rectangular laser pulse and (—)fitting (a) magnitude $-|\Gamma|$, here plotted upside down (b) log-log linear fitting of risetime against AB laser power.

to 5 ms to prevent fitting any minor secondary transients. The result is a perfectly linear log-log relationship between the time constant and the illumination power, as here there is no lock-in time constant to limit the response speed. The lowest achieved rise time is 30 µs, about a third of what was achieved under low frequency lock-in detection. The exact fitting yields a relationship

$$\tau = 0.8P_{\mathrm{AB}}^{-0.61} \tag{4.17}$$

with SI units of seconds and watts. The −0.61 exponent suggests an inverse square root relation, implying that the conductivity response time follows the AB bandgap laser amplitude, not its power.

Fast Transient

Finally, as per the goal of this section and thanks to the high bandwidth of the reflectometry setup, the D^0X transient response can be investigated under a faster pulse to detect if a faster resonant signal is present. The previous subsection established that the bulk of the signal is still tied to a slow transient response. However, this does not mean that there is not a detectable faster response, only that it is not dominant. This experiment is thus conducted with a shorter pulse sequence consisting of a 100 µs laser pulse, with the laser wavelength slowly swept through the light and heavy hole resonant peaks to further determine any notable change to the spectrum.

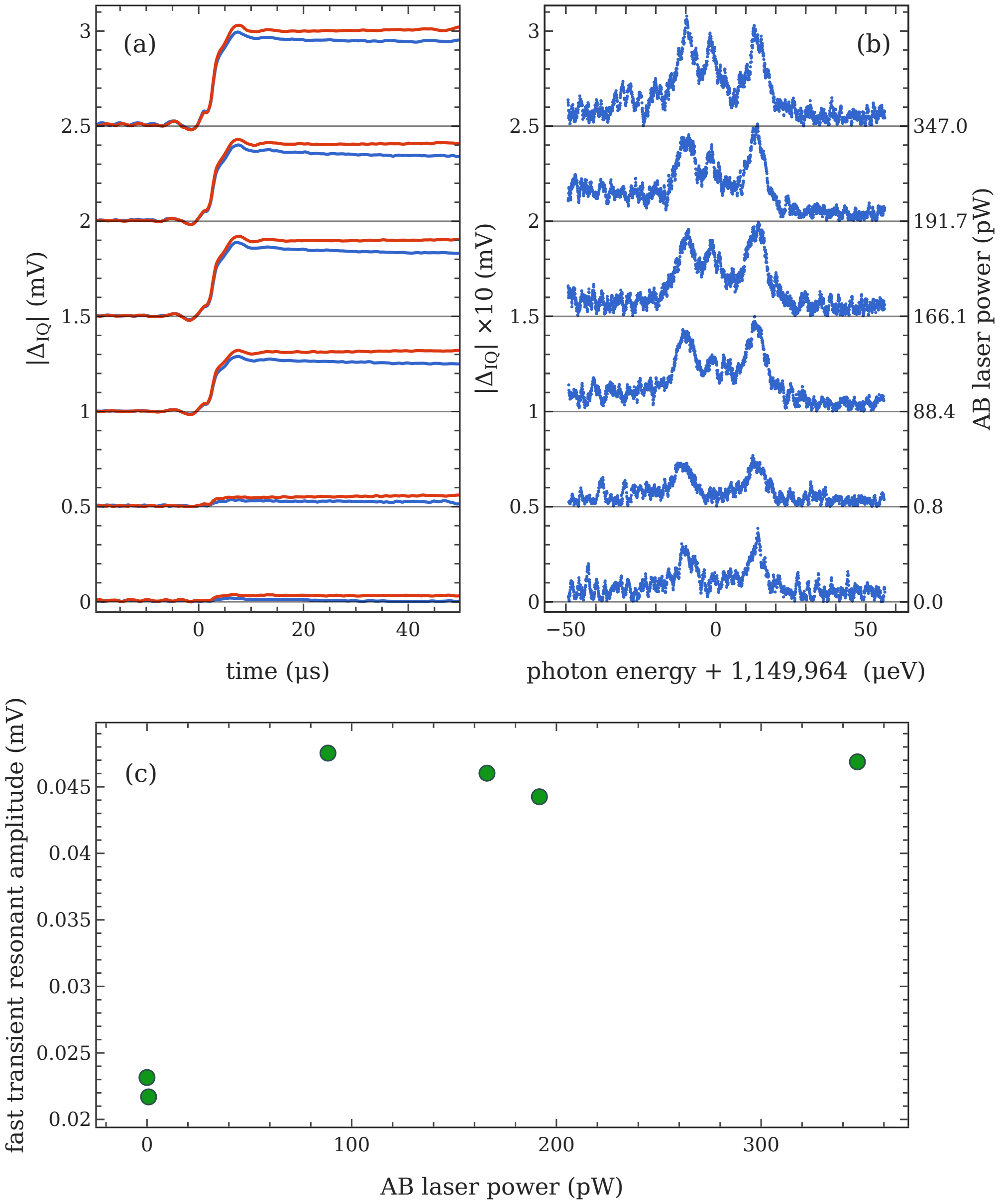

Figure 4.28: —)off-resonance ($E_{\text{off}} = 1150.025$meV) and (—)on-resonance ($E_1 = 1149.959$meV, $E_2 = 1149.981$meV) reflectometry transients from (a) Transient response amplitude (b) wavelength scan with a 20 µs detection window under variable AB illumination. (c) ∼3 µs transient amplitude against AB power.

Figure 4.28 shows without a doubt that a fast transient does indeed exist, although weak, with an apparent risetime of 3 µs, approaching the D^{0}X Auger lifetime limit of 270 ns. Notably, this transient is also detected at low and zero levels of above bandgap illumination, with a much lower amplitude compared to the high illumination signal. From powers of approximately 100 pW upwards, the amplitude of the resonant signal settles, while the non-resonant response continues to rise.

The photon energy scans in Figure 4.28(b) further highlight a new, surprising issue: the appearance of a strong central peak, likely attributable to the residual silicon bulk donors discussed in Section 4.1. This is unexpected as a short detection window would suggest a more local response, although carrier diffusion is certainly much faster than microseconds. Notably, the bulk peak is not visible, or at least not prominent, at lower levels of above bandgap illumination, most likely due to the bulk acceptor compensation leaving the bulk level donors ionised without a photocarrier population carriers.

4.4. CONCLUSIONS

This chapter explored the electrical aspects of donor bound exciton detection in silicon microscale devices. The first, novel and key finding of Section 4.1 is the suitability of the MOS contact chemistry for local donor detection, as opposed to Schottky or even highly doped pseudo-Ohmic contacts, which only yielded a signal from the bulk residual donors. This result was reproduced over multiple devices, albeit all from the same production run, and contrasts with past literature successfully employing Schottky contacts in bulk doped, larger scale devices. While a firm conclusion should not be drawn by a single device family, this work suggests the potential superiority of MOS contacts for micro-scale devices.

Two AC detection techniques were explored to optimise the electrical sensitivity and overcome the high DC impedance of the oxide. Low frequency lock-in photocurrent detection in the kilohertz region is observed to yield high signal to noise ratios. Furthermore, a frequency and illumination analysis demonstrated the validity of the capacitive detection model by Ross[25] at the microscale. LC reflectometry detection is demonstrated for the first time in a D^0X device, allowing high bandwidth measurements with a technique already popular in quantum dot charge detection. While the sensitivity observed is below that of low frequency capacitive detection, the bandwidth allowed for the detection of sub microsecond fast D^0X electrical signals approaching the Auger recombination rate. With significant room for optimisation in the resonant LC circuit, RF-reflectometry may be able to overcome the low frequency sensitivity in the future.

Finally, the novel conditions of local illumination in implanted microscale devices introduced the previously unreported issue of slow photo-response transients, which were observed under all detection techniques, symmetrical in rise and fall and strongly dependent on the background carrier density from above bandgap illumination. Reflectometry detection was also able to yield a fast, ∼1 µs transient response under fast pulsing, albeit at the cost of a strong signal loss. This problematic transient is hypothesised to originate from a field induced carrier amplification mechanism; however the matter requires further investigation.

In conclusion, this chapter successfully developed electrical techniques to detect, for the first time, as few as ~2000 donor bound excitons within only a 2 µm diameter illumination area. Furthermore, the resonant electrical detection at RF frequencies was explored for the first time. Overall, while some questions remain open, such as the origin of slow transients, this chapter provides an extensive electrical analysis of MOS D^0X devices in both the DC, low frequency and RF regimes.

5. D^0X Strain Microscopy in Silicon Devices

This chapter focuses on the strain induced spectral splitting of the D^0X resonant transition in microscale devices. As seen in the photoconductive spectra of Chapter 4, the D^0X transition is extremely sensitive to lattice strain due to the valence band spin orbit coupling. The sensitivity is such that even the strain induced by the minority ^{29}Si nuclei in $^{\mathrm{nat}}$Si lead to peak broadening when compared to isotopically purified ^{28}Si [145]. Microscale devices naturally display strain due to a multitude of factors, but most of all the mismatch in thermal expansion between device materials, high temperature fabrication stresses and the lattice damage from donor implantation, which has been observed to introduce strain broadening in particular with heavy donors such as Bismuth [125, 146] and in highly strained substrates such as SOI[29]. Consequentially, the D^0X peak shape in micro-devices is inevitably broadened and complex. On one side, this is clearly problematic for downscaling, since the closer one moves to a metal contact, the higher the strain. On the other hand, the broadening offers the potential for selectively addressing donors using strain as a discriminant, possibly allowing sub-diffraction resolution of local donors.

In this chapter, the strain effect on D^0X transitions is first explored systematically in a bulk sample, to verify the validity of existing theoretical model and derive its parameters in the relevant and low strain regime. Then, the electrical techniques developed in Chapter 4 are employed to analyse the strain in microscale devices using optical scanning microscopy, compared to finite element models of thermal strain.

5.1. D^0X Transitions in the Low Strain Regime

The donor bound exciton transition is strongly affected by lattice strain, as discussed in Chapter 2. Overall, the effect is threefold: a hydrostatic valence and conduction band shift proportional to the strain trace $Tr\{\boldsymbol{\epsilon}\}$, with parameters a' and Ξ_d respectively. Then, an axial band valley shift with parameter Ξ_u, and finally two Pikus-Bir hole spin splitting terms with parameters b' for principal strain and d' for the shear strain component. Any analysis of strained donor bound excitons must therefore first consider this model, these parameters and their validity in the relevant strain regime. Regarding the existing literature on the subject, theoretical parameters are calculated by Blacha [147] using both tight binding and pseudopotential techniques. Experimental parameters were also calculated by Lo [23] using data by Thewalt [148] under compressive conditions and high stress levels up to 150 MPa. Finally, Loippo derives Pikus Bir parameters from comparing a single, strain split magnetic swept spectrum to FEM simulations [27].

This section aims to validate the Pikus-Bir model and derive its parameters in the little explored low strain regime(∼1 MPa). Electron spin resonance detection of a ^{28}Si sample is employed due the narrow linewidths and high sensitivity involved.

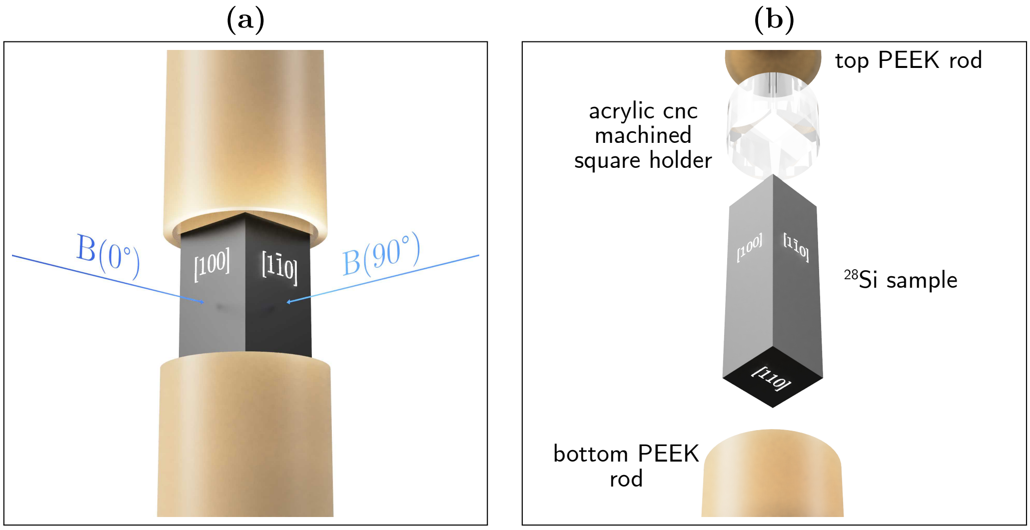

Figure 5.1: CAD renderings of the strain rod with crystal axis. (a)Assembled mounting rod with magnetic field orientation. (b)Disassembled mounting rod components.

Most of the devices analysed in this work involve low to medium levels of strain in the range of single digit Mega Pascals. Due to the lack of experimental data in this low strain regime, it is first important to verify that the theoretical model and experimental parameters remain valid in this low strain regime, similarly to how a related low strain regime analysis of the donor spin Hamiltonian led to the consideration of a novel, hyperfine strain term [28]. This low strain analysis is achieved using a bulk, isotopically purified ^{28}Si sample, strained under a custom machined rod and a set of calibrated masses. The donor bound exciton transitions are detected from the generated donor electron spin polarisation via pulsed electron spin resonance (ESR) under a ∼350 mT magnetic field applied at multiple crystal orientations.

5.1.1. ESR Detection of the Electron Spin Polarisation

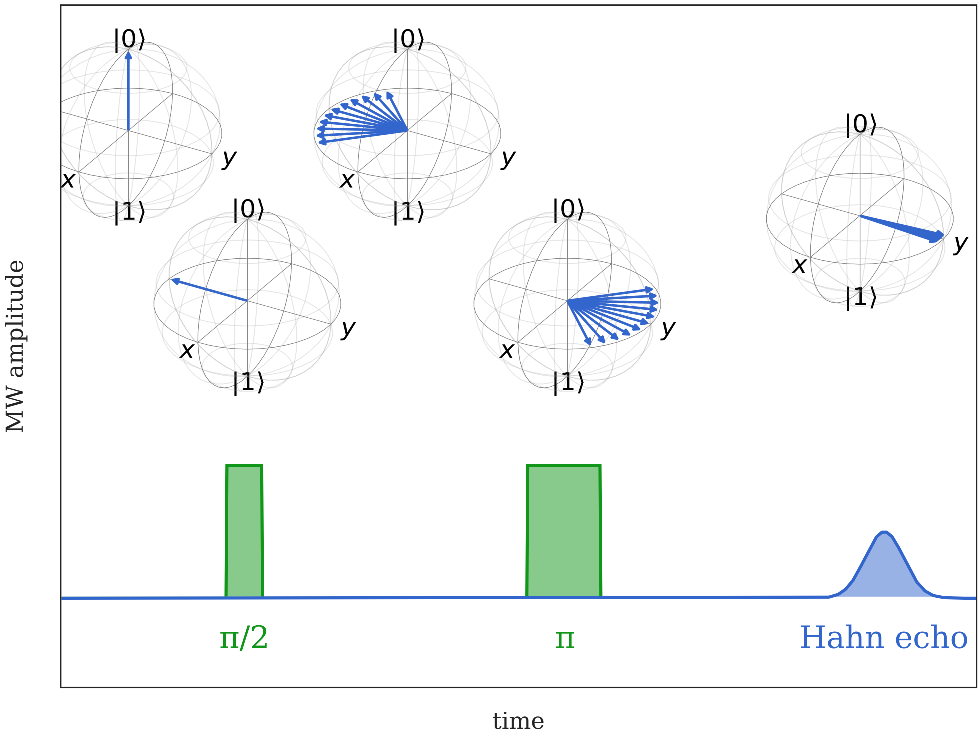

Figure 5.2: Bloch sphere representation of the Hahn echo ESR sequence employed. The $\pi/2$ pulse moves the spins perpendicular to the magnetic field. After the inhomogeneity in the Larmor precessions defocuses the spins, a π pulse inverts the population, leading to a refocusing of spin population and generating a characteristic Hahn echo. The Bloch spheres are drawn with python package qutip [149, 150].

Detection of the donor electron spin polarisation is performed via a Hahn echo electron spin resonance (ESR) sequence in the X-band at the liquid helium base temperature of 4.5 K. Hahn echo detection is preferred to a standard free-induction-decay(FID) single pulse sequence as it generates more data with both a focusing and defocusing T_2^* transient within the same sequence time, which is limited by the laser pulses. A standard Hahn echo sequence, as shown in Figure 5.2 is performed with a time spacing between the $^{\pi}/_{2}$ and π pulse $\Delta\tau = 45\mu s$ and a pulse length $\tau_\pi = 130ns$. The full laser-microwave sequence, shown in Figure 5.3, is designed to generate a D^0X spectrum. It consists of a tunable 250 ms D^0X resonant 1078 nm laser pulse polarising the spin, followed by the Hahn echo sequence for polarisation detection, and finally a 20 ms above-bandgap 1047 nm laser pulse to reset the donor spin population. A longer gap could also have been used between each Hahn echo sequence, allowing the natural relaxation of the spin population to thermal equilibrium; laser induced relaxation is preferred to speed up the experimental process. Laser or LED relaxation has been used extensively to speed up low temperature donor spin experiments, in particular at very low, millikelvin temperatures.

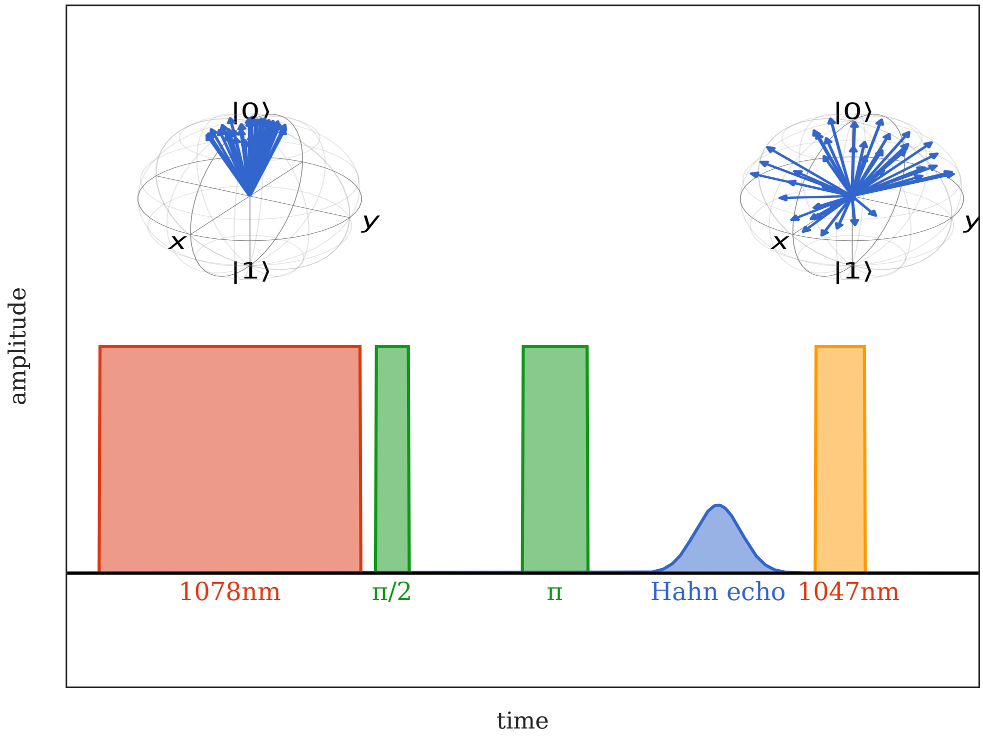

Figure 5.3: Laser-microwave sequence for the ESR detection of D^{0}X transitions. The tunable 1078 nm laser excites a donor bound exciton, polarising the donor electron spin. The Hahn Echo sequence measures this polarisation, and finally the above bandgap laser resets the sample's polarisation. The sequence is repeated while sweeping the 1078 nm wavelength, with the polarisation forming a D^{0}X transition spectrum. The Bloch spheres are drawn with python package qutip [149, 150].

The ideal Hahn echo for amplitude detection has the source frequency match the mean spin precession frequency, such that the Hahn echo is a simple gaussian, as in Figure 5.5(c). A phase IQ adjustment then allows the concentration of the whole signal in the I channel, maximising signal-to-noise and yielding a signal amplitude proportional to the spin population polarisation, with an inversion in polarisation resulting in an I-channel inversion. Under real conditions, however, small field drifts can easily offset the spin precession frequency leading to a modulation of the echo with frequency $\delta\omega = \omega_s - \omega_B$, as shown in Figure 5.5(a). Due to the narrow bandwidth of the spin population and thus long echos, even small shifts lead to visible echo oscillations. This is not a problem, as the spins are still within the $\sim$10 MHz driving and detection bandwidth, and the overall echo envelope is unchanged, as shown by the echo amplitude in Figure 5.5(b), but it does render signed amplitude detection slightly more complex. One solution would be to constantly adjust the magnetic field or source frequency to match ω_s and ω_B, but it would be unnecessarily cumbersome in a long experiment, and potentially lead to further phase issues. The standard approach is to accept small frequency shifts so long as they fall within the detection bandwidth, and instead deal with the issue computationally. For many ESR experiments this does not even matter, as the amplitude can be deduced from the IQ magnitude of Figure 5.5(b). Here however, the sign of the amplitude matters, as D^0X pumping can invert the population, and thus the complex echo must be preserved.

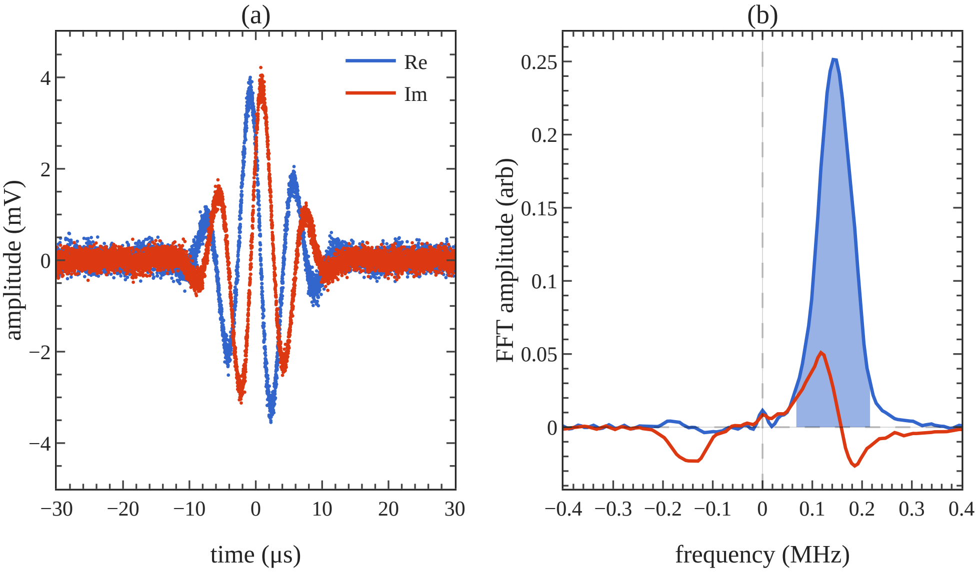

Figure 5.4: (a) Complex IQ Hahn echo of ^{28}Si phosphorus donor electron spin. The Gaussian echo is modulated by the difference between the microwave demodulation frequency Larmor precession frequency. (b) Fast-Fourier-Transform(FFT) of the Hahn Echo, with the fill indicating the integration window.

There are 3 possible approaches to deal with echo modulation in a signed amplitude measurement

Integration window narrowing The simplest solution is to reduce the echo time integration window on the symmetric I channel, such that any echo oscillation occurs outside this. This significantly reduces the signal-to-noise ratio.

Signal demodulation The echo modulation frequency is found via fitting or Fourier transform, and used to demodulate the echo via multiplication and filtering. This results in a higher SNR, however it is not computationally robust, in particular where the spin population is not precisely symmetric.

Fourier Transform Detection A fast Fourier transform (FFT) is applied to the echo, and the echo is integrated in the frequency domain, as shown in Figure 5.4. The frequency shift is addressed by simply integrating around the peak centre, rather than $f = 0$, with the desired bandwidth. This is an efficient, robust technique, and for this reason is employed here.

Figure 5.4 shows the scale of the polarisation induced amplitude changes on an echo, roughly doubling the echo amplitude when depopulating the thermally unfavourable $\left|\mathrm{S} = \frac{1}{2}, m_\mathrm{S} = +\frac{1}{2}\right\rangle_{\mathrm{D}^0}$ electron spin state via the $\left|\mathrm{S} = \frac{1}{2}, m_\mathrm{S} = +\frac{1}{2}\right\rangle_{\mathrm{D}^0} \rightarrow \left|\mathrm{S} = \frac{3}{2}, m_\mathrm{S} = -\frac{1}{2}\right\rangle_{\mathrm{D}^0\mathrm{X}}$ transition, and almost inverting the echo amplitude when depopulating the thermally favourable $\left|\mathrm{S} = \frac{1}{2}, m_\mathrm{S} = -\frac{1}{2}\right\rangle_{\mathrm{D}^0}$ via the $\left|\mathrm{S} = \frac{1}{2}, m_\mathrm{S} = -\frac{1}{2}\right\rangle_{\mathrm{D}^0} \rightarrow \left|\mathrm{S} = \frac{3}{2}, m_\mathrm{S} = -\frac{3}{2}\right\rangle_{\mathrm{D}^0\mathrm{X}}$ transition. Given the thermal polarisation at is expected to follow

$$P = \frac{N_{|-\frac{1}{2}\rangle} - N_{|+\frac{1}{2}\rangle}}{N} = \frac{1 - \mathrm{e}^{-\frac{g_\mathrm{e}\mu_\mathrm{B}B}{k_\mathrm{B}T}}}{1 + \mathrm{e}^{-\frac{g_\mathrm{e}\mu_\mathrm{B}B}{k_\mathrm{B}T}}} \tag{5.1}$$

at 4.5 K this is a small 5.1 %, implying the D^{0}X pumping is only polarising the population to a small 20 % for the $|+\frac{1}{2}\rangle \rightarrow |-\frac{1}{2}\rangle$ transition and −15 % for the $|-\frac{1}{2}\rangle \rightarrow |-\frac{3}{2}\rangle$ transition. This contrast with literature hyperpolarisation values which were observed up upwards of 90 % [23]. This can be explained by the mounting of the sample, shown in Figure 5.1, where only a small portion of the silicon is illuminated, with the rest covered by the opaque peek rod walls. The covered portion of sample is still largely within the ESR resonator, so it contributes to the ESR signal, but does not get polarised, leading to an overall lower level of polarisation.

Unlike the electron's, the g-tensor of the donor bound exciton hole is largely anisotropic, resulting in a complex Hamiltonian and a magnetic field angular dependence for the strain induced transition energy shift. This can be leveraged to obtain multiple parameters of the strain Hamiltonian, as the setup employed in this work, and particularly the geometry of the sample, only allow the application of strain in one direction, perpendicular to the [110] crystal plane, which would otherwise limit the information that can be extracted. Instead, the angle of the magnetic field is varied by rotating the sample mounting strain rod, as shown in Figure 5.1(a). The hole Zeeman Hamiltonian under such rotation angle is given by

$$H_{hz}(B,\theta) = \mu B \left\{ \left(g_1 J_z + g_2 J_z^3\right) \cos\theta + \frac{1}{\sqrt{2}} \left[g_1 \left(J_x - J_y\right) + g_2 \left(J_x^3 - J_y^3\right)\right] \sin\theta \right\} \tag{5.2}$$

The actual transition energies are given by the difference between the hole Zeeman Hamiltonian and the electron Zeeman Hamiltonian $H_\mathrm{ez} = g_\mathrm{e}\mu_\mathrm{B}B$, ignoring the hyperfine term here as the hyperfine D^{0}X transitions are not resolved. The electron g factor is treated as isotropic, although in reality a

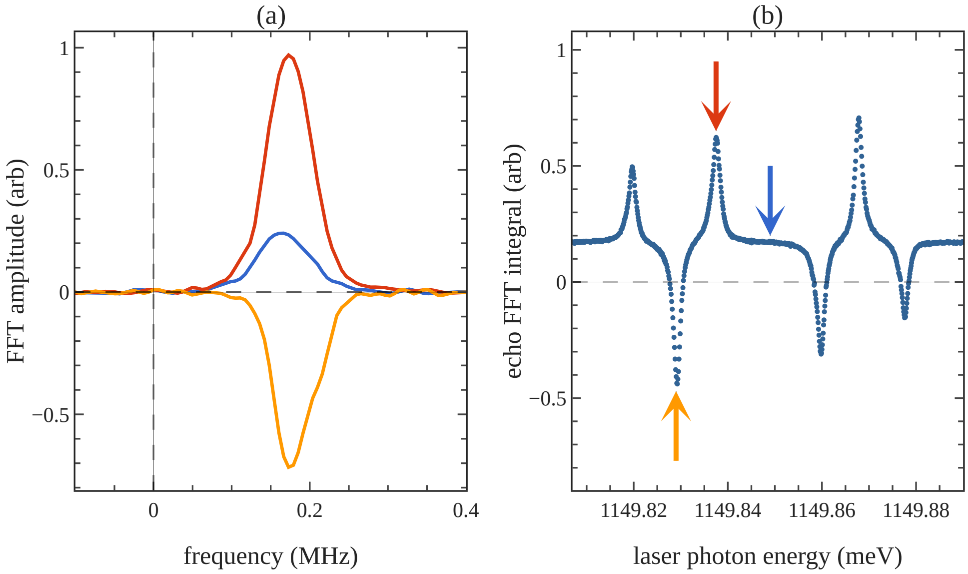

Figure 5.5: (a) FFT Hahn echos under IR laser illumination. • off resonance, • $m_S = \frac{1}{2} \rightarrow -\frac{1}{2}$ transition, • $m_S = -\frac{1}{2} \rightarrow -\frac{3}{2}$ transition. (b) Plot of the FFT echo integral against laser photon energy, generating a D^{0}X transition specturm.

small anisotropy arises under strain to valley repopulation. There is a further small, ∼ MHz tuning of the donor hyperfine under strain [115]. Both effects are ignored here as they lead to very small, unresolvable kilohertz shifts in this small strain regime.

5.1.2. D^{0}X Magnetic Field Anisotropy

Ignoring the strain matter for a moment, the rotation of the magnetic field angle itself allows the fit to the symmetric and asymmetric hole g-factor parameters g_1 and g_2, as well as the electron g-factor g_e. This is particularly important since the donor bound exciton anisotropic g_2 parameter, unlike acceptor hole states, is large and cannot be treated as a perturbation. Therefore, the D^{0}X spectrum is recorded at zero strain for 5 different angles, under a rotation on the [110] axis. Here 0° corresponds to a magnetic field normal to the [001] plane, while 90° angle has the magnetic field normal the $[1\bar{1}0]$ plane. The [111] plane is also present within rotation, although not specifically recorded, at the angle 0°. This data is fitted to the transition energies, derived from the difference between the hole spin Hamiltonian eigenvalues and the electron spin Hamiltonian eigenvalues. It should be noted that this fit could have simply been performed as part of the strain fit presented in the next subsection, however this is not done as the errors associated with the strained peaks are far larger due to peak broadening and overlaps.

The fit, shown in Figure 5.6, shows a good agreement to the theoretical model and yields parameters well in agreement with past literature. The pa-

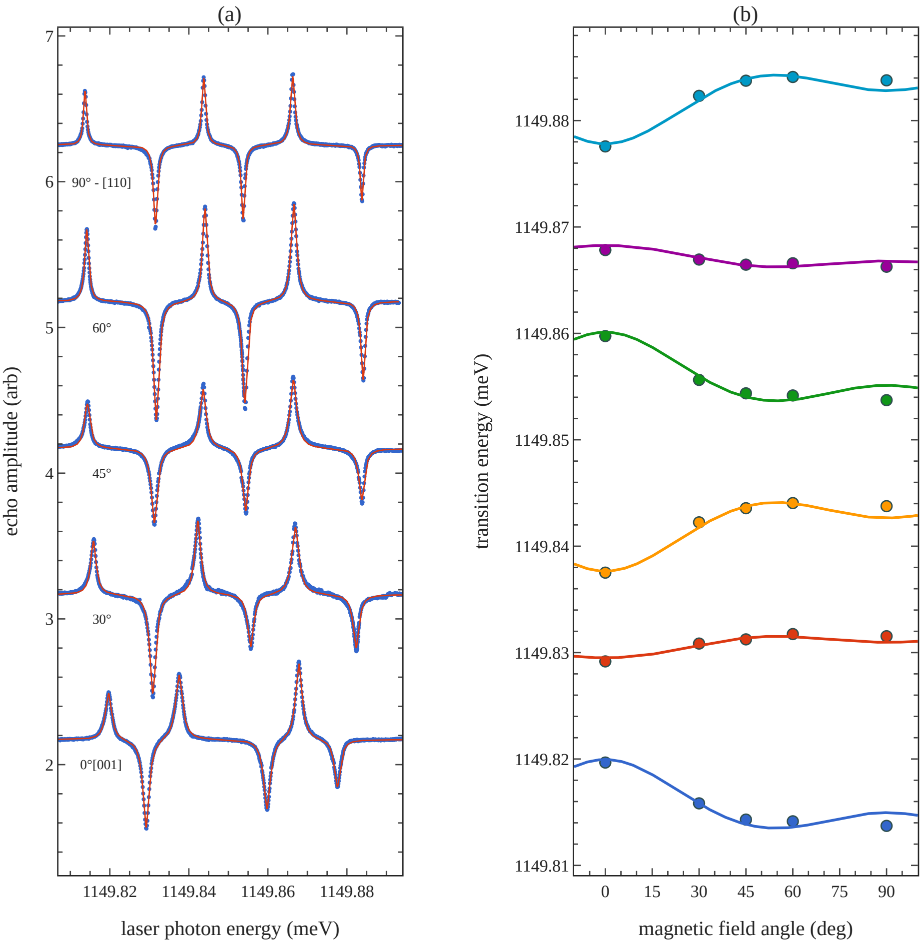

Figure 5.6: Zero stress D^0X spin polarisation spectrum under varying magnetic field orientation. (a) Angle dependent D^0X spectra (b) Fitted angular dependence of the D^0X transitions to the Zeeman theoretical model. The accurate fit demonstrates the successful rotation of the sample and derives the electron and hole g-factor parameters.

rameters are shown in Table 5.1 together with the strain parameters. This analysis and the good fit to theory further validates the experimental setup, confirming that the rotation is working as intended and the angles are sufficiently accurate.

5.1.3. D^0X SPECTRUM UNDER UNIAXIAL STRESS

Having established a robust technique to obtain D^0X polarisation spectra under variable magnetic field orientations, the experiment is repeated at every angle from Figure 5.6 with the application of stress, by placing calibrated masses on top of the rotating mounting rod. For zero-strain, the rod is slightly lifted as to not weight on the sample, and it is held by the screw holder of the Bruker resonator mount. To apply strain, the screw holder is loosened to let the rod freely rest on the sample, and subsequently higher calibrated masses are places onto the rod's top rotation platform. The maximum stress applied was ~ -0.8 MPa, slightly less than the maximum permitted by the setup. The limitation here is more to do with the degradation of the D^{0}X spectrum under stress, as can be clearly observed in Figure 5.7, partially due to broadening but also due to the peak overlaps. It is unclear if this is simply due to a degree of broadening due to uneven strain across the sample, or perhaps a fundamental broadening. The strained peaks throughout this work would suggest the former, which is certainly highlighted by to the narrow linewidth of the unstrained ^{28}Si D^{0}X transition. Figure 5.7 shows the strain effect on the D^{0}X spectra, with the clear degradation of polarisation and shift of the energy transition for the orientation $B \parallel [001]$.

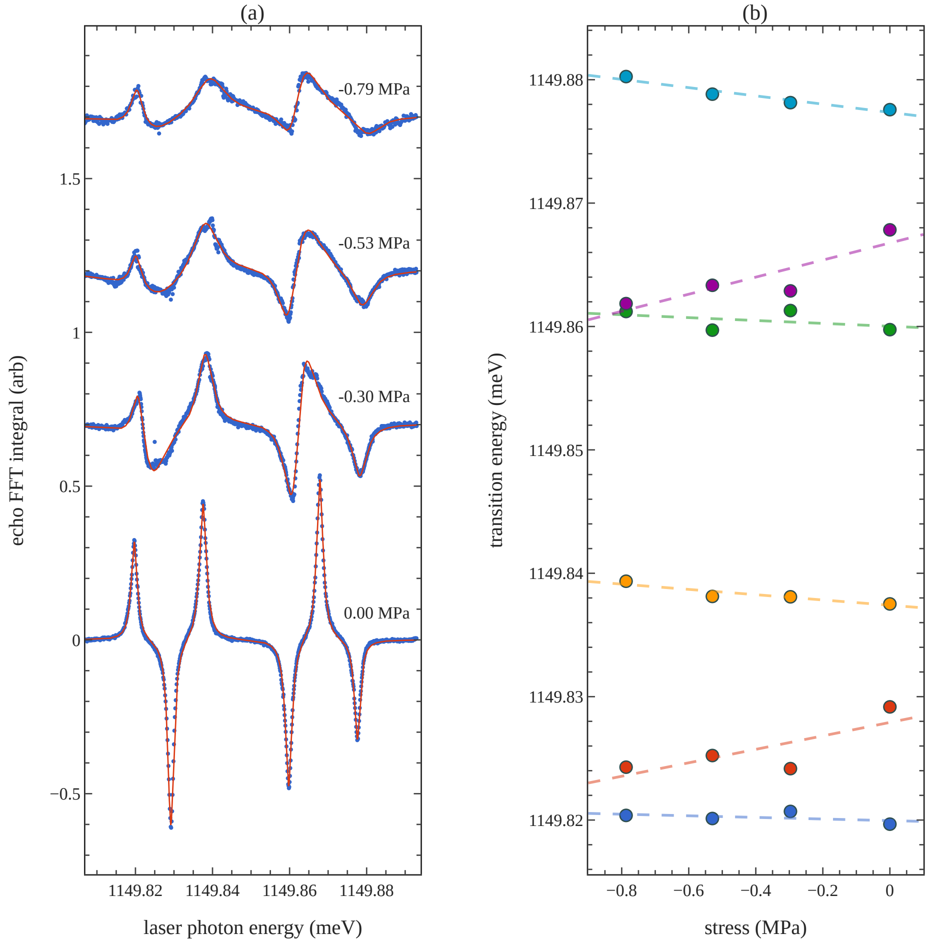

Figure 5.7: D^{0}X spin polarisation spectrum under varying stress with magnetic field along the [001] crystal axis. (a) D^{0}X spectra under stress. (b) Transition energies against uniaxial stress amplitude.

The stress is applied in the [110] plane. This stress can be obtained by performing a 45° $\hat{\boldsymbol{z}}$-axis rotation of a uniaxial stress tensor along the principal

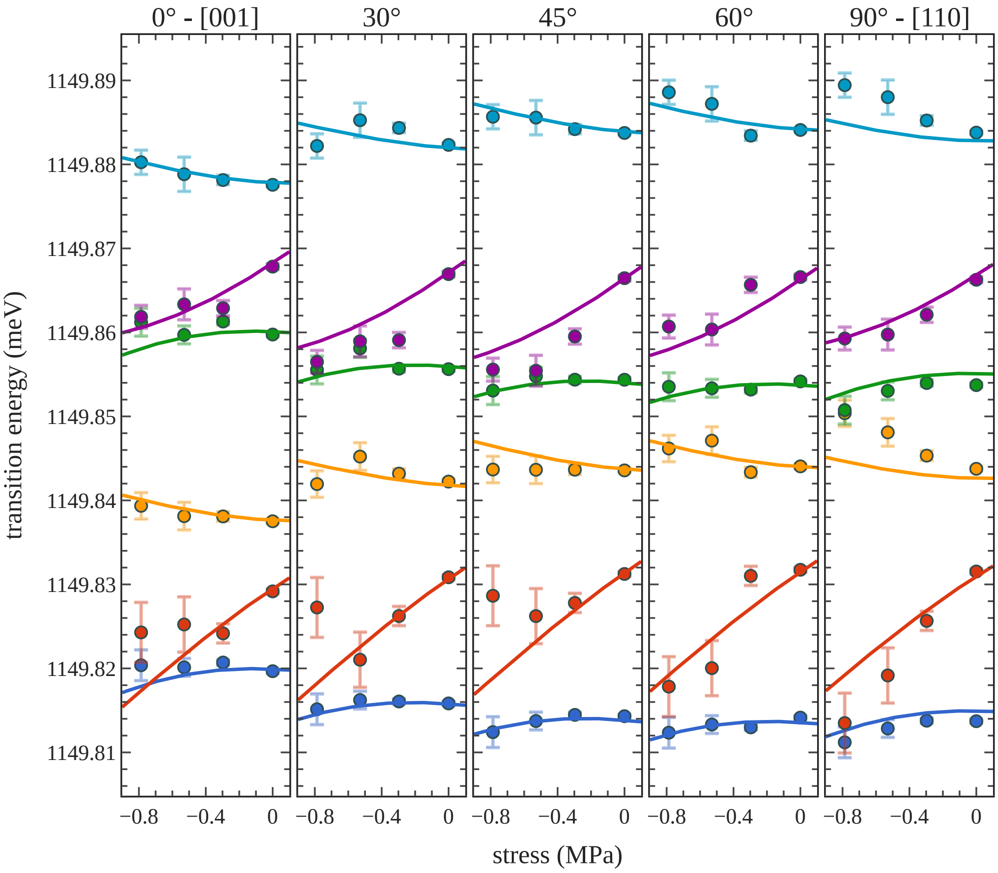

Figure 5.8: Angle dependent D^{0}X transition energy shifts fitted to the theoretical Pikus-Bir Hamiltonian eigenvalues.

axis $\hat{\boldsymbol{x}}$, as described in Section 2.3.

$$\begin{aligned}\sigma_{[110]} =& \boldsymbol{R}_z^\top\left(\frac{\pi}{4}\right)\sigma_{[100]}\boldsymbol{R}_z\left(\frac{\pi}{4}\right)\\ =& \frac{1}{2}T\begin{pmatrix}1 & 1 & 0\\ 1 & 1 & 0\\ 0 & 0 & 0\end{pmatrix}\end{aligned} \tag{5.3}$$

where T is the uniaxial strain $T = \frac{mg}{A}$. Applying the compliance relation $\boldsymbol{\epsilon} = \boldsymbol{S\sigma}$ then yields the strain tensor in terms of the stress and compliance matrix elements:

$$\boldsymbol{\epsilon}_{[110]} = T\begin{pmatrix}\frac{1}{2}\left(s_{11}+s_{12}\right) & \frac{1}{4}s_{44} & 0\\ \frac{1}{4}s_{44} & \frac{1}{2}\left(s_{11}+s_{12}\right) & 0\\ 0 & 0 & s_{12}\end{pmatrix} \tag{5.4}$$

These values in turn are be fed into the Pikus-Bir Hamiltonian. Please note that here the conduction band valley orbit terms are ignored as they lead to a

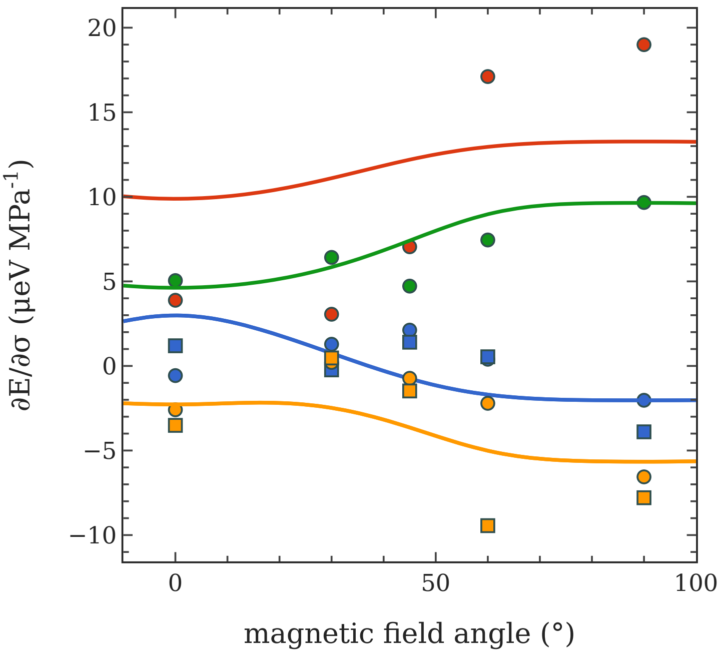

Figure 5.9: Low strain regime energy-strain gradients against magnetic field angle. 0° corresponds to $\boldsymbol{B} \parallel [001]$, 90° to $\boldsymbol{B} \parallel [1\bar{1}0]$. The transitions are grouped by colour on the four D^{0}X hole states and by marker shape on the donor spin state. The strain gradient only depends on the hole spin number.

common shift for all spin levels, which can be incorporated into the a term.

$$\begin{aligned}
\boldsymbol{H}_{\mathrm{pb}}(T) = \quad & (s_{11} + 2_{s12})\, aT + bT\left[\left(\boldsymbol{J}_x^2 + \boldsymbol{J}_y^2 - \frac{5}{2}\boldsymbol{I}\right)(s_{11} + s_{12}) + \left(\boldsymbol{J}_z^2 - \frac{5}{4}\boldsymbol{I}\right) s_{12}\right] + \\
& + \frac{d}{\sqrt{3}} T\left(\boldsymbol{J}_x \boldsymbol{S}_y + \boldsymbol{J}_y \boldsymbol{J}_x\right) s_{44} \\
= \quad & (s_{11} + 2_{s12})\, aT + bT\left(\boldsymbol{J}_z^2 - \frac{5}{4}\boldsymbol{I}\right)(s_{12} - s_{11}) + \frac{d}{\sqrt{3}} T\left(\boldsymbol{J}_x \boldsymbol{J}_y + \boldsymbol{J}_y \boldsymbol{J}_x\right) s_{44}
\end{aligned} \tag{5.5}$$

In the 0° configuration, where the magnetic field is along the z-axis, this simplifies significantly, with the b terms entirely in the diagonal resulting in a linear shift and the shear d term off diagonal resulting in a quadratic shift, as well as light-heavy hole mixing.

$$H_J(\theta = 0) = \begin{pmatrix} B\mu g_{\mathrm{HH}} + \Delta sbT & 0 & i\frac{s_{44}dT}{4} & 0 \\ 0 & B\mu g_{\mathrm{LH}} - \Delta sbT & 0 & i\frac{s_{44}dT}{4} \\ -i\frac{s_{44}dT}{4} & 0 & -B\mu g_{\mathrm{LH}} - \Delta sbT & 0 \\ 0 & -i\frac{s_{44}dT}{4} & 0 & -B\mu g_{\mathrm{HH}} + \Delta sbT \end{pmatrix} \tag{5.6}$$

where $\Delta s = s_{12} - s_{11}$, $g_{\mathrm{LH}} = \left(\frac{1}{2}g_1 + \frac{1}{8}g_2\right)$ and $g_{\mathrm{hH}} = \left(\frac{3}{2}g_1 + \frac{27}{8}g_2\right)$. This yields eigenvalues

$$\begin{aligned}\Delta_E =& \frac{1}{2}\mu B\left(g_{\mathrm{HH}} \pm g_{\mathrm{LH}}\right) \pm \sqrt{\left[B\mu\left(g_{\mathrm{HH}} \pm g_{\mathrm{LH}}\right) + b\Delta s T\right]^2 + 4d^2 s_{44}^2 T^2} \\ \approx& \mu B\left(4g_1 + 7g_2\right) \pm 2b\left(s_{11} - s_{12}\right)T + \frac{d^2 s_{44}^2}{2B\mu\left(4g_1 + 7g_2\right)}T^2\end{aligned} \tag{5.7}$$

Effectively, for the $\boldsymbol{B} \parallel [001]$ configuration the uniaxial b term results in a linear strain shift, while the shear d term only generates a quadratic shift. Hence this configuration is particularly useful to extract the b parameter, even for low strains.

As the magnetic field is rotated on the [110] axis, with the $\theta = 90\,\mathrm{deg}$ corresponding to the $\boldsymbol{B} \parallel [1\bar{1}0]$ orientation, the anisotropic $g_2 B J_i^3$ term introduces off-diagonal Zeeman elements, rendering the Hamiltonian significantly more complex. Even with a basis state rotation to keep $\hat{\boldsymbol{z}} \parallel \boldsymbol{B}$, non-diagonal terms persist due to the anisotropic $g_1 B J_i^3$ terms. The shear d term thus also generates a linear strain component and can be derived from the linear energy-strain gradient at small strains without relying on the higher order curve shape. The full eigenvalue problem, although it has an analytical solution is rather complex and not particularly informative and is therefore solved numerically.

	This Work	Thewalt[148], Lo[23]	Loippo [27]	theory [36, 147]
Exp. params				
B (mT)	345(1)	0[1]	$0 \rightarrow 300$	
σ (MPa)	$0 \rightarrow -1$	$0 \rightarrow -150$	~ 1	
Parameters				
g_{e}	2.01(2)	1.9985		
g_1	−0.83(2)	−0.8	−0.83	
g_2	−0.215(11)	−0.24	−0.22	
b (eV)	−1.4(2)	−1.7	−7	−2.2
d (eV)	−4.2(4)	−5.1	−4	−5.2
$\frac{\partial E_{\mathrm{g}}}{\partial \epsilon_{[110]}}$	1.8(2)			

[1] The strain parameters are extracted with 0 magnetic field, the hole g-factors under low magnetic fields.

Table 5.1: Fitted parameters of the strained D^{0}X Hamiltonian compared to theory and literature values.

The full fit is shown in Figure 5.8, showing good experimental agreement despite some clear outliers, most likely due to the error-prone peak fitting of some of the more broadened peaks, as shown in Figure 5.7a and for all angles in Appendix A. A useful summation of all the results is displayed in Figure 5.9, showing each of the transitions' gradient as a function of magnetic field orientation. There are only four independent gradients, as they are dependent on the D^{0}X hole state and not the D^0 electron's, leading to pairs of identical gradients for the light hole transitions from the pair of D^0 $|m_S = \pm\frac{1}{2}$ states. The agreement again is reasonable, apart from the heavy hole transition showing an abnormal anisotropy.

Finally, the extracted parameters are shown in Table 5.1 and compared to parameters from the existing literature, both theoretical and experimental. Reasonable agreement is observed with the experimental parameters from Lo [23] and the theoretical parameters calculated by Blacha [147]. The agreement is sufficient to conclude that the literature model and parameters are valid in the low strain regime. There still is an above-error discrepancy in the parameters. One potential source of error in this work might be a decrease in effective applied strain due to friction on the strain rod, overpressure from the cryostat and finally and unwanted tilt in the sample. This may explain the small, 10 % discrepancy in the d parameters, however it cannot justify the almost 50 % discrepancy in the b parameter. This dataset is not sufficient to conclude that there is a strain magnitude dependence in the parameter, however the matter should be considered carefully, and hopefully more experimental results may settle the matter.

5.2. Device Modelling

Having established the validity of the existing spin-strain Pikus-Bir model, it is important to theoretically understand the source of the experimental device strain. Micro-fabricated devices display large interface extrinsic stress at cryogenic temperatures due to the mismatch in the thermal expansion of the fabrication materials. This can be modelled effectively using finite element method (FEM) structural mechanics modelling techniques paired with the extensive literature on the thermal deformation of materials. Intrinsic stresses can also arise due to fabrication methods, and are far more difficult to model effectively, leading to some uncertainty on the magnitude of the model strain. This section discusses the modelling of device extrinsic thermal strain, which is later used to compare to experimental data, and discusses some of the extra potential sources of intrinsic strain.

5.2.1. Thermal Expansion Mismatch

All materials are subject to volumetric thermal expansion and contraction, due to the change in the lattice thermal energy. Most materials, including those treated here, expand under rising temperature due to the rising thermal energy of the lattice. Extensive literature exists with well-defined experimental values for the thermal expansion of materials for CMOS fabrication. These are usually derived by measuring a solid sample's length over a wide range of temperatures, yielding its cumulative length change, $\Delta L(T)/L_{\mathrm{T_{ref}}}$ with respect to a reference temperature, usually 293.15 K. This is then used to derive a

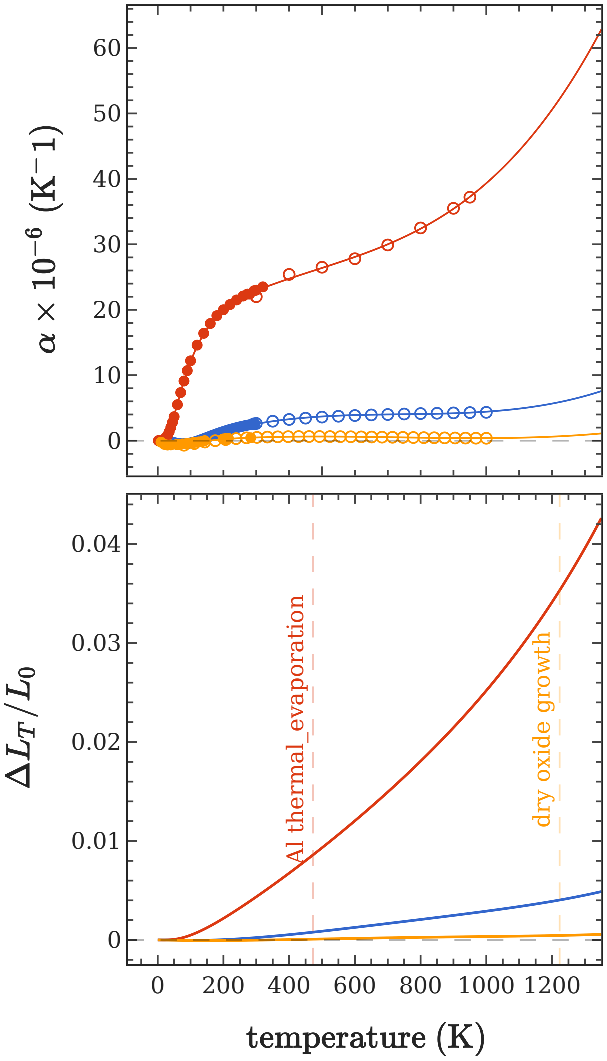

Figure 5.10: Thermal expansion of fabrication materials —silicon, —aluminium and —silicon dioxide. (a) Thermal expansion coefficients fit to a 5 node spline. Data by •Middelmann [151], ○Watanabe [152], •Kroeger [153], ○Wilson [154], •White [155], ○Hahn [156]. (b) Cumulative thermal expansion relative to the 0 K reference length.

temperature dependent coefficient of thermal expansion

$$\alpha(T) = \frac{1}{L}\frac{dL}{dT} \tag{5.8}$$

Literature thermal expansion coefficients for the relevant materials silicon, aluminium and silicon dioxide are shown in Figure 5.10. Multiple sources had to be analysed and patched together to obtain the full curve over the large temperature range 3–600 K for aluminium and 3–1200 K for silicon and its oxide. As a bonus, the good agreement of the experimental values over the temperature range overlaps acts as a useful sanity check for the accuracy and general applicability of the literature data.

Silicon's thermal expansion is fairly straightforward due to its crystalline form, as demonstrated by the excellent match in the data by Middelmann [151] and Watanabe [152]. Aluminium displays large thermal expansion and also shows good agreement at the overlapping temperatures; however some uncertainty exists with up to 50 % higher thermal expansion coefficients observed for thin films [157]. The difference seems less significant for very thin films, such as those used in this work (30 nm) [158], and therefore the bulk parameter is used, but some uncertainty remains regarding the true thermal expansion of the metal film. The main source here of uncertainty lies in the thermal evaporation process temperature. Aluminium is evaporated at high temperatures 600–800 °C, but the temperature of the deposited metal and indirectly heated substrate is difficult to characterise. Furthermore, some intrinsic film stress may build up during deposition, although this should be less significant than the large thermal stress built up at cryogenic temperatures.

Silicon oxide, which in this work is thermally grown on the silicon substrate in a dry oxygen atmosphere, presents a complex behaviour strongly dependent on growth conditions. An amorphous solid, not to be confused with crystalline quartz (c-SiO_2), silica (a-SiO_2) displays extremely low levels of thermal expansion, in the range of $0.24–0.55 \times 10^{-5}\,\mathrm{K}^{-1}$ at room temperature [159, 160]. The main uncertainty, however, arises due to the intrinsic stress which builds up during thermal growth, where the oxide eats into the silicon substrate leading to built-in intrinsic strain due to the lattice mismatch. This intrinsic strain can be significant and is generally observed to increase with growth temperature [161]. This is difficult to treat and is thus not incorporated in this works' FEM models, with the justification that the aluminium thermal expansion should still dominate, but it should still be considered an important source of uncertainty for these simulations.

Overall, the oxide and the aluminium thermal expansion mismatch cause opposite effects on the silicon substrate: compression by the metal and tension by the oxide. The metal substrate compression dominates due to the far larger mismatch in thermal expansion as well as the greater thickness of the metal layer (30 nm) than the oxide layer(11 nm).

5.2.2. Finite Element Modelling of Thermal Strain

Finite element modelling (FEM) is performed using software package COMSOL, and a fine quad mesh on the implanted area with dimensions designed to resolve the laser spot as well as the shallow depth of the donor implantation: ∼0.1 µm in the device plane and 30 nm perpendicular to the surface, while it slowly becomes coarser further away. The strain is derived for the shallow depth of 150 nm, where the phosphorus donors are implanted for the experimental D^0X devices, and the full tensor components are shown in Figure 5.11.

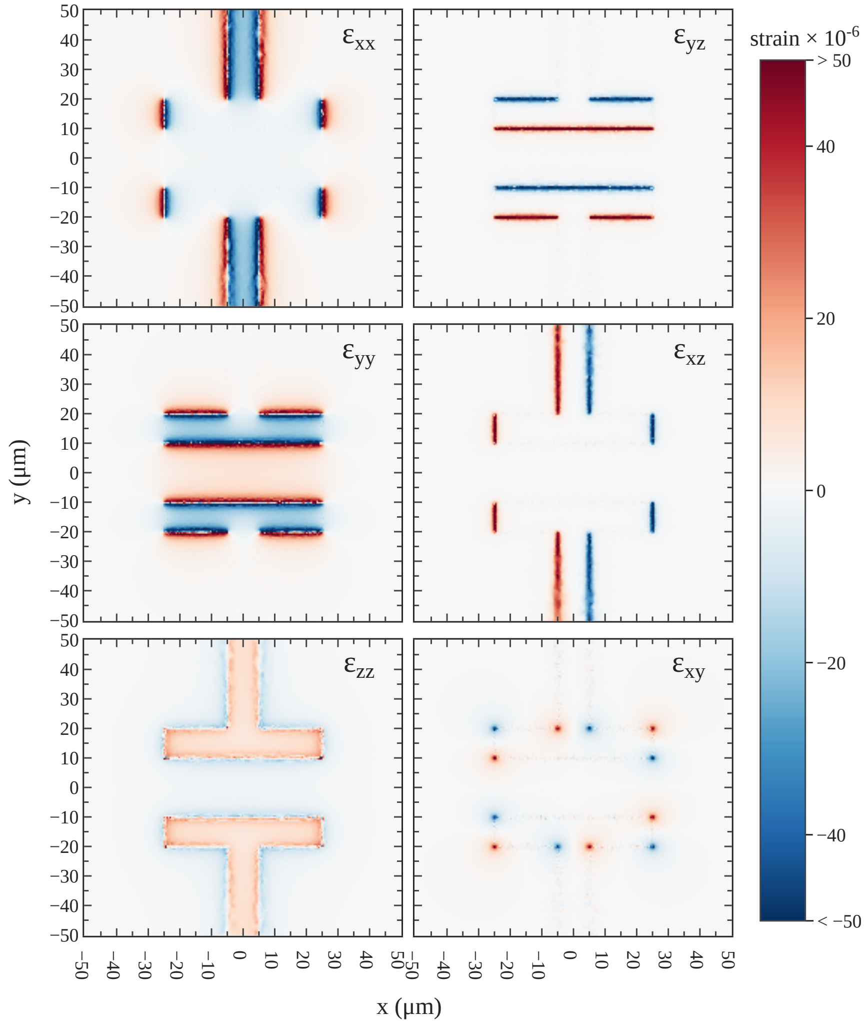

Figure 5.11: Strain tensor elements of a FEM thermal strain simulation for MOS microfabricated devices at the donor implantation depth of 100 nm. The color scale is capped at $\pm 50 \times 10^{-6}$, the true maximum observed strain is $\pm 150 \times 10^{-6}$.

Due to the higher thermal compression of aluminium, the strain is compressive directly underneath the contacts, and is dominated by principal strain component parallel to the short axis of the contact, with amplitudes around 2×10^{-5} at the centre of the contacts. Higher strains upwards of 10^{-4} are observed at the contact edges, where significant shear strain also builds up. The substrate relaxes into tensile strain off the contacts, and again is strongest at the edge of the contacts. The strain within the device implanted area is dominated by the principal component along the contact separation, with a central strain $\epsilon_{xx} \sim 6 \times 10^{-6}$ along the electric field direction giving $\boldsymbol{\sigma} \parallel \boldsymbol{E}$. The other two principal components are similar and tensile, with $\epsilon_{yy} \sim 1.5 \times 10^{-6}$ and $\epsilon_{zz} \sim 2 \times 10^{-6}$, leading to a strain tensor very much resembling one from uniaxial stress along the contact separation x-axis. The shear strain components are more than one order of magnitude smaller, only reaching significant values near the metal contacts, as one would expect due to the system's symmetry. However, one should be careful to draw conclusion as small amounts of asymmetry in a real-world device could lead to the appearance of significant shear strain components.

The strain tensor from the FEM simulations is used to calculate the D^{0}X light and heavy hole peak splitting for each spatial position within the device position. Further models are constructed for all the analysed strain geometries, very much consistent with Figure 5.11, and the resulting D^{0}X splittings are presented in the next section.

5.3. D^{0}X Scanning Microscopy

Section 5.1 established the strong sensitivity to strain of the D^{0}X transition energy, with shifts as high as 20 µeV MPa^{-1}. Micro-fabricated devices generate strain in the silicon substrate due to the mismatch in the device materials' coefficients of thermal expansion, as explored in Section 5.2. This is already notable at room temperature as fabrication often involves high temperature, such as 300–800 °C for aluminium thermal evaporation [162] and 800–1100 °C for dry oxide growth. As the silicon substrate and the oxide and metal layers cool down, the mismatch in their thermal compression leads to the build-up of stress at the interface. This mismatch is further amplified at cryogenic temperatures by cooling down another ∼300 K.

Much could be done to mitigate stress, such as moving away from interfaces and even combining materials with compensating thermal expansions, however some stress is likely to always be a factor in microscale electrical devices. This section employs the sensitive electrical techniques developed in Chapter 4 to conduct a microscopic analysis of the strained D^{0}X transition in micro-fabricated devices, comparing experimental data to theoretical models calculated using the parameters and FEM modelling described in this chapter's previous sections.

The optical setup is described in Section 3.3.1, and these experiments employ the single laser, 0.35NA objective setup, having been performed before the upgrade to the multi-laser setup. The scanning is performed via the piezo-actuator tower the sample sits on. These actuators do not have a position-feedback system, and although fairly predictable in their stepping, the hysteresis built up during a two-dimensional scan was large and well visible. Therefore, a CMOS camera and a custom image recognition software routine are employed as position feedback to the piezo-actuator, which is fully described in Section 3.3.2. The scanning sequence is straightforward, as shown in Figure 5.12, and consists in repeating a laser wavelength at every laser spot scanning position, while pulsing the laser amplitude with a pulse width of ∼10 ms to cancel current drifts. The electrical detection is a low frequency, AC photocurrent lock-in detection performed as described in Section 4.2, recorded at

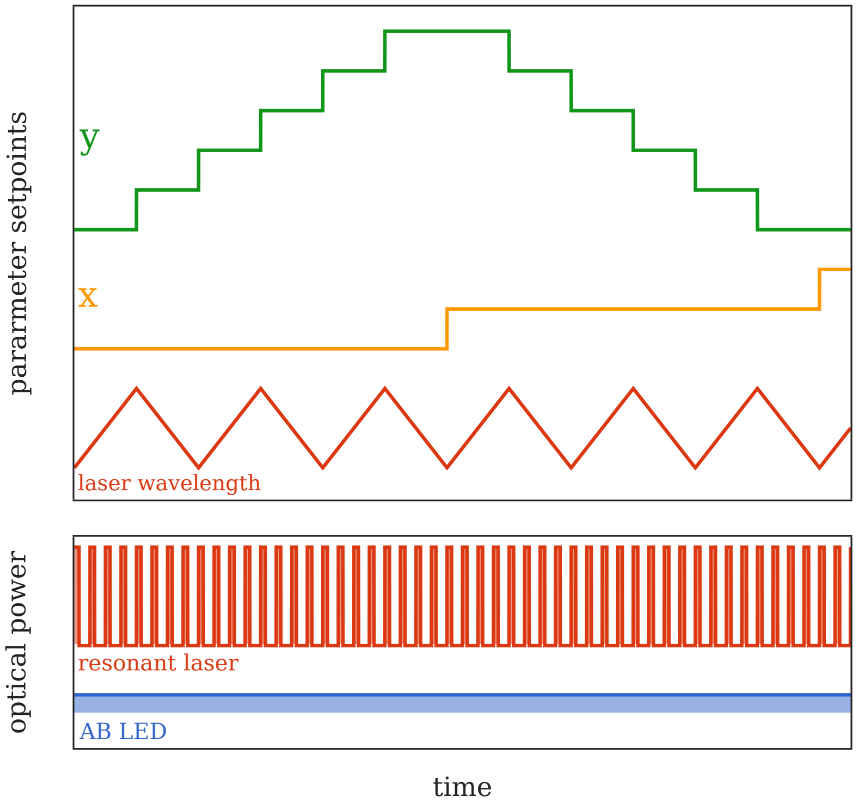

Figure 5.12: D^{0}X scanning microscopy sequence. A pulsed, wavelength dependent D^{0}X photoconductive spectrum is recorded at every laser spot position on a 2D scanning grid.

a frequency of 101.077 kHz, a source rms amplitude of 50 mV.

Effectively, this is a 3-parameter map, scanning x-position, y-position and laser wavelength, as shown in Figure 5.12. Each wavelength scan is 20–120 s long, dependent on the device, to ensure a satisfactory signal to noise ratio and to ensure no hysteresis occurs to skew the peaks. The entire experiment is fully automated, which is crucial as these runs are time consuming and took up to 48 hours. This is possible mainly thanks to the image convolution positioning system described in Section 3.3.2, but also thanks to a custom software routine designed to auto-range the lock-in amplifier and oscilloscope.

5.3.1. 20 × 50 µm DEVICE

The 20 × 50 µm device presented in this section yielded some the best signal, and it is also a twin of the device employed for the electrical analysis of Section 4.2. The scan was performed using sub-resolution steps of 1 µm, with a border going also slightly outside the donor implanted area, in order to identify the device's metal contacts, which affect the background bulk photocurrent signal.

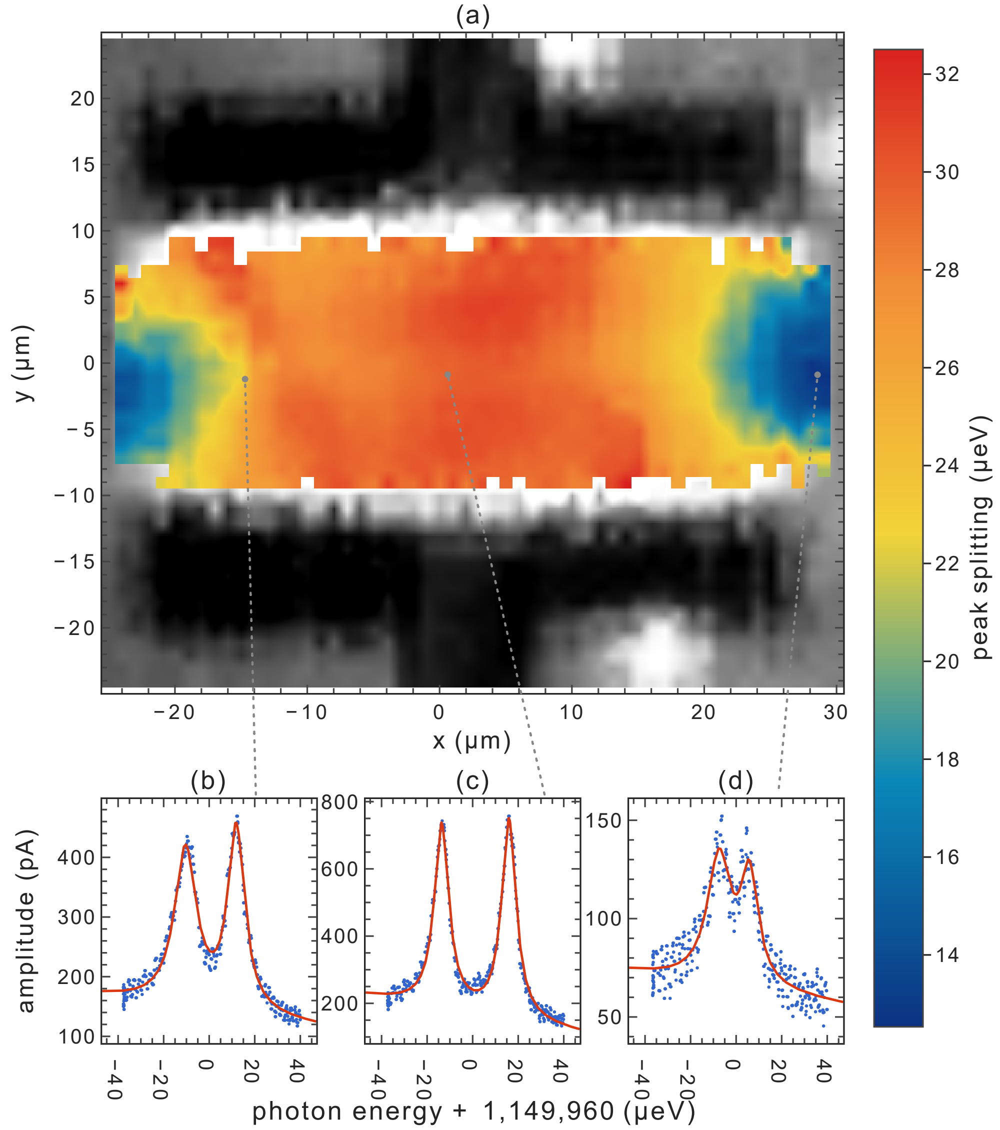

Figure 5.13: (a) Scanning microscopy 20 × 50 µm D^{0}X peak splitting map (b)(c)(d) position dependent D^{0}X spectra.

The peaks observed when illuminating the implanted donor patch are both well modelled by a Lorentzian lineshape, as shown in Figure 5.13(b,c,d). A skewed lineshape was considered but did not significantly improve the fits, nor did it meaningfully affect the peak means.

The 2D heatmap presented in Figure 5.13 shows a coloured peak splitting map of the scanning positions where a pair of peaks could be detected and reasonably fitted to a pair of Lorentzian. Where No peaks are detected, a greyscale map is displayed instead with the photocurrent amplitude averaged along the whole wavelength sweep. This is useful as a sanity check as it resolves the aluminium contacts position. Here, the dark black areas have a low photocurrent response due to the contact reflection, while the grey areas show a slightly higher photocurrent from the bulk response. The bright white areas at the edge of the implanted areas suggest the presence of implanted donors, which however do not yield visible resonant peaks. This is most likely due to a combination of the much larger strain directly under the oxide, the limited photon energy range used, and the much lower signal to noise ratio from the broadened peaks. The peak splitting scanning map shows a mostly constant peak splitting along the feedline direction, while the splitting almost halves towards the edge of the capacitor, near the edge of the implanted patch.

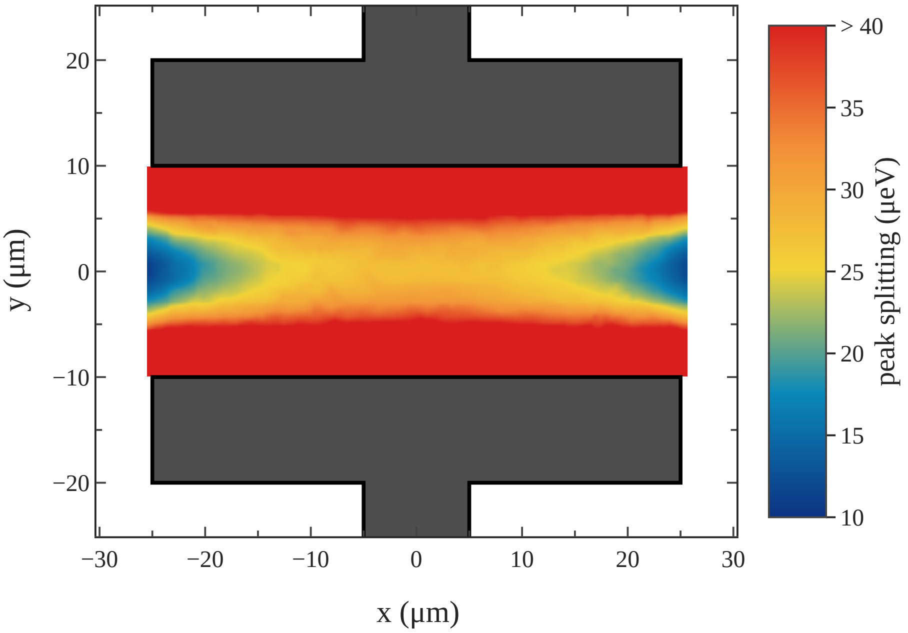

Figure 5.14: FEM simulation peak splitting map of a 20 × 50 µm D^0X D^0X device. The z-axis range is artificially capped at 40 µeV for comparison purposes: the maximum observed strain is ~0 µeV at the contact edge.

A splitting map of theoretical peak splittings is also presented for comparison in Figure 5.14, and it is calculated by feeding the strain tensor data from the FEM simulation of Figure 5.11 into the Pikus-Bir Hamiltonian. The range is intentionally capped to present a useful visual comparison to the experimental map of Figure 5.13. The match in the strain magnitude and y-axis variation is remarkable at the centre between the contacts, with both the experimental and theoretical maps showing a central peak splitting of ∼30 µeV, which halves to ∼15 µeV at the edge of the device. There is a large discrepancy in the splitting along the x-axis, with the experimental map not showing the large increase in peak splitting of the FEM map. This could possibly be explained by the relatively large laser spot Airy disk diameter of ∼4 µm and the large peak splitting gradient observed over a relatively small distance near the contact interface. The edge signal is broadened to the point where it can no longer be resolved, while the large laser spot still generates a small signal from the relatively narrow central donors. This highlights a limitation of this strain measurement techniques: it is difficult to generate narrow peaks over areas where the strain gradient is significant within the laser spot area.

5.3.2. 20 × 10 µm DEVICE

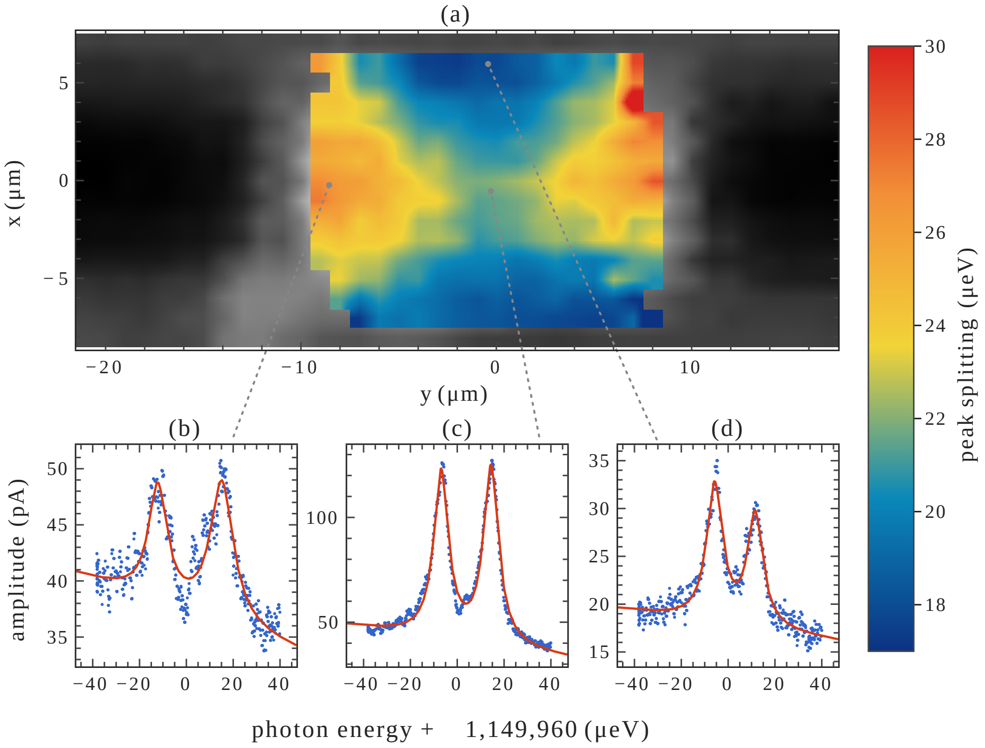

Figure 5.15: (a) 20 × 10 µm D^{0}X peak splitting map. (b)(c)(d) position dependent D^{0}X spectra.

This device, where the capacitor is only as wide as the feedline at 10 µm was studied as a low strain extreme, to show the residual strain due solely to the feedline. The strain levels observed in Figure 5.15 are quite close to those observed in the 20 × 50 µm device, but here display a more pronounce gradient also in the x-axis, with a central peak splitting as low as 20 µeV. Notably, the minimum strain at the device edge is higher than that of the 20 × 50 µm device, highlighting the strong strain induced by the feed line.

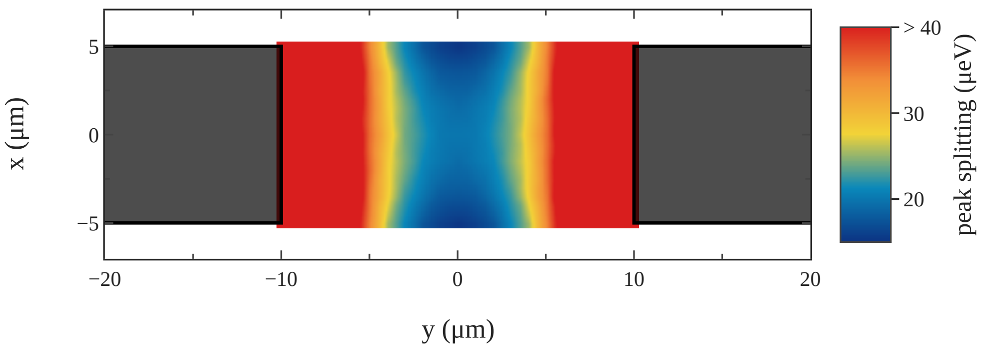

Figure 5.16: FEM Simulation peak splitting map of a 10 × 50 µm D^{0}X device.

Figure 5.16 shows a theoretical peak splitting map constructed from an FEM map, as for the previous device. The FEM simulation is identical to the one from 5.11, with the device parameters adjustments to match this device. The agreement is again remarkable, in particular at the centre of the device, although the experimental map shows a more pronounced curved strain profile around the contact. The same issue persists where the experimental map does not show the large splitting expected at the contact edge.

5.3.3. 20 × 800 µm DEVICE

The 20 × 800 µm device was studied as an extreme limit of a large device, in order to determine the variations of the strain profile on a large, near millimetre scale as well as to test an extreme use case of the microscopy technique. Due to the large scale and the time required for a single scan, the step size was increased significantly to a 2 µm for the x-axis and 3 µm for the y-axis respectively, and it still ended up taking approximately 48 hours. Due to this extreme scan duration, occasional, unexplained current magnitude shifts are observed, such as the increase amplitude observed around the $y = 200$µm in Figure 5.17. Yet, the resonant peak splitting still appeared unaffected in shape apart from a higher SNR that led to a higher discard rate. Overall, this scan shows the robustness of the scanning microscopy technique, capable of consistent multi-day scans with no apparent spatial drifts, even in the uncontrolled z-axis, nor significant current or temperature drifts.

Regarding the strain profile, the general behaviour appears to show a baseline peak splitting of ∼15 µeV, and a higher ∼25 µeV peak splitting right at the feedline junction. This is possibly the most compelling evidence that the

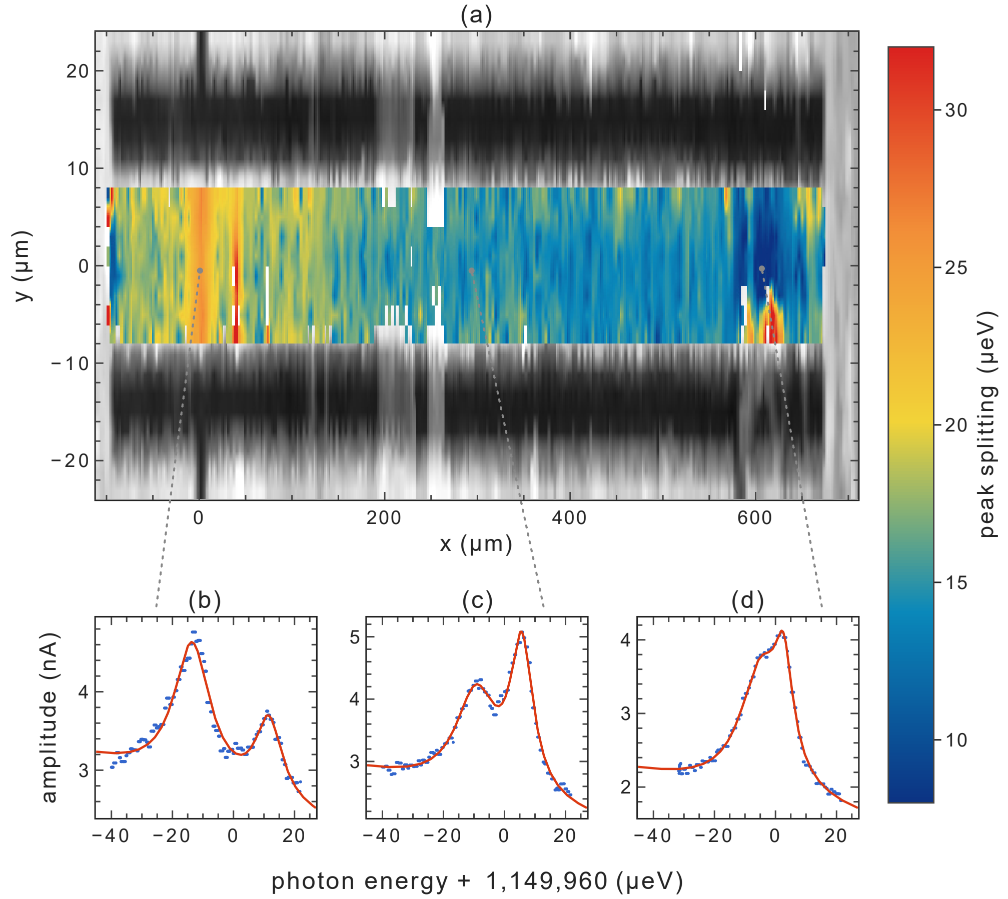

Figure 5.17: (a) Scanning microscopy 20 × 800 µm D^{0}X peak splitting map. The feed-line is at the 0 µm position and the x-y aspect ratio is not to scale. (b)(c)(d) position dependent D^{0}X spectra.

observed D^{0}X light and heavy hole peak splitting is caused by strain, as the capacitors' electric field would certainly be more evenly distributed. Finally, there is a surprising, low ∼8 µeV splitting area near the far end of the capacitor at the 600 µm mark, right above a highly strained spot. This is surprising as no obvious features are present, and the lowest strain point would be expected at the very end of the device instead. It is certainly not a fluke, as Figure 5.17(d) shows a clearly close pair of peaks with a good SNR. It is indeed possible that this is the result of a local fabrication defect, such as a hairline crack in the aluminium layer or an over-etched oxide section. The non-resonant photocurrent appears to show some sort of anomaly in the lower metal contact. Although unexpected, this result really emphasises the sensitivity of the photoconductive D^{0}X transition as a tool for microscale strain profiling. Here, there is a device with no visible defect, yet a D^{0}X map can identify an anomalous strain region suggesting a potential fabrication defect.

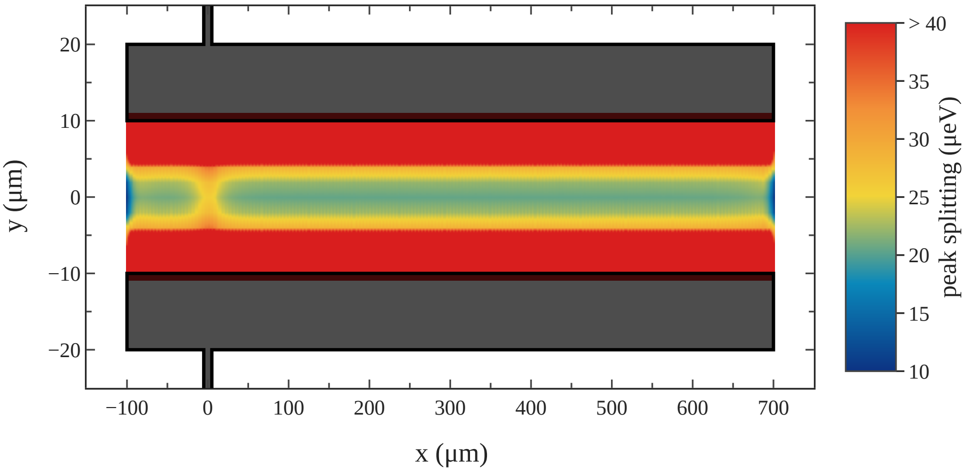

Figure 5.18: FEM Simulation peak splitting map of a 20 × 800 µm D^{0}X device.

Comparing to the FEM calculated splitting map of Figure 5.18, the central area between the contact again shows an excellent agreement. Notably, the increased strained area at the feedline location is replicated, with the experimental map possibly displaying a more extended impact from the feedline. as well as the lower strain area near the edge of the device. Naturally, the theoretical model does not predict the low strain area at $y \sim 600\,\mu\text{m}$, which is most likely due to some fabrication or local defect.

5.3.4. 5 × 400 µm DEVICE

Finally, a device with a reduced contact separation, 5 µm is explored. The class of 5 µm spacing devices is very important, as it represents a further step towards miniaturisation. The implanted phosphorus layer is fully covered by the 11 nm oxide, thus sitting only 150 nm from an oxide interface, and even at the centre only 2.5 µm from a metal contact.

As expected, the peak splitting is much larger than observed in the 20 µm spacing devices, by about an order of magnitude at ∼300 µeV. The extra peak splitting renders the laser wavelength scan significantly more complex, as it requires a temperature sweep of the Koheras Adjustik laser to cover the whole ∼500 µeV range. Considering the ∼1 meV of the laser, this is quite close to the maximum fully measurable D^{0}X splitting. Notably, the peaks here are heavily skewed, symmetrically with a sharp tail at the centre and a wider tail on the outside. The peaks are still well modelled to a Lorentzian lineshape however, as the sharp central peak is not well described by a Gaussian, even with a skew factor. Attempts were made to use skewed Voigt profiles; however the Lorentzian term is so dominant that it is preferred to dispense of the extra σ fitting parameter. The peaks are thus fitted using an asymmetric Lorentzian,

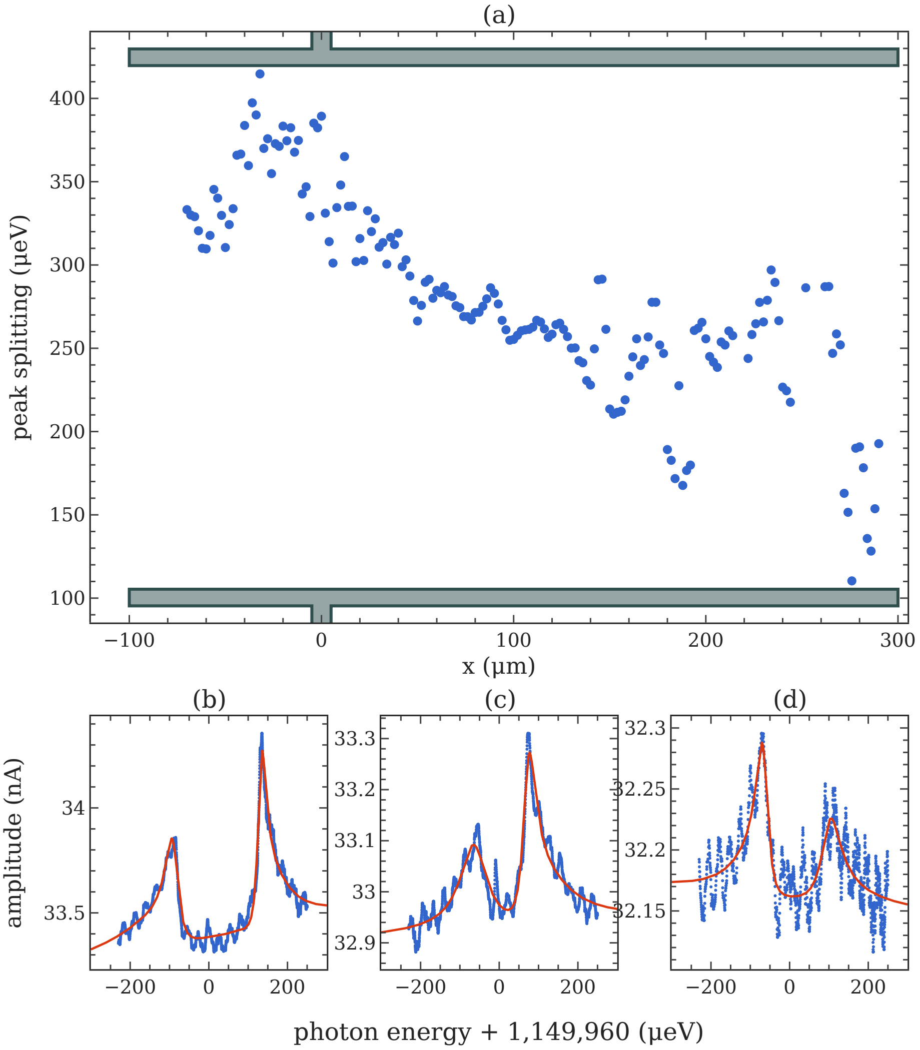

Figure 5.19: (a) Scanning microscopy 5 × 400 µm D^{0}X peak splitting scan between the contacts, averaged on the y axis. A 2D map shows almost no variation along the y axis. (b) D^{0}X spectrum at $x = 0$µm, (c) D^{0}X spectrum at $x = 100$µm, (d) D^{0}X spectrum at $x = 290$µm. The order of magnitude larger strain broadening leads to a far noisier spectrum compared to the 20 µm gap devices.

which unfortunately is a notoriously problematic lineshape. The issue with skewed Lorentzians is that they have an unbound expectation value. If one tries to calculate the expectation value of a Lorentzian distribution, the term $\int_0^\infty \frac{x}{1+x^2}dx$ diverges unless it is compensated by an equal opposite term from the other half of the distribution, cancelling out. A skew factor breaks this symmetry and thus renders the mean unbound, meaning a somewhat arbitrary choice of limits has to be made. A few options are considered such as an erf skewed Lorentian [163] and the Doniach-Sunjic lineshape [164], but the best results are obtained with the simple asymmetric Lorentzian by Stancik [165], which introduces skewness with a continuous asymmetric $\gamma(x)$.

$$\begin{aligned} L\left(x\right) =& \frac{2A}{\pi\gamma\left(x\right)\left(1+4\left(\frac{x-x_0}{\gamma(x)}\right)^2\right)} \\ \gamma\left(x\right) =& \frac{2\gamma_0}{1+e^{\alpha(x-x_0)}} \\ \langle x\rangle =& \int_{x_0-5\gamma}^{x_0+5\gamma} xL\left(x\right)\,dx \end{aligned} \tag{5.9}$$

This lineshape yields excellent fit to experimental spectra, as shown in Figure 5.19b,c,d.

The exposed implanted areas, at 5 µm along the capacitors' separation are only slightly wider than the 3 µm of laser spot, and a scan along the short axis does not expose notable variations in the peak separation. Hence, a 2D scan is performed with only 5 steps along the short x-axis, which are averaged together to yield a 1-dimensional scan along the contacts length. The result, shown in Figure 5.19a, shows a large variation of peak separations along the device length, from the ∼400 µeV near the feed line connection to the ∼150 µm at the opposite end. This suggests that the feed line generates a significant portion of the strain, and is compatible with the results of the long 20 × 800 µm device, which also showed a large increase in peak splitting at the feed line junction.

5.4. Linear Optical Polarisation in Strained D^{0}X devices

In the absence of strain, the donor bound exciton state in silicon is unpolarised due to the valley symmetry of the conduction band and the light and heavy hole degeneracy of the valence band. Strain splits the valence band with its spin angular momentum, in the $m_J = \pm 1/2$ light holes and $\pm m_J = 3/2$ heavy holes, thus introducing dipole transition selection rules and a polarisation dependence of the transition. Simplistically, in the case of linear polarisation, an electric dipole transition is allowed, in this case where $\Delta J = 1$, if $\Delta m = 0, \pm 1$. The light polarisation determines which transitions are allowed and with what amplitude.

In the simplest case of uniaxial stress, the polarisation should be linear across the principal axis, due to the sign degeneracy of the light and heavy hole states, while under realistic, complex strain tensors including multi-axis strain and shear forces the polarisation should have a combination of linear and circular components. This in turns means that the amplitude of the individual light and heavy hole peaks depends on the polarisation of the resonant laser.

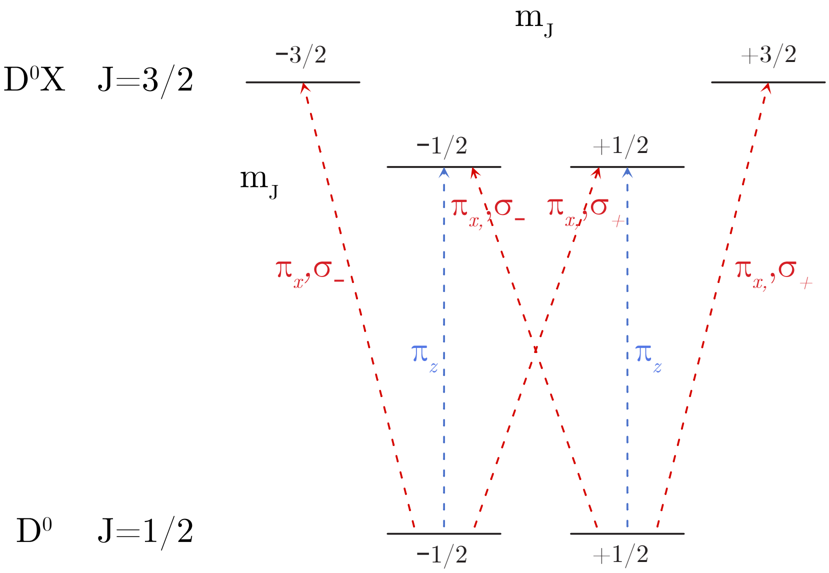

Figure 5.20: D^{0}X transitions with polarisation selection rules for illumination propagating in the $\hat{\boldsymbol{x}}$ axis.

Regarding angular momenta, the dox transition is $|J = \frac{1}{2}, m_J = \pm\frac{1}{2}\rangle \rightarrow |J = \frac{3}{2}, m_J = \pm\frac{1}{2}, \pm\frac{3}{2}\rangle$. The selection rules are highlighted in Figure 5.20. All transitions have $\Delta J = 1$. The heavy hole states require a $\Delta m_J = \pm 1$, which for linear polarisation requires a π_y polarisation. The light hole transitions can occur with both $\Delta m_J = 0, \pm 1$, although they have different transition amplitudes, with $\sqrt{\frac{2}{3}}$ for the π_z and $\sqrt{\frac{1}{3}}$ for the π_y transition. The relative amplitude of the heavy hole π_y transitions is 1 [166].

The light polarisation dependence of the D^{0}X spectra can give important information regarding the axes where strain is applied which cannot be discerned via the magnitude of light and heavy hole peak splitting. In the experiment presented in this section, the laser linear polarisation is rotated by first applying a depolariser to the linearly polarised laser beam to generate unpolarised light, and then a linear polariser on a rotating mount to obtain the linear polarisation of desired angle, as shown in Figure 5.21. The linear polariser is rotated in steps of 10° and a full D^{0}X direct current spectrum is recorded at each steps, with two examples displayed in Figure 5.22. The combination of depolariser-linear polariser was chosen over a more traditional half-waveplate setup due to the already available optical components. The linear polariser is placed on the optical table but is also first calibrated against a second linear polariser carefully placed on top of the objective, to align the angle against the cryostat and device axis. The optical setup employed here is the dual-laser benchtop setup described in Section 3.3.3, with the Toptica DL-pro laser and capacitive lock-in electrical detection from Section 4.2.

The device employed, shown in Figure 5.22, was a 20 µm separation ca-

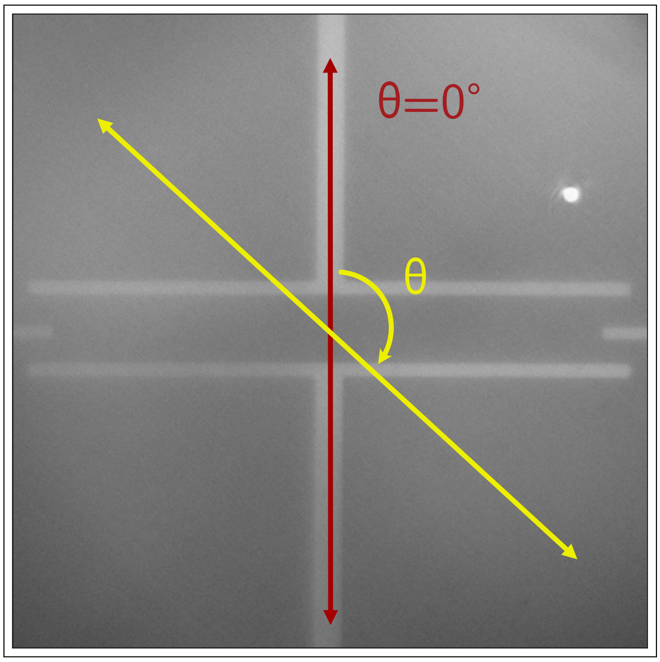

Figure 5.21: Linear polarisation rotation with respect to the device axes. $\theta = 0°$ is π_z, $\theta = 90°$ is π_y.

pacitor pair device, with the difference that a pair of metal contacts was also present at the capacitors' edges. A device from Section 5.3 was not chosen as the relevant sample had degraded after multiple load cycles, as this experiment was performed at a later time with the upgraded dual-laser benchtop optical setup, as this allowed for a finer control of the optical polarisation while not affecting the stability of the optical setup.

Figure 5.22 shows two extrema D^{0}X spectra at π_z and π_y linear polarisations, as well as the angular dependence of the light and heavy hole peaks as a function of linear polarisation angle. As expected, there is a sinusoidal, out of phase dependence for the two peaks, with a period of π, hence a $\sin^2\theta$ dependence on polarisation. The minima are aligned with the device axes, with the presumed principal strain orientation leading to a maximised light hole and a minimised heavy hole, as per the π_z transitions of Figure 5.20. As expected, both transitions have a sinusoidal dependence with a $\pi/2$ phase offset. The phase dependence of the light hole arises because the π_z transition has a higher amplitude than the π_x transition, while the phase dependence of the heavy hole transition arises because the π_x transition can only occur with perpendicular polarisation, leading to a forbidden transition under $\theta = 0°$ parallel linear polarisation. A non-negligible residual polarisation is still visible, suggesting a degree of state mixing or a tilt of the principal axis into the substrate plane.

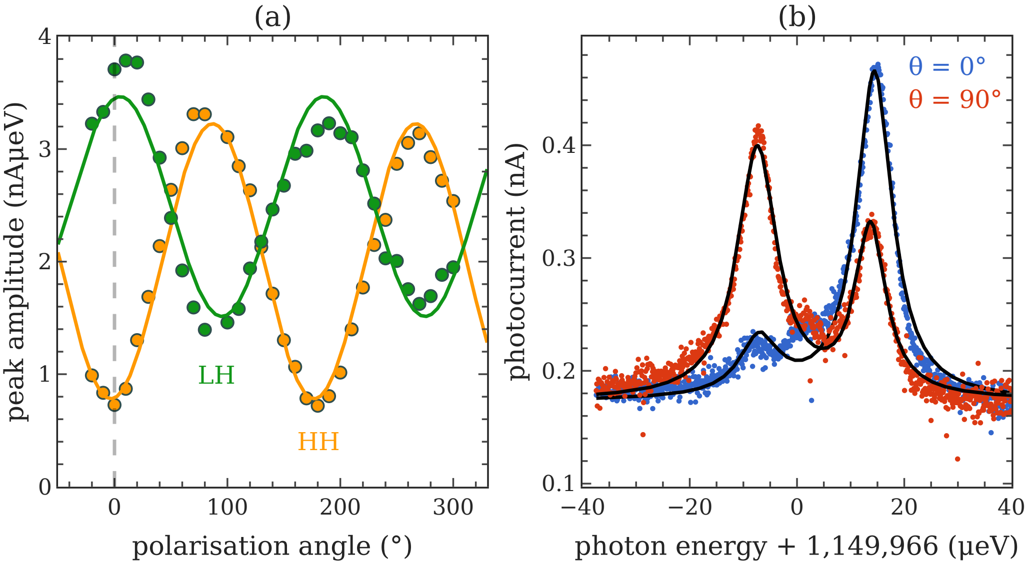

Figure 5.22: D^{0}X direct AC phocurrent measurement under varying laser linear polarisation. (a)— heavy hole and — light hole polarisation as a function of linear polarisation angle. (b)D^{0}X spectrum at the extrema ● 0° and ● 90° polarisation angles.

5.5. Conclusions

This chapter explored the subject of strain in silicon donor bound excitons. This is shown to be especially important to microfabricated devices, subject to significant interface stress from the mismatched silicon, metal and oxide thermal expansions.

Section 5.1 explored the low regime strain via controlled strain applied to a bulk $^{28}\mathrm{Si}:\mathrm{P}$ sample, confirming the validity of the existing theoretical models in the low strain regime and deriving a set of experimental parameters. While the subject had been previously explored [23, 148], validation in the low strain, ∼1 MPa regime is significant and non-trivial, as it is often encountered in microscale devices.

Section 5.3 presented a novel D^{0}X scanning microscopy technique, with D^{0}X peak splitting maps displaying good agreements with theoretical values from thermal strain FEM models. This introduces D^{0}X microscopy as a sensitive probe for near surface donor strain. Furthermore, microscale electrical detection is demonstrated in devices with contact spacings as low as 5 μm and directly underneath a thin oxide layer, in furtherance of the goal of downscaling D^{0}X detection near device interfaces.

Finally, the D^{0}X spectrum is analysed under variable angle linear optical polarisation, showing a strong $\sin(2\theta)$ sinusoidal dependence for the light and heavy peaks, compatible with a mostly in plane strain induced hole spin quantisation.

Overall, this chapter for the first time introduces donor bound exciton detection as a promising, microscale strain sensing technique. While broadening has been previously employed as a qualitative gauge for strain inhomogeneity [29, 146], the Pikus-Bir splitting can yield precise, quantitative estimates. The novel scanning microscopy further elevates the technique demonstrating microscale strain resolution. The data presented in this chapter has been written into a scientific publication soon to be submitted for review.

6. DONOR SPIN POLARISATION IN A MAGNETIC FIELD

The previous chapters described sensitive electrical techniques to detect the donor bound exciton optical transition in microfabricated silicon devices, down to a spatial resolution of 2 µm and addressing as few as 2000 donors, as well as analysing the crucial strain induced spectral shifts. One of the long term goals of this technique is to allow the read out the Si : P donor spin state. To this end, this chapter explores microscale D^0X devices in magnetic fields to split the donor spin states. Then, the pumping and readout of the donor electron spin state is investigated under continuous pumping, and transient polarisation schemes are attempted and discussed.

Although the D^0X transition has a narrow linewidth for an optical transition, and the hyperfine splitting of the donor spin is just about discernible in ^{28}Si isotopically purified samples [18, 21], the magnetic field sensitivity is far below that of magnetic resonance techniques. The D^0X transition's true importance in the fields of magnetic memory and sensing is instead as a readout for the donor spin state. Its capacity to spin-selectively ionise donors leading to spin polarisation make it a promising spin initialisation and readout technique, as demonstrated by Lo [23], Franke [24] and Ross [26].

6.1. STRAINED BOUND EXCITONS IN A MAGNETIC FIELD

The donor bound exciton hole state has an anisotropic g-tensor, as described in Equation 2.51. For magnetic fields aligned with the principal crystal axes, $\boldsymbol{B} \parallel [100]$, the Hamiltonian is diagonal, while for other orientations, the g-tensor displays off-diagonal components. On top of this, strain has to be considered together with magnetic field, as the Pikus-Bir terms from Equation 2.54 cause splitting and mixing of the hole spin states. The whole Hamiltonian $H_{\mathrm{ze}} + H_{\mathrm{pb}}$ must therefore be solved, which is best done numerically apart from a few specific diagonal cases. Here, the analysis is limited to the two configurations where the magnetic field is perpendicular $\boldsymbol{B} \perp \boldsymbol{\sigma}$ and parallel $\boldsymbol{B} \parallel \boldsymbol{\sigma}$ to the strain principal axis. Practically, as discussed in Section 5.3, these devices generally present quasi-uniaxial strain along the electric field axis, in the device plane. Therefore the perpendicular magnetic field is applied normal to the sample surface, as shown in Figure 6.1c, while the parallel field is applied along the samples short axes, as shown in Figure 6.1a,b.

The Montana S100 cryostat is configured without coil magnets, therefore the field is applied via high strength N42 and N52 neodymium ($Nd_2Fe_{14}B$) permanent magnets, limiting the analysis that can be performed to specific field strengths without the ability to sweep the field. Neodymium is chosen due to its high magnetisation, although it displays strong thermal dependence, with changes in magnetisation strength and axis rotations. Samarium Cobalt(SmCo) magnets were also considered due to their greater thermal stability, however sufficient magnetisation density could not be achieved.

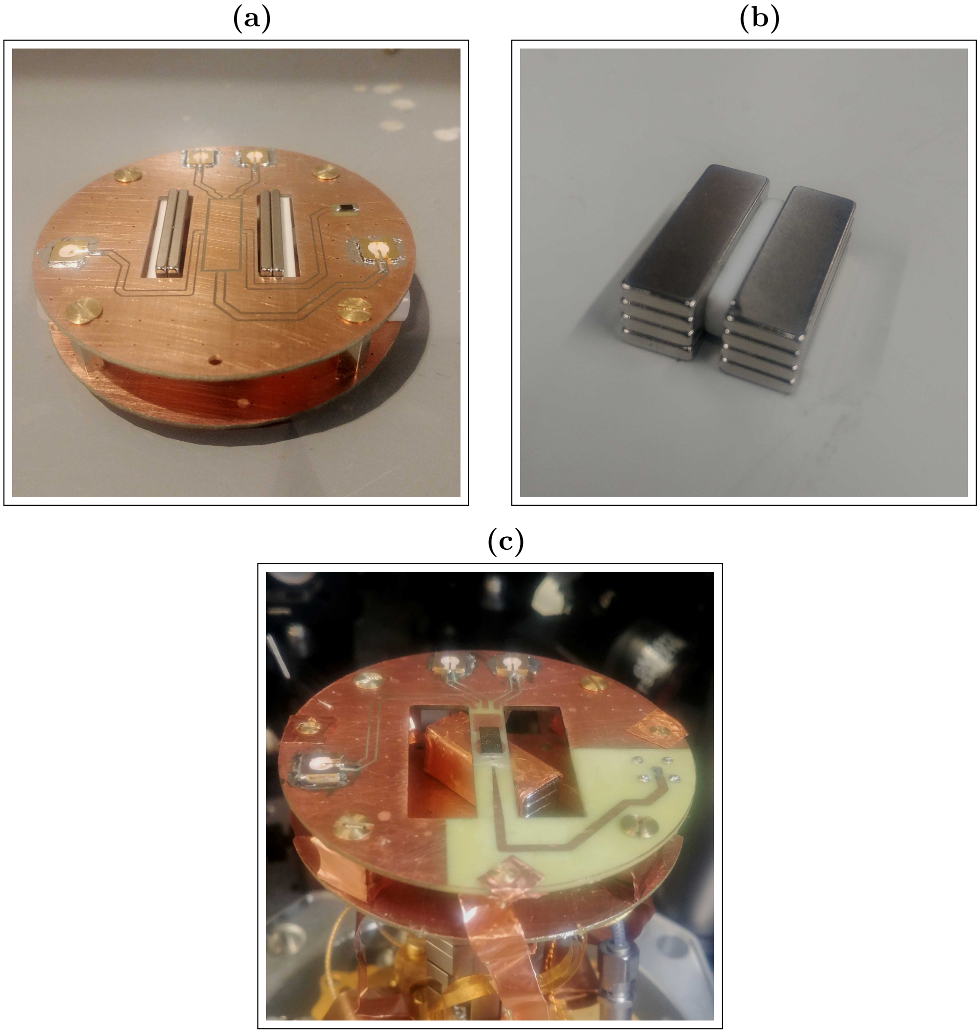

Figure 6.1: Custom-built sample mount configurations with neodymium permanent magnets (a) $\boldsymbol{B} \parallel \boldsymbol{\sigma}$ parallel magnetic field configuration, (b)$\boldsymbol{B} \parallel \boldsymbol{\sigma}$ high strength and low profile parallel magnetic field configuration, (c) $\boldsymbol{B} \perp \boldsymbol{\sigma}$ perpendicular magnetic field configuration.

Figure 6.1 shows the three of the experimental magnet configurations employed, with (a),(b) for parallel and (c) for perpendicular. The (a) configuration, consisting of a parallel plate configuration held in place by custom PLA 3D printed holders, was initially explored due to the attractive homogeneous field at the centre, however there was not enough clearance above the sample from the cryostat radiation shield, and the device had to be pushed to the edge, where less homogeneity is expected. Furthermore, the necessary separation of the magnets resulted in low field strengths of less than 100 mT. A simpler configuration was chosen instead, as shown in Figure 6.1b, where two stacks of vertically polarised magnets are placed side by side, separated by a PLA spacer, with opposite polarisations. This allows placement of the magnets right below the sample, only separated by the thickness of the substrate and PCB. It was observed that, due to the small, micrometre illuminated area, magnetic field homogeneity is not a huge concern, as any inhomogeneity occurs over a far larger scale than the 2 µm laser spot size. Indeed, the magnetic field spectra obtained display linewidths comparable to those at zero field.

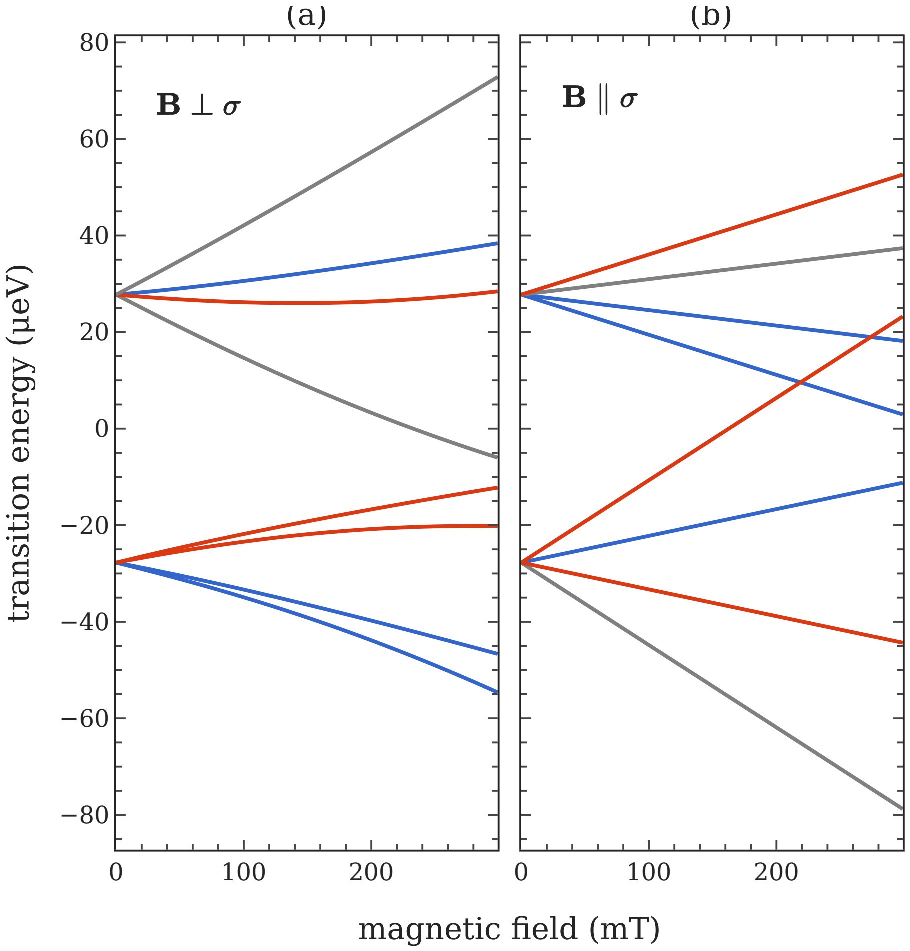

Figure 6.2: Simulation of the device strained D^0X transitions under a variable magnetic field (a)$\boldsymbol{B} \perp \boldsymbol{\sigma}$, (b)$\boldsymbol{B} \perp \boldsymbol{\sigma}$.

The vertical configuration is fairly straightforward, with a stack of rectangular magnets directly below the device, achieving magnetic fields up to 200 mT, with potential for more with the use of thinner PCBs and extra magnet stacks added laterally. In all cases, the magnet configuration was first simulated to achieve the rough magnetic field needed and tested after mounting with a Gauss meter at the sample position. Of course, this technique is not overly accurate, and variations in the region of 10–20 % were observed from the target field. One approach to solve this is usually to pair a strong permanent magnet with a low strength electromagnet outside the cryostat, thus having a strong magnetic field with some tunability without the cumbersome cryogenic electromagnet cooling requirements. This was not attempted due to concern that the delicate piezo stack would be damaged by the magnetic force between the on-stack magnets and off-stack electromagnet. The close-working distance objective right above the optical window would have further complicated this route.

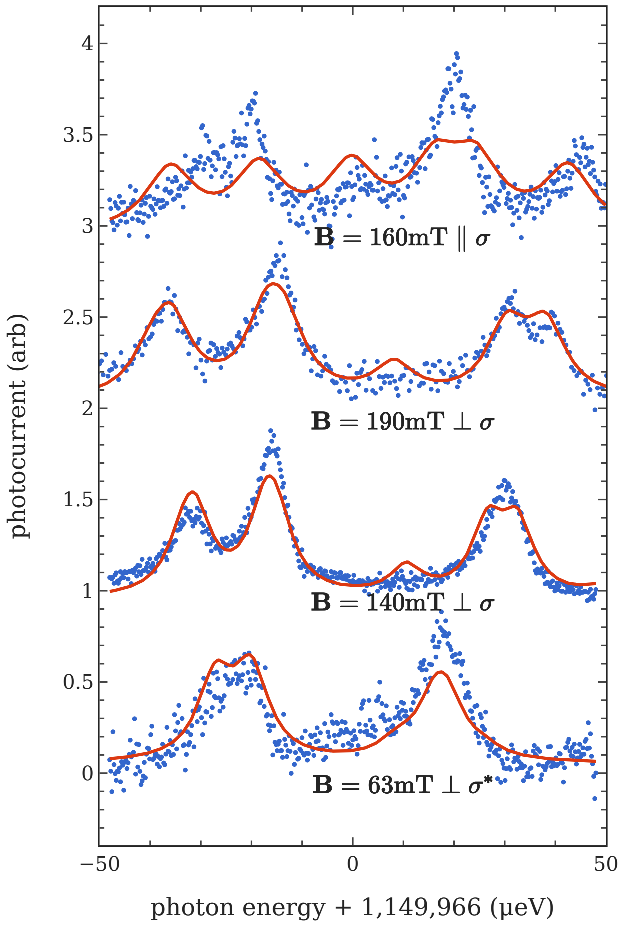

Figure 6.3: Experimental D^0X spectra under variable magnetic field conditions, fitted to a theoretical model to estimate the magnetic field strength.

Several experimental magnetic field configurations were attempted, with three notable spectra shown in Figure 6.3. The two magnetic field configurations lead to very different splittings of the light and heavy hole states, which are shown in Figure 6.2, fitted to a spectrum model with strain parameters derived in Chapter 5 with a variable multiplicative factor, and a magnetic field with fixed direction and variable magnitude. The $\boldsymbol{B} \perp \boldsymbol{\sigma}$ spectra show a very good agreement with the theoretical model of Figure 6.2, with essentially three resolved peaks each composed of a pair of transitions. At the highest magnetic field of 190 mT, even the zero-field heavy hole splitting is observed. A partially forbidden peak is not observed; however this may realistically be due to its low amplitude. The spectrum for the parallel $\boldsymbol{B} \parallel \boldsymbol{\sigma}$ correctly shows five visible peaks, with the most prominent one composed of two overlapping peaks. However, the fit to the theoretical model is not as conclusive, with a stronger splitting of the zero-field heavy hole peak expected. The lower splitting may possibly be explained by some degree of unaccounted shear strain in the device plane, which is not surprising given the complex nature of micro-fabrication. Furthermore, the signal to noise ratio was observed to be markedly worse for the parallel configuration compared to the perpendicular one, although magnetoresistance would suggest the opposite, with a worse signal where $\boldsymbol{B} \perp \boldsymbol{E}$. This is also not due to polarisation of the donor electron spin, as stronger polarisations were observed in the perpendicular configuration.

Overall, the two magnetic field configurations result in very different spectra, but in all cases, it is clear that the strongest, more defined splitting between the donor electron $m_S = |-\frac{1}{2}\rangle$ and $m_S = |+\frac{1}{2}\rangle$ states is observed in the zero-field heavy hole peak. Furthermore, the perpendicular $\boldsymbol{B} \perp \boldsymbol{\sigma}$ Figure 6.2a configuration displays a very attractive double pair of peaks, limiting the loss of signal expected from the two peaks splitting into six.

6.2. Dual Laser Pump-probe Donor Spin Polarisation

As discussed in the introduction to this chapter, the stated goal of D^0X photoconductive readout is to perform hybrid magnetic resonance manipulation and readout of phosphorus donor electron spins in microscale devices. Substantial difficulties were however encountered, leading to the suspicion that donor spin polarisation may not be stable and long lived, contrary to expectations from past work and expected donor electron relaxation times, which at 3 K should be as high as seconds [111]. To investigate the issue, a dual laser setup was devised to analyse polarisation of the donor spin via a pump-probe experiment, without the extra complication of microwave transmission as well as allowing for the detection of any short-lived polarisation via continuous optical pumping. All the experiments presented here were performed using the multi-laser benchtop optical setup of Section 3.3.3. with the 0.65NA objective.

In the simplest configuration, the continuous pump probe setup consists of a fixed wavelength pump laser and a scanning probe laser. The sequence is shown in diagram of Figure 6.4. A pump laser is on continuously at a relatively

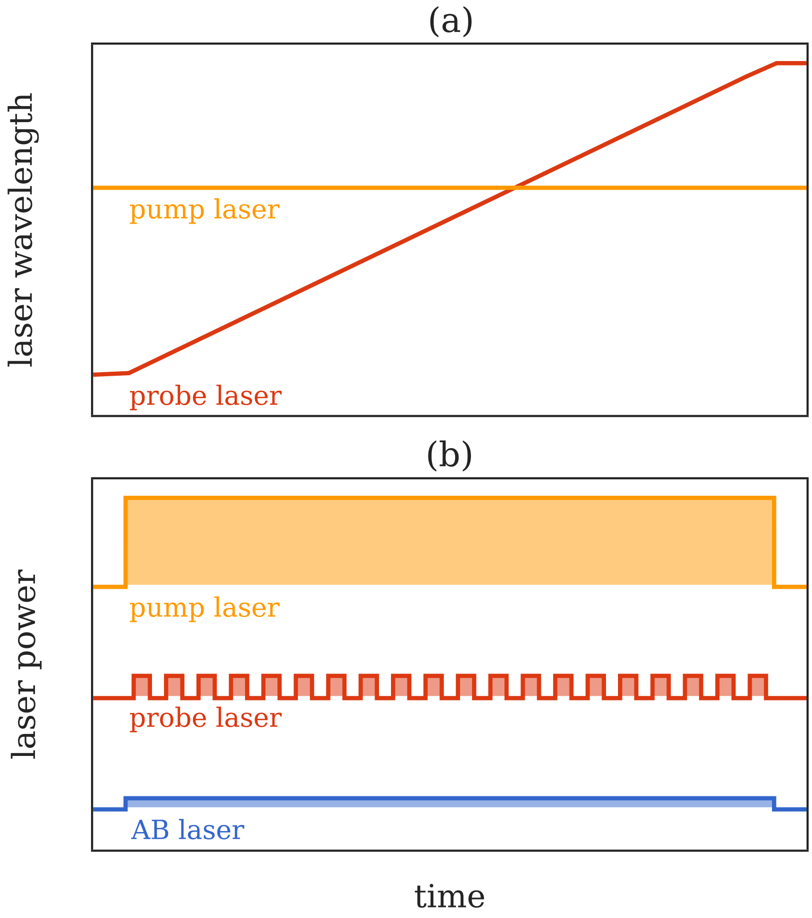

Figure 6.4: Continuous pump and pulsed probe dual laser pulse sequence. (a)The pump wavelength is fixed on a resonance while the probe is swept across the spectrum, (b) The pumps is left on continuously, while the probe is pulsed, at a lower power, so that the probe signal can be differentiated through amplitude demodulation. The above bandgap laser or lED is left on continuously.

high power, usually in the range of 100 µW, and is tuned to a fixed wavelength which is either off-resonance for reference, or on one of the resonance peaks of interest. The probe laser is set to a lower power of ∼5 µW, and pulsed with an acousto-optic modulator (AOM). The pulsing is not strictly necessary, but helps significantly in isolating any noise due to external factors, as well as drifts or fluctuations in the pump power. This is effectively a form of amplitude modulation detection. The probe laser wavelength is also swept, thus yielding the D^0X spectrum under the specific pumping conditions. This experiment is then repeated for multiple pumping wavelength, nominally on each resonance peaks in addition to one off-resonance wavelength for reference. The idea here is that any polarisation will be detected, however short, as the pumping is continuous. There is a catch here, in that pumping may also lead to the simple depopulation of the D^0 state, regardless of strain and either via resonant D^0X excitation or direct donor ionisation. This can be distinguished from donor spin polarisation as it would lead to an equal suppression of the amplitude of all the peaks, while donor spin polarisation would suppress the pumped peak and bolster the peak corresponding with the opposite donor spin state.

A small degree of polarisation is indeed observed under a perpendicular magnetic field configuration, and Figure 6.5 shows a D^0X spectrum under multiple pumping wavelengths at an estimated magnetic field of 140 mT, corresponding to a donor Zeeman electron spin splitting of ~3.9 GHz. Most importantly, the proof that this is donor spin polarisation is that pumping a specific peak not only suppresses the probe amplitude of the pumped peak, but it bolsters the amplitude of another peak, which cannot be explained by simple D^0 state depopulation. Pumping on all three peaks lead to a degree of donor spin polarisation. The two leftmost are expected, and indeed yield the strongest polarisation, as each corresponds to a matching pair of transitions from the $|+\frac{1}{2}\rangle$ and $|-\frac{1}{2}\rangle$ transition respectively. The zero-field light hole peak however should not lead to polarisation, as it includes overlapping transitions from both the electron $|+\frac{1}{2}\rangle$ and $|-\frac{1}{2}\rangle$ donor spin states. The observed degree of polarisation can most likely be explained by the dominance of one of these two transitions over the other. This is confirmed by the observation that when the $|-\frac{1}{2}\rangle$ peak at ~0.5 µeV is pumped, the rightmost peak is slightly skewed to the right, compatible with the inverted overlapping peak composition shown in Figure 6.2.

Some degree of spectral hole burning is also observed at the pump wavelength, with a hole linewidth of ~0.5 µeV. For comparison, Yang observed a spectral hole of ~70 nm in natural silicon [15] and a homogeneous linewidth of 20 neV in ^{28}Si [19]. The broadening may be due to the higher temperature of 3 K against Yang's 1.2 K, or power broadening, as Yang's pump power density is much lower, electric field broadening as discussed in section 4.1.4, or the high strain. Nonetheless, most of the pumped amplitude appears to be on the entire inhomogeneously broadened peak. It also cannot be excluded that the spectral hole burning is simple D^0 state depopulation, which is faster and does not require the slower electron capture process, while the slower donor spin polarisation encompasses the whole inhomogeneous peak.

Having established that some donor spin polarisation, however short, exists, the next step is to investigate any dependence to experimental parameters to understand what may possibly be limiting its lifetime. The next sections systematically explores the effect that major experimental parameters have on donor spin polarisation.

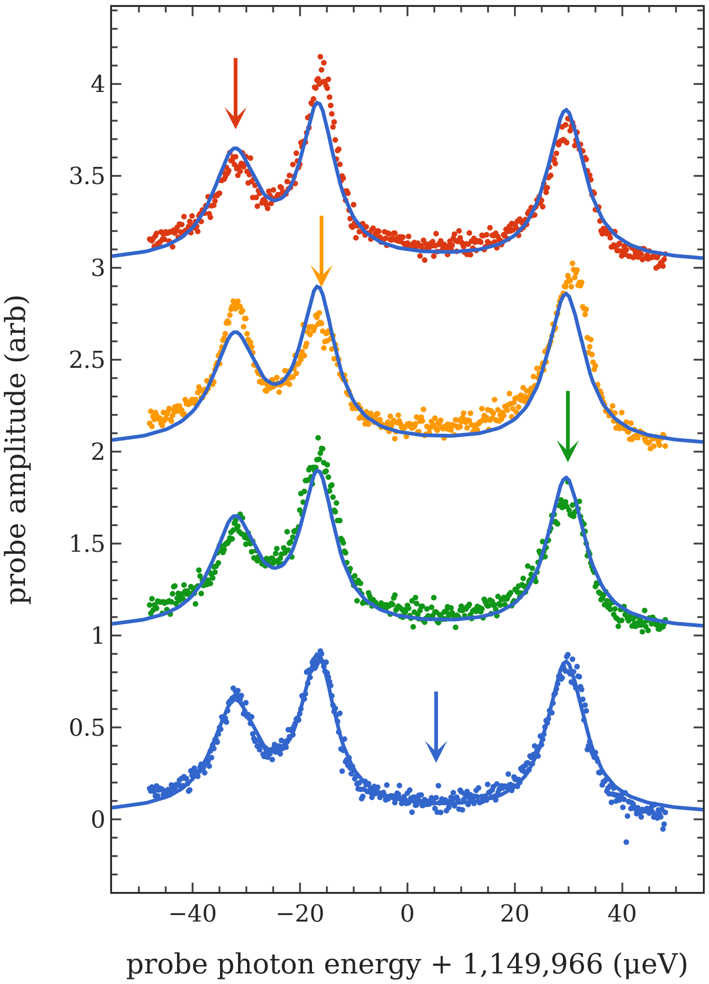

Figure 6.5: Two laser, direct current D0X photoconductive measurement under continuous pump and pulsed probe, pumped fixed wavelengths ● 1078.150nm, ● 1078.127nm, ● 1078.170nm, ●1078.185nm, indicated by the matching color arrow and swept probe wavelength. A small amplitude pumping from one peak to the other is observed. A fit of the off-resonance pump spectrum (—) is plotted under every curve for reference.

6.2.1. TEMPERATURE DEPENDENCE OF DONOR SPIN POLARISATION

The first experimental parameter to consider is the sample temperature. Although the S100 cryostat is capable of platform temperatures as low as 2.8 K, the sample temperature may be significantly higher due to imperfect heat conduction and the large mass and surface area of the dual PCB stack setup, and despite the great care that was placed in crafting robust oxygen-free copper thermal joints: the ribbons that can be observed at the bottom of Figure 6.1. In principle, temperature is unlikely to be an issue here, as the T_1 relaxation time of the Si : P donor electron spin was observed to be as high as 1 ms even at 10 K, rising to over a second at 3 K [111]. Nevertheless, this is an important sanity check of the donor spin polarisation.

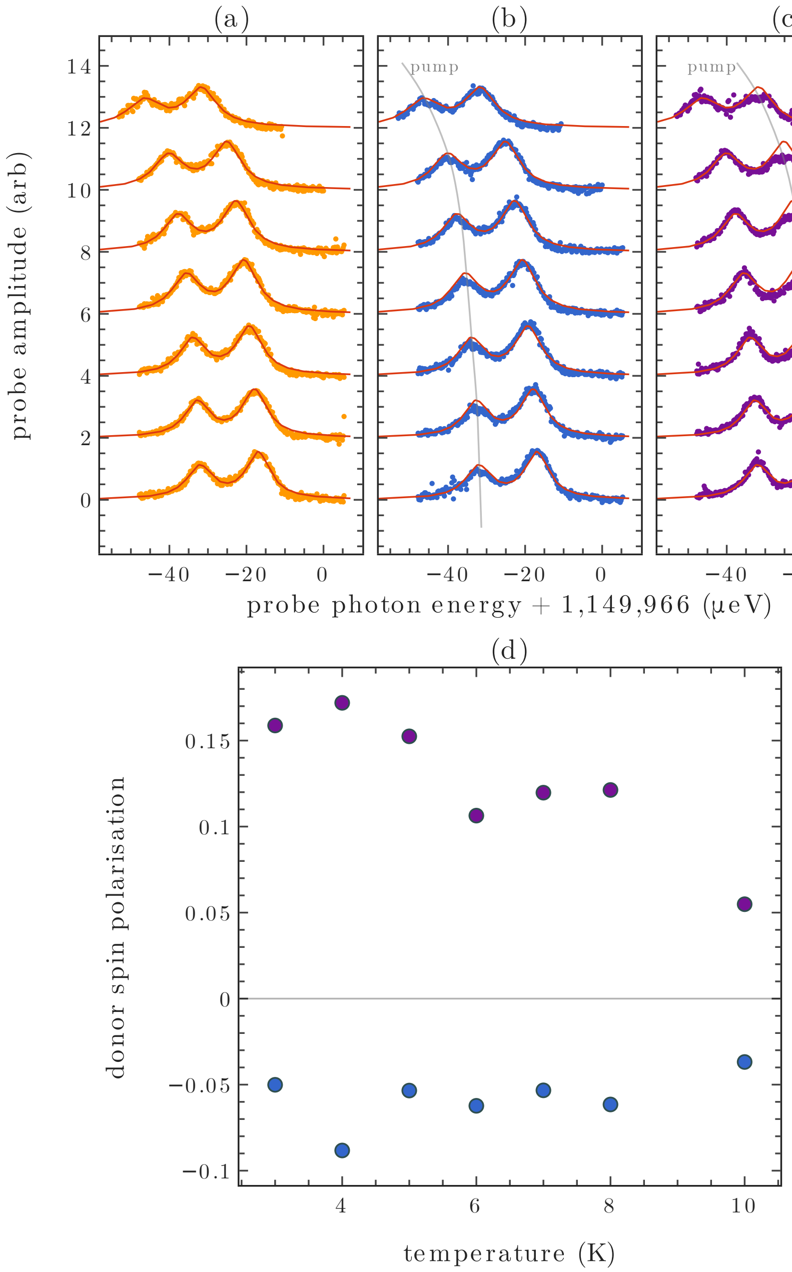

Figure 6.6: Temperature dependence of CW D^0X induced donor electron spin polarisation. (a) Off-resonance pump (b) Left peak pump (c) Right peak pump (d) Temperature dependence of the D^0X induced donor spin polarisation, calculated from Equation 6.1.

The experiment is performed by repeating the CW pump-probe sequence of Figures 6.4 and 6.5 at multiple platform temperatures, between the base 3 K and 10 K, where a significant decrease in SNR prevented the recording of higher temperature setpoints. The experiment is started at base, as thermalisation is faster than cooling, and the temperature is set manually on the S100 cryostat's PC. A settling time of ~5 min is then allowed for full thermalisation, and the CCD image is verified to make sure no significant sample shift has occurred. Only the split zero-field light hole peaks are pumped and recorded, as the zero-field light hole peak is of little interest due to its mixed donor electron m_S composition. As the $\mathrm{D}^0\mathrm{X}$ peak energies shift with temperature due to the bandgap temperature dependence, at each temperature step the off-resonance pumped sweep is first performed. The resulting spectrum is then used to determine the peak energies, and the sweep is repeated with pumps on the measured $|+\frac{1}{2}\rangle$ and $|-\frac{1}{2}\rangle$ peaks centres.

The polarisation generated by each pump is calculated from Equation 6.1 as the difference between the relative changes in population of the two peaks.

$$\Delta P = \frac{1}{2}\left(\frac{A_{\text{p1, pump}} - A_{\text{p1, no-pump}}}{A_{\text{p1, no-pump}}} - \frac{A_{\text{p2, pump}} - A_{\text{p2, no-pump}}}{A_{\text{p1, no-pump}}}\right) \tag{6.1}$$

This results in a polarisation change only where the peak amplitudes move in opposite direction, thus eliminating any non-spin related spectrum saturation effect.

Figure 6.6 shows pumped $\mathrm{D}^0\mathrm{X}$ spectra at increasing temperatures. A dependence of the donor spin polarisation is indeed observed, with an inverse relation between temperature and polarisation. It also appears that the polarisation has fully saturated below 5 K, suggesting that although a factor, the sample temperature is not the cause of short T_1 times. Figure 6.6(c) further shows an apparent increase in the spectral hole linewidth with increasing temperature, suggesting that the homogeneous line may still be thermally broadening even at base temperature.

The energy shift of the transition energy can also yield important information about the system. Here, only a portion of the spectrum is recorded, which is still useful as the energy shift is expected to be spin independent. The $\mathrm{D}^0\mathrm{X}$ transition energy shift is entirely due to the bandgap temperature dependence. Cardona observes a quartic relationship $E_\mathrm{g} = E_{\mathrm{g}0} - AT^4$ [167] in the limiting range $T \to 0$ below ~5 K, which does not much well with the examined range 3–10 K. Other work finds a quadratic relation at higher temperatures [41, 168]. Mansir [28] finds a quadratic $\mathrm{D}^0\mathrm{X}$ energy-temperature in the range 5–17 K dependence with a more reliable temperature sensing setup than the one employed in this work, with a sample thermometer and most importantly a helium filled sample space, which generally leads to more reliable thermalisation.

Figure 6.7 shows the temperature dependence fit to a quadratic equation and one with a free power parameter. The quadratic field is quite reasonable and giving a quadratic factor of 0.160(4) $\mu\mathrm{eV}^2\,\mathrm{K}^{-1}$, comparable to the 0.215(6) $\mu\mathrm{eV}^2\,\mathrm{K}^{-1}$ by Mansir. A fit with a free exponent yields a dependence $E_{\mathrm{D}^0\mathrm{X}} \propto AT^m$ with $m = 2.45$ and $A = 0.0592(4)$, which is not particularly far away from Mansir's model, especially given the reduced range, and is rather

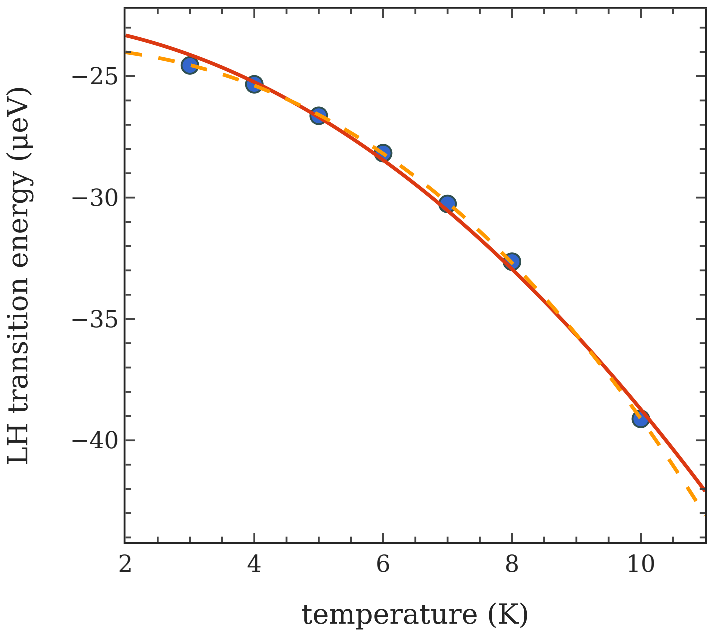

Figure 6.7: Temperature shift of the D^{0}X light hole transition energy. • Experimental data fitted to a — $E = E_0 - AT^2$ quadratic, and — $E = E_0 - AT^m$ function.

in between the higher temperature quadratic model and the low temperature quartic relation by Cardona [167]. Overall, there are some small divergences suggesting that some thermalisation occurs, however they are small enough to conclude that this effect is small, and the temperature of the sample does not significantly differ from the platform temperature.

6.2.2. ELECTRIC FIELD AND DONOR SPIN POLARISATION

The presence of an electric field is intrinsic to all hybrid optical-electrical D^{0}X measurement techniques. Long lasting donor spin polarisation has been shown in low field photoconductive setups [23–25], but electric field has also been suggested as potentially source for donor spin relaxation [169]. The discussions from Chapter 4 on donor impact ionisation further suggest the a potential competing, spin-independent source of donor ionisation [170].

The issue of electric fields is particularly relevant in microscale devices as the comparatively high voltages and low contact separations can easily lead to moderate electric field strengths upwards of $10^3\,\mathrm{V\,m^{-1}}$. Electric fields were also observed in Chapter 4 to cause shifts in the D^{0}X transition energies as well as broadening of the transition lines.

Similarly to the temperature sweep, the effect of AC electric fields is investigated by repeating a continuous wave pump-probe polarisation experiment

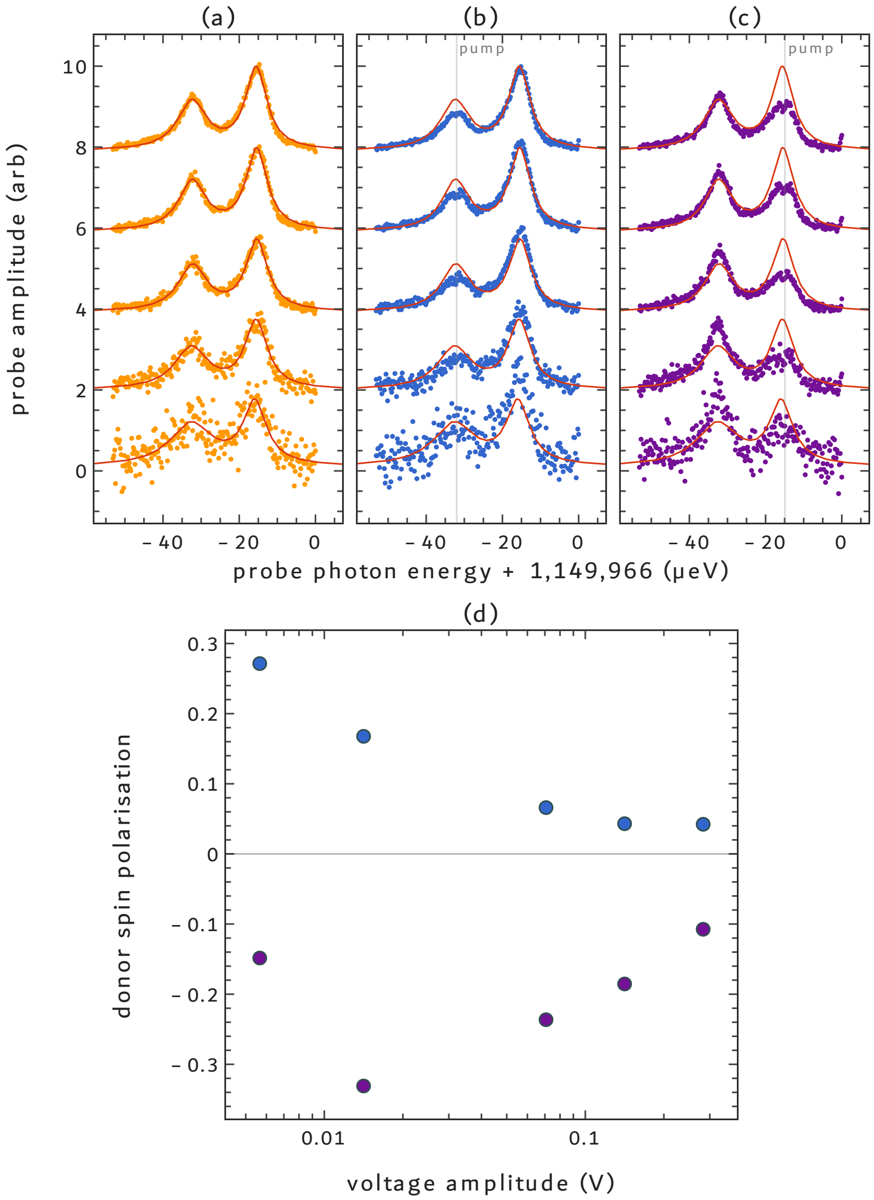

Figure 6.8: Continuous pump-probe donor spin polarisation under variable AC measurement voltage. (a) resonant peaks under off-resonance pump, (b) peaks under left peak pump (c) peaks under right peak pump (d) polarisation dependence on voltage amplitude. The polarisation is calculated from Equation 6.1.

under multiple voltage amplitudes for the AC current measurement, with V_{RMS} in the range 4–500 mV. Lower voltages were not explored due to the extreme drop in SNR, leading to prohibitively long experimental times.

Figure 6.8 shows a strong dependence of donor spin polarisation on voltage amplitude, reinforcing the suspicion that the electrical setup may affect donor spin polarisation. The highest amplitude of 300mV displays almost one third of the spin polarisation observed under a 5mV voltage amplitude, which is quite concerning. Furthermore, it is not clear whether the effect has saturated even at the lowest voltage amplitude, and it is certainly not realistic to work with lower voltages due to the SNR limitations: the lowest measurement is already visibly noisy. Regarding the source of the electric field induced relaxation, it was discussed extensively in Chapter 4 how the presence of shallow donor impact ionisation may generate a competing ionisation mechanism. The long-time constants observed, however, would suggest that the ionisation rate itself would be quite slow, in the range of milliseconds and certainly not fast enough to compete with the continuous optical pump. It may however be possible that a similar mechanism also causes faster relaxation without donor ionisation, via a non-ionising collision with a donor. The main evidence excluding it comes from the lack of a dependence on carrier density observed in Section 6.2.2.

Overall, it is unclear if this is a fundamental issue, although it certainly seems so from the available evidence. One potential solution could be to pulse the detection source voltage itself. This adds significant complexity as the lock-in amplifier in use requires a continuous source for phase lock-in and adds complications with the continuous low-pass filtering, however with the right hardware this is certainly achievable. Furthermore, due to the long transients observed in Chapter 4 it is not even necessary to collect the electrical signal during probe laser illumination, as the generated photoconductive response would last for a few milliseconds depending on the level of above bandgap illumination.

6.2.3. POWER DENSITY AND DONOR SPIN POLARISATION

The next key parameter which is a main theme throughout this work is the power density of the resonant laser. Previous D^0X work employed laser beam areas orders of magnitude larger than those achieved in this work. Specifically, of the works that achieved D^0X induced donor spin polarisation, Lo et al [23] employed a power density of $3 \times 10^3\,\mathrm{W^2\,m^{-1}}$, and Yang [19] used power densities up to $2.8 \times 10^4\,\mathrm{W\,m^{-1}}$. With an illumination diameter of only $\sim$1.5 µm, the power densities used throughout most of this work are in the much higher range of 10^4–$10^7\,\mathrm{W\,m^{-2}}$. Specifically, the pump power of 100 µW used throughout this chapter corresponds to a power density of $1 \times 10^7\,\mathrm{W\,m^{-2}}$. In part this is offset by the larger linewidths of the $^{\mathrm{nat}}$Si samples, however it still presents potential pitfalls such as power broadening, which is observed by Yang [15] at much lower power densities, albeit relative to the very narrow ^{28}Si homogeneous linewidth. Ross [26, p. 204] also suggests that high power densities in the coherent regime may lead to higher error rates due to the non-resonant direct ionisation. Contrary to expectations, however, the laser power electrical response does show signs of saturation even at high power, as shown in Section 4.1.3.

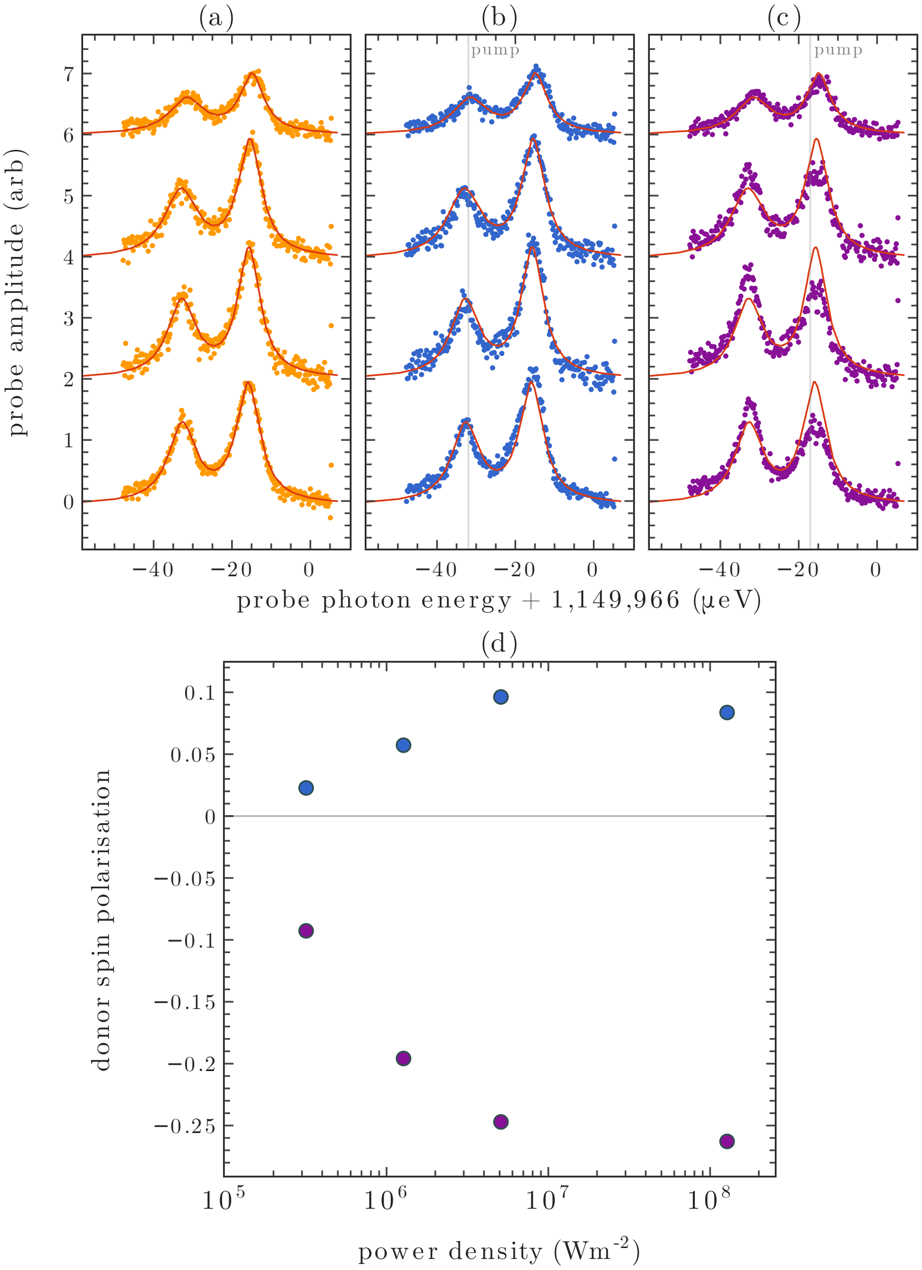

Figure 6.9: Pump laser power density dependence of donor electron spin polarisation under continuous D^0X resonant pump illumination. (a) resonant peaks under off-resonance pump, (b) peaks under left peak pump (c) peaks under right peak pump (d) polarisation dependence on pump laser power density, calculated from Equation 6.1.

The most important consequence which must be considered is the possibility that illumination is strong enough to quickly eliminate any donor spin polarisation before any transient may be measured. Another one is saturation of the D^0X transition, however the power dependence observed in Chapter 4.1.3

suggests that is not the case. Overall, it is important to determine how this new high-power regime affects the donor spin polarisation. Mostly, however, this section serves to settle the question of whether the limited polarisation observed is due to short T_1 times or fast optical population inversion.

To establish the effect of power density on donor spin polarisation, the three-wavelength-pump polarisation experiment described in Section 6.2 is repeated under fixed pump and probe power but varying the laser spot size. This is achieved by backing up a lens in the lasers' common optical path and moving it backward to slightly modify the optical path. The technique is indeed not perfect, but it showed a less pronounced airy disk than simply backing up the objective off the focus. Power density could also be varied with a fixed laser beam diameter and a varying the power of both lasers, while maintaining the power ratio, for example placing a neutral density filter in the common optical path. However, this is technically more difficult, as the signal strength drops significantly with falling power. Varying the beam diameter instead ensures that a lower power density is compensated by a larger number of illuminated donors, at least until the laser spot covers the whole implantation area. Of course, this introduces the complication that the donor population changes within the experiment, but Figure 5.13 shows that in a $20 \times 50\,\mu\text{m}$ device there is large area of donors under near identical strain conditions at the centre, so the population is mostly similar. This is confirmed by Figure 6.9, displaying a mostly identical lineshape under varying beam diameters. This was performed at diameters from the minimum of $1.5\,\mu\text{m}$ to a maximum of $20\,\mu\text{m}$.

Contrary to expectations, Figure 6.9 shows that the degree of donor spin polarisation increases with power density. This settles that the issue is short T_1 relaxation, and not fast optical population inversion, as the latter would have resulted in a flat or inverse relationship. Still, it may be possible that the issue of power density becomes relevant again under longer T_1 relaxation times, so the issue of power density must be considered a sensitive topic until lasting donor spin polarisation under high power D^0X excitation is demonstrated.

Previous D^0X research has employed collimated laser beams and laser power densities in the low range of 10^1–$10^5\,\text{W}\,\text{m}^{-2}$. Specifically, Lo [23] and Franke [24] worked at power densities of $3 \times 10^3\,\text{W}\,\text{m}^{-2}$ in ^{28}Si, while Yang et al. used $2.8 \times 10^4\,\text{W}\,\text{m}^{-2}$ [15], and specifically comment that 100-fold reduction in power does not affect the polarisation obtained, which is in the range of 60–90 %. Here, it is observed that below the polarisation falls steeply under power densities of $5 \times 10^6\,\text{W}\,\text{m}^{-2}$. It should be noted that most previous D^0X magnetisation experiments focused on isotopically enriched ^{28}Si, which has a far smaller homogeneous linewidth of 20 neV against the 70 neV of 70 neV, thus requiring lower driving powers. However, this does not justify the magnitude of the difference in the range of power densities for spin magnetisation. Furthermore, Yang et al [19] have also demonstrated donor spin polarisation in $^{\text{nat}}$Si, albeit with photoluminescence detection.

6.2.4. Above Bandgap illumination and Donor Spin Polarisation

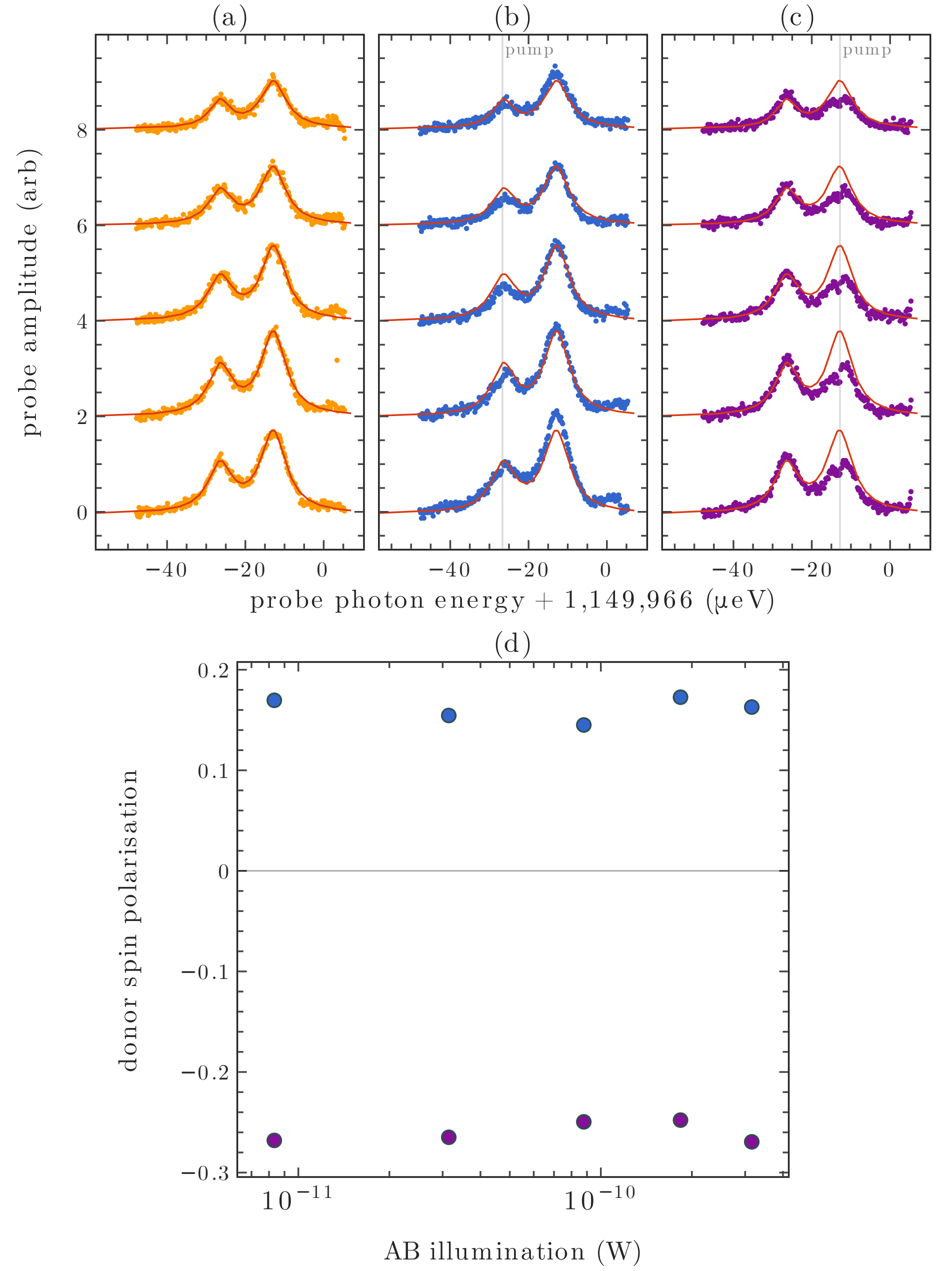

Figure 6.10: Continuous D^0X pump donor electron spin polarisation dependence on above bandgap illumination. (a) resonant peaks under off-resonance pump, (b) peaks under left peak pump (c) peaks under right peak pump (d) polarisation dependence on above bandgap illumination power, calculated from Equation 6.1.

Finally, the effect of above bandgap illumination on donor spin polarisation is explored. The carrier generation of above bandgap light has generally been regarded as an important component of D^0X detection by the existing literature. Mostly, above-bandgap illumination is used to increase the carrier density, to increase the rate recombination and the electrical response time, as shown in Chapter 4. A side effect here is that the free carriers may interact with the frozen electrons, causing decoherence. However, the complete lack of carrier and their electrical shielding and balancing may also lead to an increase in charge noise. The issue is verified by repeating the continuous pump-probe experiment described in Section 6.2 under variable levels of above bandgap illumination.

Figure 6.10 shows a completely flat degree of polarisation over a large range of above bandgap illumination, thus suggesting that it does not appear to affect donor spin polarisation in any way, with a fixed donor spin polarisation under above-bandgap powers in the picoWatt region.

There is also an important secondary conclusion to this result, as the independence of polarisation on carrier density would suggest that the electric field induced relaxation observed in Section 6.2.2 is not a carrier effect, similar to donor impact ionisation. If it were so, an increase in the carrier density would have certainly reduced the level of donor spin polarisation, yet this is not observed.

6.2.5. TRANSIENT PUMP-PROBE DONOR SPIN POLARISATION

The previous sections have established the ability of a D^0X resonant continuous optical pump to polarise the phosphorus donor electron spin to up to almost $30\,\%$. The donor electron spin shows T_1 relaxation lifetimes as long as seconds3 K [111], so the expectation is that the spin population would persist once polarised. As suggested by the dependence on electric field, however, the measurement setup may be reducing this relaxation lifetime significantly, either directly or indirectly by quickly ionising donors irrespective of spin state. This section discusses unsuccessful attempts at exploring the transient properties of such polarisation by separating the pump and probe pulses. Figure 6.11 shows the simple pulse sequence used: The pump laser is a long, high-power pulse designed to ionise the population of the excited donor spin, thus polarising the spin population to the opposite state. The probe pulse is designed to measure the spin population. This still requires donor ionisation, which is necessary for photoconductive detection; however, the aim is to make ionisation slow enough that a transient is detected. A major concern is that the high illumination power density may invert any transient polarisation too quickly for detection, although Section 6.2.3 does not reinforce saturation concern, with polarisation decreasing with increasing laser power density.

The experiment is limited in timings by the pump laser shutter with a rise-time of ∼4 ms. A faster experiment would be possible with a single laser using

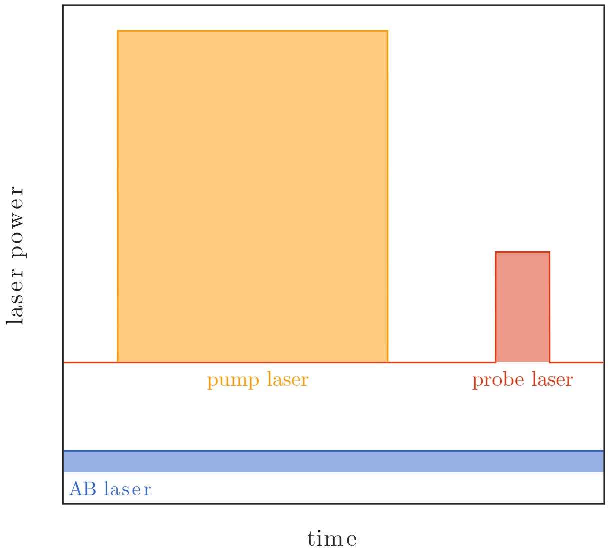

Figure 6.11: Pulsed pump-probe sequence for dual laser transient polarisation experiments. The two lasers are independent, and pulsed separately with a mechanical shutter and acousto-optic modulator (AOM) for the pump and probe respectively. The pump wavelength is fixed, and the probe is swept as shown in Figure 6.4.

the AOM as a shutter, however without different pump-probe wavelengths any polarisation would be drowned in secondary electrical effects.

Overall, this experiment failed to show any degree of donor spin polarisation, certainly reinforcing the conclusions of the previous sections that the donor spin is not long lived. Concerning future work, a dual AOM setup would allow the probing of much shorter pump-probe sequence down to the microsecond, although it would certainly be simpler to resolve the source of donor spin relaxation instead.

6.3. MAGNETIC RESONANCE

6.3.1. MICROWAVE ANTENNAS

The long-term goal of D^0X devices is the initialisation, coherent manipulation and readout of the donor spin. The D^0X optical transition addresses the initialisation and readout steps, coherent spin driving of the donor spin system is still best achieved by resonant microwave driving. Alternative schemes have been explored, such as dual optical driving [166] but the resonant microwave driving remains the leading technique of donor spin manipulation.

Two types of antennas are considered: a simple wire laid above the device and a PCB trace resonant antenna. They both have their advantages and disadvantages. The wire antenna can be placed much closer to the device, ap-

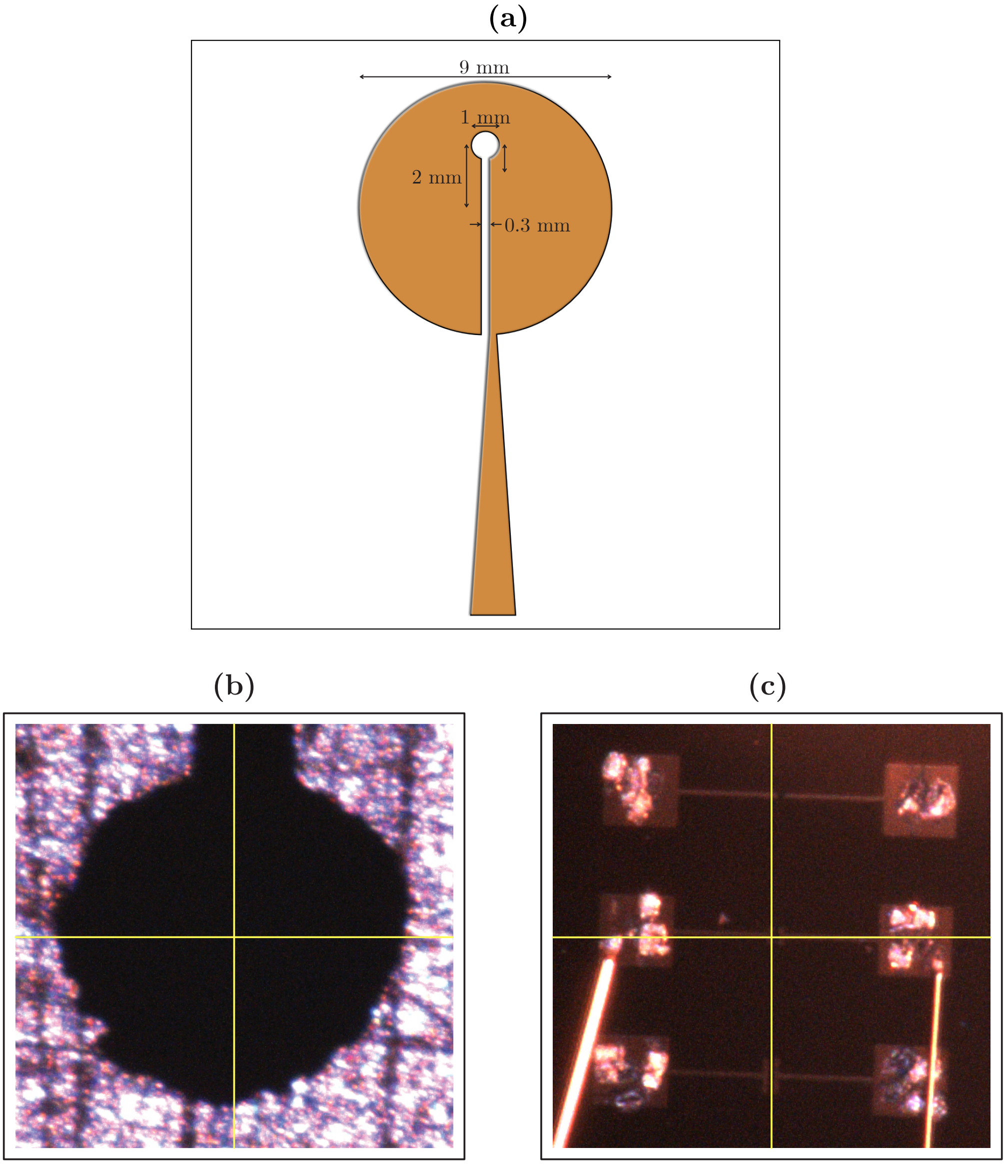

Figure 6.12: Planar broadband microwave antennna, proposed by Sasaki [171]. (a) Antenna design for $f_0 \sim 4.5$ GHz, (b),(c) Live microscopy images of the accurate placement of a D^0X device at the centre of a microwave using a microscope crosshair.

proximately 50–100 µm, but suffers from high impedance mismatch reflections at high frequency. On the other hand, the PCB planar antenna employed is a broadband wide area design aimed at homogeneous magnetic fields proposed by Sasaki [171]. The line tapering ensures impedance matching to the line impedance, thus reducing reflection losses. The resonance also yields roughly an order of magnitude amplification and a uniform, spatially focused B_1 field across the device space. The PCB antenna's distance to the device is also not particularly worse than the wire's, as the silicon's thickness is only 250 µm.

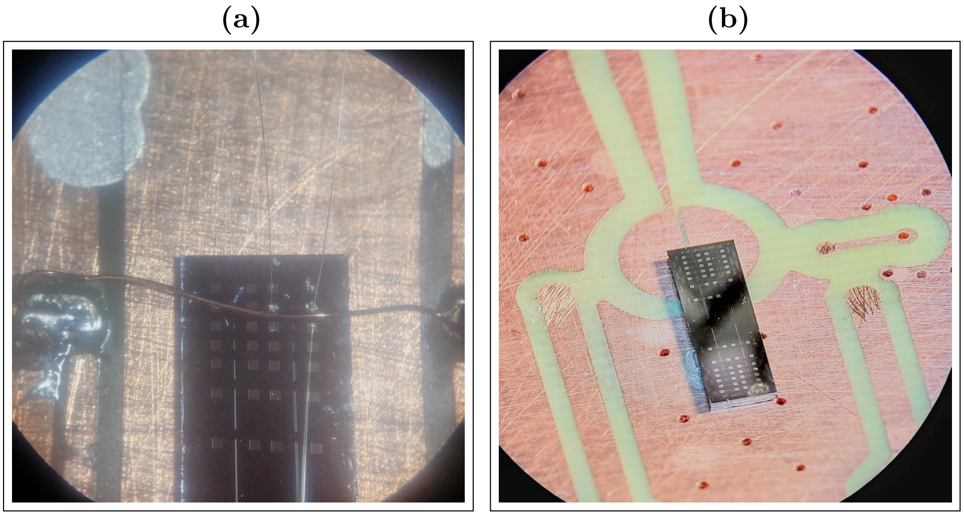

Figure 6.13: Microwave transmission experimental setup. (a) Near field transmission wire, (b) Broadband microwave antenna, original design by Sasaki [171].

The Sasaki antenna is modelled and simulated using the EM analysis software package CST Studio Suite, with the use of parametric sweeps of physical parameters to obtain the desired frequency range and impedance matching.

6.3.2. PEDMR

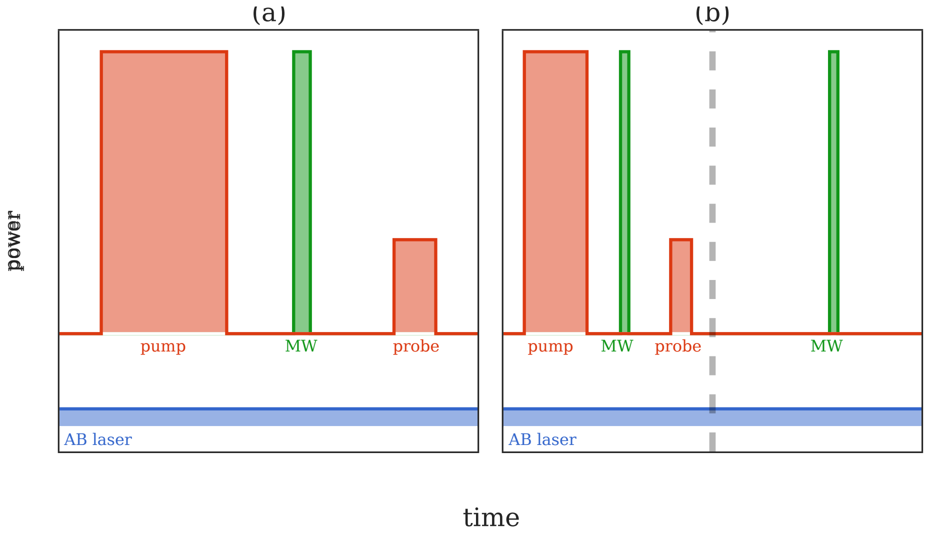

Figure 6.14: Laser-microwave pulse sequence for hybrid optical-microwave-electrical transient polarisation experiments. (a) Basic pulse sequence. (b) Split pulse sequence for the cancellation of the MW induced current offset: the sequence is repeated with and without lasers activated.

The hybrid optical-microwave scheme, shown in figure 6.14, consists of a three pulse sequence: initialisation, inversion and readout. As an example, if the D^0X resonant pump pulse ionises the $|+\frac{1}{2}\rangle$ population, the spin population is polarised into the $|-\frac{1}{2}\rangle$ state. A probe pulse on the pump wavelength, again on the $|+\frac{1}{2}\rangle$ would thus naturally present a reduced amplitude due to the spin polarisation. The microwave pulse aims to invert the population back to the $|+\frac{1}{2}\rangle$ state, with the probe pulse detecting any photoconductivity increase from the polarisation inversion.

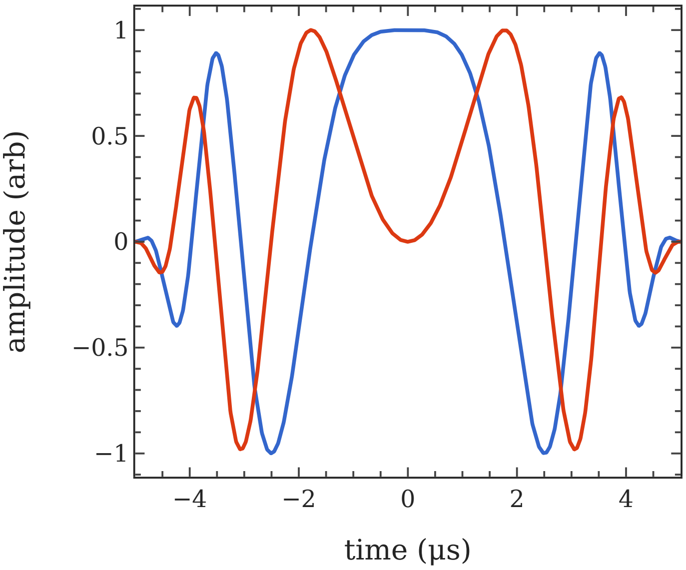

Figure 6.15: 10 µs, 10 MHz, WURST − 20 pulse. — real and — imaginary components.

Regarding the microwave pulse, an adiabatic WURST pulse is employed [172]. This is in part used to solve the issue of the unknown π inversion time constant, where an adiabatic pulse is more forgiving achieving population inversion over a wide range of amplitudes. Secondly, the WURST pulse allows for the broadening of the pulse bandwidth, which is necessary under longer pulses making the bandwidth smaller than the natural silicon phosphorus donor linewidth is 10 MHz [173].

$$\begin{aligned} \phi(t) =& \phi_0 + \frac{kt^2}{2} \\ A(t) =& A_0 \left(1 - \left|\sin\left(\pi \frac{t}{\tau}\right)\right|^n\right) \end{aligned} \tag{6.2}$$

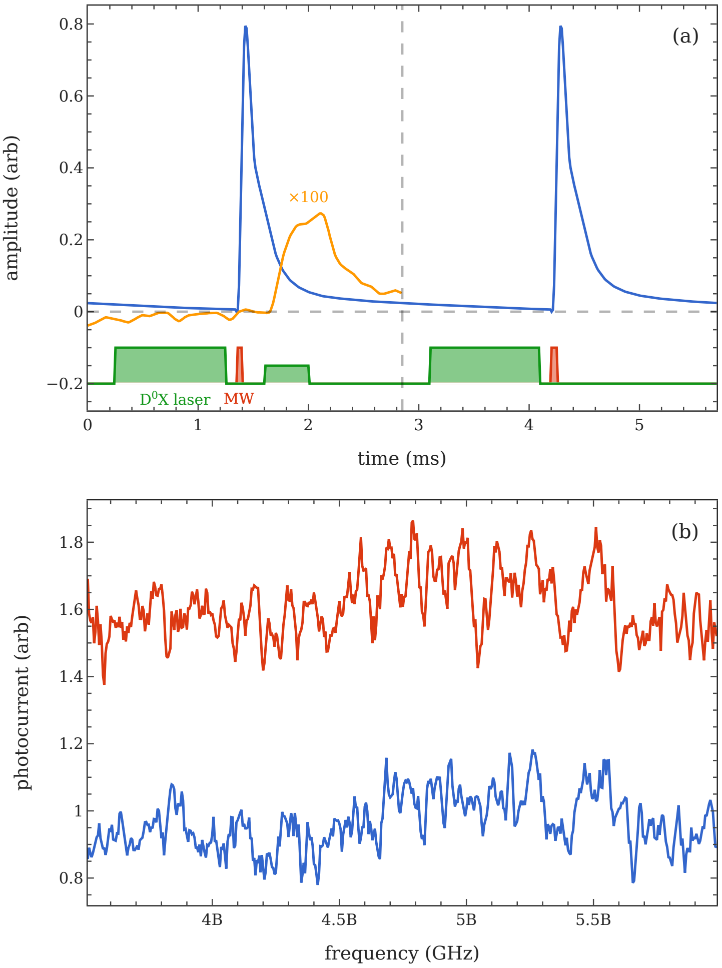

Figure 6.16: Microwave frequency PEDMR scan with dual period correction. (a) — raw and — corrected photocurrent transients; — laser and — microwave pulse sequence (b) Frequency dependent corrected photocurrent probe amplitude, — off-resonance and — on-resonance.

A single laser is employed, with its amplitude modulated with the fast AOM, thus allowing faster sequences than the dual laser setup which is limited by the slow mechanical shutter. Many attempts were made in multiple configurations, with both wire and planar antennas, low frequency and reflectometry detection, and they all ultimately failed to show a discernible degree of spin population inversion. Figure 6.16 an example scan: a low frequency, perpendicular magnetic field setup with an estimated magnetic field of approximately 150 mT, with a wire microwave antenna. The raw photocurrent curve of Figure 6.16a shows the microwave pulse leakage in the photocurrent channel. To minimise its effect, the pulse sequence includes a second correction sequence without a probe laser pulse. This is subtracted from the first half of the pulse sequence to cancel out the microwave as well as the pump signal. The resulting corrected trace shows no visible transients from the microwave and pump pulses, thus mostly eliminating any microwave frequency dependent in the frequency spectrum. It does not entirely eliminate the issue, as the microwave leakage still results in a significant increase in the noise floor. The experiment is repeated over a wide microwave range due to uncertainties on the exact magnetic field, and it is repeated with the laser both on and off a D^0X resonance. The smoking gun of spin driving and successful PEDMR would be the presence of a pair of peaks, separated by the phosphorus hyperfine 117.53 MHz [21], but exclusively in the on-resonance scan.

6.4. CONCLUSIONS

This chapter explored the topic of strained donor bound excitons in a magnetic field and the donor spin polarisation induced by the selective D^0X ionisation. This is a key aspect of the D^0X photoconductive technique, allowing for sensitive spin-to-charge conversion of only a few thousand donors, far beyond the sensitivity of traditional magnetic spin detection techniques. Significant spin relaxation is however encountered, preventing lasting spin polarisation and thus for the first time highlighting a potential complication that should be addressed for the photoconductive D^0X detection.

First, microscale photoconductive detection is demonstrated under moderate 100–200 mT magnetic fields both perpendicular to and in the plane of the substrate, with the signal significantly weakened by the Zeeman splitting of the peaks. Notably, this work successfully employs low-cost permanent neodymium magnets for B_0 field generation, as opposed to the usually employed electromagnet coil setup.

Moderate Auger induced donor spin polarisation is demonstrated under a continuous resonant laser pump, but fails to survive the timescales of pulsed laser and microwave sequences. The issue persists down to near microsecond sequences, suggesting a fast, sub-microsecond relaxation dynamic. This is a crucial issue that has not previously reported, suggesting its origin lies in the downscaling. An in-depth analysis of the experimental parameters affecting spin polarisation suggests that the electric fields may be causing fast donor spin relaxation, a topic that should be carefully considered and explored in future donor bound exciton research. Finally, an experimental procedure for a hybrid optical-electrical-microwave pEDMR is explored, but fails to show the expected spin driving resonances, most likely due to the same donor spin relaxation issues highlighted by the dual-laser pump-probe experiments.

Overall, this section successfully demonstrates a spin-polarisation, magnetic field setup for microscale D^0X devices and highlights a novel relaxation dynamic hampering the persistence of donor spin polarisation. By also suggesting potential mitigating tactics such as gated voltage sources, this chapter hopes to be a first step in the successful development of microscale D^0X pEDMR devices.

7. CONCLUSIONS

This thesis explored the novel miniaturisation of photoconductive donor bound exciton readout to the microscale and the few-donor limit employing focused laser scanning microscopy and micro-fabricated devices. The subject is explored in all its key factors, namely the electrical readout, the strained spectral lineshapes resulting from interface strain and finally the implications on the induced polarisation and relaxation of the donor electron spin. Many of the experimental conditions encountered are novel, having the subject previously been limited mostly to large scale, bulk doped detection.

A custom optical setup is developed around a near working distance optical cryostat, with numerical apertures of 0.35 and 0.65 yielding laser spot diameters down to only 2 µm (Airy disk diameter), approaching the diffraction limit. In combination with microfabricated devices and a shallow implanted donor layer, as few as 2000 donors are electrically detected.

Scanning microscopy of near surface donors is further demonstrated with two different techniques: a traditional galvo-scanning setup and a more rudimentary, yet simple and powerful technique combining the motion of a slipstick piezo-actuator and image recognition with a CMOS camera: a widely applicable software positioning technique that should be considered for experimental setups without position feedback hardware.

7.1. ELECTRICAL READOUT AT THE MICROSCALE

Electrical D^0X readout has previously been demonstrated using large device configurations and illuminations areas, with ionised donors in the orders of billions from bulk doped samples [23, 24, 27]. This work demonstrates electrical techniques pertaining to a novel detection regime, with micron-sized illumination areas and donor numbers as low as 2000.

The first important result pertains the choice of contact chemistry. It is found that metal-oxide-silicon (MOS) contacts lead to photocurrents highly sensitive to the Auger ionisation of locally implanted donors, with limited background signal from the bulk residual donors. Contrarily, Schottky metal and pseudo-Ohmic contacts did not display any photocurrent from the local donors, but a defined central, unstrained peak from the residual substrate bulk donors. This is a surprising result as virtually all previous work on electrical D^0X detection successfully employed Schottky metal contacts. The important distinction is that these works all analysed bulk doped, $N_D \geq 10^{15}\text{cm}^{-3}$ substrates, devices with far larger, $\gtrsim 100$ µm contact separations and much larger, 30–2000 µm beam diameters. Peach's work on the D^0X detection of bismuth donors [125, 146] may be an important comparison here, as the only work showing electrical D^0X detection of implanted donors in an intrinsic substrate, employing a probe capacitor setup overall not dissimilar from an MOS contact.

A capacitive, low frequency photocurrent detection technique is developed, with ideal working ranges in the 10–100 kHz range. At low levels of background illumination, the photocurrent is shown to be well modelled with a simple photoresistor-capacitor resonant circuit as proposed by Ross [25]. The simple model breaks down at higher carrier densities, suggesting the need for more complex device modelling, a notoriously difficult task at low freeze-out temperatures. A maximum signal to noise ratio of 25 is achieved over a single-shot 20 ms integration window.

Slow symmetrical rise and fall transients are observed in the photocurrent response, dependent on the carrier density through non-resonant, above-bandgap illumination, suggesting a slow electrical time limiting process. Shallow level impact ionisation is proposed as a potential explanation for the observations, and a possible source of carrier amplification, but further research is necessary on the subject.

Finally, in a bid to explore the bandwidth limits of electrical D^0X detection, detection by radiofrequency LC-resonant reflectometry is explored and successfully demonstrated. A parallel LC resonant matching circuit is assembled following the parallel inductor technique by Ahmed [144] and Schaal [174], showing a resonant D^0X reflectometry response. Reflectometry is employed to demonstrate fast, microsecond D^0X transient detection, albeit with a very small signal. The bulk of the high frequency photo-response is also shown to be dominated by the same slow, symmetrical transients characterising low frequency detection.

The data presented in this chapter will be adapted into a scientific publication to soon be submitted for review.

7.2. D^0X STRAIN MICROSCOPY

The topic of strain is explored extensively in this work due its predominant role in splitting, shifting and broadening the D^0X spectral lines. Strain is especially relevant to micro-fabricated devices due to the large interface strains from the mismatch in the fabrication materials' thermal expansion.

Firstly, the strain effect on the D^0X transition energies is systematically explored in a bulk $^{28}\text{Si}:\text{P}$ sample, to confirm the validity of existing models and experimental parameters in the $\lesssim 10^{-5}$ low strain regime. Employing a previously established technique [115], the D^0X spectrum is recorded by ESR

Hahn echo detection from the optically induced donor spin polarisation under controlled uniaxial strain and variable magnetic field angles. The D^0X transition energies are extracted and fitted to the Pikus-Bir and Zeeman eigenvalues, determining g-tensor and spin-strain parameters consistent with previous literature and theoretical predictions, thus confirming the validity of the existing models in the low strain regime.

Finite element models are computed to analyse the sources and magnitudes of thermal strain in microfabricated devices at liquid helium temperatures, using experimental thermal expansion coefficients derived from literature sources, highlighting moderate tensile strains between device contacts, compressive strain under the contacts and large, $\gtrsim 10^{-4}$ strains at contact edges. Experimental 2D scanning microscopy maps of the D^0X spectrum are recorded for a multitude of device geometries, extracting a map of light-heavy hole peak splitting. Comparison to theoretical maps from FEM solid mechanics simulations yields a remarkable agreement in magnitude and shape near the device centre, with discrepancies in the order of 20 %. The experimental splittings do not match the high FEM peak splittings observed near the contact edges, although this can likely be attributed to the high strain gradients in these regions broadening the peaks below the background floor. A high strain and ~0.5 meV split D^0X spectrum is observed directly underneath a thin thermal oxide and ~2 µm off a metal contact, pushing the limit of near interface D^0X detection.

The microdevice D^0X spectrum is also analysed under linear optical polarisation, displaying a sinusoidal dependence of both light and heavy hole peaks, albeit with amplitudes not matching theoretical predictions, which may suggest the presence of unaccounted shear strain in the devices.

Finally, the development of D^0X detection into a sensitive micro-strain sensing technique is of particular note. This is currently being adapted into a scientific publication which will be submitted for review shortly.

7.3. SPIN POLARISATION IN A MAGNETIC FIELD

A permanent magnet setup is developed to apply magnetic fields to the D^0X devices under the close optical access configuration, both perpendicular and parallel to the device surface and without any resulting peak broadening. Fitting to theory suggests the achievement of magnetic fields up to 200 mT. This demonstrates a valid, low-cost alternative to the popular electromagnet setup, in particular where the latter may not be feasible due to the constraints often imposed by close-access optical cryostats.

A two-laser setup is designed to explore the polarisation of the donor spin population, achieving mild polarisations up to 30 % under continuous resonant pump illumination, recorded by probe amplitude modulation. No lasting spin polarisation is observed in transient pump-probe experiments, suggesting the presence of a source of fast donor spin relaxation. This is investigated under continuous pump-probe conditions, highlighting that higher measurement voltage amplitudes lead to a decrease in the degree of donor spin polarisation. This is problematic as an electric field is necessary for photocurrent measurements. A potential solution may be a gated voltage source generating transient electric detection pulses. Similar investigations highlighted an apparent saturation of the temperature dependent polarisation below ∼6 K, no dependence on above bandgap illumination and a positive relationship with resonant laser power density. The latter is key as it establishes that the issue is not power saturation but indeed some competitive relaxation phenomenon.

Finally, microwave spin driving is explored with both a transmission wire and a broadband, resonant PCB lithographic antenna. Moderate-power microwaves are observed to strongly affect the electrical setup, and no microwave spin polarisation inversion is observed. This suggests the need for a careful redesign and investigation of the electromagnetic interaction between the electrical detection and microwave lines.

7.4. OUTLOOK

This work hopes to prompt further study of silicon donor bound excitons in microscale electrical devices, by introducing sensitive detection techniques and analysing some of the difficulties involved. While several successful techniques are demonstrated that should be a starting point for any future work, some key questions are raised that should be explored before optimisations and practical applications can be considered.

First, the issue of ephemeral donor spin polarisation must be addressed. The primary suspect, electric-field induced relaxation could be addressed by setting up the electrical detection with a voltage acquisition window to be activated during or right after the laser probe. There are indeed complications to do with timings and rise-times, particularly at low frequencies, but they should not be insurmountable.

Regarding the electrical detection itself, the main open question concerns the slow response time of the photocurrent, which can be as low as 20 ms and decreases with carrier density. This also raises questions on the true nature of the photocurrent signal, and whether some level of secondary carrier generation may be occurring.

The topic of high frequency reflectometry was introduced and demonstrated briefly, with a not-perfectly matched resonator. The topic should certainly be explored further, as there is significant margin for improvement. This promising, fast detection technique could unlock crucial experiments such resolving the Auger decay transients and the coherent D^0X driving regime.

The use of donor bound exciton detection for microscopy strain sensing was discussed extensively in Chapter 5, which has been drafted into a scientific article to soon be submitted for review. The subject should certainly be explored further and fully developed into a reliable strain sensing technique for cryogenic semiconductor technologies.

Finally, there is plenty of room to push the process of miniaturisation to smaller devices and the detection sensitivity to fewer donors, with this work having emphasised the importance of donor implantation and MOS contacts. It would certainly be difficult to scale more than an order of magnitude in a thick wafer sample, as the carrier density would begin to approach the residual bulk donor density. Surface-wave interdigitated devices could certainly help in the further localisation of the donor spin, as well as strain as a discriminant for local donor selectivity. SOI wafers would further ease the background signal problem, although they have proved difficult in the past due to the large strain from the bonding process.

BIBLIOGRAPHY

[1] B. E. Kane. "A Silicon-Based Nuclear Spin Quantum Computer". In: *Nature* 393.6681 (May 1998), pp. 133–137. DOI: `10.1038/30156`.

[2] A. M. Tyryshkin, S. Tojo, J. J. L. Morton, H. Riemann, N. V. Abrosimov, P. Becker, H.-J. Pohl, T. Schenkel, M. L. W. Thewalt, K. M. Itoh, and S. A. Lyon. "Electron Spin Coherence Exceeding Seconds in High-Purity Silicon". In: *Nature Materials* 11.2 (Feb. 2012), pp. 143–147. DOI: `10.1038/nmat3182`.

[3] G. Wolfowicz, A. M. Tyryshkin, R. E. George, H. Riemann, N. V. Abrosimov, P. Becker, H.-J. Pohl, M. L. W. Thewalt, S. A. Lyon, and J. J. L. Morton. "Atomic Clock Transitions in Silicon-Based Spin Qubits". In: *Nature Nanotechnology* 8.8 (Aug. 2013), pp. 561–564. DOI: `10.1038/nnano.2013.117`.

[4] K. Saeedi, S. Simmons, J. Z. Salvail, P. Dluhy, H. Riemann, N. V. Abrosimov, P. Becker, H.-J. Pohl, J. J. L. Morton, and M. L. W. Thewalt. "Room-Temperature Quantum Bit Storage Exceeding 39 Minutes Using Ionized Donors in Silicon-28". In: *Science* 342.6160 (Nov. 2013), pp. 830–833. DOI: `10.1126/science.1239584`.

[5] P. Wang, C.-Y. Luan, M. Qiao, M. Um, J. Zhang, Y. Wang, X. Yuan, M. Gu, J. Zhang, and K. Kim. "Single Ion Qubit with Estimated Coherence Time Exceeding One Hour". In: *Nature Communications* 12.1 (Jan. 2021), p. 233. DOI: `10.1038/s41467-020-20330-w`.

[6] C. D. Bruzewicz, J. Chiaverini, R. McConnell, and J. M. Sage. "Trapped-Ion Quantum Computing: Progress and Challenges". In: *Applied Physics Reviews* 6.2 (June 2019), p. 021314. DOI: `10.1063/1.5088164`.

[7] A. Bienfait, J. J. Pla, Y. Kubo, M. Stern, X. Zhou, C. C. Lo, C. D. Weis, T. Schenkel, M. L. W. Thewalt, D. Vion, D. Esteve, B. Julsgaard, K. Mølmer, J. J. L. Morton, and P. Bertet. "Reaching the Quantum Limit of Sensitivity in Electron Spin Resonance". In: *Nature Nanotechnology* 11.3 (Mar. 2016), pp. 253–257. DOI: `10.1038/nnano.2015.282`.

[8] M. Kjaergaard, M. E. Schwartz, J. Braumüller, P. Krantz, J. I.-J. Wang, S. Gustavsson, and W. D. Oliver. "Superconducting Qubits: Current State of Play". In: *Annual Review of Condensed Matter Physics* 11.1 (2020), pp. 369–395. DOI: `10.1146/annurev-conmatphys-031119-050605`.

[9] F. Arute et al. “Quantum Supremacy Using a Programmable Superconducting Processor”. In: *Nature* 574.7779 (Oct. 2019), pp. 505–510. DOI: `10.1038/s41586-019-1666-5`.

[10] P. Haikka, Y. Kubo, A. Bienfait, P. Bertet, and K. Mølmer. “Proposal for Detecting a Single Electron Spin in a Microwave Resonator”. In: *Physical Review A* 95.2 (Feb. 2017), p. 022306. DOI: `10.1103/PhysRevA.95.022306`.

[11] A. Chatterjee, P. Stevenson, S. De Franceschi, A. Morello, N. P. de Leon, and F. Kuemmeth. “Semiconductor Qubits in Practice”. In: *Nature Reviews Physics* 3.3 (Mar. 2021), pp. 157–177. DOI: `10.1038/s42254-021-00283-9`.

[12] B. Weber, Y. H. M. Tan, S. Mahapatra, T. F. Watson, H. Ryu, R. Rahman, L. C. L. Hollenberg, G. Klimeck, and M. Y. Simmons. “Spin Blockade and Exchange in Coulomb-confined Silicon Double Quantum Dots”. In: *Nature Nanotechnology* 9.6 (June 2014), pp. 430–435. DOI: `10.1038/nnano.2014.63`.

[13] M. Urdampilleta, A. Chatterjee, C. C. Lo, T. Kobayashi, J. Mansir, S. Barraud, A. C. Betz, S. Rogge, M. F. Gonzalez-Zalba, and J. J. L. Morton. “Charge Dynamics and Spin Blockade in a Hybrid Double Quantum Dot in Silicon”. In: *Physical Review X* 5.3 (Aug. 2015), p. 031024. DOI: `10.1103/PhysRevX.5.031024`.

[14] P. Harvey-Collard, N. T. Jacobson, M. Rudolph, J. Dominguez, G. A. Ten Eyck, J. R. Wendt, T. Pluym, J. K. Gamble, M. P. Lilly, M. Pioro-Ladrière, and M. S. Carroll. “Coherent Coupling between a Quantum Dot and a Donor in Silicon”. In: *Nature Communications* 8.1 (Oct. 2017), p. 1029. DOI: `10.1038/s41467-017-01113-2`.

[15] A. Yang, M. Steger, T. Sekiguchi, M. L. W. Thewalt, T. D. Ladd, K. M. Itoh, H. Riemann, N. V. Abrosimov, P. Becker, and H.-J. Pohl. “Simultaneous Subsecond Hyperpolarization of the Nuclear and Electron Spins of Phosphorus in Silicon by Optical Pumping of Exciton Transitions”. In: *Physical Review Letters* 102.25 (June 2009), p. 257401. DOI: `10.1103/PhysRevLett.102.257401`.

[16] W. Schmid. “Auger Lifetimes for Excitons Bound to Neutral Donors and Acceptors in Si”. In: *physica status solidi (b)* 84.2 (1977), pp. 529–540. DOI: `10.1002/pssb.2220840216`.

[17] M. Thewalt. “Spectroscopy of Excitons and Shallow Impurities in Isotopically Enriched Silicon—Electronic Properties beyond the Virtual Crystal Approximation”. In: *Solid State Communications* 133.11 (Mar. 2005), pp. 715–725. DOI: `10.1016/j.ssc.2004.12.023`.

[18] A. Yang, M. Steger, D. Karaiskaj, M. L. W. Thewalt, M. Cardona, K. M. Itoh, H. Riemann, N. V. Abrosimov, M. F. Churbanov, A. V. Gusev, A. D. Bulanov, A. K. Kaliteevskii, O. N. Godisov, P. Becker, H.-J. Pohl, J. W. Ager, and E. E. Haller. "Optical Detection and Ionization of Donors in Specific Electronic and Nuclear Spin States". In: *Physical Review Letters* 97.22 (Nov. 2006), p. 227401. DOI: `10.1103/PhysRevLett.97.227401`.

[19] A. Yang, M. Steger, T. Sekiguchi, M. L. W. Thewalt, J. W. Ager, and E. E. Haller. "Homogeneous Linewidth of the P31 Bound Exciton Transition in Silicon". In: *Applied Physics Letters* 95.12 (Sept. 2009), p. 122113. DOI: `10.1063/1.3238268`.

[20] D. Karaiskaj, M. Thewalt, T. Ruf, M. Cardona, H.-J. Pohl, G. Deviatych, P. Sennikov, and H. Riemann. "Photoluminescence of Isotopically Purified Silicon: How Sharp Are Bound Exciton Transitions?" In: *Physical Review Letters* 86.26 (June 2001), pp. 6010–6013. DOI: `10.1103/PhysRevLett.86.6010`.

[21] K. J. Morse, P. Dluhy, J. Huber, J. Z. Salvail, K. Saeedi, H. Riemann, N. V. Abrosimov, P. Becker, H.-J. Pohl, S. Simmons, and M. L. W. Thewalt. "Zero-Field Optical Magnetic Resonance Study of Phosphorus Donors in 28-Silicon". In: *Physical Review B* 97.11 (Mar. 2018), p. 115205. DOI: `10.1103/PhysRevB.97.115205`.

[22] D. F. Nelson, J. D. Cuthbert, P. J. Dean, and D. G. Thomas. "Auger Recombination of Excitons Bound to Neutral Donors in Gallium Phosphide and Silicon". In: *Physical Review Letters* 17.25 (Dec. 1966), pp. 1262–1265. DOI: `10.1103/PhysRevLett.17.1262`.

[23] C. C. Lo, M. Urdampilleta, P. Ross, M. F. Gonzalez-Zalba, J. Mansir, S. A. Lyon, M. L. W. Thewalt, and J. J. L. Morton. "Hybrid Optical–Electrical Detection of Donor Electron Spins with Bound Excitons in Silicon". In: *Nature Materials* 14.5 (May 2015), pp. 490–494. DOI: `10.1038/nmat4250`.

[24] D. P. Franke, M. Szech, F. M. Hrubesch, H. Riemann, N. V. Abrosimov, P. Becker, H.-J. Pohl, K. M. Itoh, M. L. W. Thewalt, and M. S. Brandt. "Electron Nuclear Double Resonance with Donor-Bound Excitons in Silicon". In: *Physical Review B* 94.23 (Dec. 2016), p. 235201. DOI: `10.1103/PhysRevB.94.235201`.

[25] P. Ross, B. C. Rose, C. C. Lo, M. L. Thewalt, A. M. Tyryshkin, S. A. Lyon, and J. J. Morton. "Electron Spin Resonance of P Donors in Isotopically Purified Si Detected by Contactless Photoconductivity". In: *Physical Review Applied* 11.5 (May 2019), p. 054014. DOI: `10.1103/PhysRevApplied.11.054014`.

[26] M. P. Ross. "Bound Exciton-Assisted Spin-to-Charge Conversion of Donors in Silicon". Doctoral. UCL (University College London), July 2017.

[27] T. Loippo, A. Kanniainen, and J. T. Muhonen. “Strain Effects in Phosphorus Bound Exciton Transitions in Silicon”. In: *Physical Review Materials* 7.1 (Jan. 2023), p. 016202. DOI: `10.1103/PhysRevMaterials.7.016202`.

[28] J. Mansir. “The Effects of Strain on Donor Spin Qubits in Silicon”. Doctoral. UCL (University College London), Mar. 2020.

[29] H. Sumikura, K. Nishiguchi, Y. Ono, A. Fujiwara, and M. Notomi. “Bound Exciton Photoluminescence from Ion-implanted Phosphorus in Thin Silicon Layers”. In: *Optics Express* 19.25 (Dec. 2011), p. 25255. DOI: `10.1364/OE.19.025255`.

[30] D. N. Batchelder and R. O. Simmons. “Lattice Constants and Thermal Expansivities of Silicon and of Calcium Fluoride between 6° and 322°K”. In: *The Journal of Chemical Physics* 41.8 (Oct. 1964), pp. 2324–2329. DOI: `10.1063/1.1726266`.

[31] F. Ferrazza. “Crystalline Silicon”. In: *Practical Handbook of Photovoltaics*. Elsevier, 2012, pp. 79–97. DOI: `10.1016/B978-0-12-385934-1.00004-0`.

[32] J. Härkönen, E. Tuovinen, P. Luukka, E. Tuominen, Z. Li, A. Ivanov, E. Verbitskaya, V. Eremin, A. Pirojenko, I. Riihimaki, and A. Virtanen. “Particle Detectors Made of High-Resistivity Czochralski Silicon”. In: *Nuclear Instruments and Methods in Physics Research Section A: Accelerators, Spectrometers, Detectors and Associated Equipment* 541.1-2 (Apr. 2005), pp. 202–207. DOI: `10.1016/j.nima.2005.01.057`.

[33] A. J. McEvoy, T. Markvart, and L. Castañer, eds. *Practical Handbook of Photovoltaics: Fundamentals and Applications*. 2nd ed. Waltham, MA: Academic Press, 2012.

[34] K. Momma and F. Izumi. “VESTA 3 for Three-Dimensional Visualization of Crystal, Volumetric and Morphology Data”. In: *Journal of Applied Crystallography* 44.6 (Dec. 2011), pp. 1272–1276. DOI: `10.1107/S0021889811038970`.

[35] J. R. Chelikowsky and M. L. Cohen. “Electronic Structure of Silicon”. In: *Physical Review B* 10.12 (Dec. 1974), pp. 5095–5107. DOI: `10.1103/PhysRevB.10.5095`.

[36] P. Y. Yu and M. Cardona. *Fundamentals of Semiconductors: Physics and Materials Properties*. Graduate Texts in Physics. Berlin, Heidelberg: Springer Berlin Heidelberg, 2010. DOI: `10.1007/978-3-642-00710-1`.

[37] W. Bludau, A. Onton, and W. Heinke. “Temperature Dependence of the Band Gap of Silicon”. In: *Journal of Applied Physics* 45.4 (Apr. 1974), pp. 1846–1848. DOI: `10.1063/1.1663501`.

[38] M. A. Green. “Intrinsic Concentration, Effective Densities of States, and Effective Mass in Silicon”. In: *Journal of Applied Physics* 67.6 (Mar. 1990), pp. 2944–2954. DOI: `10.1063/1.345414`.

[39] L. E. Ramos, L. K. Teles, L. M. R. Scolfaro, J. L. P. Castineira, A. L. Rosa, and J. R. Leite. “Structural, Electronic, and Effective-Mass Properties of Silicon and Zinc-Blende Group-III Nitride Semiconductor Compounds”. In: *Physical Review B* 63.16 (Apr. 2001), p. 165210. DOI: `10.1103/PhysRevB.63.165210`.

[40] W. C. Dunlap and R. L. Watters. “Direct Measurement of the Dielectric Constants of Silicon and Germanium”. In: *Physical Review* 92.6 (Dec. 1953), pp. 1396–1397. DOI: `10.1103/PhysRev.92.1396`.

[41] Y. P. Varshni. “Temperature Dependence of the Energy Gap in Semiconductors”. In: *Physica* 34.1 (Jan. 1967), pp. 149–154. DOI: `10.1016/0031-8914(67)90062-6`.

[42] M. Cardona, T. A. Meyer, and M. L. W. Thewalt. “Temperature Dependence of the Energy Gap of Semiconductors in the Low-Temperature Limit”. In: *Physical Review Letters* 92.19 (May 2004), p. 196403. DOI: `10.1103/PhysRevLett.92.196403`.

[43] G. G. Macfarlane, T. P. McLean, J. E. Quarrington, and V. Roberts. “Exciton and Phonon Effects in the Absorption Spectra of Germanium and Silicon”. In: *Journal of Physics and Chemistry of Solids* 8 (Jan. 1959), pp. 388–392. DOI: `10.1016/0022-3697(59)90372-5`.

[44] B. Jalali and S. Fathpour. “Silicon Photonics”. In: *Journal of Lightwave Technology* 24.12 (Dec. 2006), pp. 4600–4615. DOI: `10.1109/JLT.2006.885782`.

[45] N. Margalit, C. Xiang, S. M. Bowers, A. Bjorlin, R. Blum, and J. E. Bowers. “Perspective on the Future of Silicon Photonics and Electronics”. In: *Applied Physics Letters* 118.22 (May 2021), p. 220501. DOI: `10.1063/5.0050117`.

[46] S. Nur. “Towards Enhanced Radiative Emission for Optical Read-out of Donor Spins in Silicon”. Doctoral. UCL (University College London), Sept. 2018.

[47] N. Q. Vinh, P. T. Greenland, K. Litvinenko, B. Redlich, A. F. G. van der Meer, S. A. Lynch, M. Warner, A. M. Stoneham, G. Aeppli, D. J. Paul, C. R. Pidgeon, and B. N. Murdin. “Silicon as a Model Ion Trap: Time Domain Measurements of Donor Rydberg States”. In: *Proceedings of the National Academy of Sciences* 105.31 (Aug. 2008), pp. 10649–10653. DOI: `10.1073/pnas.0802721105`.

[48] P. T. Greenland, S. A. Lynch, A. F. G. van der Meer, B. N. Murdin, C. R. Pidgeon, B. Redlich, N. Q. Vinh, and G. Aeppli. “Coherent Control of Rydberg States in Silicon”. In: *Nature* 465.7301 (June 2010), pp. 1057–1061. DOI: `10.1038/nature09112`.

[49] D. D. Awschalom, R. Hanson, J. Wrachtrup, and B. B. Zhou. "Quantum Technologies with Optically Interfaced Solid-State Spins". In: *Nature Photonics* 12.9 (Sept. 2018), pp. 516–527. DOI: `10.1038/s41566-018-0232-2`.

[50] K. J. Morse, R. J. S. Abraham, A. DeAbreu, C. Bowness, T. S. Richards, H. Riemann, N. V. Abrosimov, P. Becker, H.-J. Pohl, M. L. W. Thewalt, and S. Simmons. "A Photonic Platform for Donor Spin Qubits in Silicon". In: *Science Advances* 3.7 (July 2017), e1700930. DOI: `10.1126/sciadv.1700930`.

[51] E. A. Ekimov and M. V. Kondrin. "Vacancy–Impurity Centers in Diamond: Prospects for Synthesis and Applications". In: *Physics-Uspekhi* 60.6 (June 2017), pp. 539–558. DOI: `10.3367/UFNe.2016.11.037959`.

[52] S. Castelletto and A. Boretti. "Silicon Carbide Color Centers for Quantum Applications". In: *Journal of Physics: Photonics* 2.2 (Apr. 2020), p. 022001. DOI: `10.1088/2515-7647/ab77a2`.

[53] S. Simmons. "A Single Silicon Colour Centre Resolved". In: *Nature Electronics* 3.12 (Dec. 2020), pp. 734–735. DOI: `10.1038/s41928-020-00516-2`.

[54] C.-M. Lee, F. Islam, S. Harper, M. A. Buyukkaya, D. Higginbottom, S. Simmons, and E. Waks. "High-Efficiency Single Photon Emission from a Silicon T-Center in a Nanobeam". In: *ACS Photonics* 10.11 (Nov. 2023), pp. 3844–3849. DOI: `10.1021/acsphotonics.3c01142`.

[55] D. A. Neamen. *Semiconductor Physics and Devices: Basic Principles.* 4th ed. New York, NY: McGraw-Hill, 2012.

[56] A. Jüngel. *Transport Equations for Semiconductors.* Vol. 773. Lecture Notes in Physics. Berlin, Heidelberg: Springer, 2009. DOI: `10.1007/978-3-540-89526-8`.

[57] C. Jagannath, Z. W. Grabowski, and A. K. Ramdas. "Linewidths of the Electronic Excitation Spectra of Donors in Silicon". In: *Physical Review B* 23.5 (Mar. 1981), pp. 2082–2098. DOI: `10.1103/PhysRevB.23.2082`.

[58] E. A. Gutierrez-D, M. J. Deen, and C. L. Claeys. *Low Temperature Electronics.* Elsevier, 2001. DOI: `10.1016/B978-0-12-310675-9.X5000-2`.

[59] P. W. Chapman, O. N. Tufte, J. D. Zook, and D. Long. "Electrical Properties of Heavily Doped Silicon". In: *Journal of Applied Physics* 34.11 (Nov. 1963), pp. 3291–3295. DOI: `10.1063/1.1729180`.

[60] W. Kuźmicz. "Ionization of Impurities in Silicon". In: *Solid-State Electronics* 29.12 (Dec. 1986), pp. 1223–1227. DOI: `10.1016/0038-1101(86)90127-9`.

[61] E. Conwell and V. F. Weisskopf. "Theory of Impurity Scattering in Semiconductors". In: *Physical Review* 77.3 (Feb. 1950), pp. 388–390. DOI: `10.1103/PhysRev.77.388`.

[62] H. Brooks and C. Herring. “Scattering by Ionized Impurities in Semiconductors”. In: *Physical Review.* Vol. 83. American Physical Society, 1951, pp. 879–879.

[63] B. K. Ridley. “Reconciliation of the Conwell-Weisskopf and Brooks-Herring Formulae for Charged-Impurity Scattering in Semiconductors: Third-body Interference”. In: *Journal of Physics C: Solid State Physics* 10.10 (May 1977), pp. 1589–1593. DOI: `10.1088/0022-3719/10/10/003`.

[64] D. Caughey and R. Thomas. “Carrier Mobilities in Silicon Empirically Related to Doping and Field”. In: *Proceedings of the IEEE* 55.12 (1967), pp. 2192–2193. DOI: `10.1109/PROC.1967.6123`.

[65] D. Klaassen. “A Unified Mobility Model for Device Simulation—I. Model Equations and Concentration Dependence”. In: *Solid-State Electronics* 35.7 (July 1992), pp. 953–959. DOI: `10.1016/0038-1101(92)90325-7`.

[66] D. B. M. Klaassen. “A Unified Mobility Model for Device Simulation—II. Temperature Dependence of Carrier Mobility and Lifetime”. In: *Solid-State Electronics* 35.7 (July 1992), pp. 961–967. DOI: `10.1016/0038-1101(92)90326-8`.

[67] N. Arora, J. Hauser, and D. Roulston. “Electron and Hole Mobilities in Silicon as a Function of Concentration and Temperature”. In: *IEEE Transactions on Electron Devices* 29.2 (Feb. 1982), pp. 292–295. DOI: `10.1109/T-ED.1982.20698`.

[68] J. M. Dorkel and P. Leturcq. “Carrier Mobilities in Silicon Semi-Empirically Related to Temperature, Doping and Injection Level”. In: *Solid-State Electronics* 24.9 (Sept. 1981), pp. 821–825. DOI: `10.1016/0038-1101(81)90097-6`.

[69] N. Sclar. “Neutral Impurity Scattering in Semiconductors”. In: *Physical Review* 104.6 (Dec. 1956), pp. 1559–1561. DOI: `10.1103/PhysRev.104.1559`.

[70] S. S. Li and W. R. Thurber. “The Dopant Density and Temperature Dependence of Electron Mobility and Resistivity in N-Type Silicon”. In: *Solid-State Electronics* 20.7 (July 1977), pp. 609–616. DOI: `10.1016/0038-1101(77)90100-9`.

[71] R. S. Crandall. “Impurity Photoconductivity and Impact Ionization of Shallow States in Semiconductors”. In: *Journal of Applied Physics* 42.10 (1971), pp. 3933–3938. DOI: `10.1063/1.1659707`.

[72] J. F. Palmier. “Impurity Ionization in n -Type Germanium”. In: *Physical Review B* 6.12 (Dec. 1972), pp. 4557–4571. DOI: `10.1103/PhysRevB.6.4557`.

[73] M. Asche, H. Kostial, and O. G. Sarbey. “Ionization of Low Donor Levels and Recombination of Hot Electrons in N-Si at Low Temperatures”. In: *Physica Status Solidi (b)* 91.2 (1979), pp. 521–530. DOI: `10.1002/pssb.2220910217`.

[74] B. Dierickx, L. Warmerdam, E. Simoen, J. Vermeiren, and C. Claeys. “Model for Hysteresis and Kink Behavior of MOS Transistors Operating at 4.2 K”. In: *IEEE Transactions on Electron Devices* 35.7 (July 1988), pp. 1120–1125. DOI: `10.1109/16.3372`.

[75] B. Dierickx. “Transient Phenomena and Noise in Silicon MOSFETs at Cryogenic Temperatures”. PhD thesis. May 1990. DOI: `10.13140/RG.2.1.1347.8248`.

[76] E. Simoen, B. Dierickx, L. Deferm, and C. Claeys. “Analytical Model for the Current-Voltage Characteristics of a Silicon Resistor at Liquid Helium Temperatures”. In: *Cryogenics* 30.12 (Dec. 1990), pp. 1152–1159. DOI: `10.1016/0011-2275(90)90225-2`.

[77] E. Simoen, B. Dierickx, L. Deferm, C. Claeys, and G. Declerck. “The Charge Transport in a Silicon Resistor at Liquid-Helium Temperatures”. In: *Journal of Applied Physics* 68.8 (Oct. 1990), pp. 4091–4099. DOI: `10.1063/1.346248`.

[78] B. Dierickx, E. Simoen, and G. Declerck. “Small-Signal a.c. Impedance of an Si Resistor at Liquid-Helium Temperatures”. In: *Solid-State Electronics* 34.11 (Nov. 1991), pp. 1215–1224. DOI: `10.1016/0038-1101(91)90060-C`.

[79] E. Simoen, B. Dierickx, C. Claeys, and G. Declerck. “Transient Response of Silicon Devices at 4.2 K. II. Application to the Case of a Metal-Oxide-Semiconductor Transistor”. In: *Semiconductor Science and Technology* 6.9 (Sept. 1991), pp. 905–911. DOI: `10.1088/0268-1242/6/9/012`.

[80] E. Simoen, C. Claeys, A. Czerwinski, and J. Katcki. “Accurate Extraction of the Diffusion Current in Silicon P-n Junction Diodes”. In: *Applied Physics Letters* 72.9 (Mar. 1998), pp. 1054–1056. DOI: `10.1063/1.120962`.

[81] A. Dargys and S. Žurauskas. “Observation of the Transition from Impact-Ionization-Dominated to Field-Ionization-Dominated Impurity Breakdown in Silicon”. In: *Solid State Communications* 52.2 (Oct. 1984), pp. 139–142. DOI: `10.1016/0038-1098(84)90613-6`.

[82] Z. Stanojevic, J. M. Gonzalez-Medina, F. Schanovsky, and M. Karner. “Quasi-Fermi-Based Charge Transport Scheme for Device Simulation in Cryogenic, Wide Bandgap, and High-Voltage Applications”. In: *IEEE Transactions on Electron Devices* 70.2 (Feb. 2023), pp. 708–713. DOI: `10.1109/TED.2022.3232321`.

[83] C. Shen, S. Jahdi, J. Yang, O. Alatise, J. Ortiz-Gonzalez, R. Wu, and P. Mellor. "Impact of Carriers Injection Level on Transients of Discrete and Paralleled Silicon and 4H-SiC NPN BJTs". In: *IEEE Open Journal of the Industrial Electronics Society* 3 (2022), pp. 65–80. DOI: `10.1109/OJIES.2022.3143946`.

[84] Y. Sun, S. E. Thompson, and T. Nishida. *Strain Effect in Semiconductors: Theory and Device Applications.* Boston, MA: Springer US, 2010. DOI: `10.1007/978-1-4419-0552-9`.

[85] M. H. Sadd. *Elasticity: Theory, Applications, and Numerics.* 2nd ed. Malden, MA: Academic Press, 2009.

[86] Z. Liu. "Temperature-Dependent Elastic Constants and Young's Modulus of Silicon Single Crystal". In: *Proceedings of the 11th Mechanical Engineering Design of Synchrotron Radiation Equipment and Instrumentation* MEDSI2020 (2021), 3 pages, 0.567 MB. DOI: `10.18429/JACOW-MEDSI2020-WEPC09`.

[87] J. S. Dai. "Euler–Rodrigues Formula Variations, Quaternion Conjugation and Intrinsic Connections". In: *Mechanism and Machine Theory* 92 (Oct. 2015), pp. 144–152. DOI: `10.1016/j.mechmachtheory.2015.03.004`.

[88] J. S. Smith, A. Budi, M. C. Per, N. Vogt, D. W. Drumm, L. C. L. Hollenberg, J. H. Cole, and S. P. Russo. "Ab Initio Calculation of Energy Levels for Phosphorus Donors in Silicon". In: *Scientific Reports* 7.1 (July 2017), p. 6010. DOI: `10.1038/s41598-017-06296-8`.

[89] E. Tiesinga, P. J. Mohr, D. B. Newell, and B. N. Taylor. "CODATA Recommended Values of the Fundamental Physical Constants: 2018". In: *Reviews of Modern Physics* 93.2 (June 2021), p. 025010. DOI: `10.1103/RevModPhys.93.025010`.

[90] J. M. Luttinger and W. Kohn. "Motion of Electrons and Holes in Perturbed Periodic Fields". In: *Physical Review* 97.4 (Feb. 1955), pp. 869–883. DOI: `10.1103/PhysRev.97.869`.

[91] W. Kohn and J. M. Luttinger. "Hyperfine Splitting of Donor States in Silicon". In: *Physical Review* 97.4 (Feb. 1955), pp. 883–888. DOI: `10.1103/PhysRev.97.883`.

[92] W. Kohn. "Effective Mass Theory in Solids from a Many-Particle Standpoint". In: *Physical Review* 105.2 (Jan. 1957), pp. 509–516. DOI: `10.1103/PhysRev.105.509`.

[93] G. Pica. "Hyperfine Stark Effect of Shallow Donors in Silicon". In: *Physical Review B* 90.19 (2014). DOI: `10.1103/PhysRevB.90.195204`.

[94] A. Debernardi, A. Baldereschi, and M. Fanciulli. "Computation of the Stark Effect in P Impurity States in Silicon". In: *Physical Review B* 74.3 (July 2006), p. 035202. DOI: `10.1103/PhysRevB.74.035202`.

[95] H. T. Hui. “An Improved Effective-Mass-Theory Equation for Phosphorus Doped in Silicon”. In: *Solid State Communications* 154 (Jan. 2013), pp. 19–24. DOI: `10.1016/j.ssc.2012.10.023`.

[96] T. H. Ning and C. T. Sah. “Multivalley Effective-Mass Approximation for Donor States in Silicon. I. Shallow-Level Group-V Impurities”. In: *Physical Review B* 4.10 (Nov. 1971), pp. 3468–3481. DOI: `10.1103/PhysRevB.4.3468`.

[97] S. T. Pantelides and C. T. Sah. “Theory of Localized States in Semiconductors. I. New Results Using an Old Method”. In: *Physical Review B* 10.2 (July 1974), pp. 621–637. DOI: `10.1103/PhysRevB.10.621`.

[98] K. Shindo and H. Nara. “The Effective Mass Equation for the Multi-Valley Semiconductors”. In: *Journal of the Physical Society of Japan* 40.6 (June 1976), pp. 1640–1644. DOI: `10.1143/JPSJ.40.1640`.

[99] C. J. Wellard and L. C. L. Hollenberg. “Donor Electron Wave Functions for Phosphorus in Silicon: Beyond Effective-Mass Theory”. In: *Physical Review B* 72.8 (Aug. 2005), p. 085202. DOI: `10.1103/PhysRevB.72.085202`.

[100] M. Usman, R. Rahman, J. Salfi, J. Bocquel, B. Voisin, S. Rogge, G. Klimeck, and L. L. C. Hollenberg. “Donor Hyperfine Stark Shift and the Role of Central-Cell Corrections in Tight-Binding Theory”. In: *Journal of Physics: Condensed Matter* 27.15 (Apr. 2015), p. 154207. DOI: `10.1088/0953-8984/27/15/154207`.

[101] “Chapter 7 - Silicium”. In: *Handbook of Stable Isotope Analytical Techniques.* Ed. by P. A. de Groot. Amsterdam: Elsevier, Jan. 2009, p. 619. DOI: `10.1016/B978-0-444-51115-7.00007-3`.

[102] P. Becker, H.-J. Pohl, H. Riemann, and N. Abrosimov. “Enrichment of Silicon for a Better Kilogram”. In: *physica status solidi (a)* 207.1 (2010), pp. 49–66. DOI: `10.1002/pssa.200925148`.

[103] J. M. Luttinger. “Quantum Theory of Cyclotron Resonance in Semiconductors: General Theory”. In: *Physical Review* 102.4 (May 1956), pp. 1030–1041. DOI: `10.1103/PhysRev.102.1030`.

[104] G. Feher. “Electron Spin Resonance Experiments on Donors in Silicon. I. Electronic Structure of Donors by the Electron Nuclear Double Resonance Technique”. In: *Physical Review* 114.5 (1959), pp. 1219–1244. DOI: `10.1103/PhysRev.114.1219`.

[105] L. M. Roth. “G Factor and Donor Spin-Lattice Relaxation for Electrons in Germanium and Silicon”. In: *Physical Review* 118.6 (June 1960), pp. 1534–1540. DOI: `10.1103/PhysRev.118.1534`.

[106] M. Usman, H. Huebl, A. R. Stegner, C. D. Hill, M. S. Brandt, and L. C. L. Hollenberg. “Measurements and Atomistic Theory of Electron g -Factor Anisotropy for Phosphorus Donors in Strained Silicon”. In: *Physical Review B* 98.3 (July 2018), p. 035432. DOI: `10.1103/PhysRevB.98.035432`.

[107] W. Kohn and J. M. Luttinger. “Theory of Donor States in Silicon”. In: *Physical Review* 98.4 (May 1955), pp. 915–922. DOI: `10.1103/PhysRev.98.915`.

[108] E. B. Hale and R. L. Mieher. “Shallow Donor Electrons in Silicon. I. Hyperfine Interactions from ENDOR Measurements”. In: *Physical Review* 184.3 (Aug. 1969), pp. 739–750. DOI: `10.1103/PhysRev.184.739`.

[109] M. W. Swift, H. Peelaers, S. Mu, J. J. L. Morton, and C. G. Van de Walle. “First-Principles Calculations of Hyperfine Interaction, Binding Energy, and Quadrupole Coupling for Shallow Donors in Silicon”. In: *npj Computational Materials* 6.1 (Nov. 2020), pp. 1–9. DOI: `10.1038/s41524-020-00448-7`.

[110] G. Feher and E. A. Gere. “Electron Spin Resonance Experiments on Donors in Silicon. II. Electron Spin Relaxation Effects”. In: *Physical Review* 114.5 (June 1959), pp. 1245–1256. DOI: `10.1103/PhysRev.114.1245`.

[111] A. M. Tyryshkin, S. A. Lyon, A. V. Astashkin, and A. M. Raitsimring. “Electron Spin Relaxation Times of Phosphorus Donors in Silicon”. In: *Physical Review B* 68.19 (Nov. 2003), p. 193207. DOI: `10.1103/PhysRevB.68.193207`.

[112] G. Wolfowicz, P.-A. Mortemousque, R. Guichard, S. Simmons, M. L. W. Thewalt, K. M. Itoh, and J. J. L. Morton. “^{29} Si Nuclear Spins as a Resource for Donor Spin Qubits in Silicon”. In: *New Journal of Physics* 18.2 (Feb. 2016), p. 023021. DOI: `10.1088/1367-2630/18/2/023021`.

[113] D. K. Wilson and G. Feher. “Electron Spin Resonance Experiments on Donors in Silicon. III. Investigation of Excited States by the Application of Uniaxial Stress and Their Importance in Relaxation Processes”. In: *Physical Review* 124.4 (Nov. 1961), pp. 1068–1083. DOI: `10.1103/PhysRev.124.1068`.

[114] H. S. Tan and T. G. Castner. “Piezocapacitance Measurements of Phosphorous- and Antimony-Doped Silicon: Uniaxial Strain-Dependent Donor Polarizabilities”. In: *Physical Review B* 23.8 (Apr. 1981), pp. 3983–3999. DOI: `10.1103/PhysRevB.23.3983`.

[115] J. Mansir, P. Conti, Z. Zeng, J. J. Pla, P. Bertet, M. W. Swift, C. G. Van De Walle, M. L. W. Thewalt, B. Sklenard, Y. M. Niquet, and J. J. L. Morton. “Linear Hyperfine Tuning of Donor Spins in Silicon Using Hydrostatic Strain”. In: *Physical Review Letters* 120.16 (Apr. 2018), p. 167701. DOI: `10.1103/PhysRevLett.120.167701`.

[116] T. G. Castner and H. S. Tan. “Uniaxial Strain-Dependent Shallow Donor Polarizabilities. II. A New Many-Valley Theoretical Formulation”. In: *Physical Review B* 23.8 (Apr. 1981), pp. 4000–4012. DOI: `10.1103/PhysRevB.23.4000`.

[117] J. Frenkel. “On the Transformation of Light into Heat in Solids. II”. In: *Physical Review* 37.10 (May 1931), pp. 1276–1294. DOI: `10.1103/PhysRev.37.1276`.

[118] J. Frenkel. “On the Transformation of Light into Heat in Solids. I”. In: *Physical Review* 37.1 (Jan. 1931), pp. 17–44. DOI: `10.1103/PhysRev.37.17`.

[119] G. H. Wannier. “The Structure of Electronic Excitation Levels in Insulating Crystals”. In: *Physical Review* 52.3 (Aug. 1937), pp. 191–197. DOI: `10.1103/PhysRev.52.191`.

[120] N. F. Mott. “Conduction in Polar Crystals. II. The Conduction Band and Ultra-Violet Absorption of Alkali-Halide Crystals”. In: *Transactions of the Faraday Society* 34.0 (Jan. 1938), pp. 500–506. DOI: `10.1039/TF9383400500`.

[121] A. Stoneham. “BOUND EXCITONS”. In: *Theory of Defects in Solids: Electronic Structure of Defects in Insulators and Semiconductors*. Ed. by A. M. Stoneham. Oxford University Press, Feb. 2001. DOI: `10.1093/acprof:oso/9780198507802.003.0026`.

[122] E. Rashba and E. G. Gurgenishvili. “Edge Absorption Theory in Semiconductors”. In: *Soviet Physics-Solid State* 4 (1962), p. 759.

[123] P. J. Dean, W. F. Flood, and G. Kaminsky. “Absorption Due to Bound Excitons in Silicon”. In: *Physical Review* 163.3 (Nov. 1967), pp. 721–725. DOI: `10.1103/PhysRev.163.721`.

[124] W. Schmid. “Experimental Comparison of Localized and Free Carrier Auger Recombination in Silicon”. In: *Solid-State Electronics* 21.11 (Nov. 1978), pp. 1285–1287. DOI: `10.1016/0038-1101(78)90194-6`.

[125] T. Peach, K. Stockbridge, J. Li, K. P. Homewood, M. A. Lourenco, S. Chick, M. A. Hughes, B. N. Murdin, and S. K. Clowes. “Enhanced Diffusion and Bound Exciton Interactions of High Density Implanted Bismuth Donors in Silicon”. In: *Applied Physics Letters* 115.7 (Aug. 2019), p. 072102. DOI: `10.1063/1.5115835`.

[126] A. K. Bhattacharjee and S. Rodriguez. “Group-Theoretical Study of the Zeeman Effect of Acceptors in Silicon and Germanium”. In: *Physical Review B* 6.10 (Nov. 1972), pp. 3836–3856. DOI: `10.1103/PhysRevB.6.3836`.

[127] Y. Fang, P. Philippopoulos, D. Culcer, W. A. Coish, and S. Chesi. “Recent Advances in Hole-Spin Qubits”. In: *Materials for Quantum Technology* 3.1 (Mar. 2023), p. 012003. DOI: `10.1088/2633-4356/acb87e`.

[128] K. L. Litvinenko, J. Li, N. Stavrias, A. J. Meaney, P. C. M. Christianen, H. Engelkamp, K. P. Homewood, C. R. Pidgeon, and B. N. Murdin. “The Quadratic Zeeman Effect Used for State-Radius Determination in Neutral Donors and Donor Bound Excitons in Si:P”. In: *Semiconductor Science and Technology* 31.4 (Apr. 2016), p. 045007. DOI: `10.1088/0268-1242/31/4/045007`.

[129] G. Bir, E. Butikov, and G. Pikus. “Spin and Combined Resonance on Acceptor Centres in Ge and Si Type Crystals—II”. In: *Journal of Physics and Chemistry of Solids* 24.12 (Dec. 1963), pp. 1475–1486. DOI: `10.1016/0022-3697(63)90087-8`.

[130] G. Bir, E. Butikov, and G. Pikus. “Spin and Combined Resonance on Acceptor Centres in Ge and Si Type Crystals—I”. In: *Journal of Physics and Chemistry of Solids* 24.12 (Dec. 1963), pp. 1467–1474. DOI: `10.1016/0022-3697(63)90086-6`.

[131] G. Bradski. “The OpenCV Library”. In: *Dr. Dobb’s Journal of Software Tools* (2000).

[132] S. Schaal. “Scalable and High-Sensitivity Readout of Silicon Quantum Devices”. Doctoral. UCL (University College London), Jan. 2020.

[133] J. H. Nielsen et al. *QCoDeS/Qcodes: QCoDeS 0.42.1*. Zenodo. Nov. 2023. DOI: `10.5281/zenodo.10159544`.

[134] H. Lee and B. Van Zeghbroeck. “A Novel High-Speed Silicon MSM Photodetector Operating at 830 Nm Wavelength”. In: *IEEE Electron Device Letters* 16.5 (May 1995), pp. 175–177. DOI: `10.1109/55.382231`.

[135] A. Grillo and A. Di Bartolomeo. “A Current–Voltage Model for Double Schottky Barrier Devices”. In: *Advanced Electronic Materials* 7.2 (Feb. 2021), p. 2000979. DOI: `10.1002/aelm.202000979`.

[136] C. Liu, W. Liu, M. Lee, W. Kuo, and B. Hsu. “A Novel Photodetector Using MOS Tunneling Structures”. In: *IEEE Electron Device Letters* 21.6 (June 2000), pp. 307–309. DOI: `10.1109/55.843159`.

[137] D. F. Blossey. “Wannier Exciton in an Electric Field. I. Optical Absorption by Bound and Continuum States”. In: *Physical Review B* 2.10 (Nov. 1970), pp. 3976–3990. DOI: `10.1103/PhysRevB.2.3976`.

[138] R. Rahman, J. Verduijn, Y. Wang, C. Yin, G. De Boo, G. Klimeck, and S. Rogge. *Bulk and Sub-Surface Donor Bound Excitons in Silicon under Electric Fields*. Sept. 2015. arXiv: `1510.00065 [cond-mat]`.

[139] H. Weman, Q. X. Zhao, and B. Monemar. “Impact Ionization and Electric Field Quenching of Photoluminescence in Silicon”. In: *Hot Carriers in Semiconductors*. Elsevier, 1988, pp. 791–794. DOI: `10.1016/B978-0-08-036237-3.50111-X`.

[140] R. J. Schoelkopf, P. Wahlgren, A. A. Kozhevnikov, P. Delsing, and D. E. Prober. “The Radio-Frequency Single-Electron Transistor (RF-SET): A Fast and Ultrasensitive Electrometer”. In: *Science* 280.5367 (May 1998), pp. 1238–1242. DOI: `10.1126/science.280.5367.1238`.

[141] M. C. Cassidy, A. S. Dzurak, R. G. Clark, K. D. Petersson, I. Farrer, D. A. Ritchie, and C. G. Smith. “Single Shot Charge Detection Using a Radio-Frequency Quantum Point Contact”. In: *Applied Physics Letters* 91.22 (Nov. 2007), p. 222104. DOI: `10.1063/1.2809370`.

[142] S. Schaal, I. Ahmed, J. A. Haigh, L. Hutin, B. Bertrand, S. Barraud, M. Vinet, C.-M. Lee, N. Stelmashenko, J. W. A. Robinson, J. Y. Qiu, S. Hacohen-Gourgy, I. Siddiqi, M. F. Gonzalez-Zalba, and J. J. L. Morton. “Fast Gate-Based Readout of Silicon Quantum Dots Using Josephson Parametric Amplification”. In: *Physical Review Letters* 124.6 (Feb. 2020), p. 067701. DOI: `10.1103/PhysRevLett.124.067701`.

[143] D. M. Pozar. *Microwave Engineering.* 4th ed. Hoboken, NJ: Wiley, 2012.

[144] I. Ahmed, J. A. Haigh, S. Schaal, S. Barraud, Y. Zhu, C.-m. Lee, M. Amado, J. W. A. Robinson, A. Rossi, J. J. L. Morton, and M. F. Gonzalez-Zalba. “Radio-Frequency Capacitive Gate-Based Sensing”. In: *Physical Review Applied* 10.1 (July 2018), p. 014018. DOI: `10.1103/PhysRevApplied.10.014018`.

[145] A. Yang, M. Steger, H. J. Lian, M. L. W. Thewalt, M. Uemura, A. Sagara, K. M. Itoh, E. E. Haller, J. W. Ager, S. A. Lyon, M. Konuma, and M. Cardona. “High-Resolution Photoluminescence Measurement of the Isotopic-Mass Dependence of the Lattice Parameter of Silicon”. In: *Physical Review B* 77.11 (Mar. 2008), p. 113203. DOI: `10.1103/PhysRevB.77.113203`.

[146] T. Peach, K. Homewood, M. Lourenco, M. Hughes, K. Saeedi, N. Stavrias, J. Li, S. Chick, B. Murdin, and S. Clowes. “The Effect of Lattice Damage and Annealing Conditions on the Hyperfine Structure of Ion Implanted Bismuth Donors in Silicon”. In: *Advanced Quantum Technologies* 1.2 (Oct. 2018), p. 1800038. DOI: `10.1002/qute.201800038`.

[147] A. Blacha, H. Presting, and M. Cardona. “Deformation Potentials of k = 0 States of Tetrahedral Semiconductors”. In: *physica status solidi (b)* 126.1 (1984), pp. 11–36. DOI: `10.1002/pssb.2221260102`.

[148] M. L. W. Thewalt and J. A. Rostworowski. “Effects of Uniaxial Stress on the Luminescence Lines Due to Multiexciton Complexes Bound to Phosphorus in Silicon”. In: *Physical Review Letters* 41.12 (Sept. 1978), pp. 808–812. DOI: `10.1103/PhysRevLett.41.808`.

[149] J. Johansson, P. Nation, and F. Nori. “QuTiP: An Open-Source Python Framework for the Dynamics of Open Quantum Systems”. In: *Computer Physics Communications* 183.8 (Aug. 2012), pp. 1760–1772. DOI: `10.1016/j.cpc.2012.02.021`.

[150] J. Johansson, P. Nation, and F. Nori. “QuTiP 2: A Python Framework for the Dynamics of Open Quantum Systems”. In: *Computer Physics Communications* 184.4 (Apr. 2013), pp. 1234–1240. DOI: `10.1016/j.cpc.2012.11.019`.

[151] T. Middelmann, A. Walkov, G. Bartl, and R. Schödel. “Thermal Expansion Coefficient of Single-Crystal Silicon from 7 K to 293 K”. In: *Physical Review B* 92.17 (Nov. 2015), p. 174113. DOI: `10.1103/PhysRevB.92.174113`.

[152] H. Watanabe, N. Yamada, and M. Okaji. “Linear Thermal Expansion Coefficient of Silicon from 293 to 1000 K”. In: *International Journal of Thermophysics* 25.1 (Jan. 2004), pp. 221–236. DOI: `10.1023/B:IJOT.0000022336.83719.43`.

[153] F. R. Kroeger and C. A. Swenson. “Absolute Linear Thermal-Expansion Measurements on Copper and Aluminum from 5 to 320 K”. In: *Journal of Applied Physics* 48.3 (Mar. 1977), pp. 853–864. DOI: `10.1063/1.323746`.

[154] A. J. C. Wilson. “The Thermal Expansion of Aluminium from 0 to 650 C”. In: *Proceedings of the Physical Society* 53.3 (May 1941), pp. 235–244. DOI: `10.1088/0959-5309/53/3/305`.

[155] G. K. White. “Thermal Expansion of Reference Materials: Copper, Silica and Silicon”. In: *Journal of Physics D: Applied Physics* 6.17 (Nov. 1973), pp. 2070–2078. DOI: `10.1088/0022-3727/6/17/313`.

[156] T. A. Hahn, R. K. Kirby, H. C. Wolfe, M. G. Graham, and H. E. Hagy. “Thermal Expansion of Fused Silica from 80 to 1000 K - Standard Reference Material 739”. In: *Proceedings of the 1971 Thermal Expansion Symposium*. Corning, New York (USA), 1972, pp. 13–24. DOI: `10.1063/1.2948551`.

[157] M. M. De Lima, R. G. Lacerda, J. Vilcarromero, and F. C. Marques. “Coefficient of Thermal Expansion and Elastic Modulus of Thin Films”. In: *Journal of Applied Physics* 86.9 (Nov. 1999), pp. 4936–4942. DOI: `10.1063/1.371463`.

[158] W. Fang and C.-Y. Lo. “On the Thermal Expansion Coefficients of Thin Films”. In: *Sensors and Actuators A: Physical* 84.3 (Sept. 2000), pp. 310–314. DOI: `10.1016/S0924-4247(00)00311-3`.

[159] C. Tsou, Y.-S. Huang, H.-C. Li, and T.-H. Lai. “Determination of Thermal Expansion Coefficient of Thermal Oxide”. In: *Sensors and Materials* 17.8 (2005).

[160] G. Carlotti, P. Colpani, D. Piccolo, S. Santucci, V. Senez, G. Socino, and L. Verdini. “Measurement of the Elastic and Viscoelastic Properties of Dielectric Films Used in Microelectronics”. In: *Thin Solid Films* 414.1 (July 2002), pp. 99–104. DOI: `10.1016/S0040-6090(02)00430-3`.

[161] L. M. Mack, A. Reisman, and P. K. Bhattacharya. “Stress Measurements of Thermally Grown Thin Oxides on (100) Si Substrates”. In: *Journal of The Electrochemical Society* 136.11 (Nov. 1989), pp. 3433–3437. DOI: `10.1149/1.2096466`.

[162] C. Mader, M. Kessler, U. Eitner, and R. Brendel. “Temperature of Silicon Wafers during In-Line High-Rate Evaporation of Aluminum”. In: *Solar Energy Materials and Solar Cells* 95.11 (Nov. 2011), pp. 3047–3053. DOI: `10.1016/j.solmat.2011.06.031`.

[163] M. Hasani, G. Klaassen, Z. Marvi, M. Pustylnik, and J. Beckers. “Quantum Dot Photoluminescence as Charge Probe for Plasma Exposed Surfaces”. In: *Journal of Physics D: Applied Physics* 56.2 (Dec. 2022), p. 025202. DOI: `10.1088/1361-6463/aca549`.

[164] S. Doniach and M. Sunjic. “Many-Electron Singularity in X-ray Photoemission and X-ray Line Spectra from Metals”. In: *Journal of Physics C: Solid State Physics* 3.2 (Feb. 1970), pp. 285–291. DOI: `10.1088/0022-3719/3/2/010`.

[165] A. L. Stancik and E. B. Brauns. “A Simple Asymmetric Lineshape for Fitting Infrared Absorption Spectra”. In: *Vibrational Spectroscopy* 47.1 (May 2008), pp. 66–69. DOI: `10.1016/j.vibspec.2008.02.009`.

[166] M. J. Gullans and J. M. Taylor. “Optical Control of Donor Spin Qubits in Silicon”. In: *Physical Review B* 92.19 (Nov. 2015), p. 195411. DOI: `10.1103/PhysRevB.92.195411`.

[167] M. Cardona, T. A. Meyer, and M. L. W. Thewalt. “Temperature Dependence of the Energy Gap of Semiconductors in the Low-Temperature Limit”. In: *Physical Review Letters* 92.19 (May 2004), p. 196403. DOI: `10.1103/PhysRevLett.92.196403`.

[168] P. Lautenschlager, P. B. Allen, and M. Cardona. “Temperature Dependence of Band Gaps in Si and Ge”. In: *Physical Review B* 31.4 (Feb. 1985), pp. 2163–2171. DOI: `10.1103/PhysRevB.31.2163`.

[169] D. K. Park, S. Park, H. Jee, and S. Lee. “Electron Spin Relaxations of Phosphorus Donors in Bulk Silicon under Large Electric Field”. In: *Scientific Reports* 9.1 (Feb. 2019), p. 2951. DOI: `10.1038/s41598-019-39613-4`.

[170] H. Weman, Q. X. Zhao, and B. Monemar. “Electric-Field-Induced Quenching of Shallow and Deep Bound Excitons in Silicon”. In: *Physical Review B* 38.9 (Sept. 1988), pp. 6185–6190. DOI: `10.1103/PhysRevB.38.6185`.

[171] K. Sasaki, Y. Monnai, S. Saijo, R. Fujita, H. Watanabe, J. Ishi-Hayase, K. M. Itoh, and E. Abe. “Broadband, Large-Area Microwave Antenna for Optically Detected Magnetic Resonance of Nitrogen-Vacancy Centers in Diamond”. In: *Review of Scientific Instruments* 87.5 (May 2016), p. 053904. DOI: `10.1063/1.4952418`.

[172] E. Kupce and R. Freeman. “Adiabatic Pulses for Wideband Inversion and Broadband Decoupling”. In: *Journal of Magnetic Resonance, Series A* 115.2 (Aug. 1995), pp. 273–276. DOI: `10.1006/jmra.1995.1179`.

[173] S. J. Hile, L. Fricke, M. G. House, E. Peretz, C. Y. Chen, Y. Wang, M. Broome, S. K. Gorman, J. G. Keizer, R. Rahman, and M. Y. Simmons. “Addressable Electron Spin Resonance Using Donors and Donor Molecules in Silicon”. In: *Science Advances* 4.7 (July 2018), eaaq1459. DOI: `10.1126/sciadv.aaq1459`.

[174] S. Schaal, S. Barraud, J. J. L. Morton, and M. F. Gonzalez-Zalba. “Conditional Dispersive Readout of a CMOS Single-Electron Memory Cell”. In: *Physical Review Applied* 9.5 (May 2018), p. 054016. DOI: `10.1103/PhysRevApplied.9.054016`.

Appendices

A. Full Strained bulk ^{28}Si D^{0}X

This appendix section includes the full, angle dependent strained fitted spectra from Section 5.1.

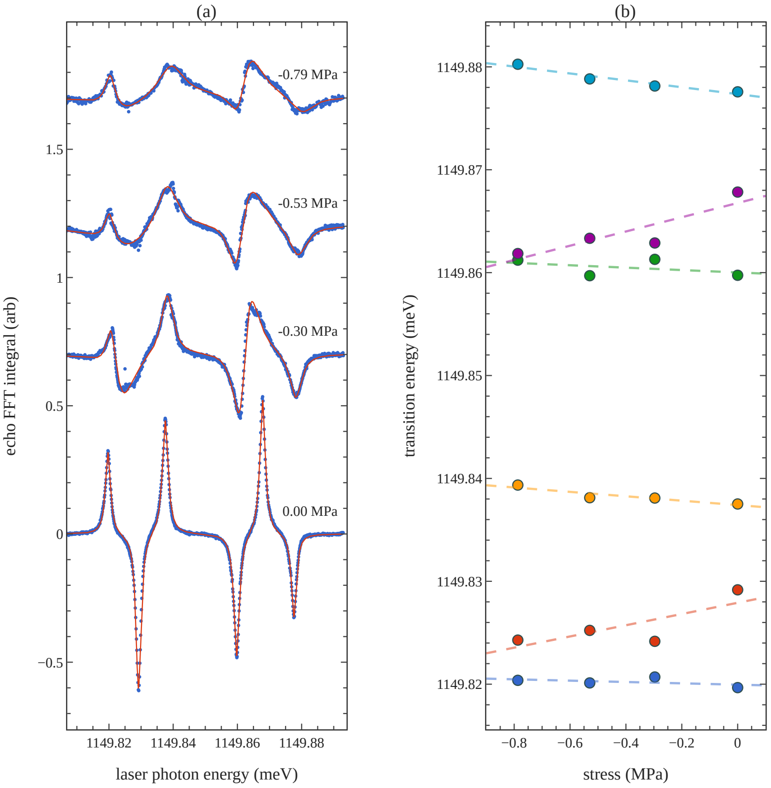

Figure A.1: Strained D^{0}X spectra with $\theta_B = 0°$, ie $\boldsymbol{B} \parallel [001]$

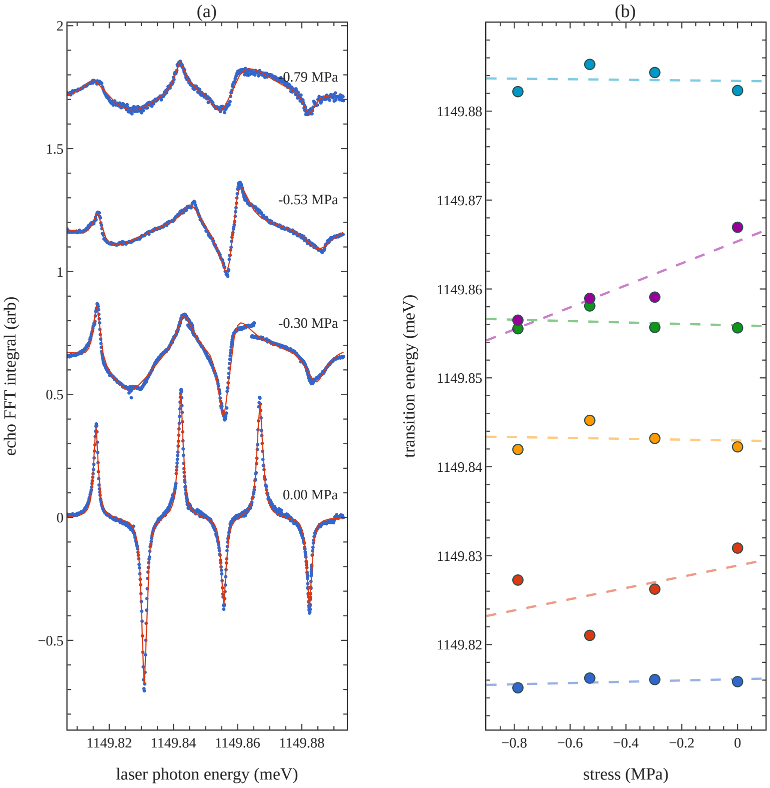

Figure A.2: Strained D^0X spectra with $\theta_B = 30°$

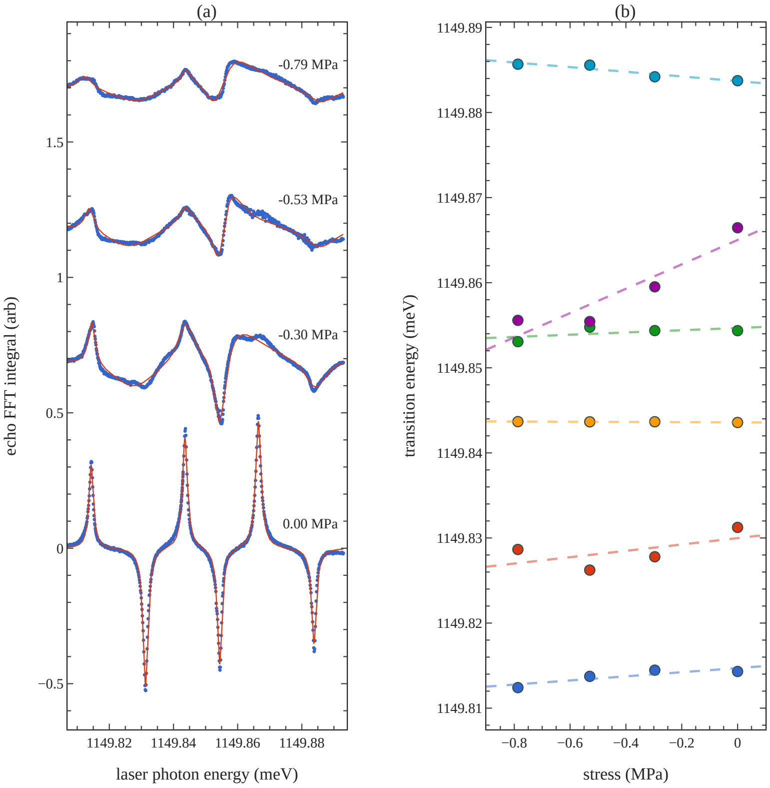

Figure A.3: Strained D^0X spectra with $\theta_B = 45°$

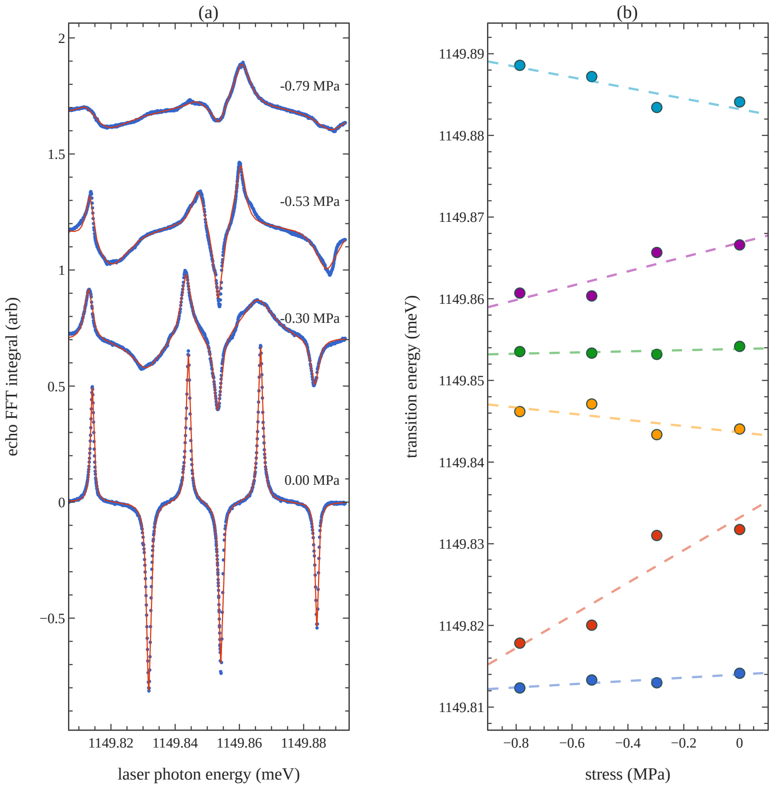

Figure A.4: Strained D^{0}X spectra with $\theta_B = 60°$

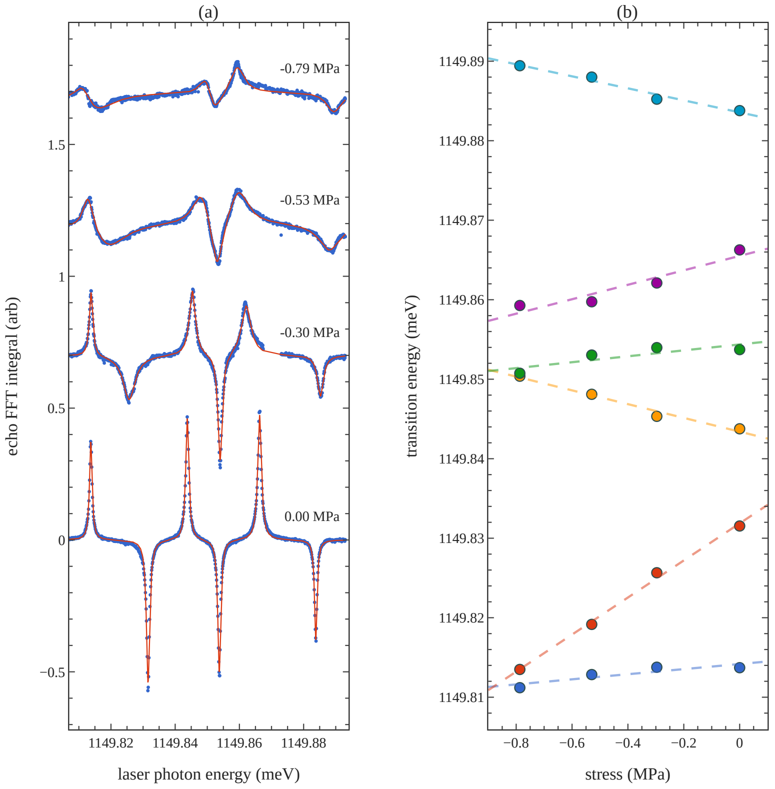

Figure A.5: Strained D^{0}X spectra with $\theta_B = 90°$, ie $\boldsymbol{B} \parallel [1\bar{1}0]$

B. D^0X Reflectometry on a Bulk Doped Substrate

This thesis focused entirely on implanted donor devices, as the thin donor layer allows for the accurate localisation of very few donors. However, ion implantation is possibly the least accessible process of an otherwise standard fabrication that could be replicated in most modern cleanrooms with a commercial float-zone silicon wafer. It is therefore of great interest to understand the behaviour of D^0X readout in devices fabricated on a commercial doped silicon substrate.

This appendix section briefly explores the subject of near-surface D^0X detection in a bulk doped substrate, employing a $20 \times 100\,\mu\text{m}$ MOS device fabricated on a $10^{15}\,\text{cm}^{-3}$ Si : P float-zone silicon wafer and the reflectometry detection techniques discussed in Section 4.3.

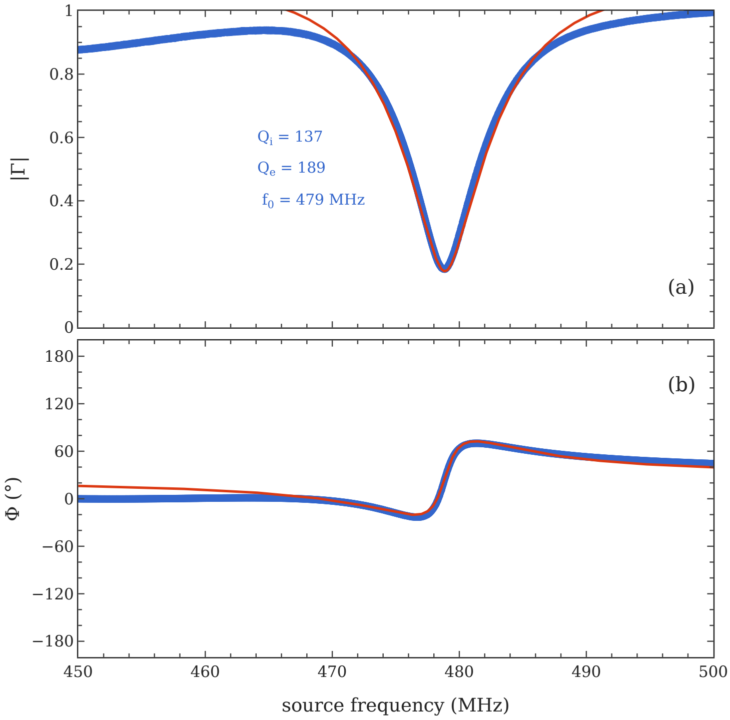

Figure B.1: Reflectometry and fitting from a cold LC resonator connected to a $20 \times 100\,\mu\text{m}$ device (a) amplitude $|\Gamma|$ (b) phase Φ.

Figure B.1 shows the cold resonance of the LC matching circuit connected to the silicon device, with a good impedance, slightly under-coupled match and a high Q-factor over 100. This shows that, despite the higher carrier density arising from the bulk doping, the device resistance is still sufficiently high to achieve high Q-factor LC resonators, which is not necessarily surprising as the majority of donors are expected to be thermally frozen in the bound D^0 state.

A zero-magnetic field laser wavelength scan shows a strong resonance reflectometry response, which can be observed in Figure B.2a. Notably, the spectrum shows two pairs of peaks with a large $\sim$40 µeV splitting. This is compatible with a large $\sim 10^{-5}$ strain comparable with that observed in the ion implanted devices explored in the main body of this thesis, thus suggesting that the D^0X signal is originating from near-surface donors and not from the bulk. Less strained bulk donors would yield a single central peak or a very small ≤ 10 µeV peak splitting as shown in Section 4.1.1.

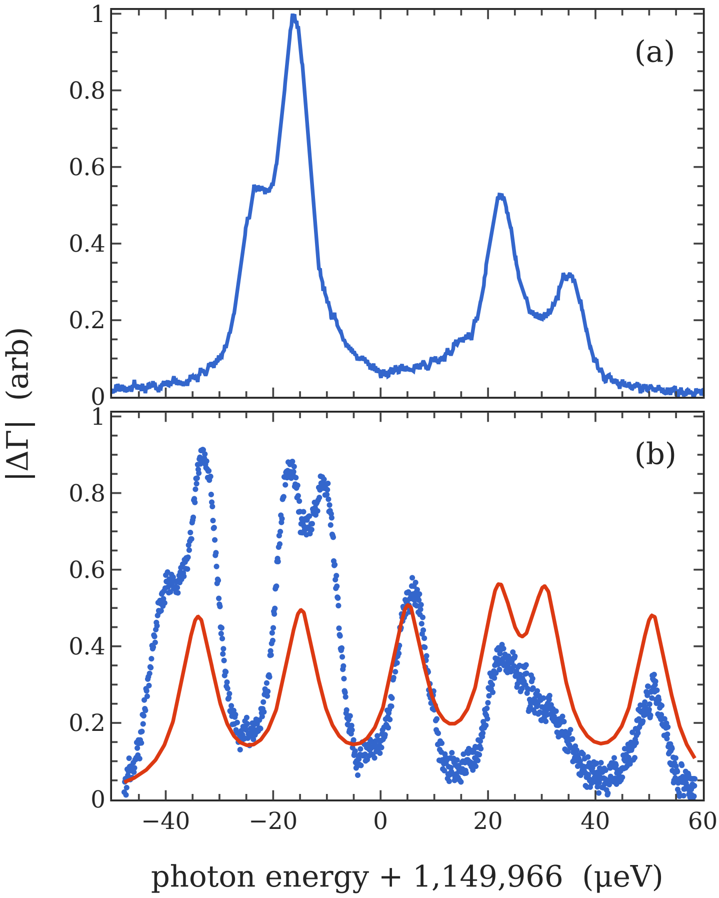

Figure B.2: D^0X strained spectra of a 20×100 µm device on doped Si:P substrate. (a) zero-field. (b) $B \approx 173$mT magnetic field spectrum, with $\boldsymbol{B} \parallel \boldsymbol{E}$ configuration.

The two peaks further splitting in relatively narrow pairs of peaks is a surprising result, as a gaussian peak broadening would naturally be expected, suggesting the presence of two depths with relatively low strain gradients forming two distinct strained donor populations. Notably, the laser off the device does not yield a single central bulk peak, but rather a much weaker spectrum similar to the on-device one, suggesting that the signal is rather from laser reflections on the device than from background donors.

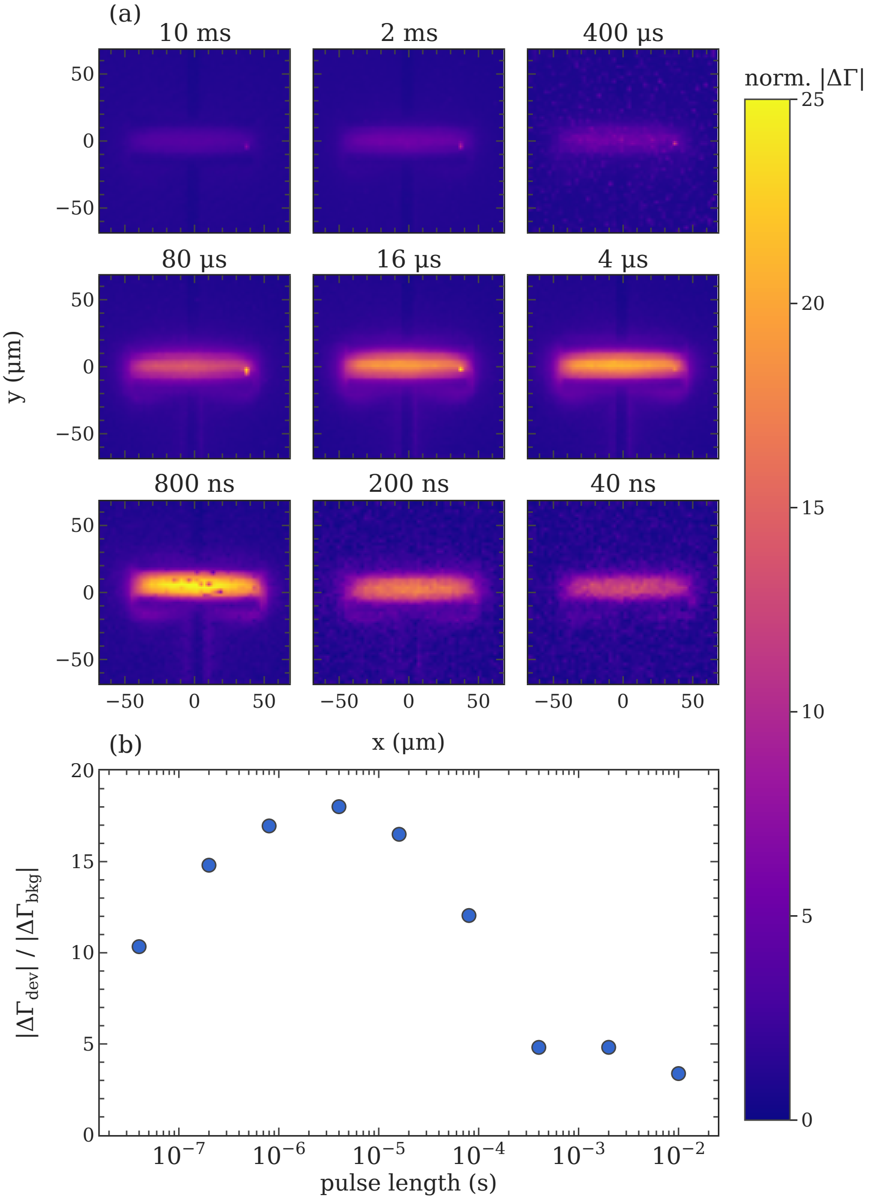

Figure B.3: Pulse length dependent D^0X reflectometry scanning microscopy map. (a) Scanning microscopy maps, reflectometry amplitude normalised to the background average. (b) Plot of the device to background signal ratio against laser pulse length.

Figure B.2b shows the same device, now with a magnetic field of along the capacitor contacts. A theoretical fit with a free magnetic field parameter yields an estimated ∼173 mT, although it naturally cannot account for the spatial peak splitting which is still visible, particularly in the two leftmost peaks.

The high bandwidth of reflectometry detection also allows for an interesting analysis of the crucial local donor signal selectivity. The galvo scanning mirrors are used to perform a 2-dimensional reflectometry map under a wide range or resonant laser pulse lengths. The result is shown in Figure B.3, with a very clear, strong central signal between the metal contacts. The ratio between on-device and off-device photo reflectometry response for long, millisecond laser pulse sequences is a low factor of 3, but increases significantly when short laser pulses are employed, with a maximum of $\sim$25 for a laser pulse length of 4 µs. The ratio decrease below this pulse length is most likely due to the actual response speed limit of the local donors, which was observed to be $\sim$2 µs in the ion implanted devices. Useful on-off ratios are still observed all the way down to a 40 ns pulse length, approaching the AOM risetime and exceeding the Auger decay rate.

Overall, Figure B.3 shows a strong local selectivity of the D^0X reflectometry signal, which can be further enhanced with fast, microsecond laser pulsing, taking advantage of the high reflectometry detection bandwidth. This is hopefully a useful result for future D^0X investigations, as it shows that local, microscale D^0X detection can also be achieved in commercial bulk doped substrates. Without ion implantation, the fabrication can be performed in most modern cleanrooms with regular procedures such as photolithography and thin layer metal deposition. These devices' oxide is a dry growth oxide, however more commonly available processes such as atomic layer deposition can potentially be employed instead.